Exact nonlinear dynamics of Spinor BECs applied to nematic quenches

Luke Michael Symes

Te Whare Wānanga o Otāgo

NEW ZEALAND

a thesis submitted for the degree of

Doctor of Philosophy

at the University of Otago, Dunedin,

New Zealand.

July 6, 2018

Abstract

In this thesis we study the nonlinear dynamics of spin-1 and spin-2 Bose-Einstein condensates, with particular application to antiferromagnetic systems exhibiting nematic (beyond magnetic) order. Firstly, we give a derivation of the spinor energy functionals with a focus on the connections between the nonlinear terms. We derive a hierarchy of nonlinear irreducible multipole observables sensitive to different levels of nematic order, and explore the various nematic states in terms of their multipolar order, representations of their symmetries, and topological defects.

We then develop an exact solution to the nonlinear dynamics of spinor Bose-Einstein condensates. We use this solution to construct efficient and accurate numerical algorithms to evolve the spinor Gross-Pitaevskii equation in time. We demonstrate the advantages of our algorithms with several 1D numerical test problems, comparing with existing methods in the literature.

We apply our numerical methods to simulating quenches of the condensate between various antiferromagnetic phases for spin-1 and spin-2. For spin-1, we carry out quenches for a theoretical uniform system in 2D, and then specialize to the parameters used in a recent harmonically trapped experiment in 3D. We connect the long-time coarsening growth law of the relevant order parameter to the decay of half-quantum vortices, which are the relevant topological defects of the ground state.

For the spin-2 system, we investigate a novel quench from two different quadrupolar-nematic phases to an octupolar-nematic "cyclic" phase which supports 1/3 fractional vortices. We develop appropriate order parameter observables which couple to the spin and superfluid currents generated by these defects, and show that a new growth law appears with exponent 1/3.

Acknowledgements

I would like to thank everyone who helped me while I worked on my PhD. To my supervisors Blair Blakie, Ashton Bradley, and Danny Baillie, thank you for your support, wisdom, and enthusiasm as I worked with you discovering new things, wrestling with code, and turning interesting results into publications.

Thanks to my colleagues Lewis Williamson, Jeremy Lee-Hand, and Xiaoquan Yu. Also, to the people in my research group and in the quantum theory office: thanks to all for your interesting, challenging, and fruitful discussions, and for being a friendly & supportive bunch.

Thanks to Magnus Borgh for hosting me at the University of East Anglia & for collaborating with me on the spin-2 system. Thanks to Ana Maria Rey for hosting me at JILA (University of Colorado Boulder) as I visited Blair on his sabbatical. Thanks to Blair for funding my scholarly travels over the past three years to France, South Korea, the US, and the UK.

Finally, thanks to my friends and family, in particular my partner Alex. Thanks for getting me through periods of existential angst and the struggles before scientific breakthrough, and being accepting of my highbrow musings at the boundaries of the spheres of knowledge. Thank you all immensely for supporting me, as I traversed the often challenging but always interesting PhD journey.

Contents

Part I

Nonlinear interactions & spinor phases

Chapter 1

Introduction and background

1.1 What is spin?

Most of us can intuitively grasp the concept of a rotation in space carrying some momentum. Objects spinning around an axis continue spinning unless acted on by an external torque, and the axis of rotation gives two directions of the "spin" angular momentum vector, depending on the angular velocity being clockwise or anticlockwise. Classically, we can view a spinning object as a sum of fundamental constituents (e.g. atoms) orbiting around the centre of mass, with the object's spin equal to the sum of the orbital angular momenta of all the pieces.

Fundamental particles are observed to have an intrinsic angular momentum, which is also called spin. Spin is a property of point particles, with composite particles having spins equal to the vector sum of constituent fundamental particle spins. The total spin of a particle, f, and the measured component of spin along an axis, m, are quantized in integer and half-integer units of $\hbar$. There is no classical analog of a spin-1/2 particle, which makes spin a decidedly non-classical property of our description of reality.

For example, if we try to describe the $\hbar/2$ spin of an electron classically, as the angular momentum of a solid sphere spinning about its centre of mass, we end up with an electron surface velocity that is faster than the speed of light, violating relativity (see Problem 4.25 in Ref. [1]). Thus at the level of nonrelativistic quantum mechanics, spin appears as an intrinsic property.

Even with extensions to relativistic quantum mechanics, where the Dirac equation

leads to spin-1/2 particles and antiparticles with opposite spins [2, 3], which may have classical interpretations [4–8], a consensus on the physical meaning of spin remains elusive [9, 10]. It is an ongoing area of research to understand the origin of spin and other properties of fundamental particles, e.g. the nature of the electron [11–13], with cold-atom systems offering a useful test-bed for simulating different theories, e.g. Dirac fermions [14–16] and quantum chromodynamics (QCD) [17–19].

While the physical origin of spin is not fully understood, it is the building block of the more familiar phenomenon of magnetism. Magnetism in our macroscopic world arises from many microscopic spins aligning, and is described classically by Maxwell's equations. Magnetism and electricity are linked together as electromagnetism, with a duality between moving electric charges and static magnetic fields, and the link being provided by relativity [20–22]. A fundamental description of magnetism may require understanding the combined effects of gravity and quantum mechanics [23]. Magnetism connects the deepest layers of physical reality, which makes it a very interesting phenomena to study.

At the quantum level, spins are quantized into discrete levels with magnetization along any axis stepping in integer multiples of Planck's constant, $\hbar$, from fully aligned up to fully aligned down. All particles in nature can be classified as either bosons or fermions. In this thesis, we will focus on composite bosons, in particular the atoms ^{87}Rb and ^{23}Na. The total spin of bosons is an integer multiple of $\hbar$. This means they have an odd number of levels and thus include a level with zero magnetization.

Spin-1 bosonic particles, for example, have possible spin components $m \in \{+1, 0, -1\}$, in units of $\hbar$. This is in contrast to fermions, whose maximum spin is a half-integer multiple of $\hbar$, leading to an even number of levels. For example, spin-$\frac{1}{2}$ fermions (like electrons) have possible spin components $m \in \{+\frac{1}{2}, -\frac{1}{2}\}$, in units of $\hbar$. The quantum statistics of bosons is such that they favour occupying the same single-particle state (so-called bosonic enhancement), whereas fermions never occupy the same state (the Pauli exclusion principle).

The zero spin component state of bosons provides a natural pathway for producing maximally entangled superpositions of bosonic spins, through spin-exchange collisions [24, 25]. It also gives rise to internal antiferromagnetic order, with states which cannot be produced classically. The internal order is like a synthetic dimension, as the classical analogy to it is a spatially extended lattice of alternating non-zero spins, so-called Néel order [26, 27].

The phenomenon of bosonic enhancement leads to the possibility of a special bosonic state with a macroscopic number of particles occupying the ground state simultaneously, called a Bose-Einstein condensate (BEC). BECs allow us to amplify a single quantum state to a macroscopically observable level. We can then study the quantum properties of an ensemble of identical bosonic particles, with the coherence of the many-body wavefunction causing it to manifest as an approximately classical field.

1.2 Bose-Einstein condensates

A Bose-Einstein condensate is a state of matter that can occur for bosonic systems due to the quantum statistics of bosons. The quantum statistics stem from the inherent indistinguishability of fundamental particles: a quantum state consisting of indistinguishable particles requires a superposition principle, where the process of swapping the particles imprints a geometric phase on the state,

$$|\psi_{ab}\rangle_{\text{identical particles}} = \frac{1}{\sqrt{2}}(|\psi_{ab}\rangle + e^{i2\pi f}|\psi_{ba}\rangle). \tag{1.1}$$

The fundamental property of bosons having integer spins (f = integer) means that interchange of two identical bosons between two single particle modes must have a symmetric wavefunction, i.e.

$$|\psi_{ab}\rangle_{\text{identical bosons}} = \frac{1}{\sqrt{2}}(|\psi_{ab}\rangle + |\psi_{ba}\rangle) \quad \text{(bosons)}, \tag{1.2}$$

$$|\psi_{ab}\rangle_{\text{identical fermions}} = \frac{1}{\sqrt{2}}(|\psi_{ab}\rangle - |\psi_{ba}\rangle) \quad \text{(fermions)}. \tag{1.3}$$

Thus for bosonic particles the wavefunctions with states a and b permuted are added together with the same sign, i.e. the same phase if we consider complex amplitudes multiplying each wavefunction. This means they add constructively, which leads to bosonic enhancement of bosons occupying the same state.

Let us now consider a system of bosons restricted to a single spin component, equivalent to $f = 0$, i.e. a spinless (scalar) system. The distribution for the single particle energy level occupation changes from that of a classical thermal gas, which has a Boltzmann distribution, to that of the Bose-Einstein distribution,

$$n_{BE}(\epsilon_i) = \frac{1}{e^{(\epsilon_i - \mu)/kT} - 1}, \tag{1.4}$$

where ϵ_i is the energy of the i-th single-particle state, μ is the chemical potential, k is the Boltzmann constant, and T is the temperature. For systems where the density of

states rises sufficiently fast with energy ϵ_i, e.g. most cases with dimension greater than two, reducing the temperature below a non-zero critical temperature exhibits a phase transition to a condensed phase. In the condensed phase, occupation of excited states saturates at a fixed amount, while occupation of the ground state becomes macroscopic. This is a quantum phase transition which is not predicted for distinguishable particles.

In the zero temperature limit, with weak interactions, the condensed phase has a many-body wavefunction which is approximately a Hartree product state, with every particle occupying the same ground state wavefunction. The system is then described by this shared wavefunction, which we denote as ψ.

If the occupation is high, then the field operator $\hat{\psi}$ can be approximated by the mean-field contribution, $\langle\hat{\psi}\rangle \approx \psi$. This simplifies analysis of the system considerably, as the classical field ψ has dynamics we can compute without requiring the exponential Hilbert space of states that $\hat{\psi}$ operates on. The potentially millions of particles in the system will then act coherently as a single wave of probability, governed by the Schrödinger equation, with nonlinear interactions taking into account the average (linear) quantum behaviour of all the particles. The resulting nonlinear Schrödinger equation is known as the Gross-Pitaevskii equation (GPE) [28, 29], and is given by

$$i\hbar\dot{\psi} = -\frac{\hbar^2}{2M}\nabla^2\psi + g|\psi|^2\psi, \tag{1.5}$$

where g is the low energy (s-wave) coupling constant, which provides an excellent description of the particle interactions at ultracold temperatures. The ∇^2 term describes single-particle diffusion due to the kinetic energy of the condensate. This equation has had great success at describing a rich variety of phenomena in BECs, providing theoretical predictions in excellent agreement with experimental results [30, 31].

1.3 Spinor condensates

We now introduce a spin degree of freedom to our bosonic particles, i.e. we allow $f > 0$ with f an integer. The system can then Bose-condense into each of the available component spin states m, giving us a multicomponent BEC. This system has new nonlinear spin-exchange interactions that describe the possible spin dynamics of the particles, and these appear as rotationally invariant functionals of the multicomponent "spinor" condensate. The spin degrees of freedom in the system give rise to new types of spin order. The case of (pseudo) spin-1/2 is familiar to most atomic physicists, where

the system can be represented by a single point on the Bloch sphere. However, even for a three-component spin-1 system we are already beyond this simple picture. Spin-1 requires two independent points on the Bloch sphere to characterize all possible types of order, and spin-2 requires four points (this is the so-called Majorana representation, e.g. see [32]). This indicates that higher spin systems exhibit new types of order in spin space, beyond just vector spin order, with a rich array of possible symmetries. These symmetries lead to complex dynamics with new symmetry-breaking phase transitions and exotic topological defects.

1.3.1 Single-particle behaviour

In the presence of a magnetic field, the spin components of spinor systems experience Zeeman shifts in their energies. Aligning the field along the spin quantization direction, a small magnitude field gives a linear Zeeman shift p and a quadratic Zeeman shift q. The single-particle behaviour of each component of the condensate is then given by

$$(H_0\psi)_m = -\frac{\hbar^2}{2M}\nabla^2\psi_m - mp\psi_m + m^2q\psi_m. \tag{1.6}$$

In this thesis, we assume there is a uniform bias field such that p and q are uniform constants. This is usually the case in spinor experiments, with gradients mainly used for Stern-Gerlach separation of the spin components during measurement. Fig. 1.1 shows the Zeeman terms and $f = 1$ hyperfine splitting for ^{87}Rb in a uniform magnetic field.

Using microwave dressing, the quadratic Zeeman shift can be independently tuned [33–35]. It is clear that p shifts the levels such that they retain their relative spacing, while q changes their relative spacing. Indeed, p induces Larmor precession of the spin about the direction of the magnetic field, and can be removed by going to a rotating frame. However, q breaks spin symmetry and thus couples to and changes the nonlinear spin dynamics. Fig. 1.2 shows the effect of the quadratic Zeeman on the sublevels of the $f = 1$ and $f = 2$ hyperfine manifolds.

1.3.2 Nonlinear interactions

The nonlinear interactions describing collisions between interacting particles appear as extra nonlinear terms in addition to the simple "density interaction" term that appears in the scalar GPE, i.e. Eq. (1.5). Along with the density interaction, they include

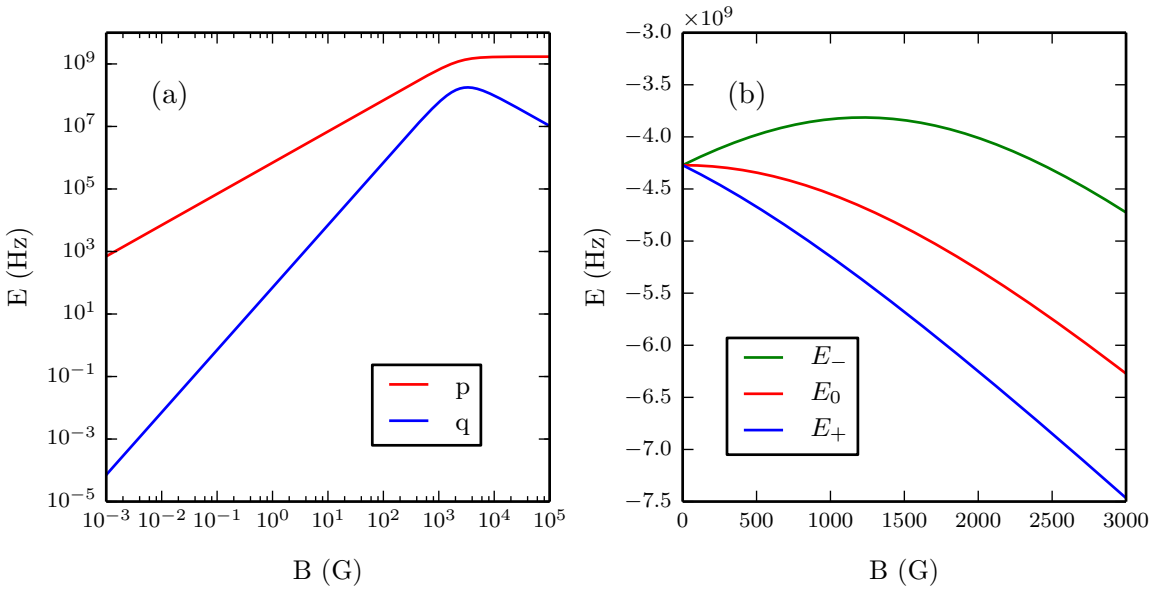

Figure 1.1: Zeeman splittings for the $f = 1$ manifold of ^{87}Rb. (a) Dependence of the linear and quadratic Zeeman shifts p and q on a weak magnetic bias field B. (b) Resulting hyperfine energy level shifts.

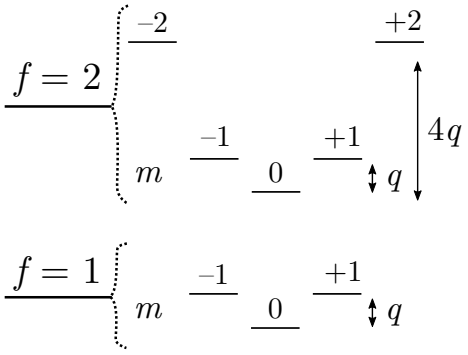

Figure 1.2: Quadratic Zeeman energy level splitting for positive q in $f = 1$ and $f = 2$ hyperfine manifolds.

interactions that can move population between spin levels. These will be explained in detail in Chapter 2.

1.3.3 Experimental species

Regarding experimentally realizable systems, in this thesis we focus on ^{87}Rb and ^{23}Na. These isotopes are bosonic atoms with a single valence electron. At ultracold temperatures, their spin structure is determined by the hyperfine coupling between the electron and the nucleus, with total spin

$$f = l + s + i, \tag{1.7}$$

where l is the electron orbital angular momentum, s is the electron spin, and i is the nuclear spin. For Rb and Na, the electronic ground state has the valence electron in an S-subshell, i.e. $l = 0$. The addition of spin is a vector operation, with the combined system (with $l = 0$) being described by multiple hyperfine manifolds with $f \in \{|s - i|, |s - i| + 1, \cdots, s + i\}$.

The single electron is a spin-1/2 particle, so contributes total spin of $s = 1/2$. The nucleus is composed of protons and neutrons, each contributing a component of spin-1/2. The lowest energy state of the nucleus for both species has total nuclear spin $i = 3/2$. This leads to the two ground state hyperfine manifolds with $f = 1$ and $f = 2$.

Thus both ^{87}Rb and ^{23}Na allow for spin-1 and spin-2 BECs, by using the $f = 1$ and $f = 2$ manifolds respectively. Fig. 1.3 shows these manifolds, with experimental energy splittings from Refs [36, 37].

1.4 Spinor timeline

The first spinor BEC, a spin-1 condensate of ^{23}Na, was produced experimentally by a group at MIT in 1998 [38]. This was 3 years after the first achievement of Bose-Einstein condensation in scalar systems with ^{87}Rb [39], ^{23}Na [40] and ^{7}Li [41]. Seminal theory works were done around the same time by Ho [42] and Ohmi and Machida [43]. Since then, experimental techniques like optical trapping and laser cooling have advanced to the point where spinor condensates have been realized with spin-1 ^{87}Rb [44], spin-2 ^{23}Na [45], spin-2 ^{87}Rb [46] and spin-3 ^{52}Cr [47].

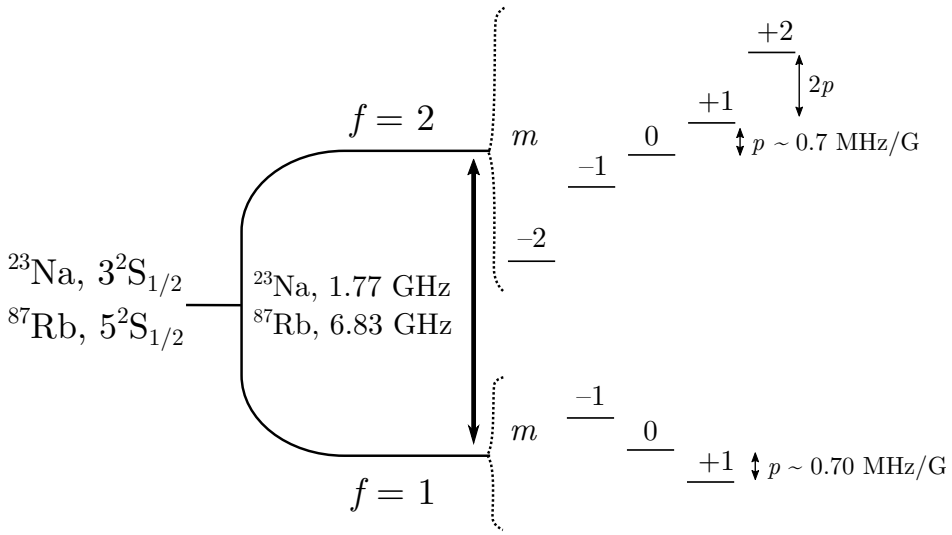

Figure 1.3: Low energy hyperfine manifolds of the bosonic alkali metals ^{87}Rb and ^{23}Na. We consider the electronic ground states, giving an $f = 1$ and an $f = 2$ manifold. Linear Zeeman splittings are relative to a weak magnetic bias field along the spin quantization axis. Reproduced from data in Fig. 3 of Refs [36, 37].

Before giving an outline of this thesis, we give a brief outline of some of the exciting experimental activity with spinor condensates that has motivated theoretical work in this system.

Experiments have investigated the rich variety of physics exhibited by spinor systems. A lot of work has been done in the single mode regime, with all spin components restricted to a single spatial mode [48, 49]. In this regime, the confining potential is sufficiently tight to freeze out spatial variations in the spin degrees of freedom. Single mode systems have been useful for studying nonlinear and quantum dynamics, notably recent work on quantum (spin) squeezing [50, 51].

Beyond the single mode regime, several experiments have investigated extended spatial dynamics. Of particular interest are quenches to phases with spontaneously broken symmetries, for example the ferromagnetic quenches of Sadler *et.al* in Ref. [52] where domains of magnetization were observed to grow following a quench. There has been considerable theoretical work on the phase-ordering dynamics (coarsening) of similar ferromagnetic quenches [53–56].

Antiferromagnetic spinor systems have had much less theoretical attention. Recent experiments have shown that antiferromagnetic condensates exhibit quadrupolar nematic

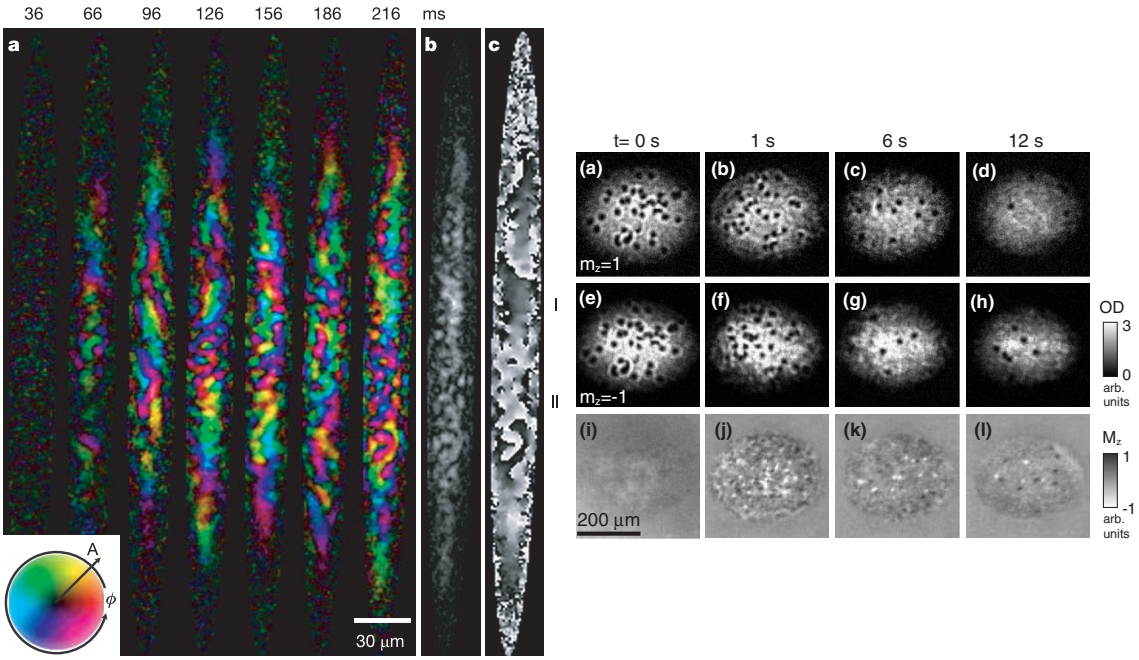

Figure 1.4: Experimental images of spin-1 experimental systems. The left plot group shows ferromagnetic domains in a quasi-one-dimensional quenched spin-1 ferromagnetic condensate, reproduced from Ref. [52]. The right plot group shows collisions of half-quantum vortices created from the dissociation of singular vortices quenched between two nematic phases in an antiferromagnetic spin-1 condensate, reproduced from Ref. [63].

order [57]. In the context of spinor systems, nematic order refers to the order resulting from unmagnetized states. This can be understood in analogy with antiferromagnetic ordering in spin lattices, where spins order in opposite directions such that their magnetization cancels out on average, but there is still an axis of alignment.

There has been a particular experimental focus in antiferromagnetic spinor systems on phase transitions resulting from a sudden change, or quench, in the quadratic Zeeman energy [58–60]. This parameter breaks the symmetry of the system by introducing a particular reference axis; quenches of the parameter can then take the system between nematic phases with different alignment axes. The resulting quench dynamics create new domains of nematic order which spontaneously break the symmetry of the initial state, and at late times enter a regime of phase-ordering coarsening dynamics [61], with the relevant topological defects being half-quantum vortices [62, 63].

1.5 Our contribution

Previous theoretical studies of the dynamics of spinor condensates have aways approximated the nonlinear dynamics of the system or resorted to numerical solution. In this thesis we develop an exact solution to the nonlinear dynamics of spin-1 and spin-2 condensates. Our approach considers the nonlinear interaction energy as an isolated subsystem, with no magnetic field or kinetic energy. This subsystem has Hamiltonian dynamics, and conserved nonlinear quantities, which we use to derive an exact solution. This solution exactly conserves the local spin and atom number density. We make maximum use of this solution by implementing symplectic (phase-space preserving) integration algorithms. These algorithms solve the full system dynamics, which include the dynamics due to the quadratic Zeeman shift of a weak magnetic field and the kinetic energy in non-uniform systems. The symplectic properties of these algorithms enable us to perform accurate and efficient simulations to very long times.

Using our new algorithms we make several advances in simulating quenches of spinor systems. Previous work in this area has focused on the ferromagnetic spin-1 system [56, 64–66]. We investigate phases with antiferromagnetic order, described by nematic tensor order parameters. Spinor systems exhibit a rich variety of new phases with discrete symmetries, with quenches into these phases exhibiting spontaneous broken symmetry and long-time phase ordering dynamics, which require tensor observables that match the phase symmetry in order to observe the growth of ordered domains.

We focus on two quenches. The first is in a spin-1 system, and goes between two nematic phases that differ only in the alignment of the state in spin space. We develop order parameters sensitive to the quadrupole nematic order and use these to investigate coarsening dynamics at long times. We connect the coarsening dynamics to the relevant topological defects, half-quantum vortices. After developing this theory and studying the 2D uniform system, we apply and expand our formalism to a recent experiment in a trapped 3D system. Using experimental parameter values, we simulate the experiment and measure their observables as well as our new nematic observables. We find good qualitative agreement with the experimental results, and show evidence of coarsening for deep quenches using our proposed observables.

The second quench is in a spin-2 system, and starts from a nematic phase analogous to the initial condition of the spin-1 quench. We perform a quench to a phase that exhibits higher order nematic symmetry, and requires developing higher order operators

to characterize the resulting phase ordering dynamics. The relevant topological defects are more complex for this quench. We measure defects in the higher order superfluid operator, which reveals 1/3 fractional vortices, and connect the decay of these vortices with the growth of order in the system.

1.6 Thesis outline

This thesis is structured into three parts. Firstly, in Part I, we develop formalism to describe spinor systems, including their nonlinear interactions, physical observables, and the particular nonmagnetic spinor phases we will be focused on in later Chapters. In Part II, we derive a new exact solution to the nonlinear dynamics of spinor systems, creating new algorithms for solving the full dynamics of spinor systems and testing these algorithms on several 1D problems. In Part III we apply our new algorithms to quenches between phases of nonmagnetic order for spin-1 and spin-2 systems with antiferromagnetic interactions.

We now give a brief outline of the contents of each chapter.

1.6.1 Part I

In Chapter 2 we go through a derivation of the nonlinear interactions of spinor systems, giving full details for the case of spin-1 and spin-2. We connect spin changing collisions with physical observables, and write the Hamiltonian energy functionals in terms of the simplest physical observables. Finally we derive expressions for irreducible multipole observables which connect directly to a hierarchy of spherical harmonic symmetries.

In Chapter 3 we give details of specific nonferromagnetic nematic phases that we wish to focus on in further Chapters. Particular attention is given to representation and visualization of the symmetries of the order parameter which give the insight needed to construct appropriate order parameters that can access the symmetry and reveal phase ordering dynamics in quenches to broken symmetry phases.

1.6.2 Part II

In Chapter 4 we analyze the dynamics of spinor systems. Using a two-way splitting, we derive a new exact solution to the nonlinear dynamics of spinor systems. We solve the spin-1 dynamics from two complementary viewpoints, then use those results to solve the spin-2 system. We give an extension to all higher spin systems for a restricted set of interactions. Finally, we give MATLAB code of the numerical implementation of our exact solutions, and details of how we use GPU parallelization to speed up our simulations.

In Chapter 5 we solve the full dynamics of the spinor system by composing the exact solutions of our split subsystems together, giving second and fourth order symplectic algorithms (which preserve the Hamiltonian properties of the solution). We review several existing algorithms in the field and compare their performance to our proposed algorithms. We also give some details of how one may apply our methods to finding ground states using imaginary time evolution.

In Chapter 6 we perform 1D numerical tests of our symplectic algorithms. For the spin-1 system, we consider an exact plane wave solution and an approximate soliton solution. For the spin-2 system, we develop an analogous plane wave exact solution. We compare our symplectic algorithms against two methods in the literature, verifying their asymptotic error behaviour, and analyzing their accuracy by how well they conserve three global constants of motion.

1.6.3 Part III

In Chapter 7 we analyze quenching a spin-1 antiferromagnetic condensate between two nematic phases. We develop formalism to measure the expected nematic order and long-time coarsening of nematic domains. We consider a 2D uniform system and perform quench simulations to very long times. We find evidence of universal coarsening with dynamical scaling of domains, with a domain growth law of $L(t) \sim [t/\ln t]^{1/2}$, where L is the size of the ordered domains and t is the time after the quench.

In Chapter 8 we analyze a recent experiment that performed the same quench we studied in Chapter 7. We perform simulations matching their experimental parameters, measuring their observables and those developed in the previous Chapter. We find good qualitative agreement between our simulation results and experimental results. At early

times our results are qualitatively similar to those predicted by uniform Bogoliubov theory, while at late times we see evidence of coarsening dynamics of nematic domains.

In Chapter 9 we consider a spin-2 system quenched from nematic phases to a phase with cyclic (tetrahedral) symmetry. We develop order parameters sensitive to cyclic order and simulate quenches for two different initial conditions of nematic order. We analyze late time ordering dynamics and relate these to defects in the order parameter sensitive to $1/3 - 2/3$ vortices which couple superfluid order to spin order.

We conclude in Chapter 10.

1.7 Papers arising

The work in Part II, i.e. Chapters 4, 5, and 6, has been published in Physical Review E as

- *"Efficient and accurate methods for solving the time-dependent spin-1 Gross-Pitaevskii equation"*, L. M. Symes, R. I. McLachlan, and P. B. Blakie, Phys. Rev. E **93**, 053309 (2016),
- *"Solving the spin-2 Gross-Pitaevskii equation using exact nonlinear dynamics and symplectic composition"*, L. M. Symes and P. B. Blakie, Phys. Rev. E **95**, 013311 (2017).

The work in Chapter 7 (with relevant details from Chapter 3) has been published in Physical Review A as

- *"Nematic ordering dynamics of an antiferromagnetic spin-1 condensate"*, L. M. Symes and P. B. Blakie, Phys. Rev. A **96**, 013602 (2017).

The remaining work of Part III, including a paper on the spin-1 experimental quench simulations of Chapter 8 and a paper on the spin-2 nematic-cyclic quenches in Chapter 9, is in preparation for publication.

Chapter 2

Spinor interactions

In this chapter we give an overview of the origin of the nonlinear interaction terms that describe two-particle collisions in a BEC. Firstly, we review the scalar case, which has a single interaction term. Then, we give the condensate field a non-trivial spin degree of freedom and explain the new collisions that emerge under the constraint of being rotationally invariant. We connect these collisions to the spin-singlet and arbitrary-order multipoles, which are the physically relevant spin observables. Viewing the system in terms of these observables, which encode specific physical symmetries, is fundamental to the methods and analysis developed in the chapters which follow.

2.1 Scalar BEC interactions

Let us consider a bosonic gas of a single species, at temperatures much lower than the condensation temperature. The condensate is then described by a complex scalar order parameter ψ, describing the spatially coherent condensed state. We model collisions of two particles in the condensate as

$$E_{int} = \frac{1}{2}\int\int d\mathbf{r}\; d\mathbf{r}'\; \psi^\dagger(\mathbf{r})\psi^\dagger(\mathbf{r}')V_{\text{scattering}}(\mathbf{r}-\mathbf{r}')\psi(\mathbf{r}')\psi(\mathbf{r}), \tag{2.1}$$

where the interaction potential $V_{\text{scattering}}(\mathbf{r}-\mathbf{r}')$ describes the spatial dependence of the interaction between bosonic atoms at positions $\mathbf{r}$ and $\mathbf{r}'$.[1] For a cold dilute gas, the low-energy interaction potential can be approximated by a partial wave expansion to

[1] In a quantum treatment, $\psi^\dagger$ would refer to a creation field operator. For classical fields, which we focus on, is the conjugate transpose, i.e. $\psi^\dagger = (\psi^*)^T$.

lowest order, i.e. s-wave scattering only, which can be described by a delta function pseudo-potential

$$V_{\text{scattering}}(\mathbf{r}-\mathbf{r}') \to g_s\,\delta(\mathbf{r}-\mathbf{r}'), \tag{2.2}$$

where the coupling constant g_s is related to the s-wave scattering length as

$$g_s = \frac{4\pi\hbar^2}{M}a_s, \tag{2.3}$$

where M is the atomic mass. Thus from Eq. (2.1) we obtain the scalar (density-dependent) interaction

$$E_{scalar} = \frac{g_s}{2}\int d\mathbf{r}\; n^2, \tag{2.4}$$

where $n = \psi^\dagger\psi$ is the local density, and g_s gives the interaction strength.

2.2 Spinor BEC interactions

For a system with a spin degree of freedom, composed of particles which each have total spin f, there are $2f+1$ possible spin states along any given quantization axis. These states range from maximally aligned in the positive direction to fully aligned in the negative direction. We denote these states as $|f,m\rangle$, where m labels the possible spin sublevels for total spin f, with $m \in \{-f, -f+1, \cdots, 0, \cdots, f-1, f\}$.

To represent a general spin-f pure state $|\psi\rangle$, we introduce the multicomponent wavefunction ψ, defined by $|\psi\rangle = \sum_m \psi_m |f,m\rangle$. Each component ψ_m gives the amplitude in the $|f,m\rangle$ state. For example, for spin-1 we have $\psi = (\psi_{+1}, \psi_0, \psi_{-1})^T$, and for spin-2 we have $\psi = (\psi_{+2}, \psi_{+1}, \psi_0, \psi_{-1}, \psi_{-2})^T$. The complex wavefunction ψ is a spinor; physical transformations on ψ are performed by $(2f+1)$-dimensional elements of the appropriate group, e.g. $SO(3)$ for 3D rotations.

Spinor systems have new interactions. Two incoming particles with individual spin values m and m' can collide to form two outgoing particles with possibly different individual spins. Following the usual approach of the literature, we proceed by assuming that: incident collision energies are low enough that we have only s-wave scattering; the interaction potential is rotationally invariant at short range; we have no spin-orbit coupling; and that there is no mixing of hyperfine states to manifolds with different f [32, 42, 43, 67].

Rotational symmetry means that total angular momentum - orbital (spatial) plus spin (internal) - is conserved. With s-wave scattering (orbital angular momentum zero), and no spin-orbit coupling, each collision conserves the total spin along the quantization axis, $m + m'$. Without loss of generality, we consider the quantization axis to be the z axis.

Collisions that change particle spins while conserving the total z spin are called spin-exchange interactions. For example, two $m = 0$ particles can collide to form two particles with equal and opposite non-zero spins, and vice-versa. For spin-1, we have the process

$$(0, 0) \leftrightarrow (+1, -1). \tag{2.5}$$

For higher spins, there arise z-spin conserving processes which can change individual m components up to the total spin of the wavefunction, f. E.g., for spin-2 we have the processes

$$(0, 0) \leftrightarrow (+1, -1) \leftrightarrow (+2, -2), \tag{2.6}$$

$$(0, 0) \leftrightarrow (+2, -2), \tag{2.7}$$

$$(\pm 1, \pm 1) \leftrightarrow (\pm 2, 0), \tag{2.8}$$

$$(\pm 1, 0) \leftrightarrow (\pm 2, \mp 1). \tag{2.9}$$

This picture is in terms of the two colliding particles, however the conservation principle is in terms of their total z spin $m + m'$. Thus, to include all the interactions rigorously we need to switch to a total-spin basis, which connects with experimental spin channel scattering lengths. We will then rewrite the resulting spin channel amplitudes in terms of the total density, spin-singlet, magnetization, and higher-order multipoles. These directly encode the geometric point symmetries of the system, and so we refer to them as "physical" observables, in contrast to spin channel amplitudes which generally connect to a mixture of symmetries. Understanding the relationship between physical observables and the spin channel amplitudes will lay the ground for the methods in the next chapters.

2.2.1 Spin-channel Hamiltonian

We now switch to a total-spin basis $|\mathcal{F}, \mathcal{M}\rangle$, which comes from the vector addition of two spin-f particles' spins. Two spin-f particles can combine to have total spin $\mathcal{F} \in \{0, 1, \cdots, 2f\}$, with $\mathcal{M} \equiv m + m' \in \{-\mathcal{F}, \cdots, \mathcal{F}\}$.

With s-wave scattering only, quantum statistics restricts our total-spin basis to have even total spin, i.e. $\mathcal{F} \in \{0, 2, \cdots, 2f\}$ [32, 67]. The interaction Hamiltonian is then decomposed into a sum of spin channel interactions labeled by $\mathcal{F}$, i.e.

$$E_{int} = \sum_{\mathcal{F}=0,2,\cdots,2f} V^{(\mathcal{F})}. \tag{2.10}$$

The total spin channel operators are given by

$$V^{(\mathcal{F})} = \frac{g_{\mathcal{F}}}{2} \int d\mathbf{r} \sum_{\mathcal{M}=-\mathcal{F}}^{\mathcal{F}} \alpha^{\dagger}_{\mathcal{F}\mathcal{M}} \alpha_{\mathcal{F}\mathcal{M}}, \tag{2.11}$$

where we have integrated out the relative spatial dependence of the interaction by using a delta function pseudo-potential similar to Eq.(2.2), with $g_{\mathcal{F}}$ being related to the s-wave scattering length in the corresponding spin channel as

$$g_{\mathcal{F}} = \frac{4\pi\hbar^2}{M} a_{\mathcal{F}}. \tag{2.12}$$

Here $a_{\mathcal{F}}$ is the s-wave scattering length for the total spin-$\mathcal{F}$ channel. The $\alpha_{\mathcal{F}\mathcal{M}}$ amplitudes are the projection of two incoming particles, each with spin-f and a total spin component $\mathcal{M}$, onto total spin $\mathcal{F}$ and component $\mathcal{M}$. These complex amplitudes are irreducible; different $\mathcal{F}$ elements are orthogonal. They are defined by

$$\alpha_{\mathcal{F}\mathcal{M}} = \psi^T A_{\mathcal{F}\mathcal{M}} \psi, \tag{2.13}$$

where the $A_{\mathcal{F}\mathcal{M}}$ are matrices of Clebsch-Gordan coefficients, i.e.

$$(A_{\mathcal{F}\mathcal{M}})_{m,m'} = \langle \mathcal{F}, \mathcal{M} | f, m; f, m' \rangle. \tag{2.14}$$

The Clebsch-Gordan coefficients are fundamentally a change of basis, which couples individual spins of particles together to describe them using their total spin (the conserved quantity of the collision). The set of $a_{\mathcal{F}}$ values, e.g. a_0 and a_2 for $f = 1$, provide a complete characterization fo the low energy collisional properties of the system.

2.2.2 Physical observables

We now connect the spin-channel amplitudes to "physical" observables. By physical, we mean observables that connect to geometric (physical) symmetries of the system. Of particular interest to us is a constructed hierarchy of multipoles, which directly connect to the physical symmetries of the interactions.

Spin-singlet

The $\mathcal{F} = \mathcal{M} = 0$ amplitude is the spin-singlet amplitude, and we would like to keep it in our list of physical observables due to its high symmetry. It is given by the formula

$$\alpha_{00} = \frac{1}{\sqrt{f(f+1)}} \sum_m (-1)^{f+m} \psi_m \psi_{-m}, \tag{2.15}$$

and describes interactions of particles in a singlet (zero total spin) superposition in the spin channel which has total spin also zero.

Spin matrices

The multipole operators are defined in terms of the so-called "spin matrices", which we denote as f_ν for $\nu \in \{x, y, z\}$. The spin matrices (and their matrix powers) operate on spin states to transform them to new spin states. Here we describe the spin matrices by their effect on pure states, which reveals their matrix elements.

We start by setting z as our quantization axis. The action of f_z on a pure state is then

$$\mathrm{f}_z |f, m\rangle = m |f, m\rangle, \tag{2.16}$$

where we neglect a factor of $\hbar$ compared with the normal angular momentum operators. Thus f_z is a diagonal matrix, given by

$$\mathrm{f}_z = \begin{pmatrix} f & & & & \\ & f-1 & & & \\ & & \cdots & & \\ & & & -f+1 & \\ & & & & -f \end{pmatrix}. \tag{2.17}$$

For the in-plane (transverse) spin matrices, i.e. f_x and f_y, it is easiest to first consider the ladder operators

$$\mathrm{f}_+ = \mathrm{f}_x + i\mathrm{f}_y, \tag{2.18}$$

$$\mathrm{f}_- = \mathrm{f}_x - i\mathrm{f}_y = \mathrm{f}_+^\dagger. \tag{2.19}$$

These two operators raise and lower pure states by one spin level as

$$\mathrm{f}_+ |f, m\rangle = \sqrt{(f+m)(f-m+1)}\,|f, m+1\rangle, \tag{2.20}$$

$$\mathrm{f}_- |f, m\rangle = \sqrt{(f-m)(f+m+1)}\,|f, m-1\rangle. \tag{2.21}$$

Note that

$$\mathrm{f}_+|f,f\rangle = 0, \tag{2.22}$$

$$\mathrm{f}_-|f,-f\rangle = 0. \tag{2.23}$$

This defines f_+ and f_- as off-diagonal matrices. Written out explicitly, f_+ is real, positive, and diagonal along the first upper diagonal, with f_- the transpose:

$$\mathrm{f}_+ = \begin{pmatrix} 0 & \sqrt{2(2f-1)} & & & & & \\ & 0 & \sqrt{3(2f-2)} & & & & \\ & & 0 & \cdots & & & \\ & & & 0 & \sqrt{3(2f-2)} & & \\ & & & & 0 & \sqrt{2(2f-1)} & \\ & & & & & 0 & \end{pmatrix} = \mathrm{f}_-^T. \tag{2.24}$$

The transverse matrices are then given by the inverse of Eqs. (2.18) and (2.19), i.e.

$$\mathrm{f}_x = \frac{1}{2}(\mathrm{f}_+ + \mathrm{f}_-), \tag{2.25}$$

$$\mathrm{f}_y = \frac{1}{2i}(\mathrm{f}_+ - \mathrm{f}_-). \tag{2.26}$$

Explicit spin matrices

For $f = 1$, we have the spin-1 matrices

$$\mathrm{f}_x = \frac{1}{\sqrt{2}}\begin{pmatrix} 0 & 1 & 0 \\ 1 & 0 & 1 \\ 0 & 1 & 0 \end{pmatrix}, \quad \mathrm{f}_y = \frac{i}{\sqrt{2}}\begin{pmatrix} 0 & -1 & 0 \\ 1 & 0 & -1 \\ 0 & 1 & 0 \end{pmatrix}, \quad \mathrm{f}_z = \begin{pmatrix} 1 & 0 & 0 \\ 0 & 0 & 0 \\ 0 & 0 & -1 \end{pmatrix}. \tag{2.27}$$

For $f = 2$, we have the spin-2 matrices

$$\mathrm{f}_x = \begin{pmatrix} 0 & 1 & 0 & 0 & 0 \\ 1 & 0 & \sqrt{\frac{3}{2}} & 0 & 0 \\ 0 & \sqrt{\frac{3}{2}} & 0 & \sqrt{\frac{3}{2}} & 0 \\ 0 & 0 & \sqrt{\frac{3}{2}} & 0 & 1 \\ 0 & 0 & 0 & 1 & 0 \end{pmatrix}, \quad \mathrm{f}_y = i\begin{pmatrix} 0 & -1 & 0 & 0 & 0 \\ 1 & 0 & -\sqrt{\frac{3}{2}} & 0 & 0 \\ 0 & \sqrt{\frac{3}{2}} & 0 & -\sqrt{\frac{3}{2}} & 0 \\ 0 & 0 & \sqrt{\frac{3}{2}} & 0 & -1 \\ 0 & 0 & 0 & 1 & 0 \end{pmatrix}, \quad \mathrm{f}_z = \begin{pmatrix} 2 & 0 & 0 & 0 & 0 \\ 0 & 1 & 0 & 0 & 0 \\ 0 & 0 & 0 & 0 & 0 \\ 0 & 0 & 0 & -1 & 0 \\ 0 & 0 & 0 & 0 & -2 \end{pmatrix}. \tag{2.28}$$

Multipole operators

The multipole operators are powers of the spin matrices $\mathbf{f} = (\mathrm{f}_x, \mathrm{f}_y, \mathrm{f}_z)$. The simplest is the zeroth-order operator, i.e. the identity, which simply gives the total density,

$$\mathcal{N}^{(0)} = \psi^\dagger \psi = n. \tag{2.29}$$

The first-order multipole is the dipole (2-pole) operator, known as the magnetization,

$$\mathcal{N}^{(1)} = \psi^\dagger \mathbf{f} \psi = (F_x, F_y, F_z) = \boldsymbol{F}. \tag{2.30}$$

This is also called the spin-density. At the mean-field level, it can vary continuously from zero to its maximum ($F \equiv |\boldsymbol{F}|_{max} = nf$), in any direction. We sometimes represent the in-plane magnetization using a complex observable, $F_\perp$, using the expectation of the ladder operators $\mathrm{f}_\pm$

$$F_\perp \equiv \psi^\dagger \mathrm{f}_+ \psi = F_+ = F_x + iF_y, \tag{2.31}$$

$$F_\perp^* = \psi^\dagger \mathrm{f}_- \psi = F_- = F_x - iF_y. \tag{2.32}$$

The next two higher order multipole moments, and the general k-th order moment, are defined as

$$[\mathcal{N}^{(2)}]_{\nu_1,\nu_2} = \mathcal{N}_{\nu_1,\nu_2} = \psi^\dagger \mathrm{f}_{\nu_1,\nu_2} \psi, \tag{2.33}$$

$$[\mathcal{N}^{(3)}]_{\nu_1,\nu_2,\nu_3} = \mathcal{N}_{\nu_1,\nu_2,\nu_3} = \psi^\dagger \mathrm{f}_{\nu_1,\nu_2,\nu_3} \psi, \tag{2.34}$$

$$[\mathcal{N}^{(k)}]_{\nu_1,\cdots,\nu_k} = \mathcal{N}_{\nu_1,\cdots,\nu_k} = \psi^\dagger \mathrm{f}_{\nu_1,\cdots,\nu_k} \psi, \tag{2.35}$$

where the nematic operator matrix is defined as $\mathrm{f}_{\nu_1,\nu_2,\cdots,\nu_m} \equiv \mathrm{f}_{\nu_1} \mathrm{f}_{\nu_2} \cdots \mathrm{f}_{\nu_m}$. Note that in our notation, the superscript k is implied when only the indices are given.

We call $k = 2$ the quadrupole (4-pole) moment, $k = 3$ the octupole (8-pole) moment, and $k = 4$ the hexadecapole (16-pole) moment. The general multipole moment is a 2^k-pole moment.

The general formula can be written in tensor notation as

$$\mathcal{N}^{(k)} = \psi^\dagger \mathbf{f}^{\otimes k} \psi, \tag{2.36}$$

where the tensor power gives a tensor of spin matrix powers, with $\mathbf{f}^0 = \mathbb{1}$. Note that these are the bare, unsymmetrized multipole moments. In this form they are not irreducible; for $k \geq 2$ they contain symmetry contributions from each lower order multipole.

We define $\mathcal{S}^{(k)}$ to be the symmetrized version of $\mathcal{N}^{(k)}$, and denote the traceless symmetric form of these observables as $\mathcal{T}^{(k)}$. By traceless we mean that summing over any two indices gives zero. The $\mathcal{T}^{(k)}$ observables *are* irreducible; they transform as spherical harmonics of order k and thus are the correct observables to characterize multipolar order in the system. We leave the derivation of $\mathcal{S}^{(k)}$ and $\mathcal{T}^{(k)}$ for the first few higher multipole moments to Section 2.4.

2.2.3 Spin-channel amplitudes to physical observables

Now that we have expressions for the irreducible amplitudes and physical observables, we need to connect them so we can rewrite the interaction Hamiltonian in terms of the physical observables.

The relationship is derived by constructing a completeness relation joining the irreducible states and the composition law of angular momentum, and then taking the expectation (see Ref. [32]). It gives us the following general formula:

$$\sum_{\nu_1,\nu_2,\cdots,\nu_k} (\mathcal{N}_{\nu_1,\nu_2,\cdots,\nu_k})^2 = \sum_{\mathcal{F}=0,2,\cdots,2f} \left[\frac{1}{2}\mathcal{F}(\mathcal{F}+1) - f(f+1)\right]^k \sum_{\mathcal{M}=-\mathcal{F}}^{\mathcal{F}} \alpha^\dagger_{\mathcal{F}\mathcal{M}}\alpha_{\mathcal{F}\mathcal{M}}. \quad (2.37)$$

Here the left-hand side is a tensor inner product, given by a sum of squares of all components of the tensor, resulting in a reduction of the tensor to a scalar energy term. Note that in a quantum treatment we would need to stipulate normal ordering of all energy terms (annihilation operators to the left of all creation operators). However, in our mean-field description here, with classical fields, the commutators involved are zero.

2.3 Hamiltonians for spin-1,2,f

Here we apply the general formula relating irreducible amplitudes and physical observables in Eq. (2.37) to derive the interaction Hamiltonian for specific spin systems. This will give us the form of the interaction parameters and how they relate to experimentally relevant scattering lengths. By inspection of the energy functional, we can describe the effect of each interaction parameter to gain some initial insight into what effect different values will have. Where appropriate, we also give useful system-specific identities used in later Chapters relating different observables.

2.3.1 Spin-1

For spin-1, two-particle s-wave collisions occur in the total spin channels $\mathcal{F} = 0, 2$. Using Eqs. (2.10) and (2.11), the Hamiltonian is

$$E_{int} = V^{(0)} + V^{(2)}, \tag{2.38}$$

$$= \frac{1}{2}\int d\mathbf{r} \left\{ g_0\, \alpha_{00}^\dagger \alpha_{00} + g_2 \sum_{\mathcal{M}=-1}^{1} \alpha_{2\mathcal{M}}^\dagger \alpha_{2\mathcal{M}} \right\}. \tag{2.39}$$

By setting $f = 1$, $k = 0, 1$ in Eq. (2.37), we get the following two identities

$$n^2 = \alpha_{00}^\dagger \alpha_{00} + \sum_{\mathcal{M}=-2}^{2} \alpha_{2\mathcal{M}}^\dagger \alpha_{2\mathcal{M}}, \tag{2.40}$$

$$F^2 = -2n^2 + 3 \sum_{\mathcal{M}=-2}^{2} \alpha_{2\mathcal{M}}^\dagger \alpha_{2\mathcal{M}}. \tag{2.41}$$

Solving for the amplitudes, we have

$$\alpha_{00}^\dagger \alpha_{00} = \frac{1}{3}(n^2 - F^2), \tag{2.42}$$

$$\sum_{\mathcal{M}=-2}^{2} \alpha_{2\mathcal{M}}^\dagger \alpha_{2\mathcal{M}} = \frac{1}{3}(2n^2 + F^2). \tag{2.43}$$

Note that the first result can be written as

$$n^2 = F^2 + 3\alpha_{00}^\dagger \alpha_{00}. \tag{2.44}$$

This decomposition of the density interaction into the magnetization interaction and the spin-singlet interaction will be useful for later Chapters.

Setting $f = 1$,$k = 2$ in Eq. (2.37), we get an identity which will also be useful later,

$$\sum_{\nu_1\nu_2} (\mathcal{N}_{\nu_1\nu_2})^2 = 2n^2 - F^2. \tag{2.45}$$

Substituting Eqs. (2.42) and (2.43) into Eq. (2.39), we get the Hamiltonian

$$E_{int} = \frac{1}{2}\int d\mathbf{r} \left(c_0 n^2 + c_1 F^2 \right), \tag{2.46}$$

where

$$c_0 = \frac{1}{3}(g_0 + 2g_2), \tag{2.47}$$

$$c_1 = \frac{1}{3}(g_2 - g_0). \tag{2.48}$$

Here c_0 is the density-dependent interaction strength, and c_1 is the spin-dependent (magnetization) interaction strength. By inspection of Eq. (2.46), we immediately see that $c_0 > 0$ is required for mechanical stability. For $c_0 < 0$ the system has attractive density interactions, and will favour becoming infinitely dense. The resulting implosion will destroy the condensate. We will thus always consider repulsive density interactions, with $c_0 > 0$.

We can also see that $c_1 < 0$ energetically favours maximizing the magnetization F, which we call ferromagnetic interactions. Conversely, $c_1 > 0$ favours minimizing the magnetization, so we call these antiferromagnetic interactions.

Note that c_1 is the difference of two scattering lengths. Experimentally, the scattering lengths in different channels are usually similar in magnitude, making their difference small. Thus, for physical systems, c_0 is usually positive and much larger than c_1.

2.3.2 Spin-2

Now let us consider the spin-2 system. The possible spin channels in this case are $\mathcal{F} = 0, 2, 4$, i.e. one more than the spin-1 case. This extra degree of freedom will lead to an extra independent nonlinear interaction term.

Using Eqs. (2.10) and (2.11), the spin-2 Hamiltonian is

$$E_{int} = V^{(0)} + V^{(2)} + V^{(4)}, \tag{2.49}$$

$$= \frac{1}{2}\int d\mathbf{r}\, \left\{ g_0\, \alpha_{00}^\dagger \alpha_{00} + g_2 \sum_{\mathcal{M}=-2}^{2} \alpha_{2\mathcal{M}}^\dagger \alpha_{2\mathcal{M}} + g_4 \sum_{\mathcal{M}=-4}^{4} \alpha_{4\mathcal{M}}^\dagger \alpha_{4\mathcal{M}} \right\}. \tag{2.50}$$

By setting $f = 2$, $k = 0, 1, 2$ in Eq. (2.37), we get the two identities

$$\sum_{\mathcal{M}=-2}^{2} \alpha_{2\mathcal{M}}^\dagger \alpha_{2\mathcal{M}} = \frac{1}{7}(4n^2 - 10\alpha_{00}^\dagger \alpha_{00} - F^2), \tag{2.51}$$

$$\sum_{\mathcal{M}=-4}^{4} \alpha_{4\mathcal{M}}^\dagger \alpha_{4\mathcal{M}} = \frac{1}{7}(3n^2 + 3\alpha_{00}^\dagger \alpha_{00} + F^2), . \tag{2.52}$$

Setting $f = 2$ and $k = 2, 3, 4$ in Eq. (2.37), and using Eqs. (2.51) and (2.52), we get the

identities

$$\sum_{\nu_1,\nu_2} (\mathcal{N}_{\nu_1,\nu_2})^2 = 12n^2 + F^2 + 30\alpha_{00}^\dagger \alpha_{00}, \tag{2.53}$$

$$\sum_{\nu_1,\nu_2,\nu_3} (\mathcal{N}_{\nu_1,\nu_2,\nu_3})^2 = 12n^2 + 13F^2 - 150\alpha_{00}^\dagger \alpha_{00}, \tag{2.54}$$

$$\sum_{\nu_1,\nu_2,\nu_3,\nu_4} (\mathcal{N}_{\nu_1,\nu_2,\nu_3,\nu_4})^2 = 156n^2 + 25F^2 + 1290\alpha_{00}^\dagger \alpha_{00}. \tag{2.55}$$

which will be useful later.

Substituting Eqs. (2.51) and (2.52) into Eq. (2.50), we get the Hamiltonian

$$E_{int} = \frac{1}{2}\int d\mathbf{r}\ \left\{c_0 n^2 + c_1 F^2 + c_2\ \alpha_{00}^\dagger \alpha_{00}\right\}, \tag{2.56}$$

where

$$c_0 = \frac{4g_2 + 3g_4}{7}, \tag{2.57}$$

$$c_1 = \frac{g_4 - g_2}{7}, \tag{2.58}$$

$$c_2 = \frac{7g_0 - 10g_2 + 3g_4}{7}. \tag{2.59}$$

Here c_0 is the density-dependent interaction strength and c_1 is the spin-dependent (magnetization) interaction strength, in analogy with the spin-1 system. The third term, with interaction strength c_2, is the spin-singlet interaction. It appears due to the extra degree of freedom in spin-2 collisions. In terms of the individual spinor components, for spin-2 the spin-singlet amplitude is given by

$$\alpha_{00} = \frac{1}{\sqrt{5}}(\psi_0^2 - 2\psi_{+1}\psi_{-1} + 2\psi_{+2}\psi_{-2}). \tag{2.60}$$

For $c_2 < 0$ it is energetically favourable to maximize the magnitude of the spin-singlet amplitude, while $c_2 > 0$ favours minimizing it. For spin-2, F and α_{00} can be changed independently by adjusting the quadrupole order [related by Eq. (2.53)], unlike the spin-1 case where they were fixed by the total density through the identity in Eq. (2.44).

2.3.3 Spin-f

The general spinor system has $f + 1$ nonlinear interaction terms. Each time the spin increases by one, we must introduce an extra spin-dependent interaction to account for the extra degree of freedom afforded by the new spin channel interaction. The

interaction terms can be written using irreducible operators, or by using multipole tensor operators. For spin-3, for example, the simplest representation of the extra degree of freedom is given by including the quadrupole tensor in the Hamiltonian.

2.4 Irreducible multipole operators

Here we expand upon the multipole operators defined previously, by symmetrizing and making them traceless. We focus on the quadrupole and octupole moments, i.e. the second and third order moments, as we will be using these in later Chapters.

The zeroth and first order multipole moments are already irreducible, i.e.

$$\mathcal{T}^{(0)} = n, \tag{2.61}$$

$$\mathcal{T}^{(1)} = \boldsymbol{F}. \tag{2.62}$$

For the higher moments, we want to consider their irreducible representation, which has no contribution from lower moments and transforms according to a spherical harmonic of the same order. This means the irreducible representation of the multipole moments isolates the different symmetries present in the system. The procedure for finding the irreducible representation is to symmetrize the bare operator and make it traceless, so that when any pair of indices is summed over (i.e. contracted, which lowers the tensor operator's order by one) it gives zero.

Given a decomposition of an irreducible multipole $\mathcal{T}^{(k)}$ in terms of reducible multipoles $\mathcal{N}^{(k)}$, we can derive identities relating the energy terms of reducible multipoles to the energy of the irreducible multipole. Combining these will give identities between the energies of irreducible multipoles. These essentially set the ground state phase diagram, by revealing the internal energetic competition between different types of multipolar order and their dependence on different interaction strengths. The energetically favoured irreducible multipole in each phase will match the symmetry of the ground state spinor, giving the correct order parameter to measure symmetry-breaking phase transitions.

2.4.1 Quadrupole

Here we consider the second order tensor observable $\mathcal{N}^{(2)}$. Its matrix operator can be decomposed into symmetric and antisymmetric parts as

$$\mathrm{f}_{ab} = \mathrm{s}_{ab} + \mathrm{a}_{ab}, \tag{2.63}$$

where $\{a, b\} \in \{x, y, z\}$, the symmetric part is

$$\mathrm{s}_{ab} = \frac{1}{2}(\mathrm{f}_{ab} + \mathrm{f}_{ba}), \tag{2.64}$$

and the antisymmetric part is

$$\mathrm{a}_{ab} = \frac{1}{2}(\mathrm{f}_{ab} - \mathrm{f}_{ba}) = \frac{i}{2}\sum_{c} \varepsilon_{abc}\mathrm{f}_{c}, \tag{2.65}$$

with the last equality coming from the commutation relations of the spin matrices, and ε_{abc} is the completely antisymmetric Levi-Civita symbol.

Taking the expectation of Eq. (2.63), the tensor inner product of the decomposition is

$$\sum_{ab} \mathcal{N}_{ab}^2 = \sum_{ab} (\mathcal{S}_{ab} + \mathcal{A}_{ab})^2 = \sum_{ab} \mathcal{S}_{ab}^2 + \sum_{ab} \mathcal{A}_{ab}^2 + 2\sum_{ab} \mathcal{S}_{ab}\mathcal{A}_{ab}, \tag{2.66}$$

where

$$\mathcal{S}_{ab} = \psi^\dagger \mathrm{s}_{ab}\psi, \quad \mathcal{A}_{ab} = \psi^\dagger \mathrm{a}_{ab}\psi, \tag{2.67}$$

and $\mathcal{N}_{ab}$ is defined in Eq. (2.33). The terms with $\mathcal{A}_{ab}$ are

$$\sum_{ab} \mathcal{A}_{ab}^2 = -\frac{1}{4}\sum_{abc} \varepsilon_{abc}^2 F_c^2 = -\frac{1}{2}\sum_{c} F_c^2 = -\frac{1}{2}F^2, \tag{2.68}$$

$$2\sum_{ab} \mathcal{S}_{ab}\mathcal{A}_{ab} = i\sum_{ab} \varepsilon_{abc}\mathcal{S}_{ab}\mathrm{f}_{c} = 0. \tag{2.69}$$

Note that the square of the antisymmetric term is symmetric and so the sum is nonzero, while the cross term is antisymmetric and so sums to zero. Thus we have

$$\sum_{ab} \mathcal{N}_{ab}^2 = \sum_{ab} \mathcal{S}_{ab}^2 + \sum_{ab} \mathcal{A}_{ab}^2, \tag{2.70}$$

$$= \sum_{ab} \mathcal{S}_{ab}^2 - \frac{1}{2}F^2. \tag{2.71}$$

Now consider the symmetric operator,

$$\mathrm{s}_{ab} = \mathrm{f}_{ab} - \frac{i}{2}\varepsilon_{abc}\mathrm{f}_{c}, \tag{2.72}$$

with trace

$$\mathrm{Tr}\{\mathrm{s}_{ab}\} = \sum_a \mathrm{s}_{aa} = \sum_a \mathrm{f}_{aa} = f(f+1)\mathbb{1}, \tag{2.73}$$

where the last equality (with $\mathbb{1}$ the identity matrix of appropriate dimension) is fundamental to the spin matrices; the total-spin-squared operator is the *Casimir operator* of the spin matrices [68], proportional to the identity.

Let us define

$$\gamma \equiv f(f+1). \tag{2.74}$$

The traceless symmetric operator is then

$$t_{ab} = \mathrm{s}_{ab} - \frac{1}{3}\gamma\mathbb{1}\delta_{ab}. \tag{2.75}$$

The traceless observable has inner product

$$\sum_{ab} \mathcal{T}_{ab}^2 = \sum_{ab} \left(\mathcal{S}_{ab} - \frac{1}{3}\gamma n \delta_{ab}\right)^2, \tag{2.76}$$

$$= \sum_{ab} \mathcal{S}_{ab}^2 - \frac{1}{3}\gamma^2 n^2. \tag{2.77}$$

Using Eq. (2.71), we can write the above result in terms of the unsymmetrized quadrupole $\mathcal{N}^{(2)}$, giving

$$\sum_{ab} \mathcal{N}_{ab}^2 = \sum_{ab} \mathcal{T}_{ab}^2 - \frac{1}{2}F^2 + \frac{1}{3}\gamma^2 n^2. \tag{2.78}$$

2.4.2 Octupole

For the third order tensor, we have

$$\mathrm{f}_{abc} = \mathrm{s}_{abc} + \frac{i}{2}\sum_d (\epsilon_{bcd}\mathrm{s}_{ad} + \epsilon_{acd}\mathrm{s}_{bd} + \epsilon_{abd}\mathrm{s}_{cd}) + \frac{1}{6}(\delta_{ab}\mathrm{f}_c + \delta_{bc}\mathrm{f}_a - 2\delta_{ac}\mathrm{f}_b), \tag{2.79}$$

where the third order symmetric matrix is given by

$$\mathrm{s}_{abc} = \mathrm{f}_{(abc)} = \frac{1}{6}\sum_{\mathrm{perm}\{a,b,c\}} \mathrm{f}_{abc} = \frac{1}{6}(\mathrm{f}_{abc} + \mathrm{f}_{acb} + \mathrm{f}_{bac} + \mathrm{f}_{bca} + \mathrm{f}_{cab} + \mathrm{f}_{cba}). \tag{2.80}$$

Taking the expectation and squaring both sides, the energy term is

$$\sum_{abc} \mathcal{N}_{abc}^2 = \sum_{abc} \mathcal{S}_{abc}^2 + \frac{1}{3}F^2 - 2\sum_{ab} \mathcal{S}_{ab}^2 + \frac{1}{2}\gamma^2 n^2. \tag{2.81}$$

The symmetric decomposition,

$$\mathrm{s}_{abc} = \mathrm{f}_{abc} - \frac{i}{2}\sum_d (\epsilon_{bcd}\mathrm{s}_{ad} + \epsilon_{acd}\mathrm{s}_{bd} + \epsilon_{abd}\mathrm{s}_{cd}) - \frac{1}{6}(\delta_{ab}\mathrm{f}_c + \delta_{bc}\mathrm{f}_a - 2\delta_{ac}\mathrm{f}_b), \tag{2.82}$$

has trace

$$\mathrm{s}_{aac} = \mathrm{f}_{aac} - \frac{1}{3}\mathrm{f}_c = \left(f(f+1) - \frac{1}{3}\right)\mathrm{f}_c, \tag{2.83}$$

with expectation

$$\mathcal{S}_{cca} = \lambda F_a, \tag{2.84}$$

where we define

$$\lambda \equiv f(f+1) - \frac{1}{3} = \left(\gamma - \frac{1}{3}\right). \tag{2.85}$$

The traceless octupole operator is then,

$$t_{abc} = s_{abc} - \frac{1}{5}\lambda(\delta_{ab}\mathrm{f}_c + \delta_{ca}\mathrm{f}_b + \delta_{bc}\mathrm{f}_a), \tag{2.86}$$

with corresponding observable

$$\mathcal{T}_{abc} = \mathcal{S}_{abc} - \frac{1}{5}\lambda(\delta_{ab}F_c + \delta_{ca}F_b + \delta_{bc}F_a). \tag{2.87}$$

This has inner product

$$\sum_{abc}\mathcal{T}^2_{abc} = \sum_{abc}\mathcal{S}^2_{abc} - \frac{3}{5}\lambda^2 F^2. \tag{2.88}$$

We can use Eqs. (2.77) and (2.81) to write Eq. (2.88) in terms of $\mathcal{N}^{(3)}$ and irreducible inner products, giving

$$\sum_{abc}\mathcal{N}^2_{abc} = \sum_{abc}\mathcal{T}^2_{abc} - 2\sum_{ab}\mathcal{T}^2_{ab} + \left(\frac{1}{3} + \frac{3}{5}\lambda^2\right)F^2 - \frac{1}{6}\gamma^2 n^2. \tag{2.89}$$

2.4.3 Hexadecapole

We have calculated the fourth order (hexadecapole) multipole operator, and decomposed it into irreducible components. The details are given in Appendix B.

2.4.4 Spin-specific identities

Spin-1

Combining the decomposition of the inner product for $\mathcal{T}^{(2)}$ in Eq. (2.78) with the identity in Eq. (2.45), and setting $f = 1$, we have

$$\sum_{ab} \mathcal{T}^2_{ab} = \frac{2}{3} n^2 - \frac{1}{2} F^2. \tag{2.90}$$

Spin-2

Combining the decomposition of the inner product for $\mathcal{T}^{(2)}$ in Eq. (2.78) with the identity in Eq. (2.53), and setting $f = 2$, and similarly for $\mathcal{T}^{(3)}$ and $\mathcal{T}^{(4)}$, we get

$$\sum_{ab} \mathcal{T}^2_{ab} = \frac{3}{2} F^2 + 30 \alpha^\dagger_{00} \alpha_{00}, \tag{2.91}$$

$$\sum_{abc} \mathcal{T}^2_{abc} = 18 (n^2 - \frac{1}{5} F^2 - 5 \alpha^\dagger_{00} \alpha_{00}), \tag{2.92}$$

$$\sum_{abcd} \mathcal{T}^2_{abcd} = \frac{54}{35} (7 n^2 + 25 \alpha^\dagger_{00} \alpha_{00}) - \frac{18}{7} F^2. \tag{2.93}$$

Chapter 3

Spinor phases and symmetry

In this Chapter we look at the ground states obtained by minimizing the mean-field spin-1 and spin-2 energy functionals, including their symmetry properties in two different representations, their phase diagrams in the presence of the quadratic Zeeman shift q, and some of their topological defects.

Most of these results have been reported already [32, 42, 67, 69], but we reproduce them here in order to specialize to the states investigated in subsequent Chapters, and unify the spin-1 and spin-2 treatments to be consistent with our notation. We include new analysis of the multipolar order of the ground states using the formalism developed in Section 2.4 of Chapter 2.

We focus on non-ferromagnetic phases, i.e. phases with zero total magnetization in the ground state. Thus we will use antiferromagnetic interactions, i.e. $c_1 > 0$, with $p = 0$, and we consider the ground state as a function of q, the quadratic Zeeman shift. For spin-1, this gives a one dimensional phase diagram. For spin-2, we will consider an additional axis set by c_2, the spin-singlet interaction strength.

We explain the symmetry of each phase of interest, giving alternate representations and corresponding visualizations. We connect each symmetry to a particular multipole operator, which can act as an order parameter for quenches into each phase. Finally, we consider spatial variation of the ground state and connect this with the relevant topological defects, i.e. vortices in the superfluid phase and spin rotation angles, which appear as phase windings in the wavefunction components.

3.1 Spin-1

The spin-1 energy functional has one independent nonlinear interaction term (apart from the density). In magnetization form, it is (see Section 2.3.1)

$$E_{int} = \frac{1}{2}\int d\mathbf{r}\ \left\{c_0 n^2 + c_1 F^2\right\}. \tag{3.1}$$

The density term is fixed for any normalized ground state, so we only have to consider the non-density term when computing the ground state. For ferromagnetic interactions, i.e. $c_1 < 0$, the ground state should be purely ferromagnetic to maximize the magnetization, with $F = n$. A representative spinor for a pure ferromagnetic state is then

$$\psi_F = \sqrt{n}\begin{pmatrix}1\\0\\0\end{pmatrix}. \tag{3.2}$$

In the absence of a magnetic field, the energy of any spinor is degenerate with respect to a global U(1) phase rotation $e^{i\theta}$, and an SO(3) spin rotation, parameterized by three Euler angles α, β, ϕ (representing z-y-z spin rotations). We represent a general spin rotation by the matrix operator

$$U(\alpha,\beta,\phi) \equiv e^{-i\phi \mathrm{f}_z} e^{-i\beta \mathrm{f}_y} e^{-i\alpha \mathrm{f}_z}, \tag{3.3}$$

$$= \begin{pmatrix} e^{-i(\alpha+\phi)}\cos^2\frac{\beta}{2} & -\frac{e^{-i\alpha}}{\sqrt{2}}\sin\beta & e^{-i(\alpha-\phi)}\sin^2\frac{\beta}{2} \\ \frac{e^{-i\phi}}{\sqrt{2}}\sin\beta & \cos\beta & -\frac{e^{i\gamma}}{\sqrt{2}}\sin\beta \\ e^{i(\alpha-\phi)}\sin^2\frac{\beta}{2} & \frac{e^{i\alpha}}{\sqrt{2}}\sin\beta & e^{i(\alpha+\phi)}\cos^2\frac{\beta}{2} \end{pmatrix}. \tag{3.4}$$

The general ferromagnetic state is then

$$\tilde{\psi}_F = e^{i\theta}U(\alpha,\beta,\phi)\psi_F = \sqrt{n}e^{i(\theta-\phi)}\begin{pmatrix} e^{-i\alpha}\cos^2\frac{\beta}{2} \\ \frac{1}{\sqrt{2}}\sin\beta \\ e^{i\alpha}\sin^2\frac{\beta}{2}\end{pmatrix}. \tag{3.5}$$

In spin-singlet form, the energy functional becomes

$$E_{int} = \frac{1}{2}\int d\mathbf{r}\left\{(c_0+c_1)n^2 - c_1|\alpha|^2\right\}, \tag{3.6}$$

where we renormalize the spin-singlet amplitude to be [c.f. Eq. (2.15)]

$$\alpha = \psi_0^2 - 2\psi_{+1}\psi_{-1}. \tag{3.7}$$

Considering antiferromagnetic interactions, i.e. $c_1 > 0$, we see that the ground state should maximize the spin-singlet amplitude, i.e. $|\alpha| = n$. A representative for a maximized spin-singlet state is

$$\psi_P = \sqrt{n} \begin{pmatrix} 0 \\ 1 \\ 0 \end{pmatrix}, \tag{3.8}$$

which we call a polar state. A general polar state is given by a $U(1) \times SO(3)$ rotation of this state, i.e.

$$\tilde{\psi}_P = e^{i\theta} U(\alpha, \beta, \phi) \psi_P = \sqrt{n} e^{i\theta} \begin{pmatrix} -\frac{e^{-i\alpha}}{\sqrt{2}} \sin\beta \\ \cos\beta \\ \frac{e^{i\alpha}}{\sqrt{2}} \sin\beta \end{pmatrix}. \tag{3.9}$$

Thus we have two "pure" ground states for the spin-1 system, ψ_F and ψ_P, and their $U(1) \times SO(3)$ rotations. To visualize their symmetry properties in spin space, it is helpful to introduce a spherical harmonic representation.

3.1.1 Spherical harmonic representation

To visualize the physical symmetry of the spinor wavefunction, we consider the spherical harmonic representation, given by

$$\Psi(\hat{\boldsymbol{s}}) = \sum_m \xi_m Y_f^m(\hat{\boldsymbol{s}}), \tag{3.10}$$

where $\hat{\boldsymbol{s}}$ is a unit vector in 3D spin space, and Y_f^m are the spherical harmonics for spin-f. For any particular spinor, we can generate a surface plot of $|\Psi(\hat{\boldsymbol{s}})|^2$ and colour it with $\arg \Psi(\hat{\boldsymbol{s}})$ to visualize the symmetry of the spinor in spin space.

Applying a spin rotation to the state, e.g. with RF pulses in an experiment, will correspondingly rotate the 3D spherical harmonic representation. This visualization thus shows the physical symmetries that the spinor field contains. In particular, we can use it to construct a picture of what is happening in various spatially extended topological states, where the point-symmetry of the spinor transforms through each point in position space in a non-trivial manner.

For spin-1, we the three $f = 1$ spherical harmonics are given by

$$Y_1^0(\theta, \phi) = \frac{1}{2}\sqrt{\frac{3}{\pi}}\cos(\theta), \tag{3.11}$$

$$Y_1^{\pm 1}(\theta, \phi) = \mp\frac{1}{2}\sqrt{\frac{3}{2\pi}}\sin(\theta)e^{\pm i\phi}. \tag{3.12}$$

We plot the the spherical harmonic representation of the spin-1 pure ferromagnetic and antiferromagnetic polar states, ψ_F and ψ_P, in Fig. 3.1. Fig. 3.1(b) shows that ψ_P has two lobes of "nematic" (nonferromagnetic) order along an axis of symmetry with a relative phase difference of π (they are "polarized" hence "polar" states).

3.1.2 Multipolar order

If we consider the quadrupole observable $\mathcal{T}^{(2)}$ for spin-1, with inner product given by Eq. (2.90), each state has total quadrupolar order

$$\sum_{ab} \mathcal{T}_{ab}^2 = \frac{2}{3}n^2 - \frac{1}{2}F^2 = \begin{cases} \frac{1}{6}n^2 & \text{for } \psi_F, \\ \frac{2}{3}n^2 & \text{for } \psi_P. \end{cases} \tag{3.13}$$

This shows that the ψ_P state contains the maximum amount of quadrupolar order. The axis of alignment of quadrupolar order in the polar state is also known as the nematic director. The state is symmetric under inversion of the director, which involves a π rotation in spin space, coupled with a π rotation of the global phase due to the polarity of the nematic lobes. It is helpful to consider the system in the Cartesian basis to reveal the nematic director more explicitly.

3.1.3 Cartesian representation

Let us keep $\psi = (\psi_{+1}, \psi_0, \psi_{-1})^T$ for the representation of the wavefunction state $|\psi\rangle$ in the spherical basis (i.e. in terms of $m \in \{+1, 0, -1\}$ spin levels), and use $\vec{\psi} = (\psi_x, \psi_y, \psi_z)^T$ for the Cartesian representation, i.e. we have

$$|\psi\rangle = \sum_m \psi_m |m\rangle = |\vec{\psi}\rangle = \sum_\nu \psi_\nu |\nu\rangle, \quad \nu \in \{x, y, z\}, \tag{3.14}$$

where the basis states of the Cartesian representation, i.e. $|\nu\rangle$, are defined by

$$\mathrm{f}_\nu |\nu\rangle = 0. \tag{3.15}$$

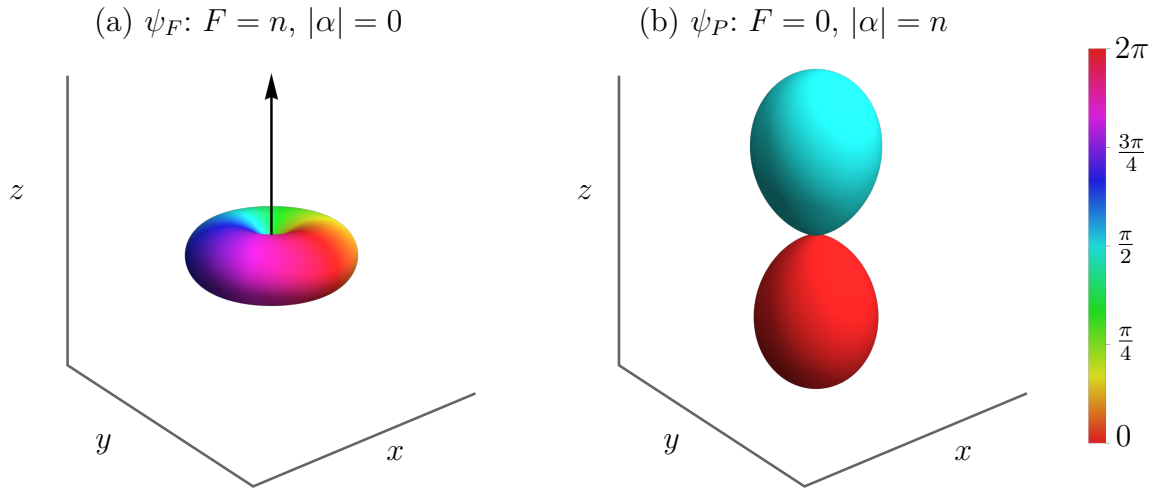

Figure 3.1: Spherical harmonic representation of pure spin-1 states in spin space. Surface plots of magnitude coloured by phase of $\Psi(\hat{\boldsymbol{s}})$ [defined in Eq. (3.10)]. (a) is the ferromagnetic state ψ_F defined in Eq. (3.2), with arrow indicating its magnetization vector. (b) is the antiferromagnetic polar state ψ_P defined in Eq. (3.8).

Considering $|m\rangle$ and $|\nu\rangle$ eigenstates of f_z, we get $|z\rangle = |0\rangle$, and we can rotate this state onto the x axis [with $\exp(i\frac{\pi}{2}\mathrm{f}_y)$] and the y axis [with $\exp(-i\frac{\pi}{2}\mathrm{f}_x)$] to get the other two basis vectors. This gives us the transformation between bases, which lets us relate the components of each representation as

$$\psi_x = \frac{1}{\sqrt{2}}(\psi_{-1} - \psi_1), \tag{3.16}$$

$$\psi_y = -\frac{i}{\sqrt{2}}(\psi_1 + \psi_{-1}), \tag{3.17}$$

$$\psi_z = \psi_0. \tag{3.18}$$

We will give results in both the cartesian $\vec{\psi}$ and spherical ψ bases as needed.

A general spin-1 spinor can be decomposed in the form

$$\vec{\psi} = e^{i\theta}(\vec{u} + i\vec{v}), \tag{3.19}$$

where θ is the global phase and $\{\vec{u}, \vec{v}\}$ are mutually orthogonal real vectors satisfying $|\vec{u}|^2 + |\vec{v}|^2 = n$, and $|\vec{u}| \geq |\vec{v}|$ (also see [43, 57, 70, 71]). The total density is given by

$$\vec{\psi}^\dagger\vec{\psi} = u^2 + v^2 = n, \tag{3.20}$$

the local magnetization (spin density) vector is

$$\boldsymbol{F} = -i\vec{\psi}^* \times \vec{\psi} = 2\vec{u} \times \vec{v}, \tag{3.21}$$

and the (symmetric) quadrupolar nematic tensor [defined in Sec. 2.4.1] is

$$(\mathcal{S}^{(2)})_{ab} \equiv \mathcal{S}_{ab} = n\delta_{ab} - \frac{1}{2}(\vec{\psi}^* \otimes \vec{\psi} + \vec{\psi} \otimes \vec{\psi}^*), \tag{3.22}$$

$$= n\delta_{ab} - (\vec{u} \otimes \vec{u} + \vec{v} \otimes \vec{v}). \tag{3.23}$$

The quadrupolar tensor describes the anisotropy of the spin fluctuations, and as a symmetric 3×3 real tensor it has the symmetry of an ellipsoid. This is revealed by diagonalizing $\mathcal{S}^{(2)}$, giving $\{\vec{u}, \vec{v}, \boldsymbol{F}\}$ as the eigenvectors with respective eigenvalues $\lambda_u = \frac{1}{2}(n - \mathcal{A})$, $\lambda_v = \frac{1}{2}(n + \mathcal{A})$ and $\lambda_F = n$. Here

$$\mathcal{A} = 2|\vec{u}|^2 - n \geq 0, \tag{3.24}$$

is the *alignment parameter* [57], which characterizes the relative fluctuations of magnetization along the directions orthogonal to $\boldsymbol{F}$. The alignment is related to the spin-singlet amplitude as

$$\mathcal{A} = |\alpha|, \tag{3.25}$$

where the spin-singlet amplitude [given in the spherical basis by Eq. (3.7)] is given in the Cartesian representation by

$$\alpha = \vec{\psi}^T \vec{\psi}. \tag{3.26}$$

It is conventional to take the eigenvector associated with the smallest eigenvalue of $\mathcal{S}^{(2)}$ as the nematic director, i.e. the vector $\vec{u}$. We can use the eigenvectors and eigenvalues to represent the nematic tensor as an ellipsoid [see Fig. 3.2(a)]. We also note that $\lambda_u = |\vec{v}|^2$ and $\lambda_v = |\vec{u}|^2$, so that the extent of the ellipsoid along the $\vec{u}$ direction is the squared length of $\vec{v}$, and the extent of the ellipsoid along the $\vec{v}$ direction is the squared length of $\vec{u}$.

Two limiting states are of interest. First, the fully magnetized ferromagnetic state with $|\boldsymbol{F}| = n$, where $|\vec{u}| = |\vec{v}| = \sqrt{n/2}$, and $\mathcal{A} = 0$. Second, and of primary concern in our spin-1 work, is the polar state, which has the form

$$\vec{\psi}_{\mathrm{P}} = e^{i\theta}\vec{u}, \tag{3.27}$$

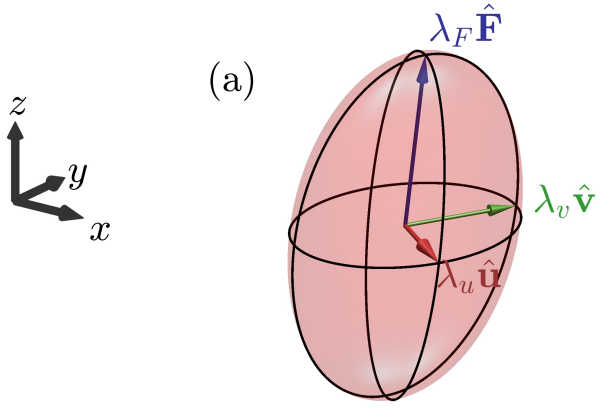

(b) Easy-Plane

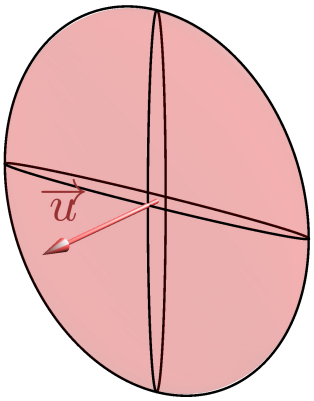

(c) Easy-Axis

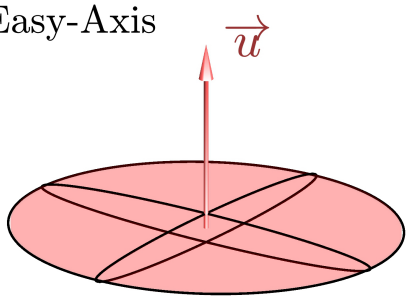

Figure 3.2: Cartesian representation of the spin-1 spinor. (a) shows a general state, with $\{\boldsymbol{F}, \vec{u}, \vec{v}\}$ defining an ellipsoid representing the symmetric quadrupolar tensor $\mathcal{S}^{(2)}$. The ellipsoid radii are given by the respective eigenvalues $\{n, \frac{1}{2}(n-\mathcal{A}), \frac{1}{2}(n+\mathcal{A})\}$. Note that the eigenvalues are such that the axis in the $\vec{u}$ direction is set by $|\vec{v}|^2$ and vice versa. (b) and (c) consider the antiferromagnetic (i.e. $c_1 > 0$) ground state: the nematic director is maximized, with the other two axes . (b) shows the ground state for $q < 0$, i.e. Easy-Plane polar, with the nematic director lying in the plane. (c) shows the ground state for $q > 0$, i.e. Easy-Axis polar, with the nematic director lying along the z axis.

with $|\vec{u}| = \sqrt{n}$, $\mathcal{A} = n$ and $\boldsymbol{F} = 0$ [see Figs. 3.2(b) and (c)]. The spin properties of this state are completely characterized by the director $\vec{u}$, and the state is invariant under the transformation

$$\theta \to \theta + \pi, \quad \text{and} \quad \vec{u} \to -\vec{u}, \tag{3.28}$$

i.e. inverting the direction of $\vec{u}$ and rotating the global phase by π. For general spin-1 states the relation of Eq. (2.44) holds, which in our interaction units is given by

$$|\boldsymbol{F}|^2 + \mathcal{A}^2 = n^2, \tag{3.29}$$

so that $\mathcal{A}$ can be used to characterize how close a state is to the limiting cases of ferromagnetic ($\mathcal{A} = 0$) or polar ($\mathcal{A} = n$) order.

3.1.4 Antiferromagnetic ground states with non-zero quadratic Zeeman energy

We now consider the effect of the quadratic Zeeman energy q on the ground state phase diagram. For antiferromagnetic interactions, with $F_z = 0$ and $p = 0$, the ground state has zero magnetization and is thus the generalized polar state $\tilde{\psi}_P$. The quadratic Zeeman energy breaks $SO(3)$ symmetry, however, by coupling to the z component of the quadrupole tensor,

$$E_q = q\mathcal{N}_{zz} = q(|\psi_{+1}|^2 + |\psi_{-1}|^2). \tag{3.30}$$

For $q = 0$ the nematic director retains full $SO(3)/Z_2$ symmetry, where Z_2 is due to the discrete axial symmetry of the nematic director. The state is given in the Cartesian basis by $\vec{\psi}_P$ [see Eq. (3.27)], which in the spherical basis [c.f. Eq. (3.9)] becomes

$$\tilde{\psi}_P = e^{i\theta} \begin{pmatrix} -\frac{1}{\sqrt{2}}(u_x - iu_y) \\ u_z \\ \frac{1}{\sqrt{2}}(u_x + iu_y) \end{pmatrix}, \tag{3.31}$$

for components u_ν of $\vec{u}$, $\nu \in \{x, y, z\}$.

For $q > 0$ the nematic director is along the z axis, and spin fluctuations are confined to the z axis, with $SO(2)/Z_2$ rotational symmetry about z. The ground state is called

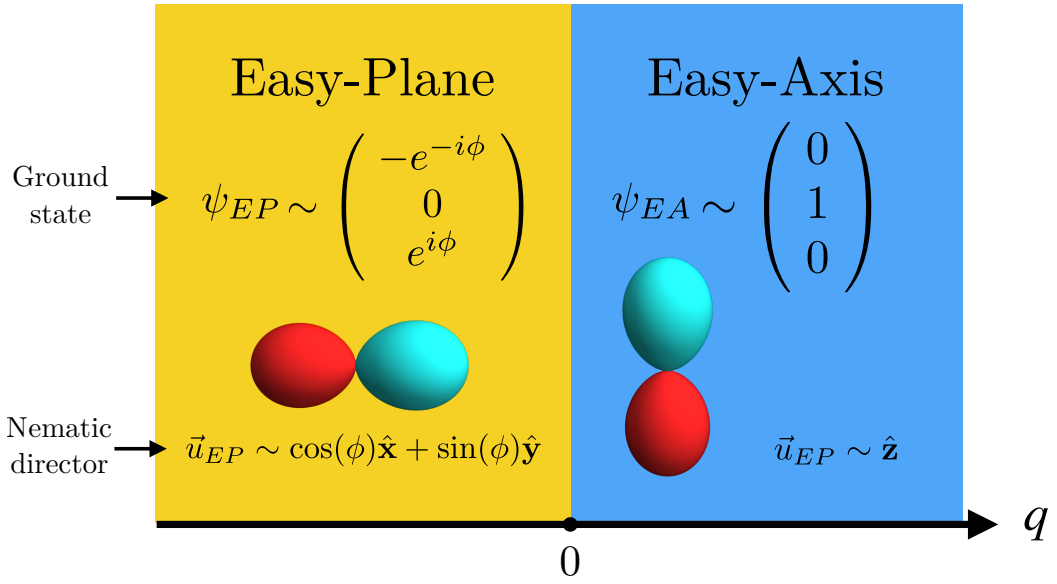

Figure 3.3: Spin-1 antiferromagnetic (i.e. $c_1 > 0$) phase diagram showing dependence on q. Shown are ground state spinors ψ_{EA} and ψ_{EP} [Eqs. (3.32) and (3.33)], their spherical harmonic representation, and nematic directors.

easy-axis polar (EA), and the ground state spinor is

$$\psi_{EA} = e^{i\theta}\psi_P = \sqrt{n}e^{i\theta}\begin{pmatrix} 0 \\ 1 \\ 0 \end{pmatrix}. \tag{3.32}$$

For $q < 0$, the nematic axis lies oriented in the $x - y$ plane, breaking $SO(2)$ symmetry. The ground state is called easy-plane polar (EP), and the ground state spinor is

$$\psi_{EP} = e^{i\theta}e^{-i\phi \mathrm{f}_z}e^{i\frac{\pi}{2}\mathrm{f}_y}\psi_P = \sqrt{\frac{n}{2}}e^{i\theta}\begin{pmatrix} e^{-i\phi} \\ 0 \\ e^{i\phi} \end{pmatrix}, \tag{3.33}$$

where ϕ breaks the spin symmetry by setting the direction of the nematic director in the $x - y$ plane.

We summarize this phase diagram in Fig. 3.3, showing the spherical ground state spinors, their spherical harmonic representation, and the form of their nematic directors. This should be compared with the equivalent Cartesian representations in Fig. 3.2(b) and (c).

3.2 Spin-2

The spin-2 energy functional has two independent nonlinear interaction terms (apart from the density). In terms of the lowest order physical operators, they are (see Section 2.3.2)

$$E_{int} = \frac{1}{2}\int d\mathbf{r}\ \left(c_0 n^2 + c_1 F^2 + c_2 |\alpha|^2\right). \tag{3.34}$$

where we renormalize c_2 to absorb a factor of $1/5$ and define the spin-singlet amplitude similarly to spin-1 as [c.f. Eqs. (2.15) and (3.7)]

$$\alpha = \psi_0^2 - 2\psi_{+1}\psi_{-1} + 2\psi_{+2}\psi_{-2}. \tag{3.35}$$

When ferromagnetic interactions dominate, i.e. $c_1 < 0$ and $c_1 < c_2$, the ground state should be purely ferromagnetic to maximize the magnetization. In the spin-2 system there are two pure ferromagnetic states, with $F = n$ and $F = 2n$, which we call the F_1 and F_2 states. Obviously F_2 is the ferromagnetic ground state since it has more magnetization, but F_1 can appear when there is competition between different interactions. Representative spinors for F_1 and F_2 are given by

$$\psi_{F_1} = \sqrt{n}\begin{pmatrix}0\\1\\0\\0\\0\end{pmatrix}, \quad \psi_{F_2} = \sqrt{n}\begin{pmatrix}1\\0\\0\\0\\0\end{pmatrix}. \tag{3.36}$$

Similar to the spin-1 case, in the absence of a magnetic field the energy of any spinor is degenerate to a $U(1) \times SO(3)$ transformation. This consists of a global U(1) phase rotation $e^{i\theta}$, and an SO(3) spin rotation which for spin-2 becomes a 5×5 matrix operator. We choose this operator in the same way as spin-1, i.e. representing z-y-z spin rotations, but now using spin-2 matrices, giving us the operator

$$U(\alpha,\beta,\phi) \equiv e^{-i\phi \mathrm{f}_z} e^{-i\beta \mathrm{f}_y} e^{-i\alpha \mathrm{f}_z}, \tag{3.37}$$

$$= e^{-i\phi \mathrm{f}_z} \begin{pmatrix} C^4 & -2C^3S & 2C^2S^2 & -2CS^3 & S^4 \\ 2C^3S & C^2(C^2-3S^2) & -\sqrt{\frac{3}{8}}\sin 2\beta & -S^2(S^2-3C^2) & -2CS^3 \\ \sqrt{6}C^2S^2 & \sqrt{\frac{3}{8}}\sin 2\beta & \frac{1}{4}(1+3\cos 2\beta) & -\sqrt{\frac{3}{8}}\sin 2\beta & \sqrt{6}C^2S^2 \\ 2CS^3 & -S^2(S^2-3C^2) & \sqrt{\frac{3}{8}}\sin 2\beta & C^2(C^2-3S^2) & -2C^3S \\ S^4 & 2CS^3 & \sqrt{6}C^2S^2 & 2C^3S & C^4 \end{pmatrix} e^{-i\alpha \mathrm{f}_z}, \tag{3.38}$$

where $C \equiv \cos\frac{\beta}{2}$ and $S \equiv \sin\frac{\beta}{2}$, and the z rotations are diagonal matrices. It is clear that the general F_2 and F_1 states pick out the first and second columns of Eq. (3.38), respectively.

When spin-singlet interactions dominate, i.e. $c_2 < 0$ and $c_2 < c_1$, the ground state should be maximize the spin-singlet amplitude. In the spin-2 system there are two "pure" spin-singlet states, both with $|\alpha| = n$. At the mean-field level they are degenerate in energy at zero magnetic field. Their spin-1 analogies are the easy-axis and easy-plane polar states. However, these spin-2 states have distinct nematic symmetries: the uniaxial nematic (UN) state has one axis of nematic symmetry, while the biaxial nematic (BN) state has two. Representative uniaxial and biaxial nematic spinors are given by

$$\psi_{UN} = \sqrt{n}\begin{pmatrix}0\\0\\1\\0\\0\end{pmatrix}, \quad \psi_{BN} = \sqrt{\frac{n}{2}}\begin{pmatrix}1\\0\\0\\0\\1\end{pmatrix}, \quad \psi'_{BN} = \sqrt{\frac{n}{2}}\begin{pmatrix}0\\1\\0\\1\\0\end{pmatrix} = ie^{-if_y\pi/2}e^{-if_z\pi/4}\psi_{BN}, \tag{3.39}$$

where we note that ψ'_{BN} is related to the BN spinor by a $U(1) \times SO(3)$ rotation. It is clear that the general UN state picks out the middle column of Eq. (3.38), while the general BN state picks out the sum of the outer columns (equivalently the second and fourth). Due to their mean-field degeneracy, the spin-singlet ground state at the mean-field level and zero magnetic field is an arbitrary combination of the UN and BN "pure" states.

There is a fifth "pure" state in the spin-2 system, found by considering antiferromagnetic interactions, i.e. $c_1 > 0$, with positive spin-singlet interaction, i.e. $c_2 > 0$. In this case the ground state minimizes magnetization and spin-singlet amplitude, with $F = |\alpha| = 0$. This is called the cyclic (C_3) state, as it has three axes of nematic symmetry. There are three representative spinors which are useful for understanding a general cyclic state; they are given by

$$\psi_{\text{cyclic},1} = \frac{\sqrt{n}}{2}\begin{pmatrix}1\\0\\i\sqrt{2}\\0\\1\end{pmatrix}, \quad \psi_{\text{cyclic},2} = \sqrt{\frac{n}{3}}\begin{pmatrix}1\\0\\0\\\sqrt{2}\\0\end{pmatrix}, \quad \psi_{\text{cyclic},3} = \sqrt{\frac{n}{3}}\begin{pmatrix}0\\\sqrt{2}\\0\\0\\1\end{pmatrix}. \tag{3.40}$$

A general cyclic state, ψ_{C_3}, is given by a $U(1) \times SO(3)$ transformation of one of these states, which are themselves related by

$$\psi_{\text{cyclic},2} = e^{-i\pi} e^{i\mathrm{f}_z \pi/4} \exp\left[-i\frac{\mathrm{f}_x - \mathrm{f}_y}{\sqrt{2}} \arccos\left(\frac{1}{\sqrt{3}}\right)\right] \psi_{\text{cyclic},1}, \tag{3.41}$$

$$\psi_{\text{cyclic},3} = e^{-i\pi} e^{i\mathrm{f}_z 3\pi/4} \exp\left[-i\frac{\mathrm{f}_x + \mathrm{f}_y}{\sqrt{2}} \arccos\left(\frac{1}{\sqrt{3}}\right)\right] \psi_{\text{cyclic},1}. \tag{3.42}$$

Thus we have five "pure" states in the spin-2 system. Two are ferromagnetic, i.e. F_1 and F_2, and three are nematic, i.e. UN, BN, and C_3. To visualize their symmetry properties in spin space, it is helpful to introduce a spherical harmonic representation.

3.2.1 Spherical harmonic representation

The basic equation for the spherical harmonic representation of the spin-2 system is the same as for spin-1, i.e. Eq. (3.10). The difference is, we now use the five $f = 2$ spherical harmonics given by

$$Y_2^0(\theta,\phi) = \sqrt{\frac{5}{16\pi}}(3\cos(\theta)^2 - 1), \tag{3.43}$$

$$Y_2^{\pm 1}(\theta,\phi) = \mp\sqrt{\frac{15}{8\pi}}\sin(\theta)\cos(\theta)e^{\pm i\phi}, \tag{3.44}$$

$$Y_2^{\pm 2}(\theta,\phi) = \sqrt{\frac{15}{32\pi}}\sin^2(\theta)e^{\pm 2\phi}. \tag{3.45}$$

In Fig. 3.4 we plot the spherical harmonic representations of the two ferromagnetic states, F_1 and F_2, and the nematic states with maximum spin-singlet amplitude, UN and BN. We see in Fig. 3.4(a) and (b) that the ferromagnetic states have SO(2) symmetry about the z axis.

Fig. 3.4(c) shows that the UN state also has $SO(2)$ symmetry, but with an additional inversion symmetry, or equivalently a rotation by π (1/2 turn) through any axis in the x-y plane. Unlike the spin-1 polar phase, the inversion only requires a spin rotation as the nematic lobes have the same phase. Fig. 3.4(d) shows that the BN state breaks SO(2) symmetry by having two perpendicular nematic axes in the x-y plane, being symmetric under a $\pi/2$ rotation (1/4 turn) about the z axis. The π difference in phase between the nematic lobes of the BN state couples the global phase to the spin-rotational symmetry.

In Fig. 3.5 we plot the spherical harmonic representation of the cyclic state, C_3. This state has the discrete symmetries of a tetrahedron. The lobes of the spherical harmonic

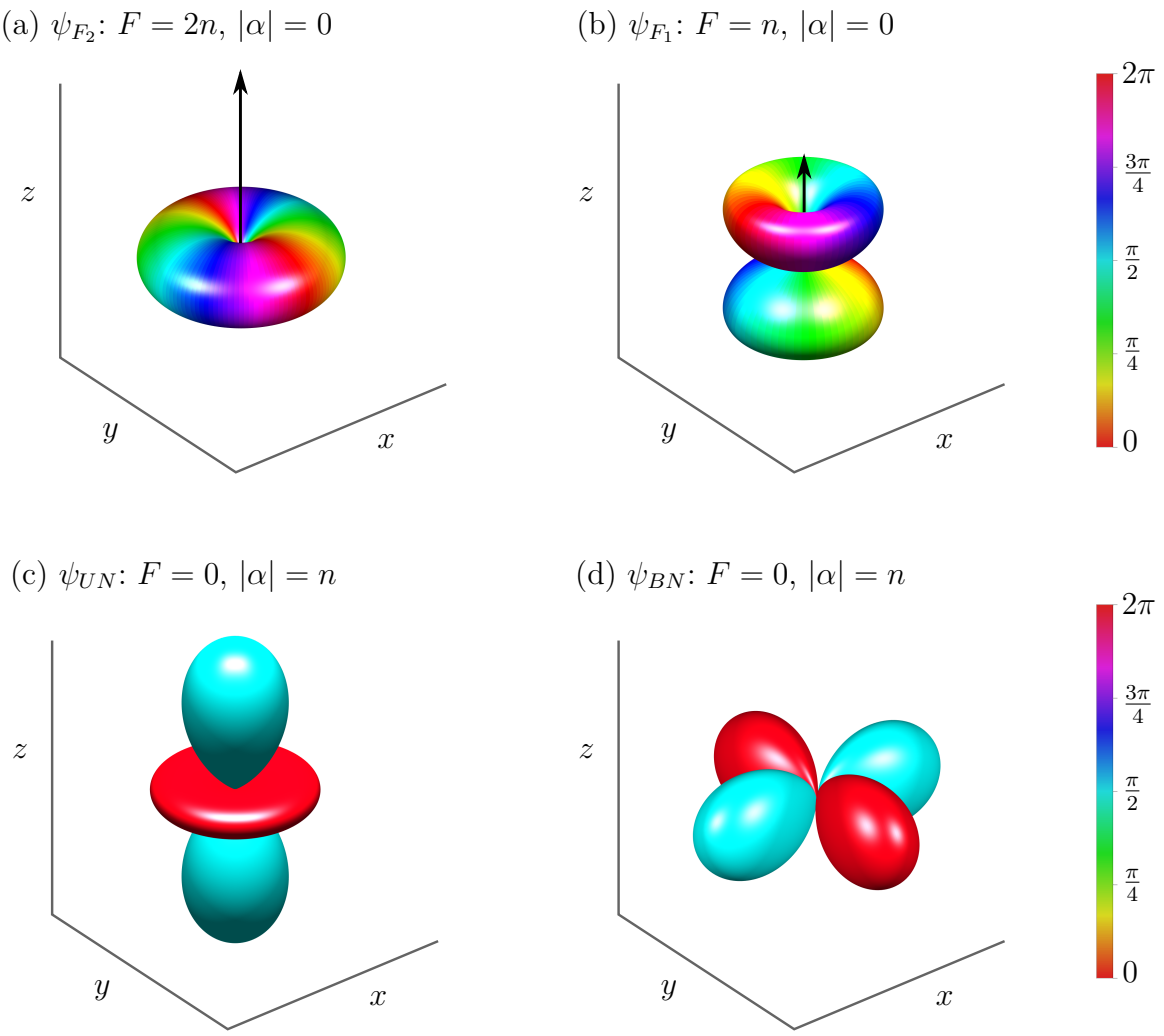

Figure 3.4: Spherical harmonic representation of the ferromagnetic and the maximized spin-singlet spin-2 states. (a) and (b) are the ferromagnetic states defined in Eq. (3.36), with arrows indicating their magnetization vector. (c) and (d) are the maximal spin-singlet states defined in Eq. (3.39).

(a) $\psi_{\text{cyclic},1}$: $F = 0$, $|\alpha| = 0$

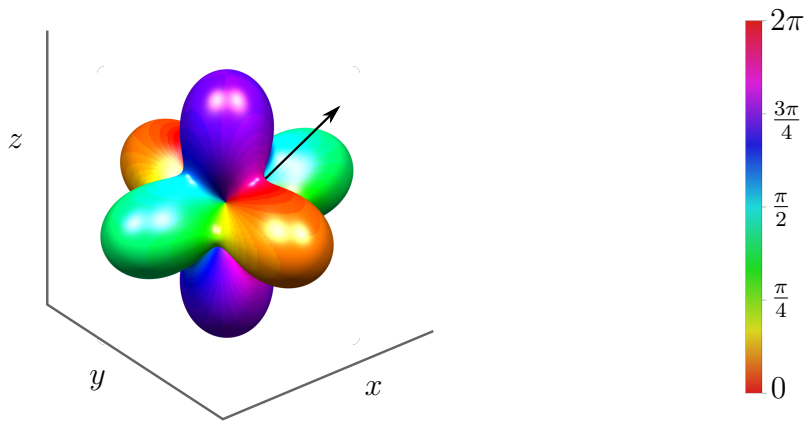

(b) $\psi_{\text{cyclic},2}$: $F = 0$, $|\alpha| = 0$

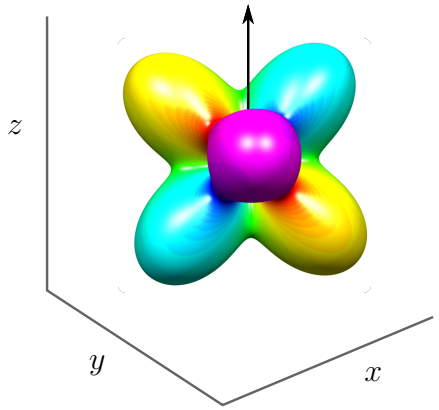

(c) $\psi_{\text{cyclic},3}$: $F = 0$, $|\alpha| = 0$

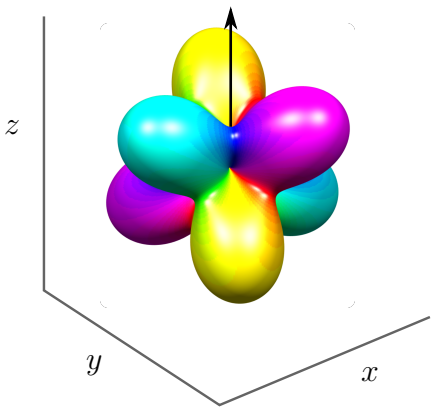

Figure 3.5: Spherical harmonic representation of the cyclic spin-2 states defined in Eq. (3.40), with arrows indicating a C_3 axis of symmetry. (a) show $\psi_{\text{cyclic},1}$, which has nematic lobes aligned with the Cartesian x,y, and z axes. (b) and (c) show $\psi_{\text{cyclic},2}$ and $\psi_{\text{cyclic},3}$, which have C_3 axes aligned with the x,y, and z axes.

representation in Fig. 3.5 reveal nematic order along three perpendicular axes, which we call $\vec{u}$, $\vec{v}$, and $\vec{w}$. Rotation about a nematic axis has $\pi/2$ symmetry. The nematic order also has third order cyclic symmetry, i.e. is symmetric under rotations of $2\pi/3$ (1/3 turn), about three diagonal C_3 axes, for example the C_3 axis given by $\vec{u}+\vec{v}+\vec{w}$.

Fig. 3.5(a) shows the state $\psi_{\text{cyclic},1}$, with $\vec{u}$, $\vec{v}$, and $\vec{w}$ axes lining up with the x,y,z cartesian axes, with the C_3 axis pointing in the $(1,1,1)^T$ direction. Alternatively, Fig. 3.5(b) and (c) show the states $\psi_{\text{cyclic},2}$ and $\psi_{\text{cyclic},3}$, which have the C_3 axis aligned with the z axis. The relationship between these three cyclic states, as given in Eqs. (3.41) and (3.42), can be inferred from these plots.

3.2.2 Multipolar order

The three nematic states; i.e. UN, C_3, and BN, have different types of nematic order, distinguished by the quadrupole, octupole, and hexadecapole multipole moments, i.e. $\mathcal{T}^{(2)}$, $\mathcal{T}^{(3)}$, and $\mathcal{T}^{(4)}$. The inner product of each multipole is

$$\sum_{ab} \mathcal{T}^2_{ab} = \frac{3}{2}F^2 + 6|\alpha_{00}|^2, \tag{3.46}$$

$$\sum_{abc} \mathcal{T}^2_{abc} = 18(n^2 - \frac{1}{5}F^2 - |\alpha_{00}|^2), \tag{3.47}$$

$$\sum_{abc} \mathcal{T}^2_{abcd} = \frac{54}{35}(7n^2 + 5|\alpha_{00}|^2) - \frac{18}{7}F^2. \tag{3.48}$$

Immediately we see that the C_3 state has no quadrupole order, but instead maximizes the octupole order, while the UN and BN phases only contain even multipolar order:

$$\sum_{ab} \mathcal{T}^2_{ab} = \begin{cases} 6n^2 & \text{for } \psi_{UN} \text{ and } \psi_{BN}, \\ 0 & \text{for } \psi_{C_3}, \end{cases} \tag{3.49}$$

$$\sum_{abc} \mathcal{T}^2_{abc} = \begin{cases} 0 & \text{for } \psi_{UN} \text{ and } \psi_{BN}, \\ 18n^2 & \text{for } \psi_{C_3}, \end{cases} \tag{3.50}$$

$$\sum_{abcd} \mathcal{T}^2_{abcd} = \frac{54}{35} \times \begin{cases} 12n^2 & \text{for } \psi_{UN} \text{ and } \psi_{BN}, \\ 7n^2 & \text{for } \psi_{C_3}. \end{cases} \tag{3.51}$$

The UN phase has second order rotational symmetry, so the second order multipole is the appropriate order parameter to reveal the symmetry of the state. The cyclic phase has third order symmetry about the C_3 axis, with the third order multipole the appropriate tensor order parameter to reveal this symmetry of the state.

For the BN state ψ_{BN}, however, the quadrupole order does not reveal the broken symmetry in the x-y plane, as

$$\mathcal{T}^{(2)} = \begin{pmatrix} -1 & 0 & 0 \\ 0 & -1 & 0 \\ 0 & 0 & 2 \end{pmatrix}, \text{ for } e^{-i\phi \mathrm{f}_z}\psi_{BN}, \tag{3.52}$$

does not depend on ϕ. The state ψ_{BN} has fourth order rotational symmetry about the z axis, hence the fourth order multipole is the appropriate tensor order parameter to reveal this symmetry, with components coupling to ϕ. The C_3 state also has some fourth order rotational symmetry. This can be seen by considering the state $e^{-i\phi \mathrm{f}_z}\psi_{\mathrm{cyclic},1}$, which has $\psi_{\pm 2}$ components similar to ψ_{BN}.

To further understand the spin-2 symmetries, and the cyclic phase in particular, it is useful to consider the spin-2 system in the Cartesian representation, where cyclic symmetry reveals itself naturally.

3.2.3 Cartesian order parameter

The spherical representation in spin-2 is $\psi = (\psi_{+2}, \psi_{+1}, \psi_0, \psi_{-1}, \psi_{-2})^T$. We also have a Cartesian representation in analogy with the spin-1 Cartesian representation, however it takes two spin-1 Cartesian order parameters to make a spin-2 Cartesian order parameter. This means the spin-2 Cartesian representation is a second order tensor χ_{ab}.

This can be taken to be (see Ref. [32]) the traceless symmetric (complex) tensor

$$\chi = \begin{pmatrix} \tilde{\chi}_{xx} - \frac{1}{2}\chi_{zz} & \chi_{xy} & \chi_{xz} \\ \chi_{xy} & -\tilde{\chi}_{xx} - \frac{1}{2}\chi_{zz} & \chi_{yz} \\ \chi_{xz} & \chi_{yz} & \chi_{zz} \end{pmatrix}, \tag{3.53}$$

$$\tilde{\chi}_{xx} = \frac{1}{2}(\psi_{+2} + \psi_{-2}), \quad \chi_{xy} = \frac{i}{2}(\psi_{+2} - \psi_{-2}), \tag{3.54}$$

$$\chi_{xz} = \frac{1}{2}(\psi_{-1} - \psi_{+1}), \quad \chi_{yz} = -\frac{i}{2}(\psi_{+1} + \psi_{-1}), \tag{3.55}$$

$$\chi_{zz} = \sqrt{\frac{2}{3}}\psi_0. \tag{3.56}$$

Using this representation, the nonlinear interaction terms can be written as [c.f. Eqs. (3.20),

(3.21) and (3.26)],

$$n = \mathrm{Tr}\{\chi^\dagger \chi\}, \tag{3.57}$$

$$F^2 = 2\mathrm{Tr}\{[\chi, \chi^\dagger]^2\}, \tag{3.58}$$

$$\alpha_{00} = \mathrm{Tr}\{\chi^T \chi\}. \tag{3.59}$$

To go beyond spin-singlet order, we look at the trace of the next power of χ. This turns out to be the singlet trio amplitude

$$\frac{1}{\sqrt{6}}\alpha_{30} = \mathrm{Tr}\{\chi^3\}, \tag{3.60}$$

$$= \frac{3}{4}\chi_{zz}^3 - 3\chi_{zz}\left(\chi_{xx}^2 + \chi_{xy}^2 - \frac{1}{2}(\chi_{xz}^2 + \chi_{yz}^2)\right) + 3\chi_{xx}\left(\chi_{xz}^2 - \chi_{yz}^2\right) + 6\chi_{xy}\chi_{xz}\chi_{yz}, \tag{3.61}$$

which we can convert to the spherical basis to get

$$\alpha_{30} = \psi_0^3 - 3\psi_0\left(\psi_{+1}\psi_{-1} + 2\psi_{+2}\psi_{-2}\right) + 3\sqrt{\frac{3}{2}}\left(\psi_{+1}^2\psi_{-2} + \psi_{+2}\psi_{-1}^2\right). \tag{3.62}$$

In fact, using the following relationship between the determinant and trace for 3×3 matrices[1]

$$\det(A) = \frac{1}{6}((\mathrm{Tr}\{A\})^3 - 3\mathrm{Tr}\{A^2\}\mathrm{Tr}\{A\} + 2\mathrm{Tr}\{A^3\}), \tag{3.63}$$

and using the fact that χ is traceless, we have

$$\det\chi = \frac{1}{3}\mathrm{Tr}\{\chi^3\} = \frac{1}{3\sqrt{6}}\alpha_{30}. \tag{3.64}$$

Thus the trio amplitude tells us about the eigenvalues of χ, since $\det\chi = \lambda_1\lambda_2\lambda_3$, where λ_m are the eigenvalues of χ. We also calculate the characteristic polynomial of χ to be

$$p(\lambda) = \lambda^3 - \frac{1}{2}\alpha_{00}\lambda - \frac{1}{3\sqrt{6}}\alpha_{30}, \tag{3.65}$$

which shows that the two singlet amplitudes (pair singlet and trio singlet) are explicitly related to the eigenvalues of χ through the cubic root formula. The characteristic equation has discriminant

$$\mathrm{discrim}(p(\lambda)) = \frac{1}{2}(\alpha_{00}^3 - \alpha_{30}^2), \tag{3.66}$$

which shows that when $\alpha_{00} = 0$, the discriminant is a perfect square and the eigenvalues are of equal magnitude and proportional to the cubic roots of unity, a signature of third order cyclic symmetry. Finally, we note that this representation can be exactly related to the theory of d-wave superconductivity, with a generalization that provides an alternate way of understanding generalized singlet parameters for higher spin [73].

[1] Derived from the characteristic polynomial, e.g. set $z = 0$ in Eq. (4) of Ref. [72].

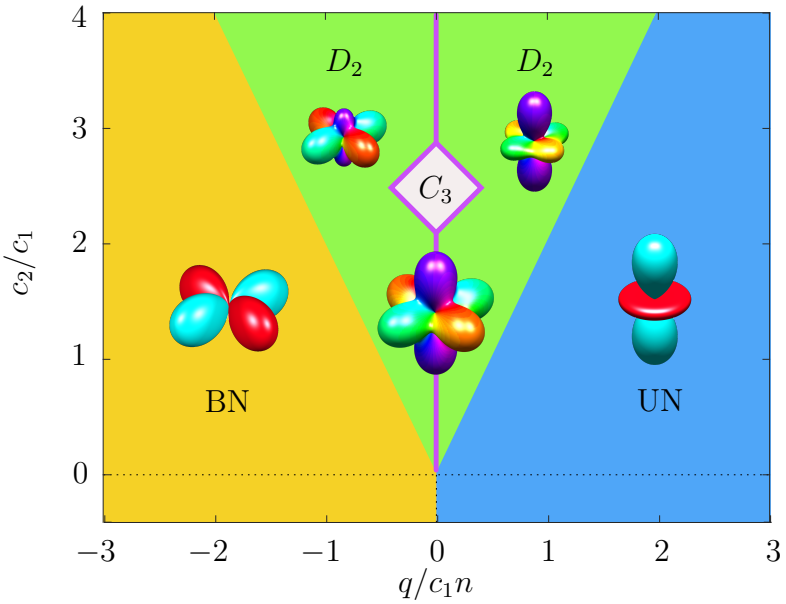

Figure 3.6: Spin-2 ground state phase diagram for $c_1 > 0$ and $F_z = 0$. For $c_2 n > 2|q|$, the D_2 phase in Eq. (3.72) continuously interpolates between the UN and BN phases in Eq. (3.39), becoming the cyclic phase C_3 at $q = 0$. We show the cyclic state $\psi_{\text{cyclic},1}$ given in Eq. (3.40).

3.2.4 Nematic ground states for q

Here we consider the uniform ground states for $F_z = 0$ and $p = 0$ by minimizing the integrand of the spin-2 energy given in Eq. (3.34) combined with the quadratic Zeeman term, i.e.

$$E = \frac{1}{2}\left(c_0 n^2 + c_1 F^2 + c_2 |\alpha_{00}|^2\right) + q\mathcal{N}_{zz}, \tag{3.67}$$

where for spin-2 we have

$$\mathcal{N}_{zz} = 4(n_{+2} + n_{-2}) + n_{+1} + n_{-1}, \tag{3.68}$$

$$= n + 3(n_{+2} + n_{-2}) - n_0. \tag{3.69}$$

In terms of multipolar order, we can use Eqs. (3.46) and (3.47) to rewrite the spin-singlet and substitute this into Eq. (3.67) to get

$$E = \frac{1}{2}\left(c_0 n^2 + \left(c_1 - \frac{1}{4}c_2\right) F^2 + \frac{1}{6}c_2 \sum_{ab} \mathcal{T}_{ab}^2\right) + q\mathcal{N}_{zz}, \tag{3.70}$$

$$= \frac{1}{2}\left((c_0 + c_2) n^2 + \left(c_1 - \frac{1}{5}c_2\right) F^2 - \frac{1}{18}c_2 \sum_{abc} \mathcal{T}_{abc}^2\right) + q\mathcal{N}_{zz}. \tag{3.71}$$

In these forms it is clear that $c_2 < 0$ favours $\mathcal{T}^{(2)}$ quadrupolar order, while $c_2 > 0$ favours $\mathcal{T}^{(3)}$ octupolar order; The $-\frac{1}{5}c_2F^2$ term in Eq. (3.71) is at most $-\frac{4}{5}c_2n^2$, while the maximal octupolar term is $-c_2n^2$ [for the ψ_{C_3} state, see Eq. (3.50)], so $c_2 > 0$ favours octupolar order as long as $c_1 > -\frac{1}{5}c_2$. Since we are considering $c_1 > 0$, we will assume that $F = 0$, which is a valid assumption as long as $c_2 < 4c_1$.

For $q \gg 0$ the ground state is UN, which minimizes $\mathcal{N}_{zz}$. For $q \ll 0$, the ground state is BN, which maximizes $\mathcal{N}_{zz}$.

For $q = 0$ and $c_2 < 0$, the mean-field ground state is an energetically degenerate superposition of UN and BN states, although quantum and thermal fluctuations break this degeneracy in an order-by-disorder process [74, 75].

When c_2 is positive and $q = 0$, the ground state is the pure cyclic state C_3. However, for small non-zero $|q|$ the ground state interpolates to UN as $2q \to c_2$, and to BN as $2q \to -c_2$. This is called the D_2 state, with representative spinor

$$\psi_{D_2} = \sqrt{n}\begin{pmatrix} \frac{i}{2}\sqrt{1-2\tilde{q}} \\ 0 \\ \sqrt{(1+2\tilde{q})/2} \\ 0 \\ \frac{i}{2}\sqrt{1-2\tilde{q}} \end{pmatrix}, \tag{3.72}$$

where $\tilde{q} = q/c_2n$, which has $\mathcal{N}_{zz} = 2(1-2\tilde{q})n$. The name D_2 refers to the symmetry of the state which is in between symmetries of the UN (D_∞) and BN (D_4) states [32].

Fig. 3.6 shows the phase diagram discussed in this section as a function of q/c_1n and c_2/c_1, illustrating the different states with their spherical harmonic representation.

3.3 Vortices

If we consider rotating a given spinor throughout space, in a closed loop so it returns to itself, we can generate topological defects in the field ψ by varying the global phase θ and performing spin rotations parametrized by the three Euler angles α,β,γ.

The requirement of single-valuedness of ψ at the origin of the loop leads to quantization of the global phase circulation, in multiples of 2π. However, different ground states (with different discrete spin symmetries) can split this circulation between the global

phase and a spin rotation throughout the loop, leading to the possibility of vortices with fractional circulation in the superfluid and spin currents [76, 77].

Here we focus on nematic states in spin-1 and spin-2. This includes the polar state for spin-1, and the UN, C_3, and BN states for spin-2. Considering $SO(2)$ rotations of these states about a particular axis leads to 1/2, 1/3, and 1/4 fractional spin-superfluid coupled vortices.

3.3.1 Spin-1 half-quantum vortices

The spin-1 polar state breaks $SO(2)$ symmetry along one nematic axis, the nematic director, and supports a topological defect where the nematic director rotates around by π. Due to the nematic lobes being polarized (with a π relative phase difference), a π spin rotation must be coupled with π circulation in the global phase θ to maintain single-valued-ness of the spinor.

These topological defects are known as half-quantum vortices (HQVs), Alice vortices, and Alice strings [78]. We also call them $1/2-1/2$ vortices based on their having a 1/2 unit of circulation in the global phase and 1/2 of a 2π spin rotation.

To illustrate the properties of HQVs we consider a single HQV located at the origin, formed by rotating the EA polar state of 3.33. An example of this defect in the spherical harmonic representation is shown in Fig. 3.8, and in the Cartesian representation in Fig. 3.7. Away from the core, the wave function is approximately of the form

$$\psi_{\text{vort}} = \sqrt{\frac{n_c}{2}} e^{iq_\theta \varphi} \begin{pmatrix} -e^{-iq_\phi \varphi} \\ 0 \\ e^{iq_\phi \varphi} \end{pmatrix} \sim \begin{pmatrix} -e^{-i\sigma_1 \varphi} \\ 0 \\ e^{i\sigma_{-1} \varphi} \end{pmatrix}, \tag{3.73}$$

where we have set $\theta \to q_\theta \varphi$ and $\phi \to q_\phi \varphi$ in Eq. (3.33), φ is the azimuthal angle about the core, and $\{q_\theta, q_\phi\}$ are the winding numbers. In Eq. (3.73) we have also introduced the component windings

$$\sigma_{\pm 1} \equiv q_\theta \mp q_\phi, \tag{3.74}$$

where σ_m denotes the net phase winding in the m-th component of the field. The σ_m must be integer for the field to be single valued. The cases $\sigma_1 = \pm 1$ (with $\sigma_{-1} = 0$) and $\sigma_{-1} = \pm 1$ (with $\sigma_1 = 0$) define the four HQVs, corresponding to $q_\theta = \pm\frac{1}{2}$, $q_\phi = \pm\frac{1}{2}$, i.e. vortices with half-quantized values of the windings in θ and ϕ (see Fig. 3.7).

Much of our theoretical understanding of HQV dynamics has come from studies of miscible two-component condensates [79–81], which also support HQVs (also see [82]). Notably, Eto *et al.* [80] have shown that the interaction potential between two HQVs separated by a distance R (for $R \gg \xi_s$) is of the form

$$U_{\rm int} \propto \kappa \ln R, \tag{3.75}$$

where

$$\kappa = q_\theta^{(1)} q_\theta^{(2)} + q_\phi^{(1)} q_\phi^{(2)} = \frac{1}{2} \sum_{m=\pm 1} \delta_{\sigma_m^{(1)}, \sigma_m^{(2)}}, \tag{3.76}$$

with $(q_\theta^{(1)}, q_\phi^{(1)})$ and $(q_\theta^{(2)}, q_\phi^{(2)})$, [or $(\sigma_1^{(1)}, \sigma_{-1}^{(1)})$ and $(\sigma_1^{(2)}, \sigma_{-1}^{(2)})$] being the sets of winding numbers specifying HQV 1 and 2, respectively. For the case where both HQVs have winding in the same component (i.e. both having $|\sigma_1| = 1$ or $|\sigma_{-1}| = 1$) then $|\kappa| = \frac{1}{2}$ and the interaction is of the same form as that for $U(1)$ vortices in a scalar condensate. When the vortices occur in different components $\kappa = 0$ and there is no long ranged interaction. However, a short ranged repulsive interaction is predicted, extending over a length scale comparable to the vortex core size [80, 82, 83]. Two HQVs with opposite circulation in the same component (e.g. a HQV with $\sigma_1 = 1$ and a HQV with $\sigma_1 = -1$) can collide and annihilate, as has been recently observed in experiments [63].

3.3.2 Spin-2 nematic vortices

The UN state is similar to the spin-1 polar state in that it has one axis of nematic alignment, and supports a topological defect with the nematic director rotating by π. However, as the nematic lobes are symmetric in their phase under inversion of the nematic director, this defect has no superfluid circulation. An example is shown in Fig. 3.9.

The BN state breaks $SO(2)$ symmetry with nematic order along two perpendicular axes. The two axes have a relative phase difference of π, and thus support $1/4 - 1/2$ fractional spin-superfluid vortices. These have $1/4 \times 2\pi$ circulation in the spin phase ϕ coupled with a $1/2 \times 2\pi$ circulation in θ. We show an example of this defect in Fig. 3.10.

The general C_3 state has three perpendicular axes of nematic order, with phases of the nematic lobes along each axis being cubic roots of unity. There are C_3 axes of third order cyclic symmetry along the diagonals between nematic axes. There is also a non-zero fourth order multipole moment [see Eq. (3.51)], however the relative phases of

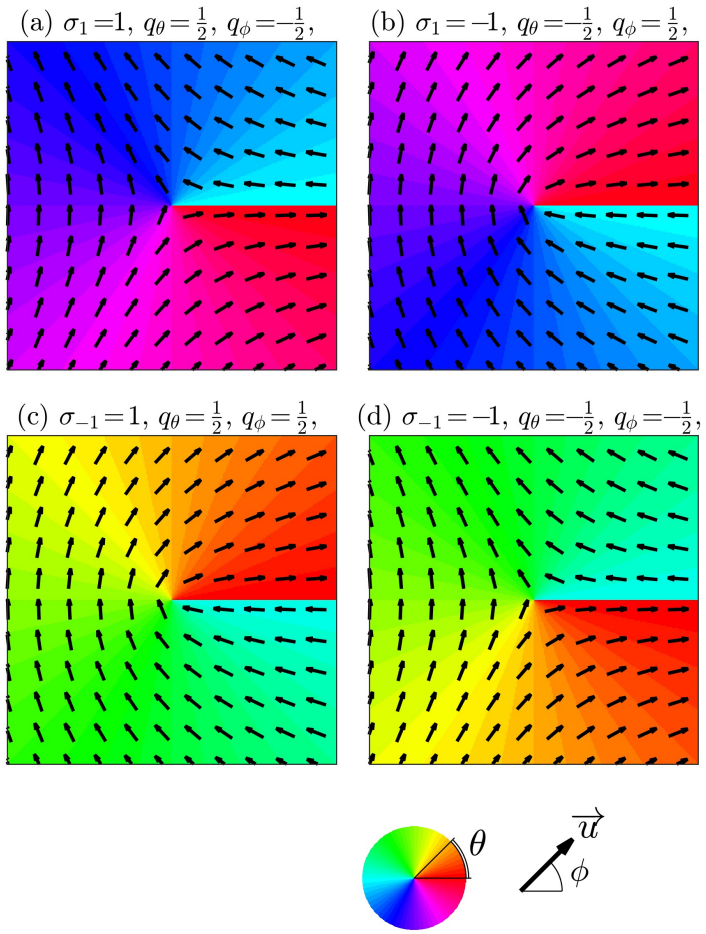

Figure 3.7: Four types of HQVs that can occur in the easy-plane polar phase [Eq. (3.33)] are illustrated using their nematic director and global phase in subplots (a)-(d) labelled by their winding numbers.

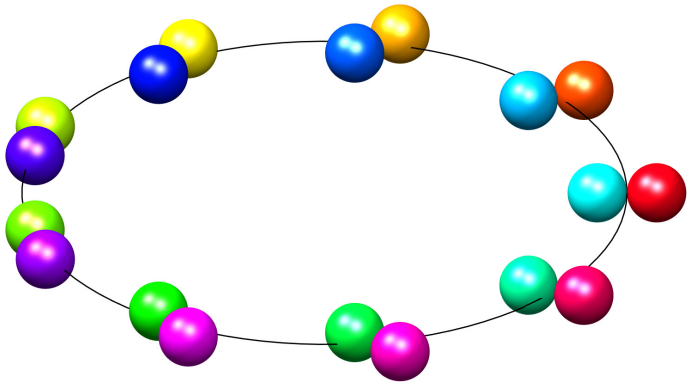

Figure 3.8: Spherical harmonic representation of a spin-1 easy-plane polar half-quantum vortex configuration.

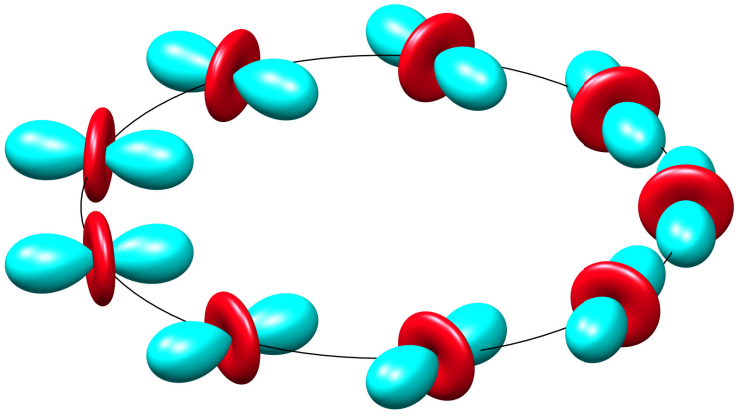

Figure 3.9: Spin-2 UN vortex configuration.

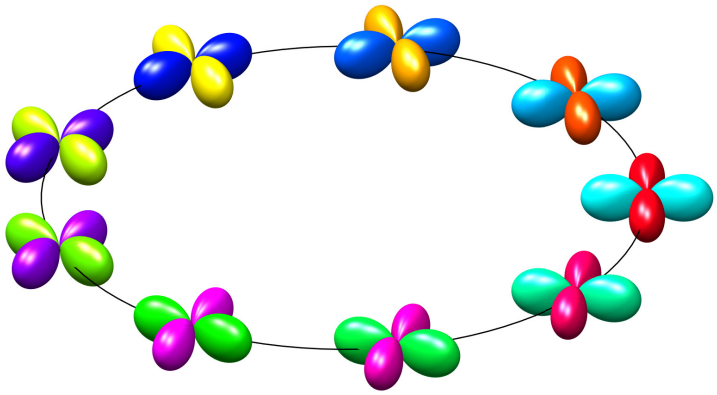

Figure 3.10: Spin-2 BN vortex configuration.

the nematic lobes are incompatible with $1/4 - 1/2$ vortices like the ones supported in the BN state.

In the remaining section we will focus on the fractional vortices that can appear in the C_3 state.

3.3.3 Spin-2 cyclic fractional vortices

The C_3 states $\psi_{\text{cyclic},2}$ and $\psi_{\text{cyclic},3}$ have C_3 axes aligned along z, and support 1/3 fractional coupled spin-superfluid vortices circulating about the z axis. These appear as vortices of unit circulation in a single (spherical) ψ_m component. Far from the vortex core, the general spinors are

$$e^{i\theta}e^{i\phi f_z}\psi^{\text{cyc}(2)} = \sqrt{\frac{n}{3}}\begin{pmatrix} 0 \\ \sqrt{2}e^{i(\theta-\phi)} \\ 0 \\ 0 \\ e^{i(\theta+2\phi)} \end{pmatrix}, \quad e^{i\theta}e^{i\phi f_z}\psi^{\text{cyc}(3)} = \sqrt{\frac{n}{3}}\begin{pmatrix} e^{i(\theta-2\phi)} \\ 0 \\ 0 \\ \sqrt{2}e^{i(\theta+\phi)} \\ 0 \end{pmatrix}. \tag{3.77}$$

Let the windings be $\Delta\theta = 2\pi\sigma_n$, $\Delta\phi = 2\pi\sigma_s$. We impose single-valued-ness on the windings in each component, i.e. $\Delta\theta_m = 2\pi\sigma_m$ with σ_m an integer. We then have

$$\sigma_n = \frac{1}{3}(2\sigma_{\pm 1} + \sigma_{\mp 2}), \tag{3.78}$$

$$\sigma_s = \mp\frac{1}{3}(\sigma_{\pm 1} + \sigma_{\pm 2}). \tag{3.79}$$

The lowest energy vortices have circulation in a single m level. We summarize the eight types of these spin vortices in Table 3.1, where each row is for one unit of circulation in ψ_m and zero in the other components.

	$\sigma_m = +1$	$\sigma_m = -1$
$m = \pm 2$	$\left(+\frac{1}{3}, \mp\frac{1}{3}\right)$	$\left(-\frac{1}{3}, \pm\frac{1}{3}\right)$
$m = \pm 1$	$\left(+\frac{2}{3}, \mp\frac{1}{3}\right)$	$\left(-\frac{2}{3}, \pm\frac{1}{3}\right)$

Table 3.1: Fractional winding of (σ_n, σ_s) related to ± 1 total winding in each m component, for 1/3 spin vortices in the cyclic order parameter with C_3 axis along z, i.e. $\psi^{\mathrm{cyc}(2)}$ and $\psi^{\mathrm{cyc}(3)}$.

This shows that vortices in ψ_m with winding $\sigma_m = \pm 1$ correspond to spin vortices with spin winding $\sigma_s = \mp 1/3$, and global phase winding $\sigma_n \in \pm\{1/3, 2/3\}$.

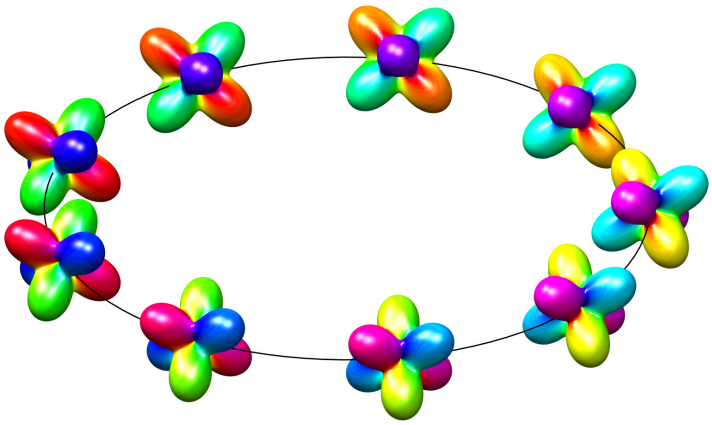

Figure 3.11: Spin-2 C_3 cyclic vortex configuration of $\psi_{\text{cyclic},2}$, with a $\sigma_s = 1/3$ spin rotation and $\sigma_n = -1/3$ global phase rotation, giving $\sigma_{+2} = -1$ circulation in ψ_{+2}.

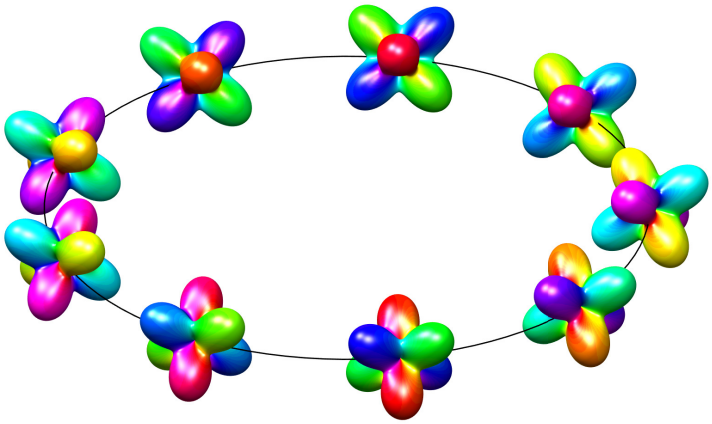

Figure 3.12: Spin-2 C_3 cyclic vortex configuration of $\psi_{\text{cyclic},2}$, with a $\sigma_s = 1/3$ spin rotation and $\sigma_n = 2/3$ global phase rotation, giving $\sigma_{-1} = +1$ circulation in ψ_{-1}.

Part II

Exact dynamics & numerical algorithms

Chapter 4

Spinor dynamics

4.1 Introduction

In this chapter we consider the Hamiltonian dynamics of spinor systems. We split the evolution equation into two subsystems: a single-particle-like subsystem and a nonlinear interaction subsystem. We solve the first subsystem exactly in Fourier space. For the nonlinear interactions, we solve the dynamics exactly for spin-1 and spin-2, and generalize their solution to any spin-f with particular interactions. Finally, we give details of how we numerically implement each subsystem solution in an efficient manner, including using GPU parallelization techniques.

4.2 Hamiltonian spinor dynamics

A Hamiltonian system is described by a collection of position coordinates q_i and corresponding momentum coordinates p_i. These are known as the canonical coordinates, with the set of all possible (q_i, p_i) giving the phase space of the system.

Real-time Hamiltonian evolution of a mechanical system is a special geometrical transformation of the initial conditions $(q_i, p_i)_{t=0}$ through phase space. The mathematical structure of phase space is that of a symplectic manifold: a surface with an associated structure that is preserved under the flow of time. This structure is the symplectic

two-form

$$\omega = \sum_i dp_i \wedge dq_i, \tag{4.1}$$

where $\wedge$ is the wedge product [84]. The symplectic two-form ω can be thought of as a sum of oriented areas for each pair of position and momentum coordinates [85, 86].

Having ω as a conserved quantity is a strict condition on the flow of a solution through phase space, which includes Liouville's theorem of the conservation of total phase space area. This is in contrast to dissipative systems, where phase space area can contract or expand over time through loss mechanisms or by coupling to external baths. Beyond Liouville's theorem, conservation of ω affects the global structures of the system, which include more than just the total conserved energy. In particular, there can be more global invariants. These invariants carve out invariant torii in phase space that the system is restricted to by initial conditions. Time evolution is then the canonical transformation of the initial conditions through phase space; a transformation that stays on these torii while preserving symplecticity (i.e. ω).

Spinor systems consisting of local spin interactions, and no more than a weak magnetic field along z, have three globally conserved quantities: total atom number N, total z-magnetization M_z, and total energy E. These are related by Noether's theorem to the following global symmetries: $U(1)$ phase symmetry, $\psi \to e^{i\theta}\psi$; $SO(2)$ z-rotation symmetry, $\psi \to e^{-i\phi \mathrm{f}_z}\psi$; and time-translation symmetry, $\dot{\psi}(t) = \dot{\psi}(t + \delta t)$. These symmetries mean that the wavefunction ψ is restricted to follow paths through phase space with constant N,M_z, and E, given by an initial condition at a reference time which we can take to be $t = 0$.

The time evolution of a Hamiltonian system is generated by the total energy. Coming from a second quantization picture, the total mean-field energy is a functional of the wavefunction ψ, which for a spinor BEC is given by

$$E[\psi, \psi^*] = E_{s.p.} + E_{int}, \tag{4.2}$$

where $E_{s.p.}$ encodes the single-particle-like terms (see Section 1.3.1 of Chapter 1) and E_{int} contains nonlinear interaction terms. $E_{s.p.}$ is given by

$$E_{s.p.} = \int d\mathbf{r} \, \left\{ -\frac{1}{2}\psi^\dagger \nabla^2 \psi - pF_z + q\mathcal{N}_{zz} + nV_{trap} \right\}, \tag{4.3}$$

where V_{trap} is a local trapping potential, $n = \psi^\dagger\psi$ is the density, p is the linear Zeeman effect, and q is the quadratic Zeeman effect. Here we adopt dimensionless units of length

x_0 and energy $E_0 = \frac{\hbar^2}{Mx_0^2}$, where M is the particle mass. Note that $F_z = \psi^\dagger \mathrm{f}_z \psi$ and $\mathcal{N}_{zz} = \psi^\dagger \mathrm{f}_z^2 \psi$. The wavefunction ψ and trap V_{trap} depend on position $\mathbf{r}$; we usually keep this dependence implicit for brevity.

The dynamics of the system are then given by the variational principle

$$i\dot{\psi} = \frac{\delta E}{\delta \psi^*}, \tag{4.4}$$

where $\frac{\delta}{\delta \psi^*}$ is the functional derivative with respect to ψ^*, which in our case gives the derivative of the integrand of the functional $E[\psi, \psi^*]$. This variational principle arises by considering ψ and ψ^* as independent generalized coordinates (the q_i of the system). For more details on ψ and ψ^* as canonical coordinates, see Refs. [87–90].

Applying the variational principle of Eq. (4.4) to Eq. (4.2) results in the Gross-Pitaevskii equation for the evolution of the order parameter,

$$i\dot{\psi} = -\frac{1}{2}\nabla^2\psi - p\mathrm{f}_z\psi + q\mathrm{f}_z^2\psi + V_{trap}\psi + \frac{\delta E_{int}}{\delta \psi^*}\psi. \tag{4.5}$$

This is a multicomponent nonlinear Schrödinger equation. The nonlinear interactions are rotationally invariant; they preserve the total spin expectation $F = \sqrt{F_z^2 + |F_\perp|^2}$. The linear Zeeman term is a local z rotation, which rotates the in-plane magnetization $F_\perp$; it preserves the total spin and thus commutes with the nonlinear interactions. The quadratic Zeeman term, however, is a nematic rotation which can transform in-plane magnetization into nematic order. Since it does not preserve the total spin, it does not commute with the nonlinear interactions.

Considering solvable subsystems of the total evolution, let us group the nonlocal and non-spin-conserving terms together as the subsystem

$$\dot{\psi} = \hat{H}_A\psi \equiv -i\left(-\frac{1}{2}\nabla^2\psi + q\mathrm{f}_z^2\psi\right), \tag{4.6}$$

with the remaining terms forming a local subsystem which conserves total spin,

$$\dot{\psi} = \hat{H}_B\psi \equiv -i\left(-p\mathrm{f}_z + V_{trap} + \frac{\delta E_{int}}{\delta \psi^*}\right)\psi. \tag{4.7}$$

The latter subsystem consists of three parts which all commute. The first two are relatively trivial, causing the time evolution

$$\psi(t) = \exp(-itp\mathrm{f}_z)\exp(-itV_{trap})\psi(0). \tag{4.8}$$

In the following sections, we first examine the time evolution caused by the $\hat{H}_A$ subsystem in Eq. (4.7), and then focus on the nonlinear interactions of the $\hat{H}_B$ subsystem, set by E_{int} in Eq. (4.7).

4.3 Kinetic energy and quadratic Zeeman

Here we consider the subsystem consisting of the spatially coupled kinetic energy interaction combined with the non-spin-conserving quadratic Zeeman interaction, defined in Eq. (4.6). The kinetic energy term couples ψ in position space, however it is local in Fourier space. For a constant (in space) quadratic Zeeman, the q term remains constant in Fourier space. We define the momentum space wavefunction to be

$$\phi(\mathbf{k}, t) \equiv \mathcal{F}\{\psi(\mathbf{r}, t)\}, \tag{4.9}$$

where $\mathbf{k}$ is a momentum vector with length k. Taking the Fourier transform of Eq. (4.6), the subsystem becomes decoupled and fully local,

$$\dot{\phi} = \hat{H}_A \phi = -i \left(\frac{1}{2} k^2 I + q f_z^2 \right) \phi. \tag{4.10}$$

This is a linear equation in ϕ, thus we can directly exponentiate to get the exact solution in momentum space

$$\phi(t) = \exp\left(\hat{H}_A t\right) \phi(0) = \exp\left(-i \left(\frac{1}{2} k^2 I + q f_z^2 \right) t \right) \phi(0), \tag{4.11}$$

and inverse Fourier transform to get the position space solution

$$\psi(t) = \mathcal{F}^{-1}\{\exp\left(-i \left(\frac{1}{2} k^2 I + q f_z^2 \right) t \right) \phi(0)\}. \tag{4.12}$$

4.4 Density interaction

The zeroth order nonlinear interaction in a spinor BEC is the same as for a scalar BEC [see Eq. (2.4) of Chapter 2],

$$E_{int} = \frac{c_0}{2} \int d\mathbf{r}\ n^2, \tag{4.13}$$

where $n = \psi^\dagger \psi$ is the density. Taking the functional derivative, the density interaction causes time evolution [c.f. Eq. (1.5) in Chapter 1] given by

$$i\dot{\psi} = c_0 n \psi. \tag{4.14}$$

This conserves n, as

$$\dot{n} = \psi^\dagger \dot{\psi} + \dot{\psi}^\dagger \psi = -i c_0 (\psi^\dagger n \psi - n \psi^\dagger \psi) = 0. \tag{4.15}$$

Since n is constant in time, the solution is found by scalar exponentiation, giving

$$\psi(t) = \exp(-i c_0 n t) \psi(0). \tag{4.16}$$

4.5 Spin-1

For spin-1 we have only one new interaction term in the energy functional, and it is usually written in terms of the magnetization of the system. Recalling Eq. (2.46), we have

$$E_{int} = \frac{1}{2}\int d\mathbf{r}\left\{c_0 n^2 + c_1 F^2\right\}. \tag{4.17}$$

Writing out the subsystem generated by this term according to the variational principle explicitly, we get a mixture of density-like terms dependent on the component magnitudes and four-wave-mixing type terms with phase dependence:

$$i\dot{\psi}_+ = c_1(n_0 + n_+ - n_-)\psi_+ + c_1\psi_0^2\psi_-^*, \tag{4.18}$$

$$i\dot{\psi}_0 = c_1(n_+ + n_-)\psi_0 + 2c_1\psi_+\psi_-\psi_0^*, \tag{4.19}$$

$$i\dot{\psi}_- = c_1(n_0 - n_+ + n_-)\psi_- + c_1\psi_0^2\psi_+^*. \tag{4.20}$$

At first glance this does not seem very intuitive to solve since the four-wave-mixing terms couple ψ_m and ψ_m^* in a way that is difficult to analyze.

Indeed, previous authors have approached this interaction term by splitting off the density-like terms to be solved exactly, and solving the remaining phase-dependent terms approximately [91].

Some deeper insight is gained by thinking about the types of order in the system. This system is special in that ferromagnetic order (F) and antiferromagnetic order (α) are constrained such that

$$F^2 + |\alpha|^2 = n^2, \tag{4.21}$$

where we now use a rescaled version of α_{00} [see Eq. (2.15)],

$$\alpha = \psi_0^2 - 2\psi_+\psi_-. \tag{4.22}$$

This shows that the local ferromagnetic order and antiferromagnetic order, relative to the local density, must add up to 1. In the GPE, the spinor interaction is more complicated than the scalar term because it comes from the vector-based ferromagnetic order. However, this equality shows that we can also describe the system in terms of antiferromagnetic spin-singlet interactions. These interactions are described by the complex scalar α. Since a complex scalar has one less degree of freedom than a real vector, the phase mixing terms of the GPE should look simpler when written this way.

4.5.1 Spin-singlet picture

Let us use the inequality to rewrite $F^2 = n^2 - |\alpha|^2$, so the energy functional now looks like

$$E_{int} = \frac{1}{2}\int d\mathbf{r}\left\{c_0 n^2 + c_1(n^2 - |\alpha|^2)\right\}. \tag{4.23}$$

This gives us a view of the system in terms of the amount of spin-singlet antiferromagnetic order. We will call this view the spin-singlet picture, as opposed to the view in terms of ferromagnetic order given by (4.17), which we will call the magnetization picture.

The GPE subsystem in the spin-singlet picture is then

$$i\dot{\psi}_+ = c_1(n\psi_+ + \alpha\psi_-^*), \tag{4.24}$$
$$i\dot{\psi}_0 = c_1(n\psi_0 - \alpha\psi_0^*), \tag{4.25}$$
$$i\dot{\psi}_- = c_1(n\psi_- + \alpha\psi_+^*). \tag{4.26}$$

This form of the nonlinear interaction has only two nonlinear terms, with n coupling to ψ and α coupling to ψ^*. To progress further with these equations we have to try to uncouple ψ and ψ^*. The conjugate equations will be useful, i.e.

$$-i\dot{\psi}_+^* = c_1(n\psi_+^* + \alpha^*\psi_-), \tag{4.27}$$
$$-i\dot{\psi}_0^* = c_1(n\psi_0^* - \alpha^*\psi_0), \tag{4.28}$$
$$-i\dot{\psi}_-^* = c_1(n\psi_-^* + \alpha^*\psi_+). \tag{4.29}$$

Let us now check the time evolution of the two nonlinear terms. Of course n commutes with the terms arising from n^2 in the energy functional, so we only have to consider the α evolution terms:

$$\dot{n} = \psi^\dagger\dot{\psi} + \dot{\psi}^\dagger\psi, \tag{4.30}$$
$$= -ic_1(-\alpha[(\psi_0^*)^2 - 2\psi_+^*\psi_-^*]) + ic_1(-\alpha^*[\psi_0^2 - 2\psi_+\psi_-]) = 0. \tag{4.31}$$

For α, we have

$$\dot{\alpha} = 2(\dot{\psi}_0\psi_0 - \dot{\psi}_+\psi_- - \dot{\psi}_-\psi_+), \tag{4.32}$$
$$= -2ic_1(n\psi_0^2 - \alpha n_0 - n\psi_+\psi_- - \alpha n_- - n\psi_+\psi_- - \alpha n_+), \tag{4.33}$$
$$= -2ic_1(n[\psi_0^2 - 2\psi_+\psi_-] - \alpha[n_+ + n_0 + n_-]) = 0. \tag{4.34}$$

So we find that $n^2 - |\alpha|^2$ conserves n, α, and thus α^*, exactly.

If we now take the time derivative of the spin-singlet-picture GPE [Eqs. (4.24)–(4.26)], we get

$$\ddot{\psi}_+ = -ic_1(n\dot{\psi}_+ + \alpha\dot{\psi}_-^*) = -c_1^2(n^2 - |\alpha|^2)\psi_+, \tag{4.35}$$

$$\ddot{\psi}_0 = -ic_1(n\dot{\psi}_0 - \alpha\dot{\psi}_0^*) = -c_1^2(n^2 - |\alpha|^2)\psi_0, \tag{4.36}$$

$$\ddot{\psi}_- = -ic_1(n\dot{\psi}_- + \alpha\dot{\psi}_+^*) = -c_1^2(n^2 - |\alpha|^2)\psi_-, \tag{4.37}$$

which, using the equality for spin-1 in Eq. (4.21), we can write as simply

$$\ddot{\psi} = -c_1^2 F^2 \psi. \tag{4.38}$$

This equation describes simple harmonic motion of ψ with angular frequency $\omega = |c_1|F$ and complex velocity $v = \dot{\psi}$. The solution is thus

$$\psi(t) = \cos(\omega t)\psi(0) + \frac{\dot{\psi}(0)}{\omega}\sin(\omega t), \tag{4.39}$$

which is given explicitly in component form as

$$\psi_+(t) = \cos(c_1 F t)\psi_+(0) - \frac{i}{F}\sin(c_1 F t)[n\psi_+(0) + \alpha\psi_-^*(0)], \tag{4.40}$$

$$\psi_0(t) = \cos(c_1 F t)\psi_0(0) - \frac{i}{F}\sin(c_1 F t)[n\psi_0(0) - \alpha\psi_0^*(0)], \tag{4.41}$$

$$\psi_-(t) = \cos(c_1 F t)\psi_-(0) - \frac{i}{F}\sin(c_1 F t)[n\psi_-(0) + \alpha\psi_+^*(0)], \tag{4.42}$$

where F, n, and α are nonlinear constants equal to their initial values.

4.5.2 Magnetization picture

Let us now link the solution of the GPE in the spin-singlet picture to the magnetization picture of the system. By taking the functional derivative of the spin-1 equality [Eq. (4.21)], we get

$$R\psi = \begin{pmatrix} n\psi_+ + \alpha\psi_-^* \\ n\psi_0 - \alpha\psi_0^* \\ n\psi_- + \alpha\psi_+^* \end{pmatrix} = n\psi - \alpha A_{00}\psi^*, \tag{4.43}$$

where

$$R \equiv \sum_{\nu\in\{x,y,z\}} F_\nu \mathrm{f}_\nu = \begin{pmatrix} F_z & \sqrt{2}F_\perp^* & 0 \\ \sqrt{2}F_\perp & 0 & \sqrt{2}F_\perp^* \\ 0 & \sqrt{2}F_\perp & -F_z \end{pmatrix}, \tag{4.44}$$

and we define a normalized version of A_{00} compared with the definition in Eq. (2.15) (removing a factor of $-1/(2f+1) = -1/3$) as

$$A_{00} = \begin{pmatrix} 0 & 0 & -1 \\ 0 & 1 & 0 \\ -1 & 0 & 0 \end{pmatrix}. \tag{4.45}$$

Substituting Eq. (4.43) into Eqs. (4.40)–(4.42), we find the solution in the magnetization picture to be

$$\psi(t) = \cos(c_1 F t)\psi(0) - \frac{i}{F}\sin(c_1 F t) R\psi(0), \tag{4.46}$$

which is given explicitly in component form as

$$\psi_+(t) = \cos(c_1 F t)\psi_+(0) - \frac{i}{F}\sin(c_1 F t)[F_z\psi_+(0) + \sqrt{2}F_\perp^*\psi_0(0)], \tag{4.47}$$

$$\psi_0(t) = \cos(c_1 F t)\psi_0(0) - \frac{i}{F}\sin(c_1 F t)[\sqrt{2}F_\perp\psi_+(0) + \sqrt{2}F_\perp^*\psi_-(0)], \tag{4.48}$$

$$\psi_-(t) = \cos(c_1 F t)\psi_-(0) - \frac{i}{F}\sin(c_1 F t)[-F_z\psi_-(0) + \sqrt{2}F_\perp\psi_0(0)], \tag{4.49}$$

where F_z, $F_\perp$, and $F = \sqrt{F_z^2 + |F_\perp|^2}$ are nonlinear constants equal to their initial values.

We have now shown that the interaction dynamics of the GPE in the magnetization picture have an exact solution. However, we would like to know how to solve the magnetization-picture GPE from first principles, as this will give us the steps we need to solve the dynamics induced by the magnetization interaction in higher spin systems.

Therefore, let us now derive Eq. (4.46) starting from the magnetization GPE [Eqs. (4.18)–(4.20)]. In the same spirit as for the spin-singlet picture, we rewrite the GPE in terms of F_x, F_y, and F_z. The system collapses down to a single matrix equation,

$$i\dot{\psi} = c_1 R\psi. \tag{4.50}$$

We now consider the time evolution of R by looking at the time evolution of F_x, F_y and F_z. Using

$$\dot{F}_\nu = \psi^\dagger f_\nu \dot{\psi} + \dot{\psi}^\dagger f_\nu \psi = -ic_1\psi^\dagger[f_\nu, R]\psi, \tag{4.51}$$

we find that

$$\dot{F}_x = -ic_1\psi^\dagger(F_z[f_x, f_z] + F_y[f_x, f_y])\psi, \tag{4.52}$$

$$= -ic_1\psi^\dagger(-iF_z f_y + iF_y f_z)\psi, \tag{4.53}$$

$$= -ic_1(-iF_z F_y + iF_y F_z) = 0. \tag{4.54}$$

Similarly,

$$\dot{F}_y = -ic_1(iF_zF_x - iF_xF_z) = 0, \tag{4.55}$$

$$\dot{F}_z = -ic_1(iF_xF_y - iF_yF_x) = 0. \tag{4.56}$$

Thus we find that R is a constant of motion, i.e. $\dot{R} = 0$. The solution to such a linear system is found by taking the matrix exponential, i.e.

$$\psi(t) = \exp(-ic_1tR)\psi(0). \tag{4.57}$$

Calculating matrix exponentials in general is difficult, but in our case we have some special properties of the matrix R. Notably, it has eigenvalues $\{F, 0, -F\}$. In particular, this means that R^2 has only one non-zero eigenvalue, i.e. F^2, so R^3 will have the same eigenvalues as R scaled by F^2.

To make this quantitative, we can use the Cayley-Hamilton theorem to analyze higher powers of R. This theorem states that every matrix satisfies its own characteristic equation. The characteristic equation for R is

$$p(\lambda) = \det(R - \lambda I_3) = \lambda(\lambda^2 - F^2) = 0. \tag{4.58}$$

Substituting in $\lambda = R$ gives us $R^3 = F^2R$.

Using this result, we can expand the matrix exponential as a Taylor series and group all terms R^m with $m \geq 3$ with the R and R^2 terms. We get

$$\psi(t) = \exp(-ic_1tR)\psi(0), \tag{4.59}$$

$$= \left(I - \frac{i}{F}\sin(c_1Ft)R - \frac{1}{F^2}[1 - \cos(c_1Ft)]R^2\right)\psi(0). \tag{4.60}$$

We recognize this as the vector Rodrigues' rotation formula for a rotation $\exp(\theta K)$, where $\theta = c_1Ft$ is the rotation angle and $K = -iR/F$ is the generator of an $SO(3)$ rotation about the axis of magnetization. This shows that the magnetization interaction can be interpreted as a spin rotation of ψ about the magnetization vector.

We shall now simplify our result further, to match the one derived in the spin-singlet picture. Consider the action of R^2. We calculate it to be

$$R^2\psi = F^2\psi. \tag{4.61}$$

This is a non-trivial result: we know that $R^2 \neq I_3$ by inspection, i.e. it is not equal to the identity matrix, so R must have some special structure. Indeed, we can understand this

by examining the eigenvectors and eigenvalues. We know the eigenvalues are $\{F, 0, -F\}$. So we would expect that $F^2\psi$ would only be valid when $v_0^\dagger\psi = 0$, where v_0 is the eigenvector of R with eigenvalue zero;

$$v_0 = \frac{1}{F}\begin{pmatrix} -\frac{1}{\sqrt{2}}F_- \\ F_z \\ \frac{1}{\sqrt{2}}F_+ \end{pmatrix}. \tag{4.62}$$

If we project ψ onto this eigenvector, we find that

$$\begin{aligned} v_0^\dagger\psi &= F_z\psi_0 - \tfrac{1}{\sqrt{2}}[F_+\psi_+ - F_-\psi_-], && (4.63)\\ &= F_z\psi_0 - [(\psi_+^*\psi_0 + \psi_0^*\psi_-)\psi_+ - (\psi_+\psi_0^* + \psi_0\psi_-^*)\psi_-], && (4.64)\\ &= F_z\psi_0 - [|\psi_+|^2\psi_0 + \psi_0^*\psi_-\psi_+ - \psi_+\psi_-\psi_0^* - \psi_0|\psi_-|^2], && (4.65)\\ &= F_z\psi_0 - [|\psi_+|^2 - |\psi_-|^2]\psi_0 = 0. && (4.66) \end{aligned}$$

Thus v_0 is orthogonal to ψ, and ψ can be written as a linear combination of the eigenvectors with eigenvalue $\pm F$. Thus follows the result of Eq. (4.61). Using this, we can simplify Eq. (4.60) to

$$\exp(-ic_1tR)\psi = \cos(c_1Ft)\psi - \frac{i}{F}\sin(c_1Ft)R\psi. \tag{4.67}$$

This now matches the solution in Eq. (4.46) we derived from the spin-singlet-picture GPE [Eqs. (4.24)–(4.26)], so we have achieved our goal of deriving the same solution from the magnetization-picture GPE [Eqs. (4.18)–(4.20); in matrix form Eq. (4.50)]. This extra work was worth the effort because it has given us the tools we need to analyze the magnetization-interaction subsystem for higher spin-f systems.

4.5.3 Full solution for spin-1 nonlinear interactions

The exact solution of the dynamics induced by the magnetization interaction conserves n and commutes with the density interaction term, the linear Zeeman term, and the trapping potential. Thus the full solution to the $\hat{H}_B$ subsystem of Eq. (4.7) is given by

$$\psi(t) = \exp(-itp\mathrm{f}_z)\exp(-it(V_{trap} + c_0n)\left(\cos(c_1Ft)\psi(0) - \frac{i}{F}\sin(c_1Ft)R\psi(0)\right), \tag{4.68}$$

which can be written in the spin-singlet picture using Eq. (4.43) as

$$\psi(t) = \exp(-itp\mathrm{f}_z)\exp(-it(V_{trap} + c_0n)\left(\cos(c_1Ft)\psi(0) - \frac{i}{F}\sin(c_1Ft)\left[n\psi(0) - \alpha A_{00}\psi^*(0)\right]\right), \tag{4.69}$$

with n, F, $R = \sum_\nu F_\nu \mathrm{f}_\nu$, and α being equal to their initial values at $t = 0$.

It is important to note that this exact solution is only physically relevant in the case of the quadratic Zeeman term (i.e. q) being identically zero. Given the experimental difficulty with exactly canceling out all stray magnetic fields, this solution should be considered an approximation to the physical spinor evolution.

When q is non-zero, the magnetization vector and the spin-singlet amplitude are no longer separately conserved quantities; indeed, q breaks $SO(3)$ symmetry, and drives evolution that transforms one type of order into the other. For the spin-1 system, there is an exact solution that includes the quadratic Zeeman term [92, 93], which involves Jacobi elliptic functions and their inverses.

The approach we have taken here, of neglecting the quadratic Zeeman term, means that the subsystem dynamics retain the full symmetry of the interaction term. The constraints of this symmetry result in conserved nonlinear quantities which can help solve the dynamics. Our approach straightforwardly generalizes to analyzing interactions in higher-spin systems containing the same symmetry as solvable lower-spin systems. In the next section, we go through this procedure in detail for the spin-2 system.

4.6 Spin-2

In the spin-2 system, we gain an extra independent interaction term. The simplest extra term we can introduce is the spin-singlet interaction. Recalling Eq. (2.56), this leads to the energy functional

$$E_{int} = \frac{1}{2}\int d\mathbf{r}\{c_0 n^2 + c_1 F^2 + \tilde{c}_2 |\alpha|^2\}, \tag{4.70}$$

where we have absorbed a factor of $1/(2f+1) = 1/5$ from α_{00} [Eq. (2.15)] into c_2 by defining

$$\tilde{c}_2 = c_2/5, \tag{4.71}$$

$$\alpha = \psi_0^2 - 2\psi_{+1}\psi_{-1} + 2\psi_{+2}\psi_{-2}. \tag{4.72}$$

This aligns with our definition of α in the spin-1 system [Eq. (4.22)]. From here we drop the tilde from c_2 for convenience.

Thanks to our knowledge of the spin-1 system, we know how to approach each of these

nonlinear terms. Let's start with the spin-singlet, which we can write as

$$\alpha = \psi^T A_{00} \psi, \tag{4.73}$$

where we use a normalized version of the Clebsch-Gordan coefficient matrix defined in Eq. (2.14),

$$A_{00} = \begin{pmatrix} 0 & 0 & 0 & 0 & 1 \\ 0 & 0 & 0 & -1 & 0 \\ 0 & 0 & 1 & 0 & 0 \\ 0 & -1 & 0 & 0 & 0 \\ 1 & 0 & 0 & 0 & 0 \end{pmatrix}. \tag{4.74}$$

Let us split up the energy functional so the spin-singlet term looks similar to the spin-1 case, i.e. so we get a c_2 term that looks like $n^2 - |\alpha|^2$,

$$E_{int} = \frac{1}{2} \int d\mathbf{r} \{(c_0 + c_2) n^2 + c_1 F^2 - c_2 (n^2 - |\alpha|^2)\}. \tag{4.75}$$

4.6.1 Spin-singlet interaction

Let us treat the adjusted spin-singlet term as a separate subsystem; we get the spin-singlet GPE

$$i\dot{\psi} = -c_2(n\psi - \alpha A_{00}\psi^*). \tag{4.76}$$

As in the spin-1 case, we find $\dot{n} = 0$ and $\dot{\alpha} = 0$, and thus can solve the system in the same way, with solution

$$\psi(t) = \cos(c_2 St)\psi(0) + \frac{i}{S}\sin(c_2 St)[n\psi(0) - \alpha A_{00}\psi^*(0)], \tag{4.77}$$

where $S \equiv \sqrt{n^2 - |\alpha|^2}$. Note that $S^2 \geq F^2/4$ [94], unlike the spin-1 case which had $S^2 = F^2$ [by virtue of Eq. (4.21)].

4.6.2 Magnetization interaction

The spin-dependent magnetization interaction can be written in a similar way to the spin-1 case, with $R = \sum_\nu F_\nu \mathrm{f}_\nu$ now being a 5×5 matrix [c.f. Eq. (4.44)]. Taking the functional derivative in the same way, we get a magnetization GPE of the same form as Eq. (4.50), i.e.

$$\dot{\psi} = -ic_1 R\psi. \tag{4.78}$$

The spin-2 subsystem still conserves R due to the commutation relations of the spin matrices holding for any spin-f, i.e. Eqs. (4.51)–(4.56) still hold for spin-2. Thus we proceed to analyze the solution by evaluating the matrix exponential of $-ic_1 tR$. The eigenvalues of R are now $\{\pm 2F, \pm F, 0\}$. If we consider the Cayley-Hamilton theorem for $Q \equiv R/F$, we get

$$p(\lambda) = \lambda(\lambda^2 - 1)(\lambda^2 - 4), \tag{4.79}$$

$$= \lambda^5 - 5\lambda^3 + 4\lambda, \tag{4.80}$$

$$\implies Q^5 = 5Q^3 - 4Q. \tag{4.81}$$

This indicates that there is a higher-dimensional analog of the Rodrigues' rotation formula for spin-2, which could be found in principle by expanding the matrix exponential in a Taylor series and replacing powers of R^m for $m \geq 5$ using the recurrence of Eq. (4.81), resulting in an expression with powers of R up to R^4.

This approach is unwieldy due to the recurrence relating multiple powers of R together, which leads to many more terms in the series expansion than in the spin-1 case. However, a closed formula for the general case of exponentiating spin matrices of arbitrary spin-f has recently been found by Curtwright *et.al.* [95]. If we adapt their spin-2 formula to our case, we get the result

$$\begin{aligned} e^{-ic_1 F t Q} = I_5 &+ i\left(\frac{1}{6}\sin(2c_1Ft) - \frac{4}{3}\sin(c_1Ft)\right)Q \\ &+ \left(\frac{4}{3}\cos(c_1Ft) - \frac{1}{12}\cos(2c_1Ft) - \frac{5}{4}\right)Q^2 \\ &+ i\left(\frac{1}{3}\sin(c_1Ft) - \frac{1}{6}\sin(2c_1Ft)\right)Q^3 \\ &+ \left(\frac{1}{4} - \frac{1}{3}\cos(c_1Ft) + \frac{1}{12}\cos(2c_1Ft)\right)Q^4. \end{aligned} \tag{4.82}$$

We might have hoped we could simplify this expression in an analogous way to the spin-1 solution. However, we cannot follow the same process since the eigenvector with zero eigenvalue is no longer orthogonal to a general spin-2 spinor. So the eigenvectors with $\{\pm 2F, \pm F\}$ eigenvalues no longer form a basis for ψ, and the action of the Cayley-Hamilton identity does not simplify any further in general. Denoting eigenvectors of Q by v_m, with eigenvalue m, the eigenvector with zero eigenvalue is

$$v_0 = \frac{1}{F^2}\sqrt{\frac{3}{2}}\begin{pmatrix} \frac{1}{2}F_-^2 \\ -F_-F_z \\ \frac{1}{\sqrt{6}}(2F_z^2 - F_+F_-) \\ F_+F_z \\ \frac{1}{2}F_+^2 \end{pmatrix}. \tag{4.83}$$

The projection onto ψ is

$$v_0^\dagger\psi = \frac{1}{F^2}\left((F_z^2 - \frac{1}{2}F_+F_-)\psi_0 + \sqrt{\frac{3}{2}}[F_+^2\psi_{+2} + F_-^2\psi_{-2} - \frac{1}{2}F_z(F_+\psi_{+1} - F_-\psi_{-1})]\right). \tag{4.84}$$

By inspection we see that if our state is magnetized along z only, with all population in a single component such that $\psi_0 = 0$ and $F_\pm = 0$, we make the projection zero and thus get simplified dynamics. We can see that something similar happens when spin-rotating any initial magnetization onto the z-axis; v_0 is then $|0\rangle$, with $F = F_z$, so the above formula is just $v_0^\dagger\psi = \psi_0$, which is left unchanged by the dynamics about the z-axis.

If we are in a state where the projection is zero, the action of the Cayley-Hamilton

identity [Eq. (4.81)] simplifies to

$$Q^4\psi = 5Q^2\psi - 4\psi, \tag{4.85}$$

and we lose the terms with coefficients constant in time,

$$\begin{aligned} e^{-ic_1Ft\,Q}\psi = \quad & \left(\frac{4}{3}\cos(c_1Ft) - \frac{1}{3}\cos(2c_1Ft)\right)\psi \\ & + i\left(-\frac{4}{3}\sin(c_1Ft) + \frac{1}{6}\sin(2c_1Ft)\right)Q\psi \\ & + \left(-\frac{1}{3}\cos(c_1Ft) + \frac{1}{3}\cos(2c_1Ft)\right)Q^2\psi \\ & + i\left(\frac{1}{3}\sin(c_1Ft) - \frac{1}{6}\sin(2c_1Ft)\right)Q^3\psi. \end{aligned} \tag{4.86}$$

Note that if we had $Q^2\psi = \psi$ we would get the spin-1 result

$$e^{-ic_1Ft\,\hat{\mathbf{n}}\cdot\mathbf{f}}\psi = \cos(c_1Ft)\psi - \frac{i}{F}\sin(c_1Ft)R\psi, \tag{4.87}$$

while if we had $Q^2\psi = 4\psi$ we would get the spin-1 result for $2F$

$$e^{-ic_1Ft\,\hat{\mathbf{n}}\cdot\mathbf{f}}\psi = \cos(2c_1Ft)\psi - \frac{i}{2F}\sin(2c_1Ft)R\psi, \tag{4.88}$$

which are valid when ψ is spanned by $v_{\pm F}$ or $v_{\pm 2F}$, respectively. This shows that the full matrix exponential mixes contributions from spin-1-like systems for F and $2F$, with an additional time-independent mixing due to the eigenvector with zero eigenvalue.

4.6.3 More magnetization interaction

Let us rewrite Eq. (4.82) as

$$\begin{aligned} e^{-ic_1Ft\,Q} = {} & I_5 - \frac{5}{4}Q^2 + \frac{1}{4}Q^4 \\ & + \cos(c_1Ft)\left(\frac{4I_5 - Q^2}{3}\right)Q^2 - i\sin(c_1Ft)\left(\frac{4I_5 - Q^2}{3}\right)Q \\ & + \cos(2c_1Ft)\frac{1}{4}\left(\frac{Q^2 - I_5}{3}\right)Q^2 - \frac{i}{2}\sin(2c_1Ft)\left(\frac{Q^2 - I_5}{3}\right)Q, \end{aligned} \tag{4.89}$$

and project ψ onto the basis of eigenvectors of Q. We write $\psi = \sum_m u_m$, where $u_m = (v_m^\dagger\psi)v_m$. We then have

$$\begin{aligned} e^{-ic_1Ft\,Q}\psi = {} & u_0 \\ & + \cos(c_1Ft)(u_{+1} + u_{-1}) - i\sin(c_1Ft)(u_{+1} - u_{-1}) \\ & + \cos(2c_1Ft)(u_{+2} + u_{-2}) - i\sin(2c_1Ft)(u_{+2} - u_{-2}), \qquad (4.90) \\ = {} & \sum_m \exp(-ic_1mFt)u_m. \qquad (4.91) \end{aligned}$$

We can match eigenvectors in each equation since they are orthogonal, and we get

$$u_0 = \left(I_5 - \frac{1}{4}(5Q^2 - Q^4)\right)\psi, \tag{4.92}$$

$$u_{\pm 1} = \left(\frac{Q \pm I_5}{2}\right)\left(\frac{4I_5 - Q^2}{3}\right)Q\psi, \tag{4.93}$$

$$u_{\pm 2} = \left(\frac{Q \pm 2I_5}{4}\right)\left(\frac{Q^2 - I_5}{3}\right)\frac{Q\psi}{2}. \tag{4.94}$$

We can see that the equation for u_0 matches the Cayley-Hamilton identity if we multiply both sides by $4Q$, showing that u_0 is the part of ψ that stops us factoring out Q from the action of the identity. The three matrix factors of the next equation can be understood as (when read from right to left): zero out u_0, zero out $u_{\pm 2}$, and zero out $u_{\mp 1}$, at each step normalizing the $u_{\pm 1}$ component. The last equation, similarly, acts to: zero out u_0, zero out $u_{\pm 1}$, and zero out $u_{\mp 2}$, at each step normalizing the $u_{\pm 2}$ component.

Thus we have shown that Eq. (4.82) computes an implicit eigenvector decomposition into subsystems of 0, F, and $2F$ using only operations of Q.

4.6.4 Full solution for spin-2 nonlinear interactions

The exact solutions of the magnetization interaction and the spin-singlet interaction each conserve n and commute with the density interaction term, the linear Zeeman term, and the trapping potential. Here we show that they also commute with each other, and thus we give the full solution as the direct composition of the two solutions.

To show they commute it suffices to show that each interaction conserves the energy terms generating the dynamics of the other interaction. We will use the following properties of A_{00} and f_ν:

$$A_{00}^T = A_{00}, \quad A_{00}^2 = I, \quad A_{00} f_\nu A_{00} = -f_\nu^*, \tag{4.95}$$

$$\psi^T A_{00} f_\nu \psi = -\psi^T f_\nu^* A_{00}\psi = -\psi^T A_{00} f_\nu \psi = 0. \tag{4.96}$$

The magnetization interaction then causes the spin-singlet amplitude to evolve as

$$\frac{\partial|\alpha|^2}{\partial t} = 2\alpha^*\psi^T A_{00}\dot{\psi} + 2\alpha\dot{\psi}^\dagger A_{00}\psi^*, \tag{4.97}$$

$$= -2ic_1 \sum_\nu F_\nu \left(\alpha^*\psi^T A_{00}\mathrm{f}_\nu\psi - \alpha(\psi^T \mathrm{f}_\nu^* A_{00}\psi)^*\right) = 0. \tag{4.98}$$

The spin-singlet interaction causes the magnetization components to evolve as

$$\dot{F}_\nu = \psi^\dagger \mathrm{f}_\nu \dot{\psi} + \dot{\psi}^\dagger \mathrm{f}_\nu \psi, \tag{4.99}$$

$$= \psi^\dagger \mathrm{f}_\nu i c_2 (n\psi - \alpha A_{00}\psi^*) - i c_2 (n\psi - \alpha A_{00}\psi^*)^\dagger \mathrm{f}_\nu \psi, \tag{4.100}$$

$$= -i c_2 \left([\alpha^* \psi^T \mathrm{f}_\nu^* A_{00}\psi]^* - \alpha^* \psi^T A_{00} \mathrm{f}_\nu \psi \right) = 0. \tag{4.101}$$

Thus the magnetization and spin-singlet interactions conserve the energy terms of each other, and therefore their dynamics commutes with each other. The general solution to the full dynamics generated by the nonlinear spin-2 interactions in the Hamiltonian of Eq. (4.75), i.e. the spin-2 solution to $\hat{H}_B$, is then the direct composition of the solutions to the constituent parts, Thus the full solution to the $\hat{H}_B$ subsystem of Eq. (4.7) is given by

$$\begin{aligned}\psi(t) = &\exp(-itp\mathrm{f}_z)\exp\left(-it[V_{trap} + (c_0 + c_2)n]\right) \\ &\times \left(\cos(c_1 F t)\psi(0) - \frac{i}{F}\sin(c_1 F t) R\psi(0)\right) \\ &\times \left(\cos(c_2 S t)\psi(0) + \frac{i}{S}\sin(c_2 S t)\left[n\psi(0) - \alpha A_{00}\psi^*(0)\right]\right),\end{aligned} \tag{4.102}$$

with n, F, $R = \sum_\nu F_\nu \mathrm{f}_\nu$, $S = \sqrt{n^2 - |\alpha|^2}$, and α being equal to their initial values at $t = 0$.

4.7 spin-f

For spin-3 and higher, the interactions are exactly solvable only if we have just the spin-dependent magnetization interaction and the spin-singlet interaction, i.e. if $c_m = 0$ for $m > 2$. We can show this by generalizing the results of the previous sections to higher spin by rewriting them as matrix equations for spin-f.

4.7.1 Spin rotations and evolution

We can generalize the results for spin-1 and spin-2 to spin-f by introducing the $2f \times 2f$ matrix $Q = R/F$, which has

$$p(\lambda) = \lambda(\lambda^2 - 1) \times \cdots \times (\lambda^2 - f^2) = 0, \tag{4.103}$$

$$u_0 = \frac{(-1)^f}{(f!)^2}(Q^2 - \mathbb{I})(Q^2 - 4\mathbb{I}) \times \cdots \times (Q^2 - f^2\mathbb{I})\psi, \tag{4.104}$$

$$u_m = \left(\frac{Q + m\mathbb{I}}{2|m|}\right) \times \prod_{n \notin \{m,0\}} \frac{Q^2 - n^2\mathbb{I}}{m^2 - n^2} \times \left(\frac{Q}{|m|}\right). \tag{4.105}$$

The dynamics are then the same form as in spin-1 and spin-2, with solution given by

$$\psi(t) = \exp(-ic_1 F t Q)\psi(0). \tag{4.106}$$

The matrix exponential may be computed using various techniques including the exact formula in Ref. [95] which involves powers of Q up to $2f$.

4.7.2 Spin-singlet evolution

Let us write the generalized spin-singlet evolution using $\Psi \equiv (\psi, \psi^*)^T$, and a normalized $(A_{00})_{m,m'} = \delta_{m,-m'}$ with $\alpha = \sum_m (-1)^m \psi_m \psi_{-m}$. Then we have the energy functional

$$E_{int} = \frac{1}{2}\int d\mathbf{r}\ \{c_2 n^2 - c_2(n^2 - |\alpha|^2)\}, \tag{4.107}$$

with GPE

$$i\dot{\Psi} = -c_2 \begin{pmatrix} n\mathbb{I} & -\alpha A_{00} \\ \alpha^* A_{00} & -n\mathbb{I} \end{pmatrix} \Psi. \tag{4.108}$$

If we take the second time derivative, we get

$$\ddot{\Psi} = -c_2^2 \begin{pmatrix} n\mathbb{I} & -\alpha A_{00} \\ \alpha^* A_{00} & -n\mathbb{I} \end{pmatrix}^2 \Psi = -c_2^2 S^2 \Psi, \tag{4.109}$$

where $S = \sqrt{n^2 - |\alpha|^2}$, as for spin-2. Thus the dynamics of Eq. (4.107) are given by

$$\psi(t) = \exp(-ic_2 n t)\left(\cos(c_2 S t)\psi(0) + \frac{i}{S}\sin(c_2 S t)\left[n\psi(0) - \alpha A_{00}\psi^*(0)\right]\right). \tag{4.110}$$

4.7.3 Full solution for spin-f nonlinear interactions

Using the generalized spin-singlet and magnetization interactions, the identities Eqs. (4.95) and (4.96) still hold and thus the interactions commute with each other. Thus the dynamics is given by the generalized version of the solution to the full spin-2 nonlinear dynamics, Eq. (4.102).

4.7.4 Higher order multipole interactions

Higher order multipole interaction terms are not exactly solvable in general. Here we examine the first of these, the quadrupole tensor.

Quadrupole tensor

The spin-3 system introduces a new independent interaction, which we can choose to be the next highest multipole observable, the quadrupole tensor. We can use the traceless symmetric tensor, which has five independent components and energy functional

$$E_{\text{quadrupole}} = \frac{c_3}{2}\int d\mathbf{r}\ \mathrm{Tr}\left\{\left[\mathcal{T}^{(2)}\right]^2\right\}, \tag{4.111}$$

$$= \frac{c_3}{2}\int d\mathbf{r}\ \left\{\mathcal{T}_{xx}^2 + \mathcal{T}_{yy}^2 + (\mathcal{T}_{xx}+\mathcal{T}_{yy})^2 + 2\left(\mathcal{T}_{xy}^2 + \mathcal{T}_{yz}^2 + \mathcal{T}_{xz}^2\right)\right\}. \tag{4.112}$$

There is no known general solution to the full dynamics of this term. For spin-3 it is related to the appearance of the first exception group G_2 as a subalgebra of $SO(7)$, with the system being underdetermined by conserved quantities due to G_2 having the same quadratic Casimir invariant as $SO(7)$ [96]. Thus the solution of this subsystem does not commute with the other subsystems. A five-way splitting can be done, with each term solved exactly. However, the five subsystems are not mutually commuting.

4.8 Numerical implementation

Numerically, we represent the wavefunction on an evenly spaced discretization grid. For each spatial dimension, we use the numerical position and momentum discretization grids given by

$$\nu_i = L_{\text{sys}}\left(-\frac{1}{2} + \frac{i-1}{2N_{\text{sys}}}\right) \in \left[-\frac{L_{\text{sys}}}{2}, \frac{L_{\text{sys}}}{2}\right), \tag{4.113}$$

$$k_{\nu,i} = \frac{\pi N_{\text{sys}}}{L_{\text{sys}}}\left(-1 + \frac{i-1}{N_{\text{sys}}}\right) \in \left[-\frac{\pi N_{\text{sys}}}{L_{\text{sys}}}, \frac{\pi N_{\text{sys}}}{L_{\text{sys}}}\right), \tag{4.114}$$

for $\nu \in \{x, y, z\}$ and $1 \leq i < N_{\text{sys}}$. We set N_{sys} to an even number of points, and a power of 2 for maximum Fourier transform efficiency.

4.8.1 Kinetic energy and quadratic Zeeman

We consider periodic spatial boundary conditions, enabling us to compute the solution of the kinetic energy subsystem $\hat{H}_A$ [Eq. (4.6)] given in Eq. (4.11) using computationally efficient Fast Fourier Transforms. The discretized Fourier space energy grid used in computing Eq. (4.11),

$$E_{k,a,b,c} = \frac{1}{2}(k_{x,a}^2 + k_{y,b}^2 + k_{z,c}^2), \tag{4.115}$$

for $1 \leq \{a, b, c\} < N_{\text{sys}}$, can be precomputed using the momentum space grid. Given relevant parameters for the momentum space grid, quadratic Zeeman energy, and time step, we give MATLAB code that shows our numerical implementation for spin-1 in Listing. 4.1. This easily generalizes to higher spin.

```
Ek = fftshift(0.5*(KX.^2 + KY.^2 + KZ.^2));
A = exp(-1i*(Ek + q)*dt);
B = exp(-1i*Ek*dt);

function psi_t = psi_kinetic_q(psi, A, B)
psi_t = {
ifftn(A.*fftn(psi{1}));
ifftn(B.*fftn(psi{2}));
ifftn(A.*fftn(psi{3}))
};
end
```

Listing 4.1: Spin-1 implementation of the $\hat{H}_A$ subsystem evolution.

4.8.2 Spin-1 nonlinear interaction

For the spin-1 nonlinear interaction, we need to calculate n to solve the density interaction, i.e. to compute the solution given in Eq. (4.16). We calculate the time evolution of the remaining nonlinear subsystem using the antiferromagnetic formulation given in Eqs. (4.40)–(4.42), i.e. in terms of the spin-singlet, since we then only have to compute the single nonlinear term α and use the n already computed for the density interaction (which we can do as n is a conserved quantity). This is as opposed to computing the two extra nonlinear terms required for the ferromagnetic form of the solution in Eqs. (4.47)–(4.49), i.e. F_z and $F_\perp$.

In Listing. 4.2 we give MATLAB-style pseudo-code of our numerical implementation, including the trap and Linear Zeeman solution given in Eq. (4.8) with the evolution due to the nonlinear interactions to solve the $\hat{H}_B$ subsystem. We use the spin-singlet formulation of the solution, as given in Eq. (4.69).

```
function [psiP_t,psi0_t,psiM_t] = calc_spin_psi_t(psiP, psi0, psiM, c0, c1, V0, p, t)
n = abs(psiP).^2 + abs(psi0).^2 + abs(psiM).^2;
alpha = psi0.^2 - 2*psiP.*psiM;
F = sqrt(n.^2 - abs(alpha).^2);
A = cos(c1*F*t);
B = sin(c1*F*t)./F;
psiP_t = (psiP.*A - 1i*(n.*psiP + alpha.*conj(psiM)).*B).*exp(-1i*(V0 + c0*n - p)*t);
psi0_t = (psi0.*A - 1i*(n.*psi0 - alpha.*conj(psi0)).*B).*exp(-1i*(V0 + c0*n)*t);
psiM_t = (psiM.*A - 1i*(n.*psiM + alpha.*conj(psiP)).*B).*exp(-1i*(V0 + c0*n + p)*t);
```

Listing 4.2: Spin-1 implementation of the $\hat{H}_B$ subsystem evolution.

4.8.3 Spin-2 nonlinear interactions

For the spin-2 nonlinear interactions, the spin-singlet and magnetic interactions are independent so we have to calculate both. We calculate the spin-singlet similarly to the spin-1 case. For the magnetization subsystem, we use the compact formula given in Ref. [95],

$$\begin{aligned} e^{i\theta n\cdot J} = I_5 &+ i\sin\theta\left(1+\frac{2}{3}\sin^2\frac{\theta}{2}\right)(n\cdot J) - 2\sin^2\frac{\theta}{2}\left(1+\frac{1}{3}\sin^2\frac{\theta}{2}\right)(n\cdot J)^2, \\ &- \frac{2i}{3}\sin^2\frac{\theta}{2}\sin\theta\,(n\cdot J)^3 + \frac{2}{3}\sin^4\frac{\theta}{2}\,(n\cdot J)^4. \end{aligned} \tag{4.116}$$

This is more compact than the version given in the previous chapter, as there are less trigonometric functions to evaluate – we calculate $\sin\theta$ and $\sin^2\frac{\theta}{2}$, rather sin and cos of

θ and 2θ. This formula also absorbs the constant term (apart from the identity) into the angle-dependent terms. Compared with the previous formula we have found this can give a speedup of about 5%.

In Listing. 4.3 we give MATLAB pseudocode for our numerical implementation, which combines the trap and Linear Zeeman solution in Eq. (4.8) with the evolution due to the density, spin-singlet, and magnetization interactions to compute the $\hat{H}_B$ subsystem as given in Eq. (4.102). We find it most efficient to evaluate the action of powers of Q by repeated application of Q rather than computing the coefficients of higher powers explicitly.

```
function psi = calc_spin2_psi_t(psiP2,psiP1,psi0,psiM1,psiM2,c0,c1,c2,V0,p,t)
nP2 = abs(psiP2).^2; nP1 = abs(psiP1).^2; n0 = abs(psi0).^2;
nM1 = abs(psiM1).^2; nM2 = abs(psiM2).^2;
n = nP2 + nP1 + n0 + nM1 + nM2;
alpha = psi0.^2 - 2*psiP1.*psiM1 + 2.*psiP2.*psiM2;
fz = 2*(nP2 - nM2) + nP1 - nM1; % calc fz for later, it is conserved so can do it now

% Evolve by spin-singlet term -c2*(n^2 - |alpha|^2)
S = sqrt(n.^2 - abs(alpha).^2);
cosT = cos(c2*S*t); sinT = sin(c2*S*t)./S; sinT(S==0) = 0;
psi = cell(1,5);
psi{1} = psiP2.*cosT + 1i*(n.*psiP2 - alpha.*conj(psiM2)).*sinT;
psi{2} = psiP1.*cosT + 1i*(n.*psiP1 + alpha.*conj(psiM1)).*sinT;
psi{3} = psi0.*cosT + 1i*(n.*psi0 - alpha.*conj(psi0)).*sinT;
psi{4} = psiM1.*cosT + 1i*(n.*psiM1 + alpha.*conj(psiP1)).*sinT;
psi{5} = psiM2.*cosT + 1i*(n.*psiM2 - alpha.*conj(psiP2)).*sinT;

% Evolve by spin term c1*F^2 and density (c0 + c2)*n^2
fp = sqrt(6)*(psi{2}.*conj(psi{3}) + psi{3}.*conj(psi{4})) + ...
    2*(psi{4}.*conj(psi{5}) + psi{1}.*conj(psi{2}));
F = sqrt(fz.^2 + abs(fp).^2); % fz is conserved by so can reuse initial fz

% multiply by powers of Q=R/F. Q, Q^2, Q^3, Q^4.
C1 = cos(c1*F*t); S1 = sin(c1*F*t);
C2 = cos(2*c1*F*t); S2 = sin(2*c1*F*t);
Qfactor = 1i*(-(4/3)*S1 + 1/6*S2);
Q2factor = (-(5/4) + 4/3*C1 - 1/12*C2);
Q3factor = 1i*(1/3*S1 - 1/6*S2);
Q4factor = (1/4 - 1/3*C1 + 1/12*C2);

fzQ = fz./F;
fpQ = fp./F;
Qpsi = calc_Qpsi(fzQ, fpQ, psi);
Q2psi = calc_Qpsi(fzQ, fpQ, Qpsi);
Q3psi = calc_Qpsi(fzQ, fpQ, Q2psi);
Q4psi = calc_Qpsi(fzQ, fpQ, Q3psi);

for ii = 1:5
    psi{ii} = psi{ii} + Qfactor.*Qpsi{ii} + Q2factor.*Q2psi{ii} ...
```

```
        + Q3factor.*Q3psi{ii} + Q4factor.*Q4psi{ii};
end

% Evolve by (c0 + c2)*n^2 + (V0 + pm)*n
total_spin_F = 2;
for ii = 1:length(psi)
    mF = total_spin_F + 1 - ii;
    psi{ii} = psi{ii}.*exp(-1i*((c0 + c2)*n + V0 + p*mF)*t);
end

end

% calculate Q*psi, where Q = R/F is a matrix operator
function Qpsi = calc_Qpsi(fz, fp, psi)
Qpsi{1} = (2*fz.*psi{1} + fp.*psi{2});
Qpsi{2} = (conj(fp).*psi{1} + fz.*psi{2} + sqrt(3/2)*fp.*psi{3});
Qpsi{3} = sqrt(3/2)*(conj(fp).*psi{2} + fp.*psi{4});
Qpsi{4} = (sqrt(3/2)*conj(fp).*psi{3} - fz.*psi{4} + fp.*psi{5});
Qpsi{5} = (conj(fp).*psi{4} - 2*fz.*psi{5});
end
```

Listing 4.3: Spin-2 implementation of the $\hat{H}_B$ subsystem evolution.

4.8.4 spin-f

The numerical generalization to spin-f has not be an active area of research in this PhD, but we expect that the large number of computations required to compute the exact solution will lead to a large accumulation of floating point errors, which will negatively affect the stability of evolution algorithms. Thus it may be more efficient for these high spin systems to use a more generic ODE solver that does not use the exact solution of the nonlinear dynamics.

4.8.5 GPU parallelization

To evaluate the spatially local nonlinear interactions efficiently on the GPU using MATLAB, we use `arrayfun` to parallelize the computation across gridpoints. The code takes each component of the local spinor as inputs, and calculates the time evolution without using matrix multiplication, since `arrayfun` only supports scalar operations.

In Listing. 4.4 we give MATLAB pseudo-code to evaluate the nonlinear dynamics of the spin-1 system on the GPU. We switch to the GPU if the wavefunction has been initialized using the `gpuArray` data type. The code to evaluate the $\hat{H}_A$ subsystem (i.e.

kinetic energy and quadratic Zeeman) is left unchanged, with MATLAB evaluating it relatively efficiently on the GPU without extra help apart from making the energy grid a `gpuArray`.

```
% Setup needed in main script to use GPU
onGPU = true;
if onGPU
    for kk=1:3
        psi{kk} = gpuArray(psi{kk});
    end
    Ek = gpuArray(Ek);
end

% Switch to GPU if using gpuArrays
function psi_t = spin1_psi_t(psi0, c0, c1, V0, p, t)
if isa(psi0{1}, 'gpuArray')
    [psi_t{1}, psi_t{2}, psi_t{3}] = ...
        arrayfun(@calc_spin_psi_t_gpu, psi0{1}, psi0{2}, psi0{3}, c0, c1, V0, p, t);
else
    [psi_t{1}, psi_t{2}, psi_t{3}] = ...
        calc_spin_psi_t(psi0{1}, psi0{2}, psi0{3}, c0, c1, V0, p, t);
end
end

% Calculate spin-1 nonlinear dynamics on the GPU
function [psiP_t,psi0_t,psiM_t] = calc_spin_psi_t_gpu(psiP,psi0,psiM,c0,c1,V0,p,t)
n = abs(psiP).^2 + abs(psi0).^2 + abs(psiM).^2;
alpha = psi0.^2 - 2*psiP.*psiM;
F = sqrt(complex(n.^2 - abs(alpha).^2));
A = cos(c1*F*t);
B = sin(c1*F*t)./F;
if F==0
    B = complex(0);
end
psiP_t = (psiP.*A - 1i*(n.*psiP + alpha.*conj(psiM)).*B).*exp(-1i*(V0 + c0*n - p)*t);
psi0_t = (psi0.*A - 1i*(n.*psi0 - alpha.*conj(psi0)).*B).*exp(-1i*(V0 + c0*n)*t);
psiM_t = (psiM.*A - 1i*(n.*psiM + alpha.*conj(psiP)).*B).*exp(-1i*(V0 + c0*n + p)*t);
end
```

Listing 4.4: Spin-1 GPU parallelization.

Chapter 5

Symplectic GPE evolution

5.1 Introduction

We can approximate the solution to the full GPE by composing the exact solutions of the two subsystems, i.e. $\hat{H}_A$ and $\hat{H}_B$ in Eqs. (4.6) and (4.7). Since the system dynamics are Hamiltonian, it is desirable to use a symplectic composition method in order to maintain the Hamiltonian geometric structure of phase space in our solution [see Section. 4.2]. Any composition of exact Hamiltonian flows is a symplectic method [97]. The exact dynamics of each subsystem preserve N, M_z and E, thus all composition methods will also preserve N, M_z and E (up to roundoff error).

In this Chapter we will present a well known second order symplectic composition and a more recently developed fourth order method. We also present some non-symplectic methods in the literature, including the usual fourth order Runge-Kutta method, as well as some initial splitting methods which did not use our exact solution to the nonlinear dynamics. We conclude with some remarks about issues, possible extensions, and alternatives arising with extending our methods to evolve under imaginary time, which is used in gradient flow methods to compute ground states.

5.2 Symplectic composition schemes

Symplectic composition methods are splitting methods that combine exact flows of Hamiltonian subsystems to approximate the time evolution of the combined Hamiltonian

system [85]. Symplectic numerical integration algorithms preserve a discretization of the symplectic two-form exactly, and thus preserve geometric features of the structure of the exact solution in phase space. Indeed, for small timesteps they give the exact Hamiltonian flow for an auxiliary (pseudo) Hamiltonian close to the exact Hamiltonian [98]. Symplectic methods have very good long-time error behaviour, making them the preferred class of algorithm for simulating long-time Hamiltonian systems.

A limitation of symplectic methods is that the time step is restricted to be uniform; variable time steps destroy the symplecticity of the standard algorithms [99], although extensions can be made to restore symplecticity [100, 101].

Additionally, all explicit splitting methods (computable from initial conditions, vs implicit methods which require iteration) introduce an inherent upper limit to the time step, the Courant-Friedrichs-Lewy (CFL) condition [102], which comes from the requirement to resolve the frequencies in each subsystem accurately or risk aliasing in the composition solution.

5.2.1 Second-order symplectic method (S2)

The Leapfrog method[1] [103] is the simplest second-order composition for advancing the wavefunction by a time step of size τ. It takes the form

$$\boldsymbol{\psi}(\tau) = e^{\hat{f}\tau}\boldsymbol{\psi}(0) \approx e^{\hat{f}_A\frac{\tau}{2}}e^{\hat{f}_B\tau}e^{\hat{f}_A\frac{\tau}{2}}\boldsymbol{\psi}(0), \tag{5.1}$$

where $e^{\hat{f}_A t}$ and $e^{\hat{f}_B t}$ represents the flow solutions of the two subsystems. We denote this scheme as S2 in the results we present. This method is well known and has been widely used in numerical simulations of dynamical systems [104], in particular because it is the simplest symplectic method [85, 105, 106].

5.2.2 Fourth-order symplectic method (S4)

It is possible to employ higher-order compositions. It is easy to find time symmetric methods by composing lower order methods together, starting with S2 for example. Various more general methods exist for construction, with the main tool being the Baker-Campbell-Hausdorff (BCH) formula which is used to analyze the error terms arising at different orders [107]. By using several stages, these error terms can be

[1] Also known as the Verlet, Störmer, or Strang splitting method in various fields [97].

canceled out to give a high-order approximation to the exact solution. Error, stability, and efficiency properties can be tuned by adding more stages and carrying out nonlinear optimization of the order conditions arising from the BCH expansion.

Here we consider a general-purpose fourth-order method, due to Blanes and Moan [108, 109], with the form

$$\begin{aligned}\boldsymbol{\psi}(\tau) &= e^{\hat{f}\tau}\boldsymbol{\psi}(0) \\ &\approx e^{\hat{f}_A a_7 \tau} e^{\hat{f}_B b_6 \tau} e^{\hat{f}_A a_6 \tau} \cdots e^{\hat{f}_B b_1 \tau} e^{\hat{f}_A a_1 \tau} \boldsymbol{\psi}(0),\end{aligned} \tag{5.2}$$

where the a-coefficients are

$$a_0 = a_6 = 0.0792036964311957, \tag{5.3}$$

$$a_1 = a_5 = 0.353172906049774, \tag{5.4}$$

$$a_2 = a_4 = -0.0420650803577195, \tag{5.5}$$

$$a_3 = 1 - 2(a_0 + a_1 + a_2), \tag{5.6}$$

and the b-coefficients are

$$b_1 = b_6 = 0.209515106613362, \tag{5.7}$$

$$b_2 = b_5 = -0.143851773179818, \tag{5.8}$$

$$b_3 = b_4 = 0.5 - (b_1 + b_2). \tag{5.9}$$

5.3 Existing algorithms

We compare our symplectic schemes against several alternative approaches. Firstly, a second order composition method which splits the system into three parts. One of the nonlinear subsystems was diagonal and solved exactly, while the other was only approximately solved. Due to this approximation of one of the subsystem flows, this method is not symplectic. For spin-1, the approximate system is solved by explicit exponentiation of the Runge-Kutta step, however for spin-2 the Runge-Kutta flow is computed by numerical diagonalization. We note that the authors of this method recently carried out a review of numerical techniques for simulating spinor BECs [110], where they referred to our exact solution of the spin-1 and spin-2 nonlinear subsystems as used in S2 and S4.

For comparison, we apply a general fourth order Runge-Kutta method to the spinor system. This is not symplectic, and is not a composition method, but can be used for

more general systems, e.g. systems with noise terms and dissipation, and for higher spin systems.

Finally, we note that there has been work done on a two-way splitting method where the nonlinear term was diagonalized at each point in time, and composed to give a first order method [111]. This method is generalizable to higher spin.

5.3.1 W2

Here we go over a second order time-splitting Fourier pseudospectral method developed by Wang for the spin-1 system in Ref. [91] (also see [112, 113]) and for the spin-2 system in Ref. [114]. It involves a three-way splitting of the GPE in a similar manner to our splitting, but additionally splits $\hat{H}_B$ into diagonal and non-diagonal terms. They solve the diagonal terms exactly but cannot solve the non-diagonal subsystem analytically. Instead, they approximate its solution with a second-order Runge-Kutta step. If this flow was solved exactly then the W2 method would be symplectic, however due to the approximation it is not, and additionally this approximation does not conserve z magnetization exactly.

Spin-1

We now review the W2 method for the spin-1 system, introduced in Ref. [91]. They consider possible rotation of the system, which we ignore here. There are three stages,

$$\psi(t) = e^{\frac{t}{2}C} e^{\frac{t}{2}D} e^{tG} e^{\frac{t}{2}D} e^{\frac{t}{2}C} \psi(0). \tag{5.10}$$

The C flow consists of the kinetic energy term,

$$\dot{\boldsymbol{\psi}} = i\tfrac{1}{2}\nabla^2 \boldsymbol{\psi}, \tag{5.11}$$

$$e^{\tau C}\boldsymbol{\psi} = \mathcal{F}^{-1}\left\{ e^{-i\tau\frac{1}{2}k^2}\mathcal{F}[\boldsymbol{\psi}] \right\}, \tag{5.12}$$

where $k = |\boldsymbol{k}|$, with $\boldsymbol{k}$ the Fourier space coordinate. The D flow has the quadratic Zeeman and density-like terms, and is solved exactly as

$$e^{\tau D}\psi_m = e^{-i\tau[qm^2 - pm + c_0 n + c_1(n - 2|\psi_{-m}|^2)]}\psi_m, \tag{5.13}$$

while the G flow has the nonlinear spin-exchange terms,

$$\dot{\boldsymbol{\psi}} = -ic_1 \begin{pmatrix} 0 & \psi_-^*\psi_0 & 0 \\ \psi_0^*\psi_- & 0 & \psi_0^*\psi_+ \\ 0 & \psi_+^*\psi_0 & 0 \end{pmatrix} \boldsymbol{\psi} \equiv -iG\boldsymbol{\psi}, \tag{5.14}$$

which cannot be solved exactly. Instead, an explicit second-order Runge-Kutta method (Heun's method) is employed

$$\int_0^\tau G(\boldsymbol{\psi}(t))d\tau \approx \tfrac{\tau}{2}(G(\boldsymbol{\psi}(0)) + G(\tilde{\boldsymbol{\psi}}(\tau)) \equiv \tau R_w = \tau \begin{pmatrix} 0 & R_{1,2} & 0 \\ R_{1,2}^* & 0 & R_{2,3} \\ 0 & R_{2,3}^* & 0 \end{pmatrix}, \tag{5.15}$$

where

$$\tilde{\boldsymbol{\psi}}(\tau) = \boldsymbol{\psi}(0) - i\tau G(\boldsymbol{\psi}(0))\boldsymbol{\psi}(0), \tag{5.16}$$

and

$$R_{1,2} = \frac{c_1}{2}(\psi_-^*\psi_0 + \tilde{\psi}_-^*\tilde{\psi}_0), \tag{5.17}$$

$$R_{2,3} = \frac{c_1}{2}(\psi_0^*\psi_+ + \tilde{\psi}_0^*\tilde{\psi}_+). \tag{5.18}$$

The G flow is then approximated by

$$e^{-i\tau G}\boldsymbol{\psi}(0) \approx e^{-i\tau R_w}\boldsymbol{\psi}(0), \tag{5.19}$$

with an analytic expression for the exponentiated matrix $e^{-i\tau R_w}$ allowing this to be evaluated accurately,

$$e^{-i\tau R_w} = \frac{1}{\lambda^2} \begin{pmatrix} |R_{2,3}|^2 + |R_{1,2}|^2\cos(\lambda t) & -iR_{1,2}\lambda\sin(\lambda t) & R_{1,2}R_{2,3}(\cos(\lambda t) - 1) \\ -i\lambda R_{1,2}^*\sin(\lambda t) & \lambda^2\cos(\lambda t) & -iR_{2,3}\lambda\sin(\lambda t) \\ R_{1,2}^*R_{2,3}^*(\cos(\lambda t) - 1) & -i\lambda R_{2,3}^*\sin(\lambda t) & |R_{1,2}|^2 + R_{2,3}R_{2,3}^*\cos(\lambda t) \end{pmatrix}. \tag{5.20}$$

We note that the D and G flows conserve M_z exactly, and each conserve their relevant energy term, the sum of which equals the density plus spin energy. But the Runge-Kutta approximation of the G flow does not conserve M_z or its associated energy exactly. This is expected since explicit Runge-Kutta methods are not symplectic. Due to using an inexact flow, the method is not symplectic; however, numerical results show that it can behave similarly to our symplectic method S2 in particular cases, e.g. see Figs. (6.5-6.6).

Spin-2

The extension of the W2 method to the spin-2 system involves a similar procedure as for the spin-1 case, except that the resulting approximation of the G flow is calculated by numerically diagonalizing the equivalent R_w matrix.

This algorithm was given in Sec. 4 of Ref. [114]. They consider an external magnetic field, which we ignore here. They write the spin-2 GPE as

$$i\dot{\psi} = (A + B + C)\psi, \tag{5.21}$$

$$(A)_{ij} = -\frac{1}{2}\nabla^2\delta_{ij}, \tag{5.22}$$

$$B = \mathrm{diag}\{H_2, H_1, H_0, H_{-1}, H_{-2}\}, \tag{5.23}$$

$$H_{\pm 2} = V + c_0 n \mp 2p + 4q \pm 2c_1 F_z + 2c_2|\psi_{\mp 2}|^2, \tag{5.24}$$

$$H_{\pm 1} = V + c_0 n \mp p + q \pm c_1 F_z + 2c_2|\psi_{\mp 1}|^2, \tag{5.25}$$

$$H_0 = V + c_0 n + c_2|\psi_0|^2, \tag{5.26}$$

$$C = \begin{pmatrix} 0 & c_{12} & c_{13} & 0 & 0 \\ c_{12}^* & 0 & c_{23} & 0 & 0 \\ c_{13}^* & c_{23}^* & 0 & c_{34} & c_{35} \\ 0 & 0 & c_{34}^* & 0 & c_{45} \\ 0 & 0 & c_{35}^* & c_{45}^* & 0 \end{pmatrix}, \tag{5.27}$$

$$c_{12} = c_1 F_- - 2c_2\psi_{-2}^*\psi_{-1}, \tag{5.28}$$

$$c_{13} = c_2\psi_{-2}^*\psi_0, \tag{5.29}$$

$$c_{23} = c_1\sqrt{\frac{3}{2}}F_- - c_2\psi_{-1}^*\psi_0, \tag{5.30}$$

$$c_{34} = c_1\sqrt{\frac{3}{2}}F_- - c_2\psi_0^*\psi_1, \tag{5.31}$$

$$c_{35} = c_2\psi_0^*\psi_2, \tag{5.32}$$

$$c_{45} = c_1 F_- - 2c_2\psi_1^*\psi_2, \tag{5.33}$$

$$F_- = F_x - iF_y = 2(\psi_1^*\psi_2 + \psi_{-2}^*\psi_{-1}) + \sqrt{6}(\psi_0^*\psi_1 + \psi_{-1}^*\psi_0), \tag{5.34}$$

where we have used interaction parameters related to theirs by $c_0 = \tau_0$, $c_1 = \tau_1$, and $c_2 = 5\tau_2$.

The A flow can be done to spectral accuracy using Fourier transforms. The B flow leaves $|\psi_m|$ invariant in time, thus it can be done exactly. The C is not diagonal and

can be evaluated using a second-order Runge-Kutta approximation:

$$\exp\left(-i\int_{t_n}^{t_{n+1}} C(\psi(\tau))d\tau\right)\psi(t_n) \approx e^{-i\frac{1}{2}\Delta t(C(\psi)+C(\tilde{\psi})}\psi = e^{-iMt}\psi, \tag{5.35}$$

$$\tilde{\psi} = \psi - i\Delta t C(\psi)\psi, \tag{5.36}$$

$$M = \begin{pmatrix} 0 & b_{12} & b_{13} & 0 & 0 \\ b_{12}^* & 0 & b_{23} & 0 & 0 \\ b_{13}^* & b_{23}^* & 0 & b_{34} & b_{35} \\ 0 & 0 & b_{34}^* & 0 & b_{45} \\ 0 & 0 & b_{35}^* & b_{45}^* & 0 \end{pmatrix}, \tag{5.37}$$

$$b_{12} = \frac{c_1}{2}(F_+ + \tilde{F}_+) - c_2(\psi_{-2}^*\psi_{-1} + \tilde{\psi}_{-2}^*\tilde{\psi}_{-1}), \tag{5.38}$$

$$b_{13} = \frac{c_2}{2}(\psi_{-2}^*\psi_0 + \tilde{\psi}_{-2}^*\tilde{\psi}_0), \tag{5.39}$$

$$b_{23} = \frac{\sqrt{6}}{4}c_1(F_+ + \tilde{F}_+) - \frac{c_2}{2}(\psi_{-1}^*\psi_0 + \tilde{\psi}_{-1}^*\tilde{\psi}_0), \tag{5.40}$$

$$b_{34} = \frac{\sqrt{6}}{4}c_1(F_+ + \tilde{F}_+) - \frac{c_2}{2}(\psi_0^*\psi_1 + \tilde{\psi}_0^*\tilde{\psi}_1), \tag{5.41}$$

$$b_{35} = \frac{c_2}{2}(\psi_0^*\psi_2 + \tilde{\psi}_0^*\tilde{\psi}_2), \tag{5.42}$$

$$b_{45} = \frac{c_1}{2}(F_+ + \tilde{F}_+) - c_2(\psi_1^*\psi_2 + \tilde{\psi}_1^*\tilde{\psi}_2). \tag{5.43}$$

$$\tag{5.44}$$

They calculate the matrix exponential by diagonalization. We can use $\texttt{expm}(-i\Delta t M)$ or also direct diagonalization $[V, D] = \texttt{eig}(-i\Delta t M)$; and $V * \texttt{diag}(\texttt{exp}(\texttt{diag}(D)))/V$.

5.3.2 RK4

The second method we consider is based on the fixed time step fourth-order Runge-Kutta method which we denote as (RK4). We have implemented this algorithm using the *interaction picture* technique [115] to exponentiate away the kinetic energy and quadractic Zeeman subsystem and improve the algorithm performance. This type of method is quite commonly used in the BEC community and we have made an immediate extension to the spinor case for the spin-1 and spin-2 systems.

Here we briefly review the RK4 algorithm, which can be applied to any spinor system. Firstly we make the interaction picture transformation using the unitary transformation

$\boldsymbol{\phi}(t) = U(t)\boldsymbol{\psi}(t)$, which is given (component-wise) by

$$\phi_m = e^{+i(t-t')\left[-\frac{1}{2}\nabla^2+qm^2\right]}\psi_m, \tag{5.45}$$

where t' is the temporal origin of the interaction picture. This interaction picture field then evolves according to the evolution equation

$$\dot{\boldsymbol{\phi}} = U(t)\hat{f}_B U^\dagger(t)\boldsymbol{\phi} \equiv \hat{f}_C(t)\boldsymbol{\phi}, \tag{5.46}$$

where $\hat{f}_B$ is the operator for the nonlinear interactions in the GPE. This equation is then solved discretely in time according to the standard fourth-order Runge-Kutta algorithm

$$\boldsymbol{\phi}(t_n) = U(t_n)\boldsymbol{\psi}(t_n), \tag{5.47}$$
$$\boldsymbol{k}_1 = \hat{f}_C(t_n)\boldsymbol{\phi}(t_n), \tag{5.48}$$
$$\boldsymbol{k}_2 = \hat{f}_C(t_n+\tfrac{\tau}{2})\left[\boldsymbol{\phi}(t_n)+\tfrac{\tau}{2}\boldsymbol{k}_1\right], \tag{5.49}$$
$$\boldsymbol{k}_3 = \hat{f}_C(t_n+\tfrac{\tau}{2})\left[\boldsymbol{\phi}(t_n)+\tfrac{\tau}{2}\boldsymbol{k}_2\right], \tag{5.50}$$
$$\boldsymbol{k}_4 = \hat{f}_C(t_n+\tau)\left[\boldsymbol{\phi}(t_n)+\tau\boldsymbol{k}_3\right], \tag{5.51}$$

yielding

$$\boldsymbol{\phi}(t_{n+1}) = \boldsymbol{\phi}(t_n) + \frac{\tau}{6}(\boldsymbol{k}_1 + 2\boldsymbol{k}_2 + 2\boldsymbol{k}_3 + \boldsymbol{k}_4). \tag{5.52}$$

To evaluate $\hat{f}_C(t)$ for general t, we have to compute two pairs of Fourier transforms. However, by choosing $t' = t_n + \frac{\tau}{2}$, we get $\hat{f}_C(t_n+\frac{\tau}{2}) = \hat{f}_B$ for Eqs. (5.49)-(5.50), and thus only need 4 pairs of Fourier transforms, i.e.

$$\boldsymbol{\phi}(t_n) = U(t_n)\boldsymbol{\psi}(t_n), \tag{5.53}$$
$$\boldsymbol{k}_1 = U(t_n)\hat{f}_B\boldsymbol{\psi}(t_n), \tag{5.54}$$
$$\boldsymbol{k}_2 = \hat{f}_B\left[\boldsymbol{\phi}(t_n)+\tfrac{\tau}{2}\boldsymbol{k}_1\right], \tag{5.55}$$
$$\boldsymbol{k}_3 = \hat{f}_B\left[\boldsymbol{\phi}(t_n)+\tfrac{\tau}{2}\boldsymbol{k}_2\right], \tag{5.56}$$
$$\tilde{\boldsymbol{k}}_4 = \hat{f}_B U^\dagger(t_n+\tau)\left[\boldsymbol{\phi}(t_n)+\tau\boldsymbol{k}_3\right], \tag{5.57}$$
$$\boldsymbol{\psi}(t_{n+1}) = U^\dagger(t_n+\tau)\left\{\boldsymbol{\phi}(t_n)+\frac{\tau}{6}(\boldsymbol{k}_1+2\boldsymbol{k}_2+2\boldsymbol{k}_3)\right\} + \tau\tilde{\boldsymbol{k}}_4/6. \tag{5.58}$$

We note that this choice also gives us

$$U(t_n) = U^\dagger(t_n+\tau) = e^{-i\frac{\tau}{2}\left[-\frac{1}{2}\nabla^2+qm^2\right]}, \tag{5.59}$$

thus for fixed time steps τ we can pre-compute the Fourier space coefficients.

5.3.3 Two-way splitting with diagonalization

In Ref.[111] an algorithm was proposed which split the spin-1 GPE into $\hat{H}_A$ and $\hat{H}_B$ subsystems similar to ours. They considered the spin-1 system, with $p = q = 0$, but can also include a non-local dipolar interaction term in their $\hat{H}_B$ subsystem. They propose to solve the $\hat{H}_A$ subsystem in Fourier space as we do, however they solve the $\hat{H}_B$ subsystem by direct exponentiation using numerical diagonalization. They compose their subsystem solutions using a first order composition; they mention the second-order leapfrog composition that we use in our S2 method (which they refer to as the Strang splitting), but give results that are first order accurate in the time step.

The benefit of their method is that it can handle arbitrary nonlinear potentials, including generalizing to higher spin systems with more difficult interaction terms that we are unable to solve. For the spin-1 and spin-2 systems without dipolar interactions, however, it is computationally more efficient to use our exact solution of the nonlinear dynamics rather than performing a numerical diagonalization at every grid point. In principle, their method could be extended to be fourth order accurate in time by using our S4 composition method to compose their subsystem solutions.

5.3.4 Comparison of algorithms

We compare the various algorithms in terms of the number of function evaluations required per time step in Table 5.1. We neglect the diagonalization method as it is similar to our S2 composition in terms of subsystem evaluations, although we note that using our exact solution to evaluate the nonlinear subsystem is computationally more efficient than their numerical diagonalization method.

The S2 and W2 algorithms require the least evaluations per time step. In 1D tests we find that the S2 is roughly 50% faster than W2 per time step, with this difference largely arising from the much simpler form of the nonlinear term to evaluate in S2. For larger problems, and particularly higher dimensional problems we expect the single round trip FFT required for the S2 algorithm (using FSAL) will be advantageous.

Algorithm	FFT roundtrips (FSAL)	Nonlinear evals
S2	2(1)	1
W2	2	3
RK4	4	4
S4	7(6)	7

Table 5.1: Number of FFT roundtrips (i.e. FFT and inverse FFT) and nonlinear-term evaluations required for each algorithm. The number in brackets indicates the number required per time-step which can be reduced by the first same as last (FSAL) property (i.e. last stage is evaluated at the same point as the first stage of the next step).

5.4 Imaginary time evolution for ground states

We can find ground states by evolving the spinor system in imaginary time. This gives damped evolution in which high energy modes decay fastest, and requires a projection step after each time step in order to maintain the conserved quantities of the system, including total norm of the wavefunction. Imaginary time evolution for finding ground states relates to a class of methods known as gradient flow methods, in which there has been much work done for spin-1 systems [116–120]. In these methods, rather than using an exact solution of the nonlinear dynamics, various combinations of time discretizations are used such as backwards and forwards Euler or Crank-Nicholson steps to achieve different levels of stability and efficiency. Implicit discretizations like backwards Euler and Crank-Nicholson require iteration at each time step to achieve convergence, however this gives them enhanced stability and time-step-size properties which can make them competitive with explicit methods.

To evolve our system in imaginary time using our $\hat{H}_A$ and $\hat{H}_B$ splitting, all time steps must be positive due to $\hat{H}_A$: in imaginary time it gives the heat equation, which is only stable when evolved forwards in time. For composition methods this gives an order barrier, as no method of order greater than two has all positive time steps [121, 122]. This means we cannot use S4, and are restricted to S2. To go beyond second order using composition methods would require a corrected nonlinear potential that incorporates the commutator $[B,[B,A]]$ [123].

In addition, the main benefit of symplectic methods, i.e. structure preservation, in-

cluding conservation of conserved quantities like the total norm/atom number and z-magnetization for spinor systems, is only realized for real time propagation. Thus it makes sense that for imaginary time there are efficiency gains to be made by using more general composition methods, such as using complex time steps [124] or multi-product operator splittings [125].

To conserve total number and total z-magnetization under imaginary time evolution, the appropriate projection step for spin-1 is given in Ref. [118, 119]. For spin-2 see Section 3A of Ref. [126] and also Section 5.2.2 of Ref. [110].

Chapter 6

Numerical 1-D tests

In this Chapter we consider several 1D numerical tests of our S2 and S4 algorithms for the spin-1 and spin-2 systems, comparing their performance with W2 and RK4 methods reviewed in the previous Chapter.

The outline of this Chapter is as follows. First we review the numerical discretization of the system. Then, we carry out tests for the spin-1 system, using an exact continuous-wave solution and an approximate solitonic solution. We then carry out a test for the spin-2 system, using a continuous-wave solution which we develop by direct extension of the method used to derive the spin-1 solution.

6.1 One-dimensional discretization and stability

We consider a spinor condensate in one spatial dimension discretized on a mesh of M points over the interval $[-\frac{L}{2}, \frac{L}{2})$. We assume periodic spatial boundary conditions, allowing us to implement the kinetic energy operator using Fast-Fourier Transforms.

We note that splitting the kinetic energy operator apart from the nonlinear potential in the GPE introduces an instability for any composition method [102, 127], which can only be avoided by choosing the time step size subject to the CFL condition (i.e. resolving the largest frequency) given by

$$\Delta t \lesssim t_{\text{stab}} \equiv \frac{\pi}{\max_j \left|\frac{1}{2}k_j^2 + q\right|}, \tag{6.1}$$

where k_j are the reciprocal space discretization points, which says that the highest

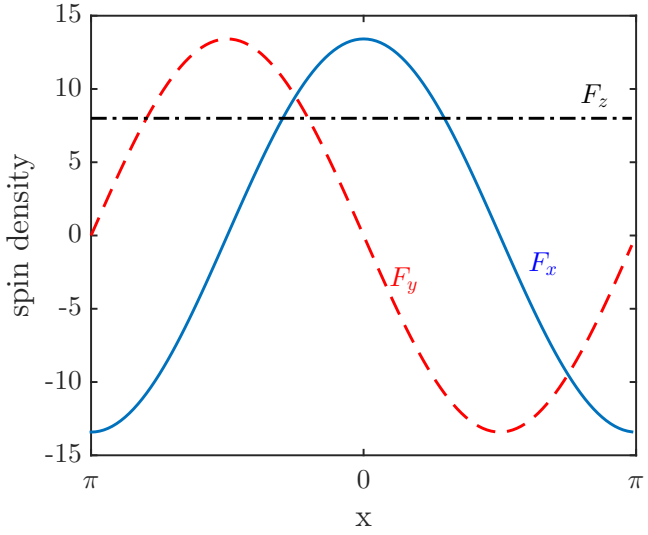

Figure 6.1: The components of the spin density are shown for a continuous wave solution with parameters: $k_+ = 5$, $k_- = 3$, $\theta_+ = 0$, $\theta_- = 0$, $A_+ = 3$, $A_- = 1$ with $c_0 = 10$, $c_1 = 1$ and $q = 0.5$. The remaining parameters are determined by the relations given in Ref. [128].

frequency of the $\hat{H}_A$ subsystem must be resolvable over each time step. Satisfying this condition is necessary but not sufficient for ensuring global numerical stability. It is a severe restriction, with high spatial resolution simulations leading to very small time steps for global stability. Often the step size can be much larger if the integration time of interest is shorter than the time required for the instability to grow.

6.2 Spin-1 Numerical Tests

6.2.1 Continuous-wave comparison

Analytic solution

Recently an analytic theory was developed for a family of continuous-wave solutions to a uniform spin-1 condensate [128]. This solution has the feature that it allows the chemical potentials and wavevectors of the components to be different, and thus forms a non-trivial test for numerical methods.

These waves are analytic solutions to the uniform spin-1 GPE for $p = 0$ and $c_1 \neq 0$ and have the form

$$\psi_+(x) = A_+ e^{i(\theta_+ + k_+ x - \omega_+ t)}, \tag{6.2}$$

$$\psi_0(x) = A_0 e^{i(\theta_0 + k_0 x - \omega_0 t)}, \tag{6.3}$$

$$\psi_-(x) = A_- e^{i(\theta_- + k_- x - \omega_- t)}. \tag{6.4}$$

Here the amplitudes $\{A_-, A_0, A_+\}$ for the three planewave components are taken to be real nonnegative numbers with phases $\{\theta_-, \theta_0, \theta_+\}$. These amplitudes determine the density $n = \sum_m A_m^2$ and magnetization density $F_z = A_+^2 - A_-^2$, with all amplitudes being conserved quantities. We have also introduced the component wavevectors $\{k_-, k_0, k_+\}$ and chemical potentials $\{\omega_-, \omega_0, \omega_+\}$. When two of the three amplitudes, phases and wavevectors are chosen the remaining values, and the chemical potentials, are determined. There is also an additional parity-like parameter n_p which can take the value of 0 or 1, that determines an additional π shift in the phase θ_0 relative to $\theta_\pm$. The equations linking these quantities are given in Ref. [128].

An example of this solution is shown in Fig. 6.1, visualized in terms of the components of spin-density [see Eq. (2.30)]. We see that this solution is a nonlinear spin-wave in $F_\perp$ with the F_x and F_y components of spin density precessing about the constant F_z as the wave propagates.

Numerical results

In Fig. 6.2 we examine how the various schemes conserve the constants of motion of total atom number N, total z-magnetization M_z, and total energy E. Since these quantities should remain constant we characterize the relative error by the absolute relative change in these quantities, i.e. as

$$\text{Rel. Error } Q \equiv \left| \frac{Q(t) - Q(0)}{Q(0)} \right|, \qquad Q \in \{N, M_z, E\}, \tag{6.5}$$

where $Q(t)$ indicates the quantity evaluated at time t during the propagation. Generally the results show that the symplectic algorithms (i.e. S2 and S4) and W2 outperform the Runge-Kutta algorithm at conserving the constants of motion, which is expected since symplectic algorithms preserve the geometric properties of phase space.

The S2 and S4 are more accurate than the W2 algorithm. Although S2 and W2 are both second-order, the W2 method only approximately treats the nonlinear spin exchange

terms and uses a three-way splitting (which, even for exact flows, is generally less accurate) and thus has larger error coefficients than the S2 method.

We note that W2 and RK4 show linear growth with time t for all three conserved quantities. S2 and S4 achieve bounded oscillating errors for N (indeed, S2 oscillates around the discretization limit of 2×10^{-16}), and linear error growth in the long-time limit for M_z and E.

Symplectic methods should have bounded E errors, while other conserved quantities can be either bounded or linear in time. Bounded errors should grow in time solely due to roundoff errors which accumulate like a random walk, scaling as $t^{1/2}$, however this can be difficult to achieve in practice due to systematic errors [129]. Figure 6.2(c) shows that S2 and S4 achieve $t^{1/2}$ error scaling until a linear systematic error begins to dominate after $t \sim 1$.

One source of systematic error for our methods comes from our implementation of the $\hat{f}_A$ flow not being exact to numerical precision. Of course given a continuous wave our Fourier-space solution is calculated using an exact quadrature, and for other waves achieves exponential accuracy, i.e. it approaches roundoff accuracy in the limit of a large number of discretization points M (although this is quickly offset by increased floating point arithmetic errors from FFTs). In this test the $\hat{f}_A$ flow is accurate to $\sim 10^{-15}$. We note that this error is asymmetric across the three components of the wavefunction due to the asymmetry of the wavevectors k_m, which means the observed error behaviour is difficult to analyze theoretically.

A more complete test of the numerical error being introduced by each method is to directly compare the wavefunction propagated to time t [which we denote as $\boldsymbol{\psi}^{\text{num}}(t)$] against the exact analytic solution $\boldsymbol{\psi}(t)$ given in Eqs. (6.2)-(6.4). We do this by evaluating the maximum global error introduced by each algorithm, which we define as

$$\text{Global Error} \equiv \max_{x_j,m} \left|\psi_m^{\text{num}}(x_j,t) - \psi_m(x_j,t)\right|. \tag{6.6}$$

In Fig. 6.3(a) we show the growth of the global error over time for a propagation of fixed time step $\tau = 6.25 \times 10^{-4}$. This is the same propagation examined in Fig. 6.2. The global error shows that S4 is the best at approximating the exact analytic solution by a significant margin, with S2 better than W2, and all of these are better than RK4. Global error grows linearly for all methods until $t \sim 1$ [i.e. the time when the energy error starts growing linearly for S4 in Fig. 6.2(c)]. At this point both fourth-order methods shift their global error behaviour to be quadratic in time.

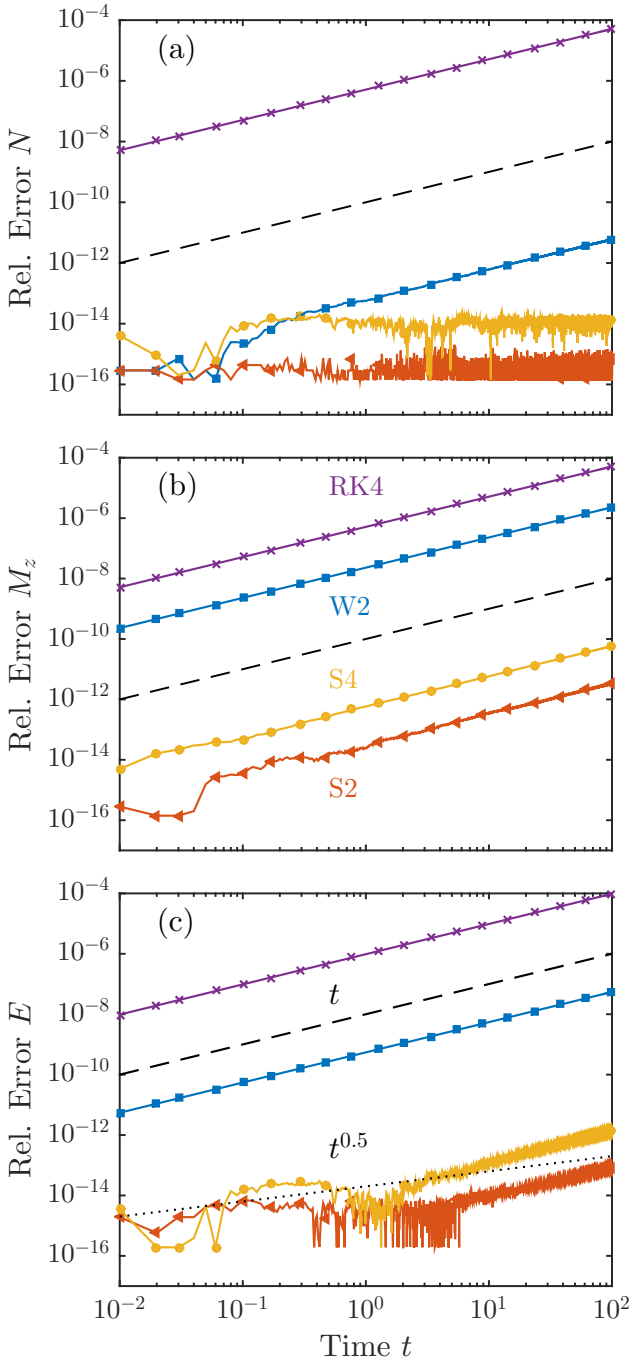

Figure 6.2: Relative errors in the conserved quantities (a) normalization, (b) magnetization and (c) energy for the propagation of the continuous wave solution. The various algorithms, as labeled in (b), all use the same time step ($\tau = 3.125 \times 10^{-4}$) and mesh ($M = 256$, $L = 2\pi$). The initial condition and other simulation parameters are given in Fig. 6.1. Dashed (dotted) line is a guide to the eye to indicate linear (square root) scaling with time t.

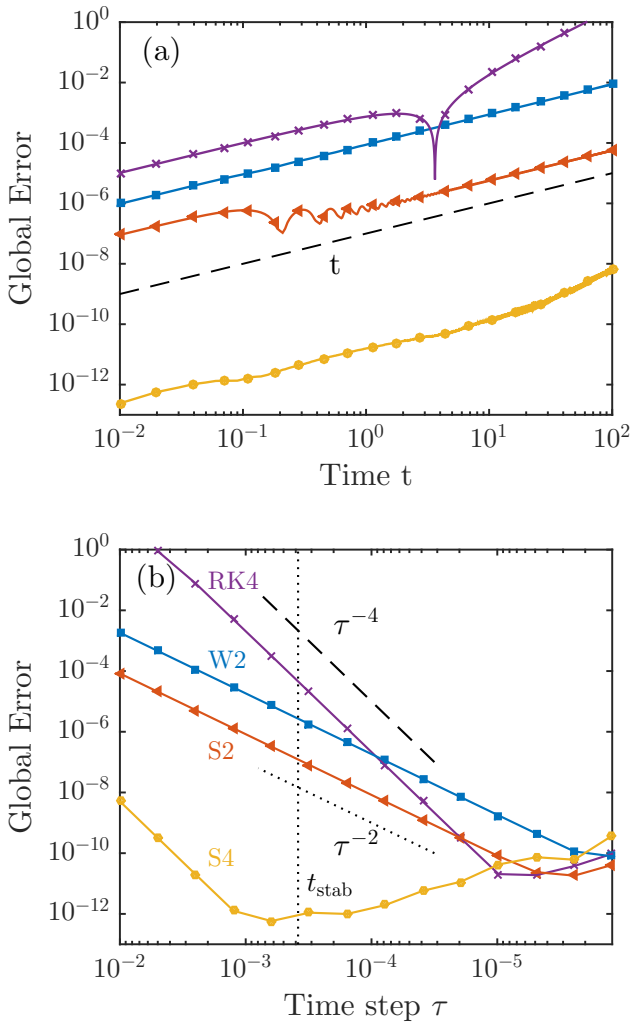

Figure 6.3: Global error in propagating the continuous wave solution. (a) Global error during a propagation using a time step of $\tau = 6.25 \times 10^{-4}$. Dashed line is a guide to the eye showing linear scaling with time t. (b) Scaling of the global error after propagation to time $t_f = 0.1$ as a function of the as function of the time step τ. The line types for the various algorithms are indicated in (b), as is the estimated stable time step size ($t_{\mathrm{stab}} = 3.8 \times 10^{-4}$). The dashed (dotted) lines in (b) indicate fourth-order (second-order) power law scaling with respect to τ. Other parameters for the solution are as indicated in Fig. 6.2.

In Fig. 6.3(b) we propogate our numerical solution for a fixed amount of time and consider the scaling of the global error with different time steps τ. These results confirm the expected second-order scaling of the global error with τ for S2 and W2, as well as the expected fourth-order scaling for RK4 and S4. For this case the prefactor on the global error for RK4 is up to 9 orders of magnitude larger than S4 depending on the choice of τ. With the S4 method the improvement in global error saturates with decreasing τ at $\tau \sim 10^{-3}$, slightly above the stability threshold, while the other methods show improvement in global error down to $\tau \sim 10^{-5}$. This is because S4 has the most function evaluations per time step and thus accumulates more roundoff errors than the other methods. We note that due to our choice of a short propagation time, the splitting instability for timesteps greater than t_{stab} does not have time to manifest and we observe the expected scaling for all the methods even when $\tau > t_{\text{stab}}$.

6.2.2 Quasi-soliton comparison

Analytic form of spinor quasi-solitons

In the experimentally relevant limit of small spin-dependent interaction, i.e. $0 < |c_1| \ll c_0$, the spin-1 system is asymptotically equivalent to the Yajima-Oikawa (YO) system, which is integrable by inverse scattering and thus has soliton solutions [130]. We simulate the collision of two such quasi-solitonic solutions using the initial conditions [given by Eqs. (37)-(38) of Ref. [130]]

$$\psi_{\pm}(x) = \sqrt{\frac{\mu}{2} - \frac{\nu}{2}[\operatorname{sech}^2(x_+) + \operatorname{sech}^2(x_-)]}\exp\left(-i\sqrt{\frac{\nu}{\mu}}[\tanh(x_+) - \tanh(x_-)]\right), \quad (6.7)$$

$$\psi_0(x) = \nu^{3/4}\sqrt{\frac{\xi}{\eta\sqrt{\mu}}}\left[\operatorname{sech}(x_+)e^{i[\sqrt{\mu/\nu}-(\xi/\nu)]x_+} + \operatorname{sech}(x_-)e^{-i[\sqrt{\mu/\nu}-(\xi/\nu)]x_-}\right], \quad (6.8)$$

where $\nu \equiv 4\eta^2\delta$, $\delta \equiv c_1/c_0$, μ is the chemical potential, η, ξ are arbitrary parameters, and $x_{\pm} = \sqrt{\nu}(x \pm x_0)$ are the initial positions of the centres of the two pulses. We take the interaction parameter ratio to be $\delta = 0.0314$ (which is close to the value expected for ^{23}Na atoms) and choose the other parameters to reproduce the collision studied in Ref. [130]. The spinor evolution during the collision is shown in Fig. 6.4 (cf. Fig. 1 of [130]). The quasi-solitons are revealed as identical density dips (dark solitons) in the ± 1 component densities at the same location that the $m = 0$ component has a density peak (bright soliton). For each quasi-soliton, the two dark solitons guide the bright soliton along. We see that under dynamical evolution the two quasi-solitons collide (at $t = 19$)

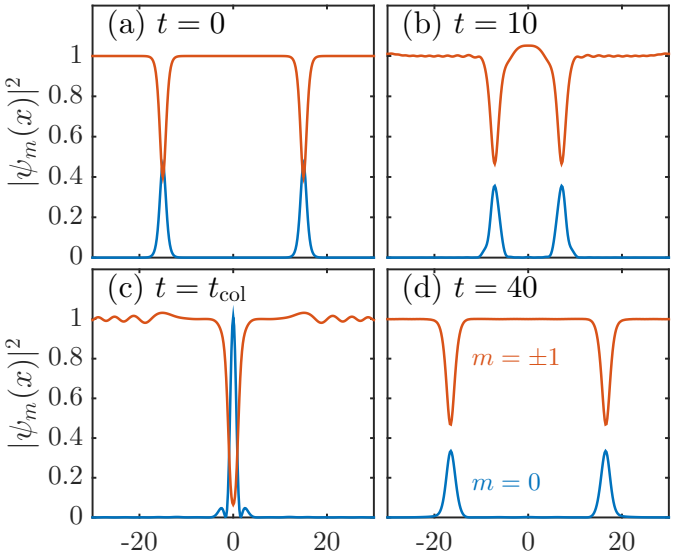

Figure 6.4: Quasi-soliton collision: (a)-(d) snapshots of dynamics showing component densities during the collision dynamics at a range of times. We define the collision time as $t_{\rm col} = 19$. These results were calculated using S4 with $\tau = 0.01$ and match the results presented in Fig. 1 of Ref. [130]. Other parameters: $L = 384$, $M = 2048$, $x_0 = 1$, $c_1 = 0.314$, $q = 0$, $\eta = 3.091$, $\xi = 1.54$, $\mu = 2$.

and then emerge, roughly keeping their shape. Because the quasi-soliton is not a true soliton some radiation is emitted during the dynamics, visible as oscillations in the background component densities. The domain of the simulation $L = 384$ is chosen to be much larger than the region of interest containing the solitons in Fig. 6.4 to ensure that this radiation does not wrap around (due to periodic boundary conditions) and return to the solitons within the duration of the simulation.

Numerical results

We compare the the various schemes for the problem shown in Fig. 6.4. First, in Fig. 6.5 we compare the relative errors in the conserved quantities N [Fig. 6.5(a)] and E [Fig. 6.5(c)]. The symplectic algorithms and W2 are seen to conserve N much better than RK4 at the step size considered in Fig. 6.5(a), with error growth behaviour like $t^{1/2}$ which is indicative of being limited by roundoff. The symplectic algorithms and W2 also show bounded error growth for E in Fig. 6.5(c). In contrast, for RK4 the error in N and E grows linearly with time. The S4 method demonstrates much better conservation of E than all other methods, with $t^{1/2}$ error growth suggesting it has reached a roundoff

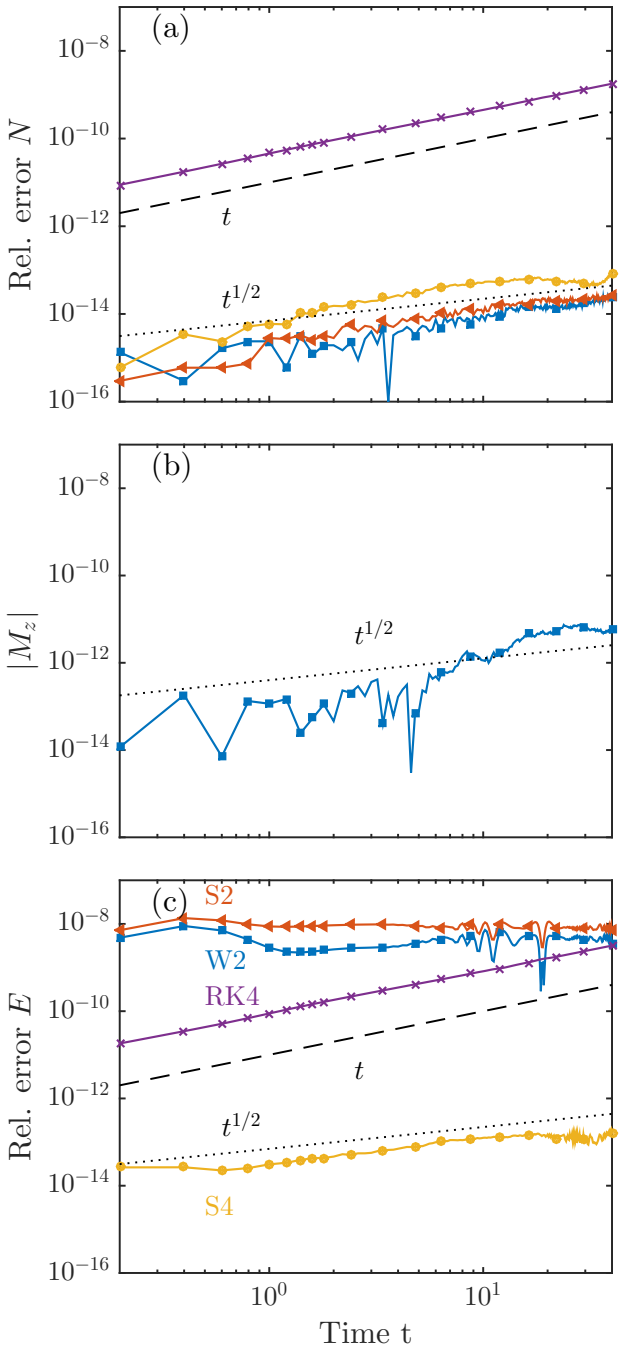

Figure 6.5: Quasi-soliton evolution: Relative errors in non-zero conserved quantities (a) N and (c) E. (b) shows the magnitude of M_z that develops in the W2 scheme, noting $|M_z|$ remains zero for the other methods. Dashed (dotted) lines are guides to the eye showing linear (square root) scaling with respect to time t. Simulations are for the scenario (initial condition, time and mesh parameters) given in Fig. 6.4.

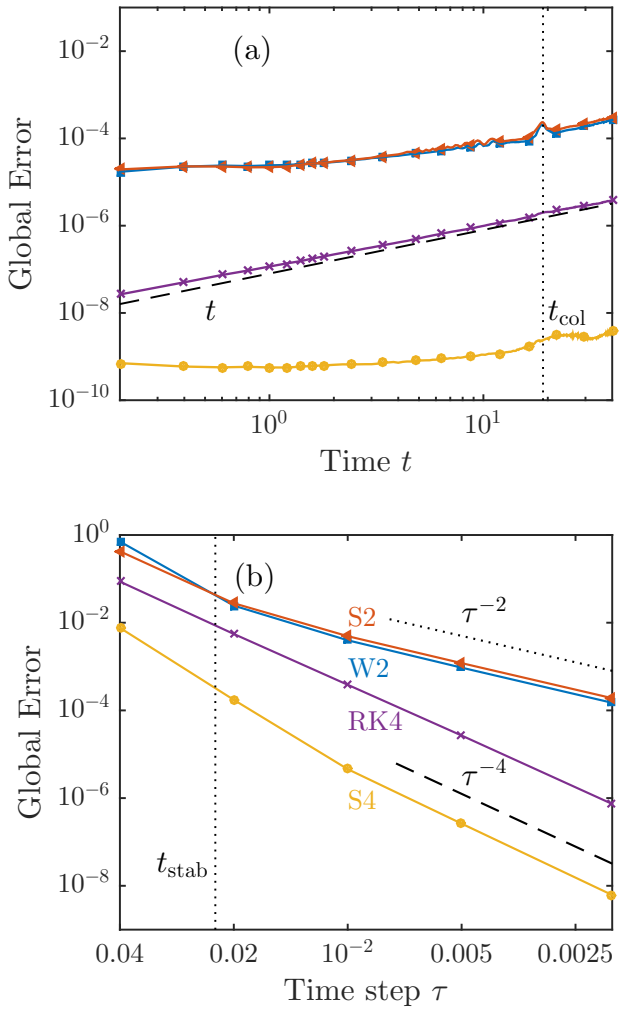

Figure 6.6: Global error in propagating the quasi-solitons using reference S4 solution with $\tau = 5 \times 10^{-4}$. (a) Global error during a propagation using a time step of $\tau = 0.02$. Dashed line is a guide to the eye that scales linearly with time t, while vertical dash-dotted line shows the time of collision of the quasi-solitons ($t_{\mathrm{col}} = 19$). (b) Scaling of the global error with time step τ of the solitons propagated to $t = 2$. Dashed (dotted) line indicates fourth-order (second-order) power law scaling with respect to τ, while vertical dash-dotted line shows the estimated stable time step size ($t_{\mathrm{stab}} = 0.022$). Simulation parameters and solution mesh are as discussed in Fig. 6.4.

limit.

The quantity M_z is zero for this soliton (since $|\psi_+|^2 = |\psi_-|^2$), thus it is not sensible to use the relative error to compare how well the methods conserve M_z. Instead in Fig. 6.5(b) we plot the absolute value of M_z for the W2 method, which is the only scheme that develops a non-zero value. This is not simply due to roundoff, which would give $t^{1/2}$ scaling, but because the W2 method uses an approximate solution to the nonlinear spin exchange terms which does not explicitly conserve F_z.

Because we do not have an exact analytic solution for the dynamics of the soliton collision we are unable to make the same global error comparison we performed for the continuous wave solutions. However, we use the S4 method with $\tau = 5 \times 10^{-4}$ to produce reference results which we compare the methods against for appreciably larger time steps. In Fig. 6.6(a) we show the scaling of the global error with time t. RK4 scales almost linearly while the symplectic methods and W2 slowly increase as they evolve to the collision at t_{col}. The results in Fig. 6.6(b) demonstrate the expected fourth-order scaling with τ for S4 and RK4, and the second-order scaling for W2 and S2. S4 is again the most accurate method by several orders of magnitude. In contrast to the Fig. 6.3(b), here RK4 is more accurate than S2 and W2 due to the fourth-order scaling having set in faster.

6.3 Spin-2 Numerical Test

6.3.1 Continuous wave solution

We test our algorithm numerically using an exact solution to the spin-2 GPE for a translationally invariant system (i.e. with $V = 0$). Since the spinor GPE is a non-integrable nonlinear partial differential equation it does not have a general solution, and for this test we have developed a continuous wave solution which has the $m = \pm 1$ levels unoccupied. The form of our solution is

$$\psi_m = A_m e^{i(k_m x - \omega_m t + \theta_m)}, \qquad m = -2, 0, 2, \tag{6.9a}$$

$$\psi_{\pm 1} = 0, \tag{6.9b}$$

where we determine the relationships between the (positive, real) amplitudes $\{A_m\}$, wave vectors $\{k_m\}$, frequencies $\{\omega_m\}$, and phase shifts $\{\theta_m\}$ for this to be a solution below. Taking the stationary limit ($k_m, \omega_m \to 0$) this ansatz approaches the so-called

cyclic ground state solution of the uniform system (e.g. see [131]). The absence of $m = \pm 1$ occupation means that our continuous wave solution has zero transverse magnetization, but it will in general have a non-zero z-magnetization and spin-singlet amplitude. Thus it is a good candidate to test evolution algorithms for the spin-2 system.

Since we only have three fields to solve for, we can follow a similar procedure to that used to obtain a spin-1 continuous wave solution in Ref. [128]. Requiring Eq. (6.9) to be a solution of the spin-1 GPE [Eqs. (4.24)–(4.26)], we find the following relationship between the quantities determining the phases of the three non-zero fields:

$$k_0 = \frac{1}{2}(k_2 + k_{-2}), \tag{6.10}$$

$$\omega_0 = \frac{1}{2}(\omega_2 + \omega_{-2}), \tag{6.11}$$

$$\theta_0 = \frac{1}{2}(\theta_2 + \theta_{-2} + \bar{n}\pi), \tag{6.12}$$

where $\bar{n}$ is an integer. Similarly, examining the magnitudes of the continuous wave solution in the GPE yields

$$\omega_0 = \tilde{\omega}_0 + (-1)^{\bar{n}} c_2 |A_{00}|, \tag{6.13}$$

$$\omega_{\pm 2} = \tilde{\omega}_{\pm 2} + c_2 |A_{00}| \frac{A_{\mp 2}}{A_{\pm 2}} + 4q, \tag{6.14}$$

where

$$\tilde{\omega}_m = \frac{1}{2}k_m^2 + c_0(A_2^2 + A_0^2 + A_{-2}^2) + c_1 m(A_2^2 - A_{-2}^2), \tag{6.15}$$

and

$$|A_{00}| = \frac{1}{5}[(-1)^{\bar{n}} A_0^2 + 2A_2 A_{-2}]. \tag{6.16}$$

Asserting Eq. (6.11), we get

$$A_0^2 = (-1)^{\bar{n}+1} 2A_2 A_{-2} \left(1 + \frac{(k_2 - k_{-2})^2/8 + 4q}{c_2(A_2 - (-1)^{\bar{n}} A_{-2})^2}\right). \tag{6.17}$$

Thus we can set $A_{\pm 2}$, $k_{\pm 2}$, c_2, q, and $\bar{n}$, subject to the consistency requirement that A_0 is real and non-negative, and this determines A_0, k_0, θ_0, and $\omega_{\pm 2,0}$. We note that since the amplitudes $\{A_m\}$ are conserved, the total density, z spin-density and $|A_{00}|$ are all conserved quantities of the solution.

6.3.2 Results

Here we compare the algorithm we have described in this work to two other approaches to solving the spin-2 GPE. In particular, we use both our second-order (S2) and fourth-order (S4) symplectic algorithms, obtained by composing the exact solutions we have developed using the schemes described in Section 5.2. For comparison we have implemented the algorithm developed by Wang [114] (W2) which is second-order accurate in time. We also consider a fourth-order accurate method based on the Runge-Kutta method which we denote as (RK4). This type of method is quite commonly used for simulating condensate dynamics and is easily extended to the spinor case. We note that in implementing this algorithm we have utilized the *interaction picture* technique (e.g. see [115]) to exponentiate the kinetic energy term and improve the algorithm performance. We observe that for the test problems our implementation of W2 performs about an order of magnitude slower than S2 due to requiring a numerical diagonalization at each mesh point. The other algorithms performance, relative to S2, is similar to the behaviour seen in Ref. [132].

As a first test we simulate the evolution of a continuous wave solution from $t = 0$ to $t = 100$ and monitor changes in conserved quantities to quantify algorithm accuracy. We assume periodic spatial boundary conditions, allowing us to implement the kinetic energy operator using Fast-Fourier transforms for all methods. We have chosen parameters for a continuous wave solution (see Fig. 6.7) that result in a stable solution with no modulational instability over the time-scales we have considered. To quantify the changes in conserved quantities we compute the maximum relative error in conserved quantities at each time step, i.e.

$$\text{Rel. Error } Q \equiv \left| \frac{Q(t) - Q(0)}{Q(0)} \right|, \tag{6.18}$$

where $Q \in \{N, M_z, E\}$ are the three conserved quantities we consider (which we discussed in Section 4.2) and $Q(t)$ indicates the quantity evaluated at time t during the propagation.

Generally the results in Fig. 6.8 show that the symplectic algorithms (i.e. S2 and S4) and the W2 algorithm outperform the RK4 algorithm at conserving the constants of motion. This is expected since symplectic algorithms preserve the geometric properties of phase space. The energy and z-magnetization are more accurately conserved with the S2 and S4 algorithms than the W2 algorithm. We note that our formulation of the nonlinear subsystem solution in Eq. (4.68) exactly conserves z-magnetization. Indeed, S2 and

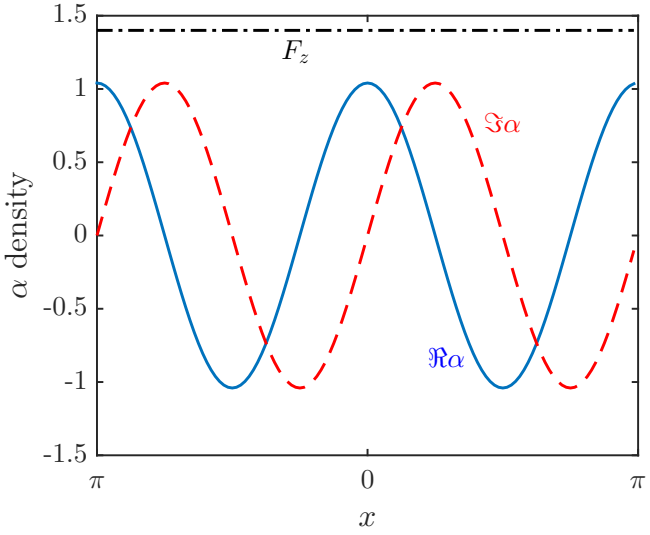

Figure 6.7: The continuous wave solution we use to test our numerics at $t = 0$. The magnetization density (dash-dot line), and the real (solid line) and imaginary (dashed line) parts of the singlet amplitude. Parameters of the solution are $c_0 = 10|c_2|$, $c_1 = 4|c_2|$, $c_2 = -5$, $q = 0$, $\bar{n} = 0$, $k_2 = 3$, $k_{-2} = -1$, $A_2 = 0.85$, $A_{-2} = 0.15$.

S4 initially exhibit $t^{1/2}$ scaling in the z-magnetization error, indicating this is limited only by roundoff, until a linear error begins to dominate. The energy error remains bounded for S2 which is a signature of symplectic methods (e.g. see [109]). In contrast, the W2 method only approximately treats the nonlinear spin exchange terms so is not symplectic, and this is reflected in the linear growth in error and z-magnetization. As a symplectic method, S4 should have bounded energy errors, but here it accumulates a linear error at each time step which is greater than the oscillatory component.

As a second test we can look more closely at the evolution of the spinor field. Because we know the exact continuous wave solution we can quantify the maximum global error at each time step, which we define as

$$\text{Global Error} \equiv \max_{x_j,m} |\psi_m^{\text{num}}(x_j,t) - \psi_m(x_j,t)|\,, \tag{6.19}$$

where ψ_m^{num} denotes the numerically obtained solution, and ψ_m is the exact solution [Eqs. (6.9)]. In Fig. 6.9(a) we show the growth of the global error over time for a propagation of fixed time step $\tau = 0.05$, i.e. the same propagation examined in Fig. 6.8. The global error shows that S4 is the best at approximating the exact analytic solution by more than four orders of magnitude, with S2 very similar to W2, and all of these are better than RK4. Global error grows linearly for all methods until $t \sim 1$ [i.e. the time

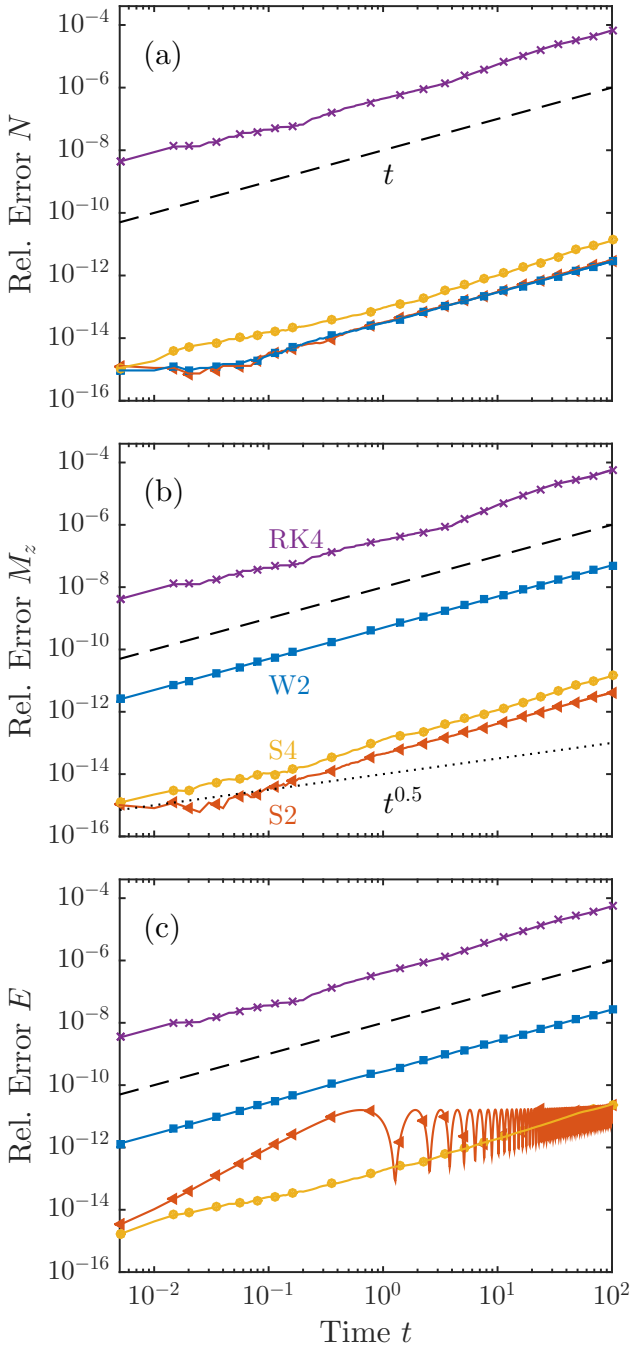

Figure 6.8: Relative errors in the conserved quantities (a) normalization, (b) magnetization and (c) energy for the propagation of the continuous wave solution. The various algorithms, as labeled in (b), all use the same time step ($\tau = 0.005$) and mesh $\{x_j\}$ of 64 points over the spatial interval $[-\pi, \pi)$. The initial condition parameters are given in Fig. 6.7. Dashed (dotted) line is a guide to the eye to indicate linear (square root) scaling with time t.

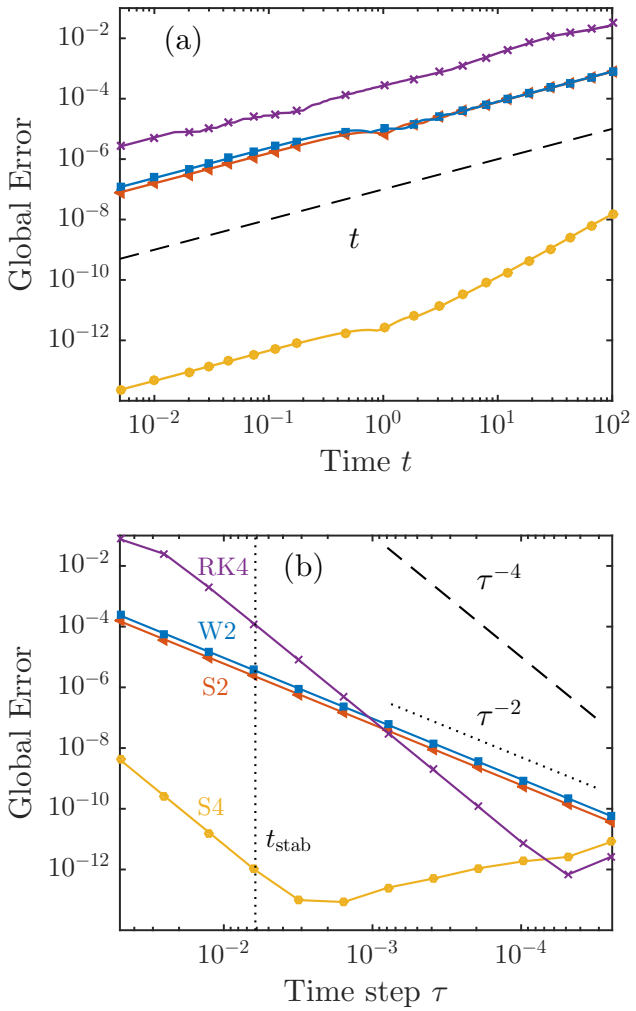

Figure 6.9: Global error in propagating the continuous wave solution. (a) Global error during a propagation using a time step of $\tau = 0.005$. Dashed line is a guide to the eye showing linear scaling with time t. (b) Scaling of the global error after propagation to time $t_f = 0.1$ as a function of the time step τ. The line types for the various algorithms are indicated in (b), as is the estimated stable time step size ($t_{\mathrm{stab}} = 0.006$) due to using a spectral solution for $\hat{f}_A$ [127]. The dashed (dotted) lines in (b) indicate fourth-order (second-order) power law scaling with respect to τ. Other parameters for the solution, and mesh, are as indicated in Fig. 6.8.

when the energy error starts oscillating for S2 in Fig. 6.8(c)]. At this point S4 starts having faster than linear error growth, while the other methods continue with linear growth.

In Fig. 6.9(b) we propagate our numerical solution for a fixed amount of time and consider the scaling of the global error with different time steps τ. These results confirm the expected second-order scaling of the global error with τ for S2 and W2, as well as the expected fourth-order scaling for RK4 and S4. For this case the prefactor on the global error for RK4 is up to 8 orders of magnitude larger than S4 depending on the choice of τ. With the S4 method the improvement in global error saturates with decreasing τ at $\tau \sim 10^{-3}$, below the stability threshold, while the other methods show improvement in global error down to $\tau < 10^{-4}$. This is because S4 has the most function evaluations per time step and thus accumulates more roundoff errors than the other methods. In our simulations we tried using denser spatial grids and this led to faster accumulation of floating point errors for both composition methods but especially for S4. We note that due to our choice of a short propagation time, the splitting instability for timesteps greater than t_{stab} does not have time to manifest and we observe the expected scaling for all the methods even when $\tau > t_{\text{stab}}$.

Part III

Nematic quenches with phase-ordering dynamics

Chapter 7

Spin-1 Antiferromagnetic quench

7.1 Introduction

As we have shown in Chapters 2 and 3, the spin-1 system with antiferromagnetic interactions exhibits quadrupolar nematic order. The concept of nematic order is typically discussed in the context of liquid crystals, where the order is associated with the orientation of long molecules. Indeed, many beautiful studies of phase transition dynamics and coarsening have been performed in liquid crystal systems (e.g. see [133–139]). A sudden change in conditions (e.g. temperature or pressure) is used to quench this system from an isotropic phase (unoriented molecules) into the nematic phase, and the formation of order and defect dynamics can be observed optically.

In this Chapter, we develop a theory for the ordering dynamics (coarsening) of an antiferromagnetic spin-1 condensate. Our interest is in the symmetry breaking phase transition from an EA phase (with nematic alignment along the direction set by the external magnetic field) at positive quadratic Zeeman energy q, to an EP phase (nematic alignment transverse to the external field) at negative q (see Chapter 3 especially Fig. 3.2(d) and Refs. [59–61, 140, 141]). We consider a quench between these phases implemented by a sudden change in q, e.g. using microwave dressing (see [59, 61, 141]). Upon entering this new phase, the system breaks the continuous axial symmetry of the initial state by developing transverse spin-nematic domains. Here our interest lies in

characterizing the dynamics of the phase transition, with a particular emphasize on the late-time coarsening dynamics. That is, to understand the universal aspects of how small domains created after the quench anneal together to bring the system towards an ordered equilibrium state.

Using our formalism from Chapters 2 and 3, we develop an appropriate order parameter for the EP phase. Using numerical simulations we study how the EP order forms in the system. We demonstrate that the late-time coarsening behaviour exhibits dynamical scaling with a diffusive domain growth law of $L(t) \sim [t/\ln(t)]^{1/2}$, where L is the size of the ordered domains and t is the time after the quench. We separately consider the superfluid order and show that it grows with an identical law to the spin-nematic order, in contrast to recent results for the ferromagnetic spin-1 system [66].

The order parameter growth is determined by the dynamics of half-quantum vortices (HQVs) in the system, and we verify that the number of these vortices scales as $L(t)^{-2}$, i.e. that coarsening proceeds by vortex anti-vortex pairs mutually annihilating. Recent experiments have demonstrated that it is possible to measure HQVs in antiferromagnetic spin-1 condensates [62, 63] due to their ferromagnetic cores [142]. Thus, measuring the HQV distribution as a function of time after the quench could be a practical method for experiments to quantify the coarsening of this system. Alternatively, it may be possible to directly image [143, 144] or probe [145] nematic properties of the condensate.

We note that the symmetries and defects of the EP phase are similar to those of a (two-component) binary condensate in the miscible regime. Indeed, work by Karl *et al.* [146] discussed the role of the equivalent vortices in the ordering dynamics of a two-component system, although that work focused on understanding the emergence of power-law behavior in various momentum correlation functions, and relating these to turbulence cascades.

7.2 Phase ordering dynamics (coarsening)

Here we give a brief overview of the idea of phase ordering dynamics, also know as coarsening. These dynamics arise when an initially isotropic system is quenched across a phase boundary to a broken symmetry phase [148, 149].

Dynamic instabilities arise due to the initial state no longer being the ground state of the system. These instabilities cause the system to develop spatial domains of an

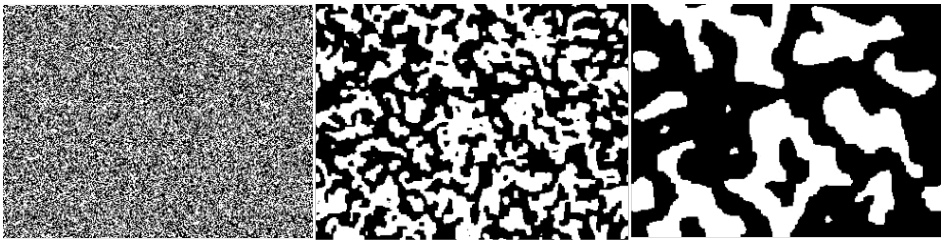

Figure 7.1: Coarsening of up and down (black and white) spin domains in the Ising model, reproduced from Ref. [147].. An initially isotropic phase (left) develops spin domains (middle) which then grow over time in a scale-invariant way (right).

order parameter sensitive to the new ground state, with each domain spontaneously breaking the initial symmetry in random directions (phases) throughout space. The domains then grow larger over time through phase ordering dynamics as they compete to become the global equilibrium ground state.

This coarsening of domains, where the size of the average domain $L(t)$ grows with time, can enter a universal regime for certain systems. In the universal coarsening regime, the domain size is the largest length scale of the system, and the exact microscopic details no longer affect the dynamics. Here the correlations of the order parameter become universal, i.e. scale independent when rescaled by $L(t)$. Domains then grow as $L(t) \sim t^{1/z}$, where z is a universal scaling exponent that depends on the universality class of the system. For example, if $\phi(\mathbf{r}, t)$ is the order parameter at time t after the quench, then the correlation function $G(\mathbf{r}, t) = \langle \phi(\mathbf{r}, t)\phi(0, t) \rangle$ becomes time independent when scaled by $L(t)$, i.e. $H(\mathbf{r}) \equiv G(\mathbf{r}/L(t), t)$ is a time-independent universal function. This self-similar behaviour of phase ordering systems is known as the dynamic scaling hypothesis.

The classic example of coarsening is the Ising model. In this classical spin-1/2 system, an initial isotropic mixture of up and down spins is quenched below the transition temperature to the ordered phase. Domains of up and down spin form and grow over time in a scale invariant way. We show examples of the states of an Ising system at various stages of a quench in Fig. 7.1.

The universality class of the system only depends on the nature of the order parameter for the new ground state and various aspects of the system such as transport mechanisms, not the microscopic interaction strengths. For example, the exponent z that emerges for the Ising model depends on the dynamics of the system. If the order parameter

(z-magnetization) is non-conserved (i.e. spins are free to flip), then $z = 2$, i.e. the order grows diffusively. On the other hand, if the it is conserved then the spin has to be transported through the system to allow domains to grow, slowing down the dynamics and leading to a growth law with $z = 3$.

To analyze coarsening it is paramount to use an appropriate order parameter that is zero in the initial isotropic ground state and sensitive to the broken symmetry of the new ground state. In this Chapter, we investigate a quench between antiferromagnetic phases in the spin-1 system, which requires us to develop a nematic order parameter sensitive to this broken symmetry.

7.3 The antiferromagnetic quench

We are concerned with an antiferromagnetic spin-1 condensate in which a quench is performed by a sudden change in the quadratic Zeeman energy from a positive value to a negative value[1] crossing a quantum phase transition between two different ground states [see Fig. 3.2(d)]. From the formalism developed in Chapter 3, we have that the antiferromagnetic ground state is fully polar $\vec{\psi} = e^{i\theta}\vec{u}$. For $q > 0$ the director ($\vec{u}$) is along the z axis [EA phase, see Fig. 3.2(c)]. For $q < 0$ the director lies in the xy-plane [EP phase, see Fig. 3.2(b)]. Thus the EP phase breaks the axial symmetry (invariance to spin rotations about z) of the Hamiltonian. This type of quench in an antiferromagnetic spinor condensate of ^{23}Na atoms has been performed in a number of experiments [59–61, 141, 150], however the EP nematic order was not directly probed in these studies (c.f. [57]). We also note that other phase transitions can be considered in this system, e.g. Witkowska *et al.* [151] considered a q quench for an antiferromagnetic condensate with a non-zero (conserved) z-magnetization, where a transition to a phase separated state occurs.

7.3.1 Nematic order parameter

We would like to obtain an order parameter that can distinguish between these two states, notably the order parameter should be zero in the EA phase and non-zero in the EP phase. To do this we note that in the EA phase the quadrupole nematic tensor $\mathcal{T}^{(2)}$

[1] The z-magnetization $M_z \equiv \int d^2\mathbf{x}\, F_z$ of the system is conserved, and here we focus on the case $M_z = 0$ where the transition occurs at $q = 0$.

(defined in Section 2.4.1) is isotropic in the xy-plane [see Fig. 3.2(c)], while in the EP phase the nematic tensor is anisotropic in the xy-plane [see Fig. 3.2(b)]. To quantify the EP nematic order, and taking motivation from nematic liquid crystals [152], we use a traceless symmetric tensor to quantify order in this system. Particular to the EA to EP phase transition we use the planar tensor:

$$\mathcal{Q} = \mathcal{S}_{2\times 2} - \tfrac{1}{2}\mathrm{Tr}\{\mathcal{S}_{2\times 2}\} I_2, \tag{7.1}$$

$$= \begin{pmatrix} \mathcal{Q}_{xx} & \mathcal{Q}_{xy} \\ \mathcal{Q}_{xy} & -\mathcal{Q}_{xx} \end{pmatrix}, \tag{7.2}$$

where $\mathcal{S}_{2\times 2}$ is the xy-submatrix of $\mathcal{S}^{(2)}$ (the symmetric quadrupole tensor, see Sections 2.4 and 2.4.1), and I_2 is the identity matrix. Evaluating this expression we find that $\mathcal{Q}_{xx} = \mathrm{Re}\{\psi_1^*\psi_{-1}\}$ and $\mathcal{Q}_{xy} = \mathrm{Im}\{\psi_1^*\psi_{-1}\}$, i.e. it depends on the relative phase coherence between the ψ_1 and ψ_{-1} components of the system. While $\mathcal{Q}$ is traceless by construction, $\mathrm{Tr}(\mathcal{Q}^2) = 0$ only when the spin fluctuations are isotropic in the xy-plane. The EP phase is thus revealed by $\mathrm{Tr}(\mathcal{Q}^2)$ becoming non-zero, thus demonstrating how $\mathcal{Q}$ serves as an order parameter. We can write the eigenvalues of $\mathcal{Q}$ as $\{-\frac{1}{2}\mathcal{A}_\perp, \frac{1}{2}\mathcal{A}_\perp\}$, where we have defined a "transverse alignment" parameter[2] [c.f. the full alignment parameter $\mathcal{A}$ given in Eqs. (3.24) and (3.25)]

$$\mathcal{A}_\perp = |\alpha_\perp|, \tag{7.3}$$

and have introduced the perpendicular spin-singlet amplitude [c.f. Eq. (3.26)]

$$\alpha_\perp \equiv -2\psi_1\psi_{-1}. \tag{7.4}$$

Using this result gives $\mathrm{Tr}(\mathcal{Q}^2) = \frac{1}{2}\mathcal{A}_\perp^2$. If we consider the general EP polar phase given in Eq. (3.33), we have

$$\psi_{\mathrm{EP}} = \sqrt{\frac{n_c}{2}} e^{i\theta} \begin{pmatrix} -e^{-i\phi} \\ 0 \\ e^{i\phi} \end{pmatrix}, \tag{7.5}$$

where the angle ϕ is associated with the spin-nematic order [i.e. $\vec{u} \propto \cos\phi\,\hat{\mathbf{x}} + \sin\phi\,\hat{\mathbf{y}}$], and the global phase θ is associated with the superfluid order. Calculating $\mathcal{Q}$ and $\alpha_\perp$

[2] $\mathcal{A}_\perp$ is sensitive to anisotropy of $\mathcal{Q}$, but does not completely distinguish between polar and ferromagnetic states as does $\mathcal{A}$. E.g., the fully ferromagnetic state with $\mathbf{F} = n\hat{\mathbf{x}}$ has $\mathcal{A} = 0$, but $\mathcal{A}_\perp = \frac{1}{2}n$ (c.f. the pure EP polar state with $\vec{u} = \sqrt{n}\hat{\mathbf{x}}$ for which $\mathcal{A} = \mathcal{A}_\perp = n$). As is apparent from Fig. 3.2(a) a state with $\mathbf{F} \neq 0$ also has an anisotropic nematic tensor, just to a lesser extent than a polar state.

for ψ_{EP}, we find that

$$\mathcal{Q}_{xx} = -\frac{n_c}{2}\cos(2\phi), \tag{7.6}$$

$$\mathcal{Q}_{xy} = -\frac{n_c}{2}\sin(2\phi), \tag{7.7}$$

$$\alpha_\perp = n_c e^{2i\theta}. \tag{7.8}$$

This shows that the nematic order parameter $\mathcal{Q}$ is sensitive to the spin phase ϕ, while $\alpha_\perp$ is an order parameter that is sensitive to the global phase θ. In Appendix D we present an alternative Cartesian derivation of these results.

7.4 Simulation results

7.4.1 Quasi-two-dimensional quench

In order to explore the quench dynamics we focus on a quasi-2D system. In this regime the extent of the condensate in one direction (which we take to be z) is less than the spin healing length, so spin motion is effectively frozen out in this direction. This regime has been realized in experiments by applying a tight optical trap in this direction (e.g. see [52, 62]). Additionally, we neglect any transverse confinement and take the condensate to be homogeneous in the plane. The dynamics of this system is described by the spin-1 Gross-Pitaevskii equation (GPE)

$$i\hbar\frac{\partial\psi}{\partial t} = \left(-\frac{\hbar^2\nabla^2}{2M} + q\mathrm{f}_z^2 + c_0 n + c_1 \boldsymbol{F}\cdot\boldsymbol{f}\right)\psi. \tag{7.9}$$

Note we have neglected the linear Zeeman shift which can be removed from the equation of motion by transforming to a rotating frame.

To numerically solve this equation, we introduce the characteristic spin energy $q_0 \equiv 2c_1 n_c$, and associated spin healing length $\xi_s = \hbar/\sqrt{Mq_0}$ and spin time $t_s = \hbar/q_0$ as convenient units. We represent each component of the spinor field ψ on a 2D square region of dimensions $l \times l$ covered by an $N \times N$ grid of equally spaced points. We use a spatial resolution of 1.28 grid points per spin healing length in order to resolve spin dynamics while remaining coarse enough to observe the growth of large domains. Taking periodic boundary conditions for the solution, we evaluate spatial derivatives in the kinetic energy term of Eq. (7.9) with spectral accuracy using fast Fourier transforms. To evolve the GPE in time we use the second order symplectic method S2 presented in Chapter 5.

We use a time step of $\Delta t = 0.1$, where the maximum stable time step according to Eq. (6.1) is $(\Delta t)_{max} = 0.37$.

The initial condition for the simulations is a uniform EA ground state [in the spherical basis, see Eq. (3.32)]

$$\psi(\mathbf{x}, t = 0) = \sqrt{n_c} \begin{pmatrix} 0 \\ 1 \\ 0 \end{pmatrix} + \boldsymbol{\delta}(\mathbf{x}), \tag{7.10}$$

where n_c is the condensate (areal) density and $\boldsymbol{\delta}$ is a small noise field added to seed the growth of unstable modes following the quench. The late-time results are insensitive to the form of white spatial noise we add to the initial state as long as the noise is weak ($|\boldsymbol{\delta}|^2 \ll n_c$). We choose to add noise according to the truncated Wigner prescription [153], which is consistent with the quantum vacuum noise on the initial state. Thus we set the noise field to be

$$\boldsymbol{\delta}(\boldsymbol{x}) = \sum_{\boldsymbol{k}} \begin{pmatrix} \alpha^{+}_{\boldsymbol{k}} e^{i\boldsymbol{k}\cdot\boldsymbol{x}} \\ \alpha^{0}_{\boldsymbol{k}} u_k e^{i\boldsymbol{k}\cdot\boldsymbol{x}} - \alpha^{0*}_{\boldsymbol{k}} v_k e^{-i\boldsymbol{k}\cdot\boldsymbol{x}} \\ \alpha^{-}_{\boldsymbol{k}} e^{i\boldsymbol{k}\cdot\boldsymbol{x}} \end{pmatrix}, \tag{7.11}$$

where the $\{\alpha^{m}_{\boldsymbol{k}}\}$ are independent complex Gaussian random variables with

$$\langle \alpha^{m'*}_{\boldsymbol{k}'} \alpha^{m}_{\boldsymbol{k}} \rangle = \frac{1}{2} \delta_{mm'} \delta_{\boldsymbol{k}'\boldsymbol{k}}, \tag{7.12}$$

and we set $\alpha^{0}_{\boldsymbol{0}} = 0$ to omit adding noise to the condensate mode. The $\{u_k, v_k\}$ are Bogoliubov amplitudes given by

$$u_k = \sqrt{\frac{\epsilon_k + c_0 n_0}{2\sqrt{\epsilon_k\left(\epsilon_k + 2c_0 n_0\right)}} - \frac{1}{2}}, \quad v_k = \sqrt{u_k^2 - 1}, \tag{7.13}$$

with $\epsilon_k = \hbar^2 k^2 / 2M$. The noise added this way corresponds to adding a half-quantum of occupation to the Bogoliubov modes for the EA polar state at large q [154].

7.4.2 Early-time dynamics: development of local order

Immediately following the quench the initial EA state is unstable and begins to evolve towards the new phase. Aspects of these early time dynamics, and the emergence of

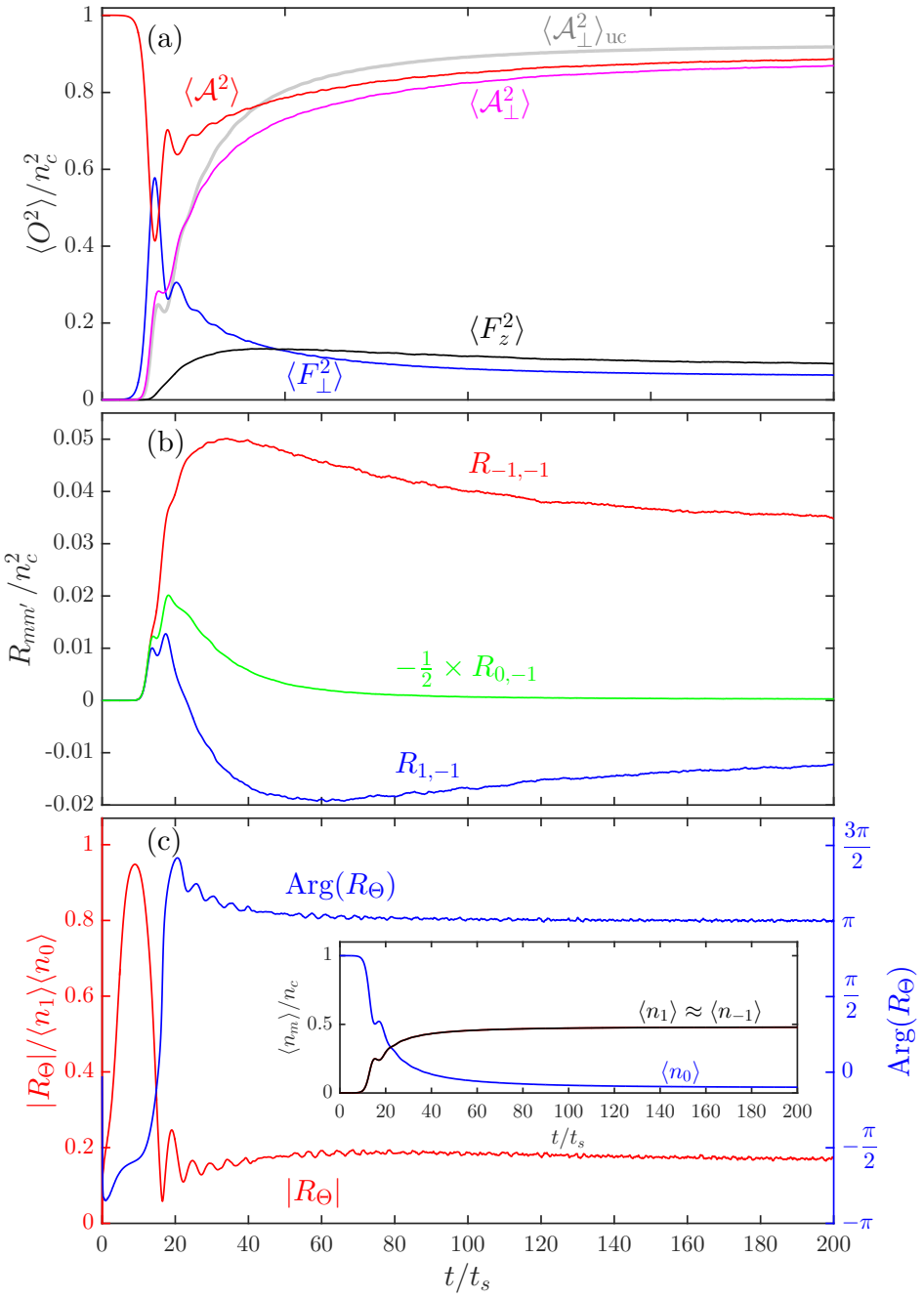

Figure 7.2: Growth of densities, local pair correlations and R_Θ following a quench from the EA to EP phase. (a) The local densities $O = \{n, \mathcal{A}, \mathcal{A}_\perp, \mathbf{F}\}$ are evaluated from the results of a single simulation trajectory according to Eq. (7.14). (b) The local pair correlations functions, as defined in Eq. (7.15). (c) The relative phase correlation function R_Θ as defined in the Eq. (7.17). Inset: The evolutions of the mean component densities, noting that the $m = \pm 1$ results are approximately identical. Simulation is for a quench to $q = -0.5q_0$ with $c_0 = 3c_1$. The simulation is for a condensate density $n_c = 10^4/\xi_s^2$ of size $l = 400\,\xi_s$ with $N = 512$ points in each direction.

local EP order can be revealed by studying the behaviour of the spin and alignment densities. Since some of these densities (e.g. F_z) can be locally negative, we quantify the development of a particular density of interest O by spatially averaging O^2, i.e. we evaluate

$$\langle O^2(t)\rangle = \frac{1}{l^2}\int d^2\mathbf{x}\, O^2(\mathbf{x},t). \tag{7.14}$$

We present results for a variety of densities of interest in Fig. 7.2(a). These results show that immediately following the quench the EA state becomes dynamically unstable to magnon excitations which grow exponentially and cause the system to develop transverse magnetization [i.e. $\mathbf{F}_\perp = (F_x, F_y)$]. The precise nature of the instability and the wavevectors of the unstable modes depends upon the value of q, and aspects of this have already been explored in experiments [59–61, 150]. The axial magnetization (F_z) similarly experiences exponential growth. The general behavior of spin density growth we observe is similar for quenched condensates with ferromagnetic interactions (e.g. see [34, 154–156]). Noting that the average z-magnetization of the initial state is zero (and conserved), the quantity $\langle F_z^2(t)\rangle$ corresponds to the fluctuations in magnetization studied in recent experiments [150].

More direct insight into the change in nematic order is provided by the alignment densities $\{\mathcal{A}, \mathcal{A}_\perp\}$ discussed in Sections 3.1.3 and 7.3.1. The initial EA state is fully aligned (i.e. $\mathcal{A} = n_c$), but this dips down in the early dynamics as the magnetization develops [as required by the relation (3.29)]. As the alignment is restored for $t \gtrsim 20\, t_s$ it is of a different character, consistent with EP order emerging. We see this by evaluating the transverse alignment $\mathcal{A}_\perp$ order which is initially negligible, but then grows and is seen to saturate towards the value of $\mathcal{A}$.

Various *in situ* measurements of correlations between components of the density have been performed in spinor condensate experiments (e.g. see [61, 63, 150, 157]). Most relevant to our system are the measurements of Vinit *et al.* [61] of the time evolution of the local pair correlation function following the EA to EP quench of a quasi-one-dimensional antiferromagnetic condensate. The correlation functions measured were[3]

$$R_{mm'}(t) = \langle \delta n_m \delta n_{m'}\rangle, \tag{7.15}$$

where $\delta n_m(\mathbf{x},t) = n_m(\mathbf{x},t) - \langle n_m\rangle$ is the m-component density fluctuation operator, with $n_m = |\psi_m|^2$ and $\langle n_m\rangle$ being the mean density of this component. We have evaluated

[3]Here and for the remainder of this subsection all expectations will be taken to be spatially averaged as in Eq. (7.14).

the same correlation functions measured in experiments (c.f. Fig. 3 of Ref. [61]) and present the results in Fig. 7.2(b). We find similar qualitative behavior to their results, however note that their measurements were for a shallow quench (to $q \approx -0.02q_0$) and with appreciable thermal effects. These same types of local density measurements could be used to evaluate the alignment densities. Indeed, noting that $\langle \mathcal{A}_\perp^2 \rangle = 4\langle n_1 n_{-1} \rangle$ [see Eqs. (7.3) and (7.4)] , taking n_1 and n_{-1} as uncorrelated, we can make the estimate

$$\langle \mathcal{A}_\perp^2 \rangle_{\rm uc} \approx 4\langle n_1 \rangle \langle n_{-1} \rangle. \tag{7.16}$$

For the uniform system $\langle n_m \rangle = N_m/l^2$, and thus $\langle \mathcal{A}_\perp^2 \rangle_{\rm uc}$ is determined by the component populations $N_m = \int d^2\mathbf{x}\, n_m$, which are readily measured in experiments. As can be seen from Fig. 7.2(a) the uncorrelated approximation tends to overestimate the EP order ($\langle \mathcal{A}_\perp^2 \rangle$) once it develops ($t \gtrsim 20\, t_s$). Noting that $\langle n_1 n_{-1} \rangle = \langle n_1 \rangle \langle n_{-1} \rangle + R_{1,-1}$, this overestimate of Eq. (7.16) is due to the negative value $R_{1,-1}$ takes for $t \gtrsim 20\, t_s$ [Fig. 7.2(b)]. Evidence for $R_{1,-1}$ becoming negative was also found in experiments at late times [61].

Finally we examine the system evolution to quantify the local "phase locking" of the $m = \pm 1$ components relative to the $m = 0$ component. This was recently observed in experiments by applying a spin rotation to the system and measuring the resulting magnetic fluctuations [57]. In our simulations we can directly access this from the local (spatially averaged) correlation function

$$R_\Theta(t) \equiv \langle \psi_{-1} \psi_1 \psi_0^* \psi_0^* \rangle \,. \tag{7.17}$$

Taking $\psi_m = \sqrt{n_m} e^{i\theta_m}$, we see that $R_\Theta \sim e^{i(\theta_1 + \theta_{-1} - 2\theta_0)}$, which conventionally defines the relative phase $\Theta \equiv \theta_1 + \theta_{-1} - 2\theta_0$. To understand the physical relevance of this correlation function, we note that the transverse spin density squared and the alignment density squared are

$$\langle |F_\perp|^2 \rangle = 2\langle n_0 (n_{-1} + n_1) \rangle + 4{\rm Re}\{R_\Theta\}, \tag{7.18}$$

$$\langle \mathcal{A}^2 \rangle = \langle n_0^2 \rangle + 4\langle n_1 n_{-1} \rangle - 4{\rm Re}\{R_\Theta\}, \tag{7.19}$$

respectively. Thus varying the real part of R_Θ the system can enhance or reduce the spin density, while having the opposite effect on the alignment [also see Eq. (3.29)]. Antiferromagnetic systems prefer $\Theta = \pi$ to reduce the spin-density. The behaviour of R_Θ is shown in Fig. 7.2(c), noting that we have normalized R_Θ by the average densities of each component [using $\langle n_{-1} \rangle \approx \langle n_1 \rangle$, also see inset to Fig. 7.2(c)] so that

the magnitude measures the concentration of Θ. These results show that after the early dynamics settles down ($t \gtrsim 25t_s$) the function R_Θ approaches a negative real value, i.e. $\Theta \to \pi$. The $m = 0$ component is unoccupied in the EP ground state, but maintains a small population [see inset to Fig. 7.2(c)] at late times due to heating from the quench. The $m = 0$ component of the system is noisy (consistent with a thermalized gas, e.g. see [64]) and the amplitude of the R_Θ correlation function is significantly reduced by these fluctuations. However, our results show that there is still a tendency for the spin-dependent interactions to lock the relative phase of the $m = \pm 1$ components relative to the $m = 0$ component.

7.4.3 Late-time Universal coarsening dynamics

In addition to considering the emergence of local spin-nematic order we wish to examine the spatial dependence of the textures (domains) that develop and how these evolve in time. In Fig. 7.3 we visualize the system order in a region of a simulation soon after local order is established [Fig. 7.3(a)] and at a later time [Fig. 7.3(b)]. This visualization is performed by decomposing the spinor field at each simulation point according to Eq. (3.19) to obtain $\vec{u}(\mathbf{x})$ and $\theta(\mathbf{x})$. The results in Fig. 7.3 demonstrate that the spin-nematic and superfluid (i.e. global phase θ) order tends to extend over larger length scales as time passes, showing that the system is coarsening toward an EP state with (quasi)-long range order.

To quantify the spatial dependence of the ordering we introduce the correlation functions

$$G_\phi(\mathbf{r}, t) = \frac{2}{n_c^2} \langle \mathrm{Tr}\, \{\mathcal{Q}(\mathbf{0})\mathcal{Q}(\mathbf{r})\} \rangle_t \,, \tag{7.20}$$

$$G_\theta(\mathbf{r}, t) = \frac{1}{n_c^2} \langle \alpha_\perp^*(\mathbf{0})\alpha_\perp(\mathbf{r}) \rangle_t \,, \tag{7.21}$$

for the spin-nematic and superfluid orders, respectively, evaluated at time t after the quench. See Appendix D.1 for more details about how these correlation functions relate to the atomic field operators.

To illustrate the use of these correlation functions, we consider the EP ground state spinor given in Eq. (7.5). Taking θ and ϕ to be spatially dependent random variables, we use ψ_{EP} to evaluate the correlation functions (7.20) and (7.21), yielding

$$G_\phi^{\mathrm{EP}}(\mathbf{r}) = \langle \cos 2[\phi(\mathbf{r}) - \phi(\mathbf{0})] \rangle, \tag{7.22}$$

$$G_\theta^{\mathrm{EP}}(\mathbf{r}) = \left\langle e^{i2[\theta(\mathbf{r}) - \theta(\mathbf{0})]} \right\rangle . \tag{7.23}$$

In practice we compute the spin-nematic order parameter correlation function as

$$G_\phi(r,t) = \int d\Omega_r \int \frac{d^2\mathbf{x}'}{l^2} \frac{2}{n_c^2} \langle \mathrm{Tr}\{\mathcal{Q}(\mathbf{x}')\mathcal{Q}(\mathbf{x}'+\mathbf{r})\}\rangle_t, \tag{7.24}$$

which includes averaging to improve the statistics of our results: $\langle\,\rangle_t$ denotes an average over trajectories (simulations with different seeding noise). The integral $\int d\Omega_r$ is an angular average in 2D position space (utilizing the isotropy of the system) and $l^{-2}\int d^2\mathbf{x}'$ denotes spatial averaging. The convolutions are efficiently computed using fast Fourier transforms. We also apply these additional averaging steps when computing the $G_\theta(r,t)$ correlation function.

Results for the evolution of $G_\phi(r,t)$ are shown in Fig. 7.4(a). As time increases the correlation function is seen to decay more slowly, indicating that the in-plane spin-nematic order is extending over larger distances. We can investigate if the growth of this order exhibits dynamic scaling whereby the nematic domains are statistically self-similar at different times, up to an overall length scale that grows with time. This property often holds in the late time (when the domain sizes are much larger than microscopic length scales of the system) phase ordering dynamics of systems [158]. To verify dynamic scaling we demonstrate that the correlation function collapses to a universal (time-independent) function under time-dependent rescaling of space, i.e. by showing that with an appropriate choice of $L_\phi(t)$ we have

$$H_\phi(r) = G_\phi(r/L_\phi(t), t). \tag{7.25}$$

Results showing the collapse are presented in Fig. 7.4(b), where we have taken $L_\phi(t)$ to be the correlation length defined by the distance over which the correlation function decays to $\frac{1}{4}$ of its local value, i.e. $G_\phi(L_\phi,t) = \frac{1}{4}G_\phi(0,t)$. The collapse is reasonably good except at short length scales ($r \ll L_\phi$) where the correlation function sharpens as t increases.

The length scale $L_\phi(t)$ is not unique and can be multiplied by a constant and still yield correlation function collapse. However, as chosen $L_\phi(t)$ gives a reasonable characterization of the domain size[4] in the ordering EP system. From considering the evolution of $L_\phi(t)$ we can extract the dynamic critical exponent z_ϕ as $L_\phi(t) \sim t^{1/z_\phi}$, providing a key characterization of dynamic universality class of the system. In Fig. 7.4(e) we show the time evolution of $L_\phi(t)$ on a log-log graph and find that at late times ($t \gtrsim 10^3\, t_s$) this grows as $L_\phi(t) \sim [t/\ln(t/t_0)]^{1/2}$, i.e. with a dynamic critical exponent of $z_\phi = 2$ and

[4]Domain size cannot be uniquely defined because the in-plane nematic order varies continuously.

logarithmic corrections. We find that the growth law exhibits a slight bulge (i.e. above the asymptotic growth law) extending from early times up until times of the order $10^3 t_s$. We find that this correlates with the time period over which the magnetic fluctuations evolve appreciably in the system [see Fig. 7.4(f)], suggesting that the decay of magnetic fluctuations may set an important time scale for the system entering into the late-time coarsening regime (also see [150]).

The $L_\phi(t) \sim [t/\ln(t/t_0)]^{1/2}$ growth law we obtain here is the same form of growth known from the dissipative 2D XY model [159, 160] (also see [161]), and was established in early work considering the coarsening dynamics of smectic liquid crystal films [162] (also see [163–165]). Singh *et al.* [164] have predicted an analytic form of H_ϕ for nematic liquid crystals, which they have favourably compared to the results of Monte Carlo simulations using of a spin-nematic liquid crystal model [138]. We however, find that this result is not a good fit to the H_ϕ we obtain.

We can also consider the superfluid scaling in this system, with examples of the evolving G_θ correlation function shown in Fig. 7.4(c). We verify dynamic scaling in a similar way to the spin-nematic order by finding a length scale $L_\theta(t)$ such that we have correlation function collapse:

$$H_\theta(r) = G_\theta(r/L_\theta(t), t). \tag{7.26}$$

Results showing this collapse are presented in Fig. 7.4(d), where again we have taken $L_\theta(t)$ to be the distance over which the correlation function decays to $\frac{1}{4}$ of the its local value. These results also reveal that the late-time superfluid correlation function G_θ has a similar shape to the spin-nematic correlation function G_ϕ. By definition both correlation functions have the same local value, i.e. $G_\theta(0) = G_\phi(0) = \langle \mathcal{A}_\perp^2 \rangle / n_c^2$. However, in general the superfluid correlation function decays more slowly and has a slightly longer characteristic length than the spin-nematic correlation function [e.g. see inset in Fig. 7.4(c)].

In Fig. 7.4(e) see that L_θ grows in a similar way to L_ϕ, consistent with the same dynamical critical exponent, i.e. $z_\theta \approx z_\phi \approx 2$ (to within log-corrections). Thus we find that the superfluid and spin-nematic order grow together in this system. This is different to recent results for the ordering of an EA ferromagnetic phase of a spin-1 condensate, which found that the superfluid order grows significantly slower than the spin order [66] (also see [65]). We also note that Ref. [66] demonstrates how the late-time coarsening results are insensitive to the resolution of the numerical grid used in simulations. Our

particular choice of grid point spacing $\Delta x = l/N = 0.78\,\xi_s$ is to resolve the unstable modes that dominate the early-time dynamics following the quench.

It is conventional to also analyze the structure factors associated with the order parameter correlation function. The structure factor for spin-nematic order is defined as

$$S_\phi(\mathbf{k}, t) = \int d^2\mathbf{r}\, G_\phi(\mathbf{r}, t) e^{i\mathbf{k}\cdot\mathbf{r}}. \tag{7.27}$$

The structure factors also collapse with dynamic scaling according to

$$S_\phi(\mathbf{k}, t) = L_\phi(t)^2 \hat{h}\left(\mathbf{k} L_\phi(t)\right), \tag{7.28}$$

where $\hat{h}$ is the Fourier transform of H_ϕ (7.25). Results for the S_ϕ structure factor are shown in Fig. 7.5. For k vectors in the range $L_\phi^{-1} < k \ll \xi_s^{-1}$ (i.e. length scales between the microscopic healing length and the domain size) the structure factor exhibits a power law decay that is approximately of the form k^{-3}. This differs from the generalized Porod law result of k^{-4} decay expected in 2D spin models [165, 166]. The k^{-3} decay law is also found for the first order structure factors (single-particle momentum spectra) in studies of binary condensates in relevant regimes [146], and is analyzed in terms of turbulence scaling.

We can similarly define a superfluid structure factor S_θ from G_θ. This structure factor has a similar collapse and power-law decay to what we have presented for $S_\phi(k)$.

7.4.4 Topological defects

Coarsening dynamics can be viewed in terms of the dynamics of topological defects of the order parameter which are generated in the early stages of the quench dynamics.

It is thus of interest to consider HQVs, which are the topological defects supported by the EP order parameter. For background details on HQVs, see Section 3.3.1.

The windings associated with these defects disrupt the order, and as they mutually annihilate order is able to extend over larger length scales. We show the locations of HQVs in Fig. 7.3, which reveals a qualitative relationship between the domain sizes and the vortex locations. To quantify the role of defects we detect the number of vortices in our simulations during the evolution. In practice we identify vortices by detecting integer phase windings of the field that occur around plaquettes of the numerical grid. If such phase windings occur only in the $m = 1$ or -1 component of the field, and are

spatially isolated from other vortices then they can be identified as one of the four types of HQVs. Furthermore, HQVs have a z-magnetized core which we observe in our simulations. In the early time dynamics not all vortices detected are HQVs, but we find that only HQVs persist at late times ($t \gtrsim 100\, t_s$). In Fig. 7.6 we show the averaged total number of vortices $N_{\rm vort}$ as a function of time. The number of vortices decreases as the coarsening progresses. We can compare these results to the characteristic length scales discussed in Sec. 7.4.3. Crudely, if the characteristic length scale is taken to be the distance between vortices then we would expect

$$N_{\rm vort}(t) \sim \frac{l^2}{L_\nu(t)^2}, \qquad \nu \in \{\phi, \theta\}. \tag{7.29}$$

We have added these results for the characteristic length to Fig. 7.6 verifying that the relationship (7.29) holds.

As we noted above a pair of $\sigma_1 = 1$ and $\sigma_1 = -1$ HQVs (or a $\sigma_{-1} = 1$ and $\sigma_{-1} = -1$ pair) evolve similarly to a vortex anti-vortex pair in a scalar condensate, and have the potential to mutually annihilate. In such a case each component vortex experiences a Magnus force which causes the pair to move with uniform velocity in a direction perpendicular to the line joining them. Such motion, without some other source of dissipation, does not lead to the vortices meeting and annihilating. This is in contrast to oppositely charged polar core spin vortices (the topological defects of the easy-plane ferromagnetic phase) that accelerate towards each other and annihilate [167, 168]. We expect that in our system dissipation will arise from the interaction between the vortices and the sound waves (spin waves) excited by the quench. However, recent results on HQVs suggest an additional dissipative mechanism even in the absence of spin waves: GPE simulations of a quiet binary condensate (without excitation) have found that such a pair of HQVs move together and annihilate (see Sec. IV of [81]). This effect was observed to be dependent on the interaction parameter regime, only occurring for $\gamma > 0.5$, where γ is the ratio of the inter- to intra-species interaction in the binary condensate. In the spin-1 system[5] this parameter relates to the interaction parameters as $\gamma \approx (c_0 - c_1)/(c_0 + c_1)$. Since our main simulations presented are for $\gamma = 0.5$, where this additional dissipative effect is expected to be negligible, it is of interest to see if our coarsening dynamics changes for a larger value of γ. To explore this issue we have conducted quench simulations for $c_1 = c_0/12$ ($\gamma \approx 0.85$). The results for these simulations are roughly comparable to our main results in Fig. 7.4 (which are for $c_1 = c_0/3$), and do not indicate that the coarsening proceeds at a faster rate.

[5]This mapping is made by neglecting the ψ_0 component in the spin-1 GPE.

7.5 Experimental measurement of nematic order

Experiments can most easily measure F_z, via a Stern-Gerlach method. To measure other observables, they apply spin rotations (using RF pulses) that rotate the desired observable into F_z. For example, to measure F_x, we can rotate about the y axis by $\pi/2$ so that F_x now points along the z axis. Measuring F_z now measures the rotated F_x.

In our nematic quench we want to measure the correlation function

$$G_\phi \sim \Re\{\psi^*_{+1}(x)\psi_{-1}(x)\psi^*_{-1}(x')\psi_{+1}(x')\}, \tag{7.30}$$

$$\sim \cos(2[\phi(x) - \phi(x')]). \tag{7.31}$$

To calculate this, we consider measuring the two independent components of the 2D nematic tensor, i.e.

$$\mathcal{Q}_{xx} = \frac{1}{2}(\mathcal{S}_{xx} - \mathcal{S}_{yy}) = \frac{1}{2}(\psi^*_{+1}\psi_{-1} + \psi^*_{-1}\psi_{+1}) \sim \cos(2\phi), \tag{7.32}$$

$$\mathcal{Q}_{xy} = \mathcal{S}_{xy} = \frac{1}{2i}(\psi^*_{+1}\psi_{-1} - \psi^*_{-1}\psi_{+1}) \sim \sin(2\phi), \tag{7.33}$$

$$G_\phi \sim \mathrm{Tr}\{\mathcal{Q}(x)\mathcal{Q}(x')\} = 2\mathcal{Q}_{xx}(x)\mathcal{Q}_{xx}(x') + 2\mathcal{Q}_{xy}(x)\mathcal{Q}_{xy}(x'), \tag{7.34}$$

where $\mathcal{S}_{ab}$ for $a, b \in \{x, y\}$ (with operator s_{ab}) are components of the symmetric quadrupole tensor defined in Section 2.4.1.

However, we can only measure one of these quantities at a time since they are in different quadratures. In fact, the three operators $\{\mathrm{f}_z, \mathrm{s}_{xx} - \mathrm{s}_{yy}, \mathrm{s}_{xy}\}$ form an $SU(2)$ [equivalently $SO(3)$] subspace of $SU(3)$ [the space of the spin matrices and their second powers]. To determine the correct rotation to perform, consider the following commutation relations (see Supplementary Information of Ref. [169] for the full $SU(3)$ commutation relations table)

$$[\mathrm{f}_y, \mathrm{s}_{yz}] = i\mathrm{s}_{xy}, \tag{7.35}$$

$$[\mathrm{f}_{zz}, \mathrm{f}_x] = 2i\mathrm{f}_{yz}, \tag{7.36}$$

$$[\mathrm{f}_y, \mathrm{f}_z] = i\mathrm{f}_x. \tag{7.37}$$

Given a non-zero commutator $[a, b]$, a $\pi/2$ rotation by a can move the commutator $[a, b]$ into the quadrature of b. E.g.

$$\tilde{\psi} = \exp\left(i\frac{\pi}{2}\mathrm{f}_y\right)\psi, \tag{7.38}$$

$$\tilde{\psi}^\dagger \mathrm{f}_z \tilde{\psi} = \psi^\dagger \exp\left(-i\frac{\pi}{2}\mathrm{f}_y\right)\mathrm{f}_z \exp\left(i\frac{\pi}{2}\mathrm{f}_y\right)\psi, \tag{7.39}$$

$$= \psi^\dagger \mathrm{f}_x \psi = F_x. \tag{7.40}$$

In our case, by performing the sequence

$$\tilde{\psi} = \exp\left(i\frac{\pi}{2}\mathrm{f}_y\right)\exp\left(i\frac{\pi}{2}\mathrm{s}_{zz}\right)\exp\left(i\frac{\pi}{2}\mathrm{f}_y\right)\psi, \tag{7.41}$$

the commutation relations in Eqs. (7.35)–(7.37) mean that we shift the observable $\mathcal{S}_{xy} \to \mathcal{S}_{yz} \to \frac{1}{2}F_x \to \frac{1}{2}F_z$. By measuring F_z of this rotated state we access $2\mathcal{S}_{xy}$ of the initial state.

Note that $\mathrm{s}_{zz} = \mathrm{n}_{zz} = \mathrm{f}_z^2$ is the operator for $\mathcal{N}_{zz}$, which couples to the quadratic Zeeman shift q [see Section 1.3.1 and Eq. (4.3)]. Experiments can thus achieve the quadrature rotation of Eq. (7.41) by performing a $\pi/2$ spin rotation, followed by a short hold time at non-zero q such that the quadrupole rotation is performed, and finally another $\pi/2$ spin rotation before measuring F_z.

Using nondestructive phase contrast imaging [144], it may be possible to measure both components $\{\mathcal{Q}_{xx}, \mathcal{Q}_{xy}\}$, similarly to how experiments can measure both components of $F_\perp$ (e.g. Ref. [52]). If the quadrature rotations and measurements were performed quickly, the system could be returned to its initial quadrature with minimal disruption, and measurements could continue tracking the quench dynamics *in-situ* at regular intervals.

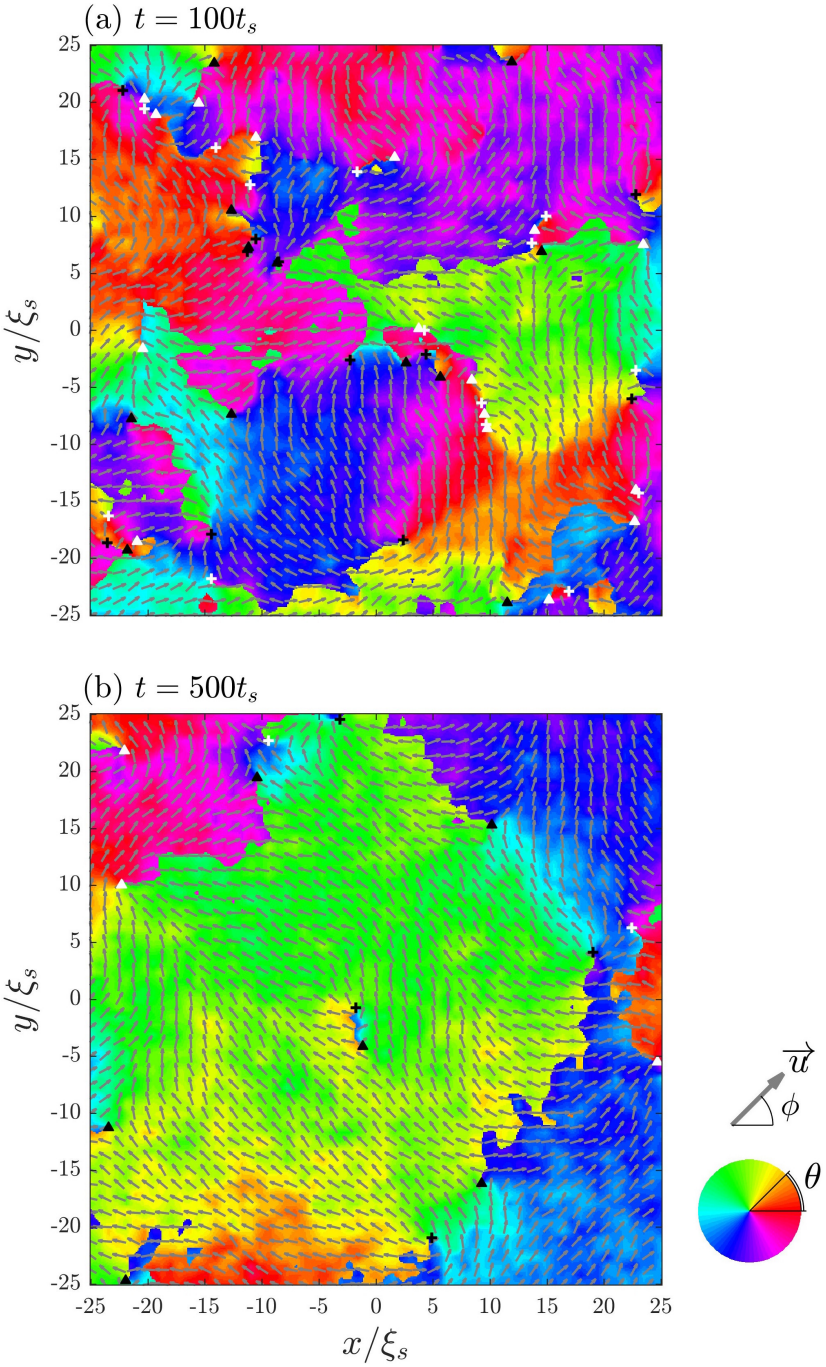

Figure 7.3: Evolution of order after the quench in a $50\,\xi_s \times 50\,\xi_s$ sub-region of a simulation at (a) $t = 100\,t_s$ and (b) $t = 500\,t_s$. The arrows indicate planar projection of the director $\vec{u}$ and the colours indicate the phase order θ in these regions. In general there are two possible values $\vec{u}$ and θ for the spinor at each simulation point [see Eq. (3.19)] because of the symmetry (3.28), and we impose the further condition $u_y \geq 0$. We also show the locations of HQVs (see Sec. 7.4.4) with circulations $\sigma_1 = 1$ (black plus), $\sigma_1 = -1$ (black triangle), $\sigma_{-1} = 1$ (white plus), and $\sigma_{-1} = -1$ (white triangle). Simulation parameters: $c_0 = 3c_1$, $q = -0.5\,q_0$, $n_c = 10^4/\xi_s^2$, $l = 200\,\xi_s$ and $N = 256$ points.

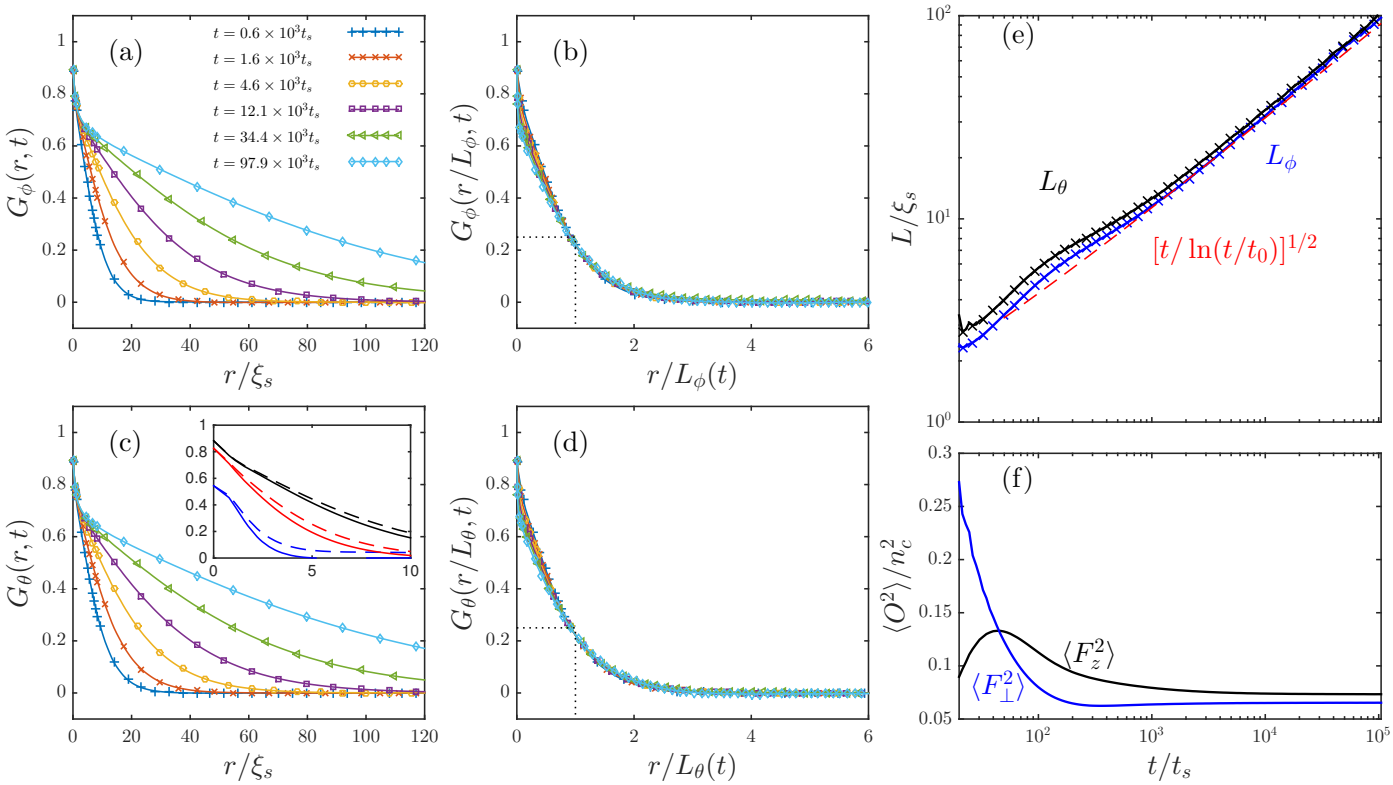

Figure 7.4: Evolution and dynamic scaling of order parameter correlation functions. (a) The spin-nematic order correlation function G_ϕ at various times after the quench. (b) Collapse of the G_ϕ correlation functions when space is scaled by the length scale $L_\phi(t)$. (c) The superfluid order correlation function G_θ at various times after the quench. Inset compares G_ϕ (solid lines) and G_θ (dashed lines) at $t/t_s = 25.6$ (blue), 99.0 (red) and 399 (black). (d) Collapse of the G_θ correlation functions when space is scaled by the length scale $L_\theta(t)$. (e) The evolution of the length scales L_ϕ and L_θ compared to a $[t/\ln(t/t_0))]^{1/2}$ growth law, where $t_0 = 0.5t_s$. Simulations are performed on domain of size $l = 1600\,\xi_s$ covered by $N = 2048$ points, and averaged over 15 trajectories. Interactions are $c_0 = 3c_1$, $n_c = 10^4/\xi_s^2$ and $q = -0.5\,q_0$.

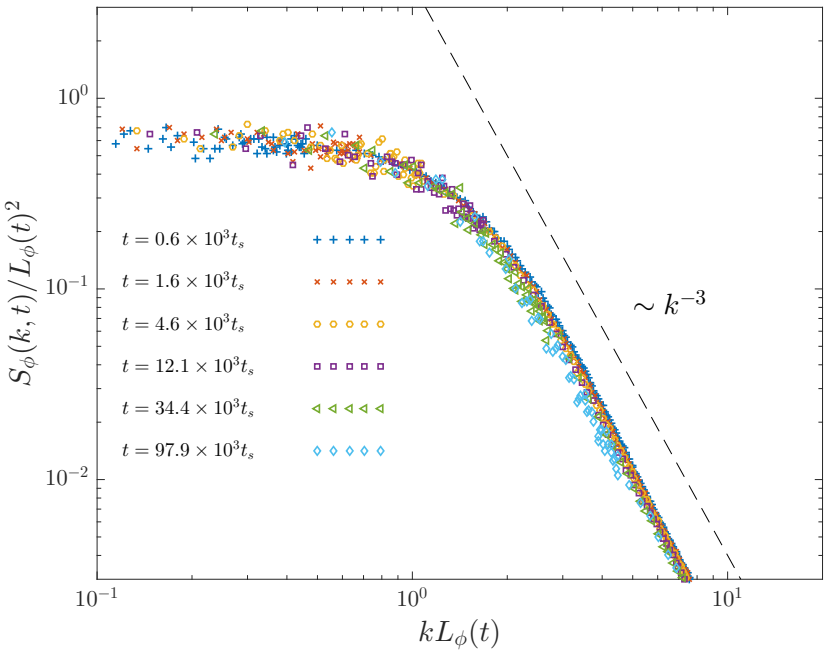

Figure 7.5: S_ϕ structure factor scaled by $L_\phi(t)$ to reveal scaling collapse. The power law decay for $kL_\phi > 1$ reveals the Porod tail, with a guide line indicating k^{-3} scaling for reference. Other parameters as in Fig. 7.4.

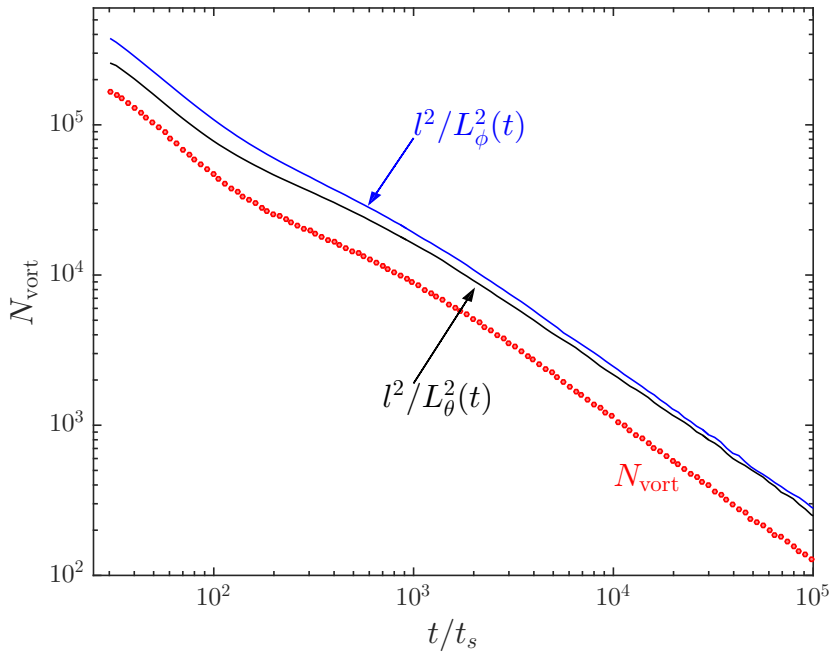

Figure 7.6: HQV number as a function of time for the simulation case examined in Fig. 7.4. The vortex number is computed as the total number of unit phase winding singularities in the $m = \pm 1$ components averaged over the trajectories. The vortex number is compared to the *number of domains* l^2/L_ν^2, using the characteristic length scales $L_\nu = \{L_\phi, L_\theta\}$ [from Fig. 7.4(e)] as labelled in the plot.

Chapter 8

Spin-1 Experimental Quench

8.1 Introduction

A recent experiment carried out a quench from positive to negative quadratic Zeeman energy q with an antiferromagnetic spin-1 ^{23}Na condensate in a quasi-2D harmonic trap [150]. This quench caused the system to transition from the initial EA polar phase to the EP polar phase. The analysis of the experiment was performed in terms of the emergence and decay of a spin turbulence, evidenced by the non-exponential decay of axial spin domains, and associated energy cascade-like behaviour. HQVs were also observed to form in the phase transition dynamics. The quench was studied as the final q value was varied, which controls the amount of energy realized in the quench. They found a $|q|^{1/2}$ scaling for the characteristic time and length scales forming after the quench over the range of q values explored.

This experiment predated our original work on antiferromagnetic phase ordering, i.e. the work in Chapter 7 published in Ref. [170], by a few months, and was not influenced by our work. Nevertheless these experiments provide us with a unique test to compare our simulations of quench dynamics to experimental results. To do this we need to include the influence of a harmonic trapping potential and use values for the interaction parameters relevant to ^{23}Na. Both of these adjustments place additional demands on the simulations, most notably while the system is quasi-2D with respect to spin-degrees of freedom, this is not true for the density degrees of freedom and thus we need to perform full 3D calculations.

This experiment provides an excellent test bed for our symplectic simulation methods, as one of the few quantitative tests available to verify our ability to simulate realistic quench dynamics in a spinor system. It gives us benchmark data to validate our simulations in terms of the experimentally measured observables. In addition, we assess the system evolution in terms of phase ordering by an immediate application of the formalism and observables developed in the previous chapter for the 2D uniform system.

This chapter is structured in the following way. First, we give details of the experiment done in Ref. [150], including experimental parameters and how the quench was carried out. Then, we detail how we set up simulations to closely match the experimental details. We choose appropriate observables to measure and compare with measurements made in the experiments. We extract correlation lengths and measure the number of half-quantum vortices (HQVs), based on the formalism and results developed in the previous chapter for the uniform system. We discuss our new results for the trapped experimental system, and their significance for experiments, before finally concluding.

8.2 The experiment

Here we describe the experiment performed in Ref. [150], giving details on the experimental parameters they reported for their system. We calculate the thermal energy of the system based on their estimates of thermal population, and verify they are working in a Thomas-Fermi (TF) approximation. We also give an overview of the quench and measurement procedure.

8.2.1 Initial condensate

A BEC of about 8 million ^{23}Na atoms was prepared in the $|f = 1, m = 0\rangle$ EA ground state at large positive quadratic Zeeman energy q, confined in an oblate harmonic trapping potential

$$V_{\text{trap}}(\mathbf{x}) = \frac{1}{2}M(\omega_x^2 x^2 + \omega_y^2 y^2 + \omega_z^2 z^2), \tag{8.1}$$

with frequencies

$$(\omega_x, \omega_y, \omega_z)/2\pi = (3.8, 5.5, 400) \text{ Hz}. \tag{8.2}$$

The experiment reported a chemical potential of $\mu/h = 880$ Hz and Thomas-Fermi radii

$$(R_x, R_y, R_z) \approx (232, 160, 2.2)\ \mu\text{m}. \tag{8.3}$$

The peak spin-interaction energy of the condensate was quoted as $c_1 n_{\text{peak}}/h = 14$ Hz, where n_{peak} is the peak density occurring at the centre of the trap.

The relevant scattering lengths in the system (derived theoretically in Section 2.3.1) are given by the experimental values [49, 171]

$$a_n = \frac{a_0 + 2a_2}{3} = 51.1 a_B, \tag{8.4}$$

$$a_s = \frac{a_0 - a_2}{3} = 0.823 a_B, \tag{8.5}$$

where a_B is the Bohr radius, with corresponding density- and spin-dependent interaction strengths

$$c_0 = 4\pi a_n \hbar^2/M, \tag{8.6}$$

$$c_1 = 4\pi a_s \hbar^2/M. \tag{8.7}$$

For these parameters the spin healing length is $\xi_s = \hbar/\sqrt{2mc_1 n_{\text{peak}}} \approx 4.0\ \mu$m, which is larger than R_z, and thus we can conclude that spin textures are frozen out in this direction and the system can be regarded as being quasi-2D with respect to the spin degrees of freedom. The density healing length was $\xi_n = \hbar/\sqrt{2mc_0 n_{\text{peak}}} \approx \hbar/\sqrt{2m\mu} = 0.5\ \mu$m, which is smaller than R_z, thus the system remains 3D with respect to the density degrees of freedom.

System temperature

The initial condensate was produced with a thermal fraction of less than 10%. We can approximate the temperature as a fraction of T_c using the ideal Bose gas relation

$$\frac{T}{T_c} = \left(1 - \frac{N^c}{N}\right)^{1/3} = 0.1^{1/3} = 0.46. \tag{8.8}$$

We can estimate T_c using the relation for a non-interacting harmonically trapped Bose gas,

$$T_c \approx 4.5 \left(\frac{\bar{f}}{100\ \text{Hz}}\right) N^{1/3}\ \text{nK} = 183\ \text{nK}. \tag{8.9}$$

This then gives an approximate system thermal energy of

$$0.46 k_B T_c = k_B \times 85\ \text{nK} = h \times 1778\ \text{Hz} \approx 2\mu. \tag{8.10}$$

Comparison with Thomas-Fermi

In the Thomas-Fermi regime (neglecting kinetic energy) we have

$$\frac{\mu}{h} = \frac{15^{2/5}}{2}\left(\frac{Na}{\bar{a}}\right)^{2/5}\frac{\bar{\omega}}{2\pi}, \tag{8.11}$$

where the characteristic length scale of the trap is given by

$$\bar{a} = \sqrt{\frac{\hbar}{M\bar{\omega}}} = 8.8 \times 10^4 a_B, \tag{8.12}$$

and

$$\bar{\omega} = (\omega_x\omega_y\omega_z)^{1/3} = 2\pi \times 20.3\text{Hz}, \tag{8.13}$$

is the geometric mean of the 3D trap frequencies.

Computing the Thomas-Fermi chemical potential using the reported number of atoms gives $\mu/h = 879$ Hz. Fixing μ/h to the reported value of 880 Hz and calculating N, we get $N^c = 8.03 \times 10^6$. Thus the experimentally reported N^c and μ are consistent with the 3D TF approximation. From the reported $c_1 n_{peak}/h = 14$ Hz, we would expect $\mu/h \approx c_0 n_{peak}/h = 869$ Hz, which within about 1% of the reported value. Thus the reported system parameters are consistent with a Thomas-Fermi description.

8.2.2 The quench and measurements

The experiment implemented the quench by suddenly turning on a microwave dressing field which tuned q to a negative value in the range $q/h = [-1.4, -20]$ Hz. For a uniform condensate the difference in energy per particle between the EA phase and the EP phase is given by

$$\Delta\epsilon = q, \tag{8.14}$$

and is thus the energy liberated by the quench (for $q < 0$), which increases with $|q|$.

We address various details of the measurements later when we present our simulation results. However, generally the experiment considered short-time and long-time behaviour. The short-time behaviour concerns the unstable modes that cause the initial condensate to deplete through the formation of local magnetization. The long-time behaviour then concerned the turbulent rethermalization of the system into the new phase, and was

characterized by observing the evolution of the axial magnetic fluctuations and HQVs. In general measurements were made over times from $t = 5$ms up to $t = 10$s, with lifetime and technical heating issues becoming important over such long observation times.

8.3 Simulations

Here we give details on our approach to numerically simulating the experiment of Ref. [150]. We go through the requirements and rationale of choosing a spatial discretization grid to compute the numerical wavefunction on, based on resolving a maximum cutoff energy which we choose consistent with the thermal energy of the experiment. We then construct an initial state based on solving the 3D GPE in the pre-quench EA ground state, with additional thermal and quantum noise (in the truncated Wigner prescription) to seed the unstable post-quench dynamics. Lastly we give details on the numerical simulation procedure and the spatial windowing used to measure observables in the same way as the experiment.

8.3.1 Computational grid

The computational grid must be carefully chosen to represent the initial noise for classical field simulations, while taking into account the thermalization that happens over long time scales. We work with a rectangular cubic grid on which fast Fourier transforms can be easily evaluated. The range L_ν and number of points N_ν in each direction $\nu \in \{x, y, z\}$ is chosen so that we can ensure energies up to a certain cutoff E_{cut} can be accurately simulated. We do this using a single-particle energy argument in each direction: the maximum potential energy along the ν-axis is

$$V_{\text{max},\nu} = \frac{1}{2} M \omega_\nu^2 (L_\nu/2)^2, \tag{8.15}$$

while the maximum kinetic energy in the same direction is

$$T_{\text{max},\nu} = \hbar^2 k_{\nu,\text{max}}^2 / 2M, \tag{8.16}$$

where the maximum k-vector on the grid,

$$k_{\nu,\text{max}} = \pi N_\nu / L_\nu, \tag{8.17}$$

is determined by the usual Fourier relationship between the reciprocal grids. Separately requiring $V_{\max,\nu}$ and $T_{\max,\nu}$ to both exceed $E_{\rm cut}$ we can determine requirements on $\{L_\nu, N_\nu\}$ for the grid.

Here we choose $E_{\rm cut}$ to be $k_B T$, where T is the initial temperature of the system. Consistent with having a non-condensate population of about 10% [see 8.8], we take $T = 0.45 T_c$.

We then use the following grid

$$(L_x, L_y, L_z) = (700, 482, 14.7)\,\mu\text{m}, \tag{8.18}$$

$$(N_x, N_y, N_z) = (672, 464, 32), \tag{8.19}$$

which meets the requirement that modes of energy up to $k_B T$ are accurately simulated.

8.3.2 Initial state

We use an initial condition for the quench simulation composed of an EA ground state with noise added according to the truncated Wigner prescription. The EA ground state is equivalent to a scalar BEC, with scattering length a_n given in Eq. (8.4), and so we solve the scalar GPE

$$\mu_{GP}\psi_0(\mathbf{x}) = \left[-\frac{\hbar^2}{2M}\nabla^2 + c_0|\psi_0(\mathbf{x})|^2 + V_{\rm trap}(\mathbf{x})\right]\psi_0(\mathbf{x}), \tag{8.20}$$

for the ground state wavefunction[1] $\psi_0(\mathbf{x})$, normalized to $N^c = 8\times 10^6$.

We construct the initial state according to

$$\psi(\mathbf{x}, t=0) = \begin{pmatrix} 0 \\ \psi_0(\mathbf{x}) \\ 0 \end{pmatrix} + \delta(\mathbf{x}), \tag{8.21}$$

where the components of the noise vector $\delta(\mathbf{x})$ are given by

$$\delta_m(\mathbf{x}) = {\sum_j}' \alpha_{m,j}\,\phi_j(\mathbf{x}), \tag{8.22}$$

where $\{\phi_j(\mathbf{x})\}$ are the single-particle harmonic oscillator basis[2] for the trapping potential with respective energy eigenvalues $\{\varepsilon_j\}$, and the prime on the summation indicates

[1] The GPE solution has chemical potential $\mu_{\rm GP}/h = 892$Hz, and peak density $c_1 n_{\rm peak}/h = 14.3$ Hz, which is reasonably close to the Thomas-Fermi estimates given in [150]. Also see Fig. 8.1

[2] Using the harmonic oscillator basis for the noise is an approximation to putting noise into the exact Bogoliubov excitation modes, which are not analytically known and would require a large computational effort to use.

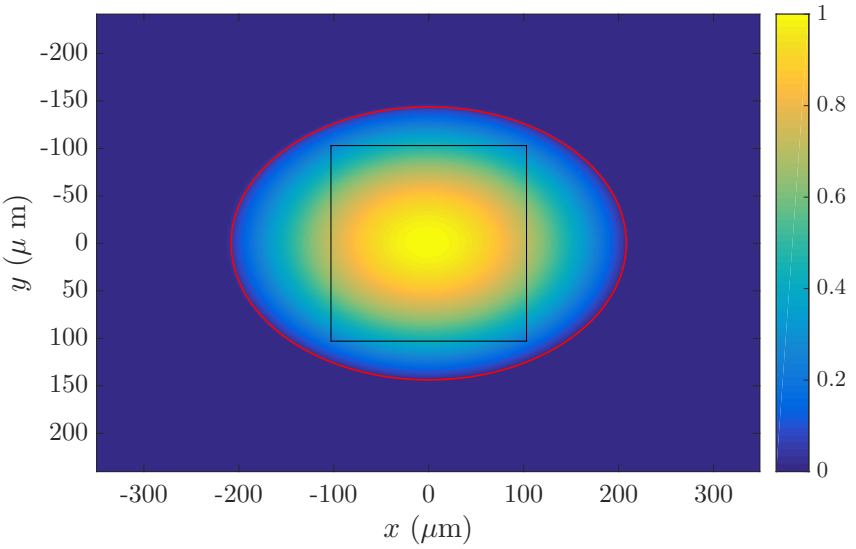

Figure 8.1: Column density of the GPE ground state density, $|\psi_0|^2$, obtained by integrating along z. Red line is the Thomas-Fermi boundary. The black square outline is the spatial window used for averaging.

that it is restricted to basis states with $\varepsilon_j < k_B T$. The $\{\alpha_{m,j}\}$ are independent complex Gaussian random numbers with zero mean and the non-zero correlation

$$\langle |\alpha_j|^2 \rangle = \begin{cases} \frac{1}{2} & \text{for } m = \pm 1, \\ \bar{n}_j + \frac{1}{2} & \text{for } m = 0, \end{cases} \tag{8.23}$$

where

$$\bar{n}_j = (e^{\epsilon_j / k_B T} - 1)^{-1}, \tag{8.24}$$

is the mean thermal occupation. Thus, our initial condition approximately corresponds to the experimentally prepared situation of a condensate at temperature T in the $m = 0$ component, and only ($T = 0$) vacuum noise in the $m \pm 1$ components. The choice of using $k_B T$ to set E_{cut}, when obtaining the numerical grids, was to ensure that sufficiently many of the low energy excited states are thermally occupied. Because we cut off the thermal excitations, the mean number of thermal atoms sampled in our simulation (i,e. $\sum_j' \bar{n}_j$) is only about 2% of the condensate population, with the remaining 8% in the sparingly occupied modes above our cutoff. Care has to be taken with increasing the cutoff in classical field simulations, as the excitations will thermalize to an equipartition distribution rather than a Bose-Einstein distribution, and the difference between these two increases with energy. We have explored changing the cutoff in our simulations and find that it makes little difference. We note that the initial dynamics is driven by the

vacuum seeding in the $m = \pm 1$ modes, and is not sensitive to the thermally occupied modes.

8.3.3 Quench simulations

We set the quadratic Zeeman interaction to its final value and propagate the 3D initial state (8.21) forward in time using the S2 symplectic integration algorithm developed in Chapter 5. We use a time step of half the upper bound for the maximum stable time step, where the upper bound is given by

$$(\Delta t)_{\max} = \min\left\{\frac{\pi}{\hbar^2 k_{\max}^2/2M + |q|}, \frac{\pi}{c_0 n + V_{\text{trap}}}\right\}. \tag{8.25}$$

where $k_{\max} = \max_\nu\{k_{\nu,\max}\}$, and the second term is represents the minimum value over all spatial coordinates. In practice we work in units of the z-trap frequency ω_z, and find $(\Delta t)_{\max} = 0.091/\omega_z$. We set an integration time step of half this value. This choice maintains numerical stability and keeps errors in the conserved quantities within acceptable tolerances; we find the errors corresponding to the relative change in conserved quantities (energy, normalization, and axial magnetizations) are less than 1% at the end of the full integration time. We use the S2 method here over the S4 method because it is numerically more efficient, and as we are simulating a 3D grid to reasonably long times (25×10^3 spin times) we need to be quite economical for the computational time to be feasible. We would use S4 if we wanted lower errors, or if stability meant that S2 required smaller time steps as S4 can use time steps closer to $(\Delta t)_{\max}$ while remaining stable.

To analyze our simulation results, we follow the experimental procedure of considering column densities of observables (i.e quantities integrated over z). Often we limit the analysis to a central spatial region of size $206\mu\text{m} \times 206\mu\text{m}$. This choice of an analysis window was made in experiments to exclude the low density wings of the condensate. We plot the window boundary on top of the column density of the ground state (without noise) in Fig. 8.1 for reference.

Windowing

The observation window should fit inside the Thomas-Fermi profile. Starting from the 3D Thomas-Fermi approximation,

$$\mu\psi = \left(c_0 n + \frac{1}{2}M(\omega_x^2 x^2 + \omega_y^2 y^2 + z^2)\right)\psi, \tag{8.26}$$

the 2D Thomas-Fermi boundary is defined by setting $z = 0$ and $n = 0$, giving the ellipse

$$\frac{x^2}{R_x^2} + \frac{y^2}{R_y^2} = 1, \tag{8.27}$$

where the Thomas-Fermi radii are defined by

$$R_\nu^2 = \frac{M\omega_\nu^2}{2\mu},\ \nu \in \{x, y, z\}. \tag{8.28}$$

For a square window of radius R_w (width $2R_w$), the condition is based on the corners being inside the TF boundary, given by

$$1 \geq R_w^2\left(\frac{1}{R_x^2} + \frac{1}{R_y^2}\right), \tag{8.29}$$

$$\implies 2R_w \leq 2\sqrt{\frac{2\mu}{\omega_x^2 + \omega_y^2}} = 237\ \mu\text{m}. \tag{8.30}$$

We use the experimental value, $2R_w = 206\mu m$, which satisfies the condition. We plot the 2D projection of our initial ground state with the TF boundary outline and the observation window in Fig. 8.1.

8.4 Approximate Bogoliubov analysis

To gain further insight into the early-time dynamics of the trapped system, we develop a Bogoliubov treatment of the system. This approach is valid when the excitations are small compared to the condensate so that linearization is appropriate. Because the unstable modes that develop following the quench grow exponentially, eventually the Bogoliubov treatment becomes inapplicable, and nonlinear multimode dynamics will become important. The full Bogoliubov treatment of the trapped system is a computationally difficult problem and provides little insight into the system. Here, instead, we pursue a simplified approach where we treat the system within the central observation widow (described above) as a quasi-2D uniform condensate. This allow us to directly apply the analytic uniform Bogoliubov theory.

8.4.1 Reduction to a uniform quasi-2D system

We can construct a quasi-2D representation of the 3D trapped system by integrating out the spatial variation of the ground state wavefunction in the z direction. Since the ground state is not exactly Gaussian in the z direction, this leads to position-dependent 2D interaction parameters and an extra position-dependent trap term. We can then average these to get an approximate uniform system in the central windowed region.

First, as discussed above, we consider the ground state of the time-independent scalar GPE in Eq. (8.20). By integrating the 3D density over z we get the 2D areal density

$$n^{2D}(\boldsymbol{\rho}) = \int dz\, |\psi_0(\boldsymbol{\rho}, z)|^2, \tag{8.31}$$

where we have set $\boldsymbol{\rho} = (x, y)$, and obtain the $\boldsymbol{\rho}$-dependent axial profile function

$$\chi(\boldsymbol{\rho}, z) \equiv \frac{\psi_0(\boldsymbol{\rho}, z)}{\sqrt{n^{2D}(\boldsymbol{\rho})}}. \tag{8.32}$$

By definition, the axial profile function is normalized with respect to the z-coordinate. We emphasize that the decomposition $\psi_0(\boldsymbol{\rho}, z) = \sqrt{n^{2D}(\boldsymbol{\rho})}\chi(\boldsymbol{\rho}, z)$ is a completely general representation of a real ground state.

Because the experimental trap frequency is almost two orders of magnitude stronger in the axial direction, motion in this direction is largely frozen out. In the limit of vanishing interactions it becomes the 1D harmonic oscillator ground state (of the z-harmonic confinement), and is independent of $\boldsymbol{\rho}$. When this approximation is applicable the system is said to be in the quasi-2D regime. However, because of the large number of atoms we consider this is not the case, indeed $\mu \approx 2\hbar\omega_z$. Because μ is not much larger than $\hbar\omega_z$, a Thomas Fermi description in this direction is not valid. A variational Gaussian treatment (using the oscillator width as a variational parameter) would be possible, but instead here we use $\chi(\boldsymbol{\rho}, z)$ extracted from our full GPE solution.

We reduce the system to a generalized quasi-2D description by integrating out the z-degree of freedom. The imaging is along this direction in the experiment and effectively performs this integration. Additionally, as noted earlier, because of the small spin-dependent interaction the spin degrees of freedom are frozen out in z. In doing this, we obtain the effective 2D interaction parameters

$$c_\alpha^{2D}(\boldsymbol{\rho}) \equiv c_\alpha \int dz\, |\chi(\boldsymbol{\rho}, z)|^4, \quad \alpha \in \{0, 1\}, \tag{8.33}$$

which vary with $\boldsymbol{\rho}$ due to the changing shape of χ. In order to develop a quasi-2D Bogoliubov treatment we need to approximate an average interaction energy. For the region of the system within the window, we define the density-weighted average interaction energies

$$(c_\alpha n)^{2D}_{\rm av} \equiv \frac{\int_w d\boldsymbol{\rho}\, c^{2D}_\alpha(\boldsymbol{\rho}) n^{2D}(\boldsymbol{\rho})}{\int_w d\boldsymbol{\rho}\, n^{2D}(\boldsymbol{\rho})}, \quad \alpha \in \{0,1\}, \tag{8.34}$$

where $\int_w d\boldsymbol{\rho}$ denotes 2D integration over the central 206μm $\times$ 206μm window region. Applying this procedure to the full GPE solution, we obtain

$$(c_\alpha n)^{2D}_{\rm av} = 0.61 c_\alpha n_{\rm peak}, \quad \alpha \in \{0,1\}, \tag{8.35}$$

where $n_{\rm peak}$ is the peak 3D density of the ground state which occurs at trap centre.

Short-time dynamics

Here we analyze the short-time dynamics in terms of the Bogoliubov excitations around the initial polar condensate which we have approximated as a uniform 2D system: $\psi^{2D} = (0, \sqrt{n^{2D}}, 0)^T$. Here $n^{2D} = N_w/A_w$ is the average 2D density in the window, where N_w and A_w are the number of atoms within the window and the window area, respectively. Our treatment here follows, but extends, the linearized treatment present in Ref. [155] to the case of antiferromagnetic interactions.

First we expand field operators as

$$\hat{\psi}_m(\boldsymbol{\rho}) = \frac{e^{-i(c_0 n)^{2D}_{\rm av} t/\hbar}}{\sqrt{V}} \sum_{\mathbf{k}} e^{i\mathbf{k}\cdot\boldsymbol{\rho}} \hat{a}_{m,\mathbf{k}}. \tag{8.36}$$

Setting $\mathbf{r} = \boldsymbol{\rho} - \boldsymbol{\rho}'$, $r = |\mathbf{r}|$, we introduce the correlation functions

$$\hat{\rho}_{mm'}(\boldsymbol{\rho}) \equiv \hat{\psi}^\dagger_m(\boldsymbol{\rho})\hat{\psi}_{m'}(\boldsymbol{\rho}), \tag{8.37}$$

$$\rho_{mm'}(\mathbf{r}) \equiv \langle \hat{\psi}^\dagger_m(\boldsymbol{\rho})\hat{\psi}_{m'}(\boldsymbol{\rho}')\rangle, \tag{8.38}$$

$$\rho_{m_1m_2m_3m_4}(\mathbf{r}) \equiv \langle \hat{\psi}^\dagger_{m_1}(\boldsymbol{\rho})\hat{\psi}_{m_2}(\boldsymbol{\rho})\hat{\psi}^\dagger_{m_3}(\boldsymbol{\rho}')\hat{\psi}_{m_4}(\boldsymbol{\rho}')\rangle, \tag{8.39}$$

$$\sigma_{m_1m_2m_3m_4}(\mathbf{r}) \equiv \langle \hat{\psi}^\dagger_{m_1}(\boldsymbol{\rho}')\hat{\psi}^\dagger_{m_2}(\boldsymbol{\rho}')\hat{\psi}_{m_3}(\boldsymbol{\rho})\hat{\psi}_{m_4}(\boldsymbol{\rho})\rangle. \tag{8.40}$$

There are three excitation branches for a spin-1 BEC. For the EA polar initial state with $c_1 > 0$, a spin-wave branch (in fact two degenerate branches) becomes unstable when $q < 0$. The Bogoliubov dispersion relation for this unstable branch is given by

$$E_k = \sqrt{(\epsilon_k + q)\,(\epsilon_k + q + 2(c_1 n)^{2D}_{\rm av})}. \tag{8.41}$$

Within the Bogoliubov approximation (a quadratic expansion of the full quantum Hamiltonian that linearizes the dynamics about the condensate) plane-wave operators evolve as

$$\hat{a}_{m,\mathbf{k}}(t) = b_k \hat{a}_{m,\mathbf{k}}(0) - i s_k \hat{a}^\dagger_{-m,-\mathbf{k}}(0), \tag{8.42}$$

where

$$s_k = \frac{(c_1 n)^{2D}_{\rm av}}{E_k} \sin\left(\frac{E_k t}{\hbar}\right), \tag{8.43}$$

$$b_k = \cos\left(\frac{E_k t}{\hbar}\right) - i\frac{\epsilon_k + q + (c_1 n)^{2D}_{\rm av}}{E_k} \sin\left(\frac{E_k t}{\hbar}\right). \tag{8.44}$$

We define

$$S(\mathbf{r}) \equiv \frac{1}{A_w}\sum_{\mathbf{k}} e^{i\mathbf{k}\cdot\mathbf{r}} |s_k|^2, \tag{8.45}$$

$$C(\mathbf{r}) \equiv \frac{1}{A_w}\sum_{\mathbf{k}} e^{i\mathbf{k}\cdot\mathbf{r}} s_k b_k. \tag{8.46}$$

We now set $\hat{a}_{0,\mathbf{k}} \approx \sqrt{N_w}\delta_{\mathbf{k},\mathbf{0}}$ corresponding to the approximation $\hat{\psi}_0(\mathbf{x}) \approx e^{-i(c_0 n)^{2D}_{\rm av} t/\hbar}\sqrt{n^{2D}}$, i.e. that the macroscopic occupation of the initial state means we can approximate the condensate operator by a complex number. This leads to the normally ordered results[3]

$$:\rho:_{m_1 m_2 m_3 m_4}(\mathbf{r}) = \delta_{m_1 m_2}\delta_{m_3 m_4} S(\mathbf{0})^2 + \delta_{m_1 m_4}\delta_{m_2 m_3} S(\mathbf{r})^2 + \delta_{m_1,-m_3}\delta_{m_2,-m_4}|C(\mathbf{r})|^2, \tag{8.47}$$

$$\sigma_{m_1 m_2 m_3 m_4}(\mathbf{r}) = \delta_{m_1,-m_2}\delta_{m_3,-m_4}|C(\mathbf{0})|^2 + (\delta_{m_1 m_3}\delta_{m_2 m_4} + \delta_{m_1 m_4}\delta_{m_2 m_3}) S(\mathbf{r})^2. \tag{8.48}$$

We can use these results to estimate the key correlation functions[4]

$$G_{F_z}(\mathbf{r}) \equiv \langle F_z(\boldsymbol{\rho}) F_z(\boldsymbol{\rho}')\rangle \approx\ 2(S(\mathbf{r})^2 - |C(\mathbf{r})|^2), \tag{8.49}$$

$$G_{F_\perp}(\mathbf{r}) \equiv \langle F_\perp(\boldsymbol{\rho}) F_\perp(\boldsymbol{\rho}')\rangle \approx 4n^{2D}(S(\mathbf{r}) + \Im\{C(\mathbf{r})\}), \tag{8.50}$$

$$G_\phi(\mathbf{r}) \approx S(\mathbf{r})^2 + |C(\mathbf{r})|^2, \tag{8.51}$$

$$G_\theta(\mathbf{r}) \approx 4(S(\mathbf{r})^2 + |C(0)|^2). \tag{8.52}$$

[3]The quantum operator theory is in terms of normally ordered operators (i.e. creation operators to the right of annihilation operators). Here :: indicates normal ordering of the enclosed operators.

[4]Our simulations take an ensemble average over random initial conditions, with quantum noise included using the truncated Wigner prescription. This corresponds to symmetric ordering of Bogoliubov field operators. The difference between symmetric ordering and normal ordering corresponds to overall shifts and contributions to the $\mathbf{r} = 0$ value, which we neglect here.

The first two functions characterize spin correlations and are introduced because they are important in the early-time dynamics. Indeed, the unstable branch leads to the initial formation of spin density in the system. The last two correlation functions were introduced in our analysis of the uniform system in Chapter 7 to describe the nematic and superfluid order in the EP phase.

To compare with experimental results, we measure

$$\eta(t) \equiv N_0(t)/N, \tag{8.53}$$

$$N_m(t) = \int_w d\boldsymbol{\rho}\, |\psi_m(t)|^2. \tag{8.54}$$

The experiment measured η as the $m = 0$ fraction of the total condensate. We tried various momentum-space and position-space windowing options to approximate capturing just the condensate fraction and got very similar results for all. Here we focus on the population inside the observable window since we can link this to Bogoliubov theory for an approximate uniform system.

8.5 Results

8.5.1 Comparison with experimental observations

The initial population of the condensate depletes as the unstable modes cause spin exchange collisions to drive atoms from the $m = 0$ component into the initially unoccupied $m \pm 1$ components. This also causes the spin density in the system to become non-zero.

Condensate depletion

In the experiments the $m = 0$ condensate population was measured as a function of time, and characterized by

$$\eta(t) \equiv N_0(t)/N_0(0), \tag{8.55}$$

where $N_0(t)$ is the $m = 0$ condensate population. Because we only have $\sim 2\%$ non-condensate in our simulations the distinction between condensate and thermal is negligible in the early-time dynamics. In practice we take $N_0(t)$ equal to the total $m = 0$

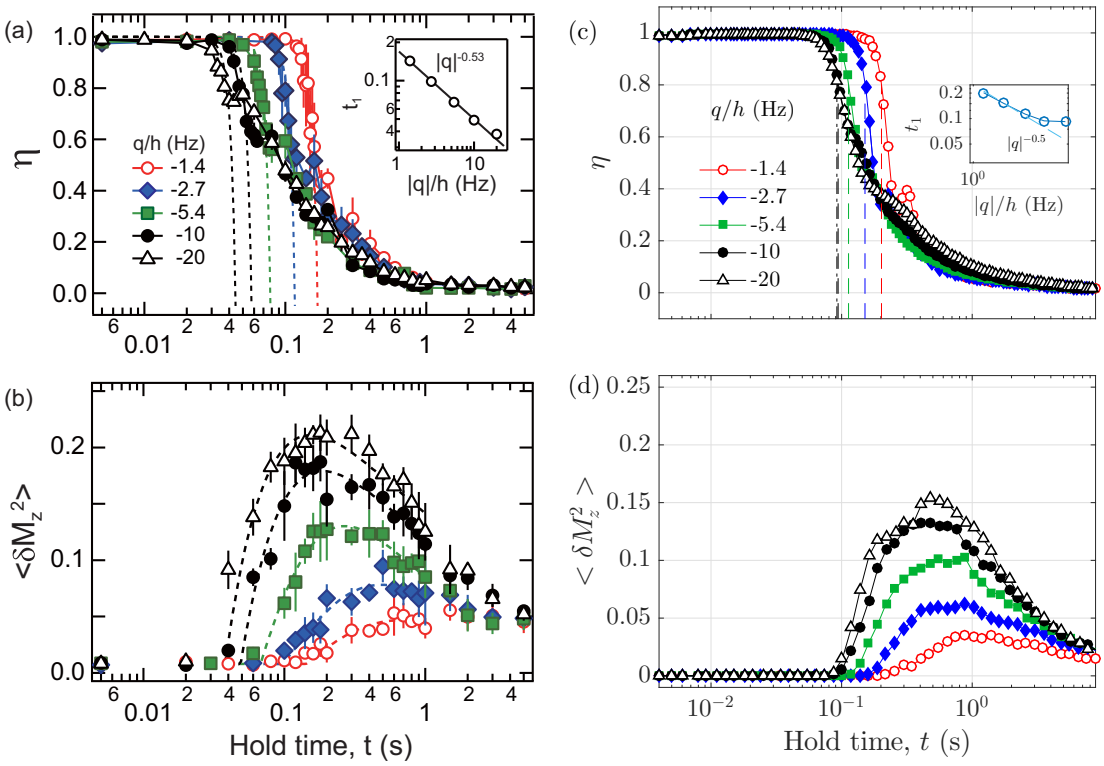

Figure 8.2: Decay of η. Inset shows t_1, where $\eta(t_1) = 0.8\eta(0)$. Simulations were averaged over four trajectories with independent noise in the initial conditions of each trajectory.

population within the analysis window. In Fig. 8.2 we compare the experimental results [Fig. 8.2(a)] with our simulation results [Fig. 8.2(c)]. We observe qualitatively similar behaviour for the decay of η. In the experiments a decay time t_1 for η was introduced, defined by

$$\eta(t_1) = 0.8. \tag{8.56}$$

Experimentally t_1 was seen to scale as $t_1 \sim |q|^{-0.5}$ [see inset to 8.2(a)], whereas we see a clear departure from this in our simulations for larger $|q|$ values [see inset to 8.2(c)]. At the Bogoliubov level the $|q|^{-0.5}$ scaling is predicted for shallow quenches (i.e. $|q| < c_1 n$), where the imaginary part of the unstable Bogoliubov energies (8.41) is $\Gamma_k = \mathrm{Im}\{E_k\} \sim \sqrt{|q|}$. For the deepest two quench values we observe deviation from the $t_1 \sim |q|^{-0.5}$ scaling seen in the experiment for all quench values. Using (8.35) we have $(c_1 n)^{2D}_{\mathrm{av}}/h \approx 8.7\,\mathrm{Hz}$, so the departure from $|q|^{-0.5}$ scaling we find occurs when $|q|$ exceeds $(c_1 n)^{2D}_{\mathrm{av}}$. We return to discuss this growth rate in Sec. 8.5.3.

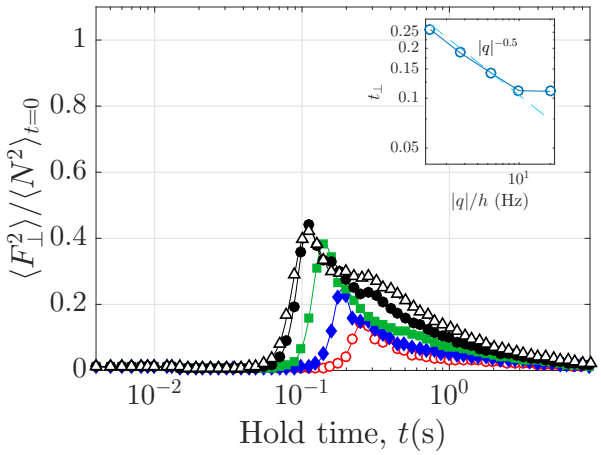

Figure 8.3: Evolution of $x - y$ magnetization (squared, normalized to mean total density squared at time $t = 0$). Inset shows the time $t_\perp$ for the planar magnetization to reach its peak, as a function of the quench depth $|q|$. The line showing $|q|^{-0.5}$ scaling is a guide to the eye.

Axial spin fluctuations

Adopting the notation of the experimental group we also quantify the axial magnetic fluctuations

$$\langle \delta M_z^2 \rangle \equiv \frac{1}{A_w N_{w,t=0}^2} \int_w d\boldsymbol{\rho} F_z(\boldsymbol{\rho})^2, \tag{8.57}$$

noting that since $M_z = \int d\boldsymbol{\rho} F_z(\boldsymbol{\rho})$ is zero (by the initial condition) and conserved, the above expression gives the fluctuations arising from the dynamics following the quench. We also note that $\langle \delta M_z^2 \rangle = G_{F_z}(0)$. We see qualitatively similar behaviour for $\langle \delta M_z^2 \rangle$ between experiment [Fig. 8.2(b)] and simulation [Fig. 8.2(d)], although the experimental values are larger for deeper quenches and the two deepest quenches are appreciably different in experiment while in simulation they are more similar.

8.5.2 Other local observables

To understand the early-time dynamics it is also useful to consider two other local observables, which were not examined in the experiment.

In Figures 8.3 and 8.4 we show the evolution of the transverse magnetization, i.e. $|F_\perp|^2$, and transverse alignment, i.e. $|\mathcal{A}_\perp|^2$ in the central spatial window. These are the local

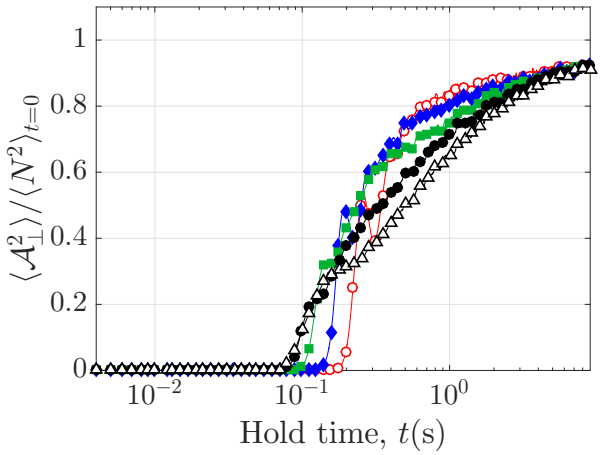

Figure 8.4: Evolution of $x-y$ alignment (squared, normalized to mean total density squared at time $t = 0$).

order parameters for characterizing planar ferromagnetic and antiferromagnetic order respectively, which can reveal the presence of the post-quench planar EP ground state.

We observe the transverse magnetization grows first, driven directly by the unstable Bogoliubov excitations. As this reaches a maximum and begins to decay, the transverse alignment grows as the order of the final state emerges locally. The time of the peak value of $|F_\perp|^2$ is plotted in the inset as $t_\perp$, and shows $|q|^{-0.5}$ scaling for all but the deepest quench (this timescale is longer than t_1, but has similar behaviour, see Fig. 8.2). As the Bogoliubov theory predicts the transverse magnetization to grow exponentially, $t_\perp$ locates an upper limit to the times over which the Bogoliubov treatment is valid.

The decay of $|F_\perp|^2$ after $t_\perp$ is much quicker than the decay of F_z seen in Fig. 8.3, which is consistent with the system moving towards an antiferromagnetic ground state with HQVs whose cores are filled with F_z.

In Fig. 8.4 we show the evolution of perpendicular alignment, i.e. $|\mathcal{A}_\perp|^2$, in the central spatial window. This is an important observable because $|\mathcal{A}_\perp|^2$ characterizes the nematic order of the new antiferromagnetic EP ground state after the quench. Indeed, we see that the perpendicular alignment grows towards saturation at long times. Coupled with the decay of perpendicular magnetization, this indicates the presence of the EP state.

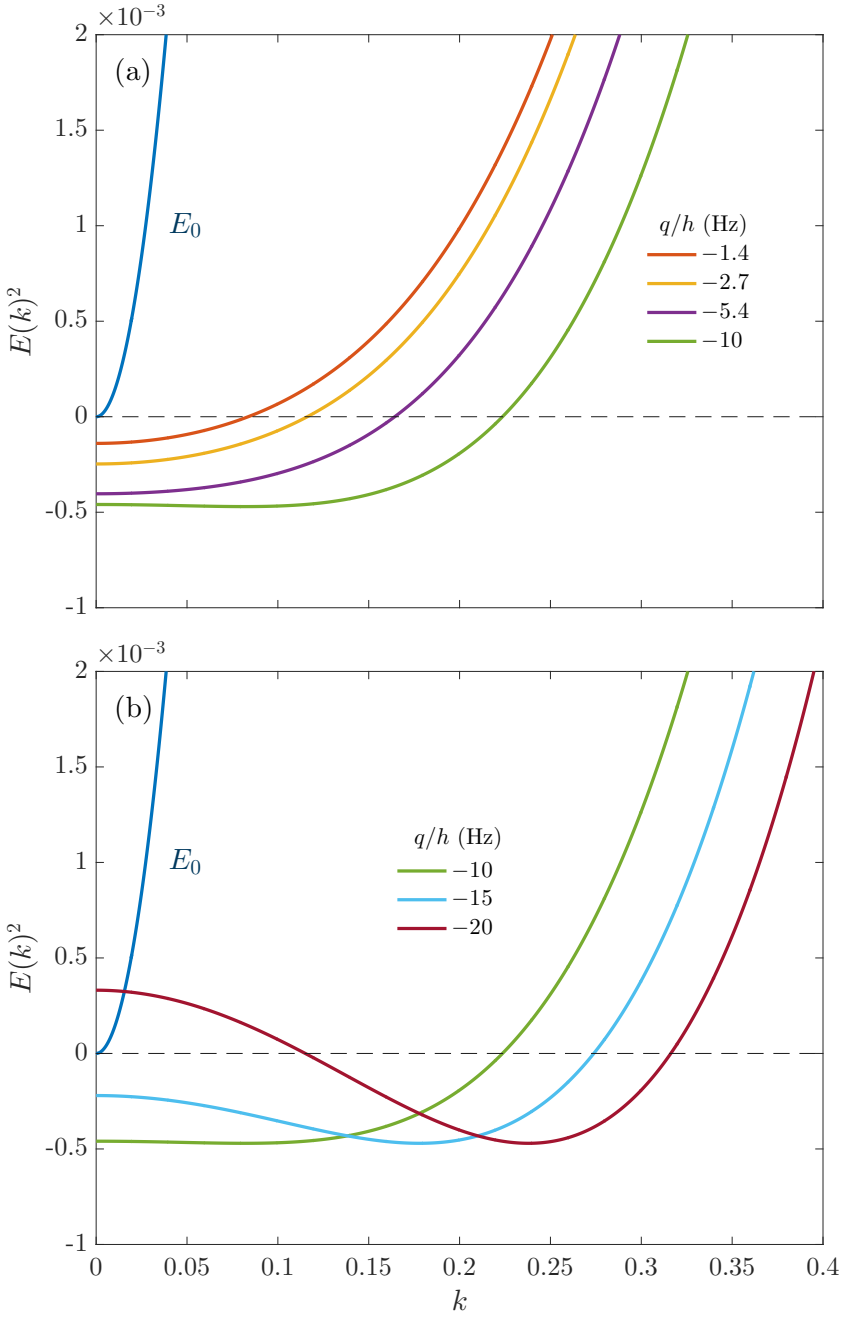

Figure 8.5: Excitation spectra of initial EA polar state immediately after the quench. We plot the squared Bogoliubov energies, so that negative values indicate a dynamical instability at the corresponding wavevector. We show the stable phonon mode E_0 for scale, and plot the unstable branch, composed of the axial and transverse magnon modes (degenerate at $p = 0$). (a) shows shallow quench values, with $E_{\pm 1}(0) \sim |q|^{-0.5}$. (b) shows deep quench values, with the most unstable energy being constant with q.

8.5.3 Early-time Bogoliubov comparison

Excitation spectra after the quench

In Fig. 8.5 we show the excitation spectra of the initial state immediately after quenching to negative q. The three dispersion relations for the Bogoliubov excitations are

$$E_0(k) = \sqrt{\epsilon_k(\epsilon_k + 2(c_0 n)^{2D}_{\rm av})}, \tag{8.58}$$

$$E_{\pm 1}(k) = \sqrt{(\epsilon_k + q)(\epsilon_k + q + 2(c_1 n)^{2D}_{\rm av})} \mp p, \tag{8.59}$$

corresponding to density/phonon (E_0) and spin wave ($E_{\pm}1$) excitations respectively. Because we have $F_z = 0$ in our initial condition, we have $p = 0$, and the $E_{\pm 1}$ spin-wave branches are degenerate. As discussed earlier, it is these branches that go unstable following the quench. Figure 8.5(a) shows that for shallow quenches [$|q| < (c_1 n)^{2D}_{\rm av} \approx h \times 8.7\,\mathrm{Hz}$] the maximum instability is at $k = 0$, with $E_{\pm 1}(0) \sim |q|^{-0.5}$. Figure 8.5(b) shows that for deeper quenches the wave-vector k of maximum instability takes on a finite non-zero value, with the unstable energy staying constant with q. This behaviour seems to qualitatively agree with our numerical calculations that show that t_1 saturates for $|q| \gtrsim (c_1 n)^{2D}_{\rm av}$.

Decay of η

For $q < 0$ the Bogoliubov energy is imaginary for a range of k. The most imaginary energy is $E_{\rm mi} = \sqrt{\bar{q}(\bar{q}+2)}(c_1 n)^{2D}_{\rm av}$ for $-1 < \bar{q} < 0$, and $E_{\rm mi} = i(c_1 n)^{2D}_{\rm av}$ for $\bar{q} < -1$, with $\bar{q} \equiv q/(c_1 n)^{2D}_{\rm av}$. We can then approximate $S(0) \sim e^{2|E_{\rm mi}|t/\hbar}$ which gives

$$\log_{10} \frac{(c_1 n)^{2D}_{\rm av} t_1}{\hbar} = c - \frac{1}{2} \begin{cases} \log_{10}|\bar{q}| + \log_{10}(\bar{q}+2) & -1 < \bar{q} < 0 \\ 0 & \bar{q} < -1 \end{cases} \tag{8.60}$$

as shown in Fig. 8.6, where c is an arbitrary constant. This simple approximation is seen to agree very well with with our simulations of the trapped 3D system [crosses in Fig. 8.6].

In general we find good agreement between the Bogoliubov predictions and our GP simulations with truncated Wigner initial conditions. However, these both predict that the growth time of excitations saturates when $|q|$ exceeds $(c_1 n)^{2D}_{\rm av}$. In contrast, the experiment finds that the time scale for deeper quenches continues to decrease with $|q|$ as $1/\sqrt{|q|}$. We have explored artificially increasing the noise in the initial condition of

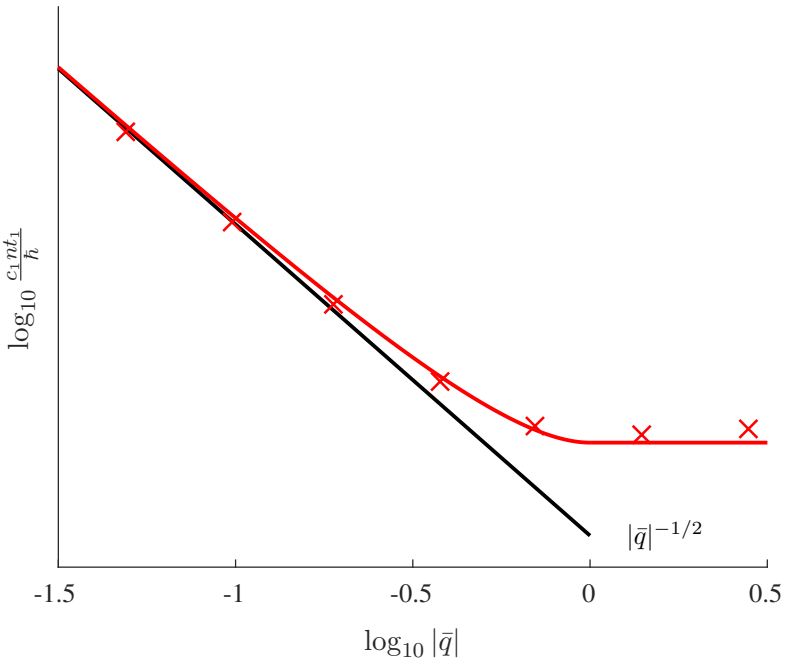

Figure 8.6: Approximate Bogoliubov prediction for t_1 [i.e. Eq. (8.60)] (red) and $|\bar{q}|^{-1/2}$ (black). Red crosses are numerical data for the trapped system (average of 64 trajectories).

our simulation to make the instability faster, but were unable to get good agreement without making very large changes. Possible explanations for this discrepancy include uncertainty in the number of atoms in the condensate, uncertainty in the experimental interaction parameters, heating from the microwave dressing, and effects from magnetic field gradients in the experiment.

Growth of correlations

In addition to considering local observables in the short-time evolution it is also of interest to consider the non-local correlation functions given earlier in Eq. (8.49) - (8.52). We show some examples of how these correlation functions evolve in Figs. 8.7 -8.9 which differ in the value of q. In each case we plot the results for the Bogoliubov quasi-2D uniform predictions against the full trapped GP simulations for times up until when the initial $m = 0$ condensate is depleted to 25% of its initial population, at which point the Bogoliubov theory is clearly invalid.

Because the GP simulations are not for a translationally invariant system they depend on

the centre of mass and relative coordinates. Thus we evaluate the correlation functions by spatially averaging over the windowed region:

$$G_Q(\mathbf{r}) = \int_w d\boldsymbol{\rho} \int_w d\boldsymbol{\rho}'\, G_Q(\boldsymbol{\rho}, \boldsymbol{\rho}')\delta(\boldsymbol{\rho} - \boldsymbol{\rho}' - \mathbf{r}), \tag{8.61}$$

where $Q = \{F_z, F_\perp, \theta, \phi\}$. In practice we evaluate these from our simulations using the convolution theorem, i.e. as

$$G_Q(\mathbf{r}) = \int d\mathbf{k} \left| \int_w d\boldsymbol{\rho} e^{i\mathbf{k}\cdot\boldsymbol{\rho}} M(\boldsymbol{\rho}) \right|^2 e^{-i\mathbf{k}\cdot\mathbf{r}}, \tag{8.62}$$

where M is the appropriate operator to be correlated. We radially average, i.e. $\mathbf{r} \to r$, and normalize by the area in the spatial window A_w. We also normalize by an extra factor of $1/4n$ for $G_{F_\perp}$ and a factor of $1/4$ for G_θ. All correlation plots then use the same dimensionless colour scale varying from -1 (blue) to 1 (yellow).

These results show that the evolution of the correlation functions is quite rich as q varies. For the homogeneous Bogoliubov theory this behaviour clearly emerges from the changing nature of the dispersion relation (see Fig. 8.5). For example, the fine spatial structures that develop in the quenches to large $|q|$ values, where the most unstable modes occur at finite k values. We also observe that the spatially averaged results from the full trapped calculations are in many cases qualitatively well described by uniform Bogoliubov theory, especially for shallow quenches.

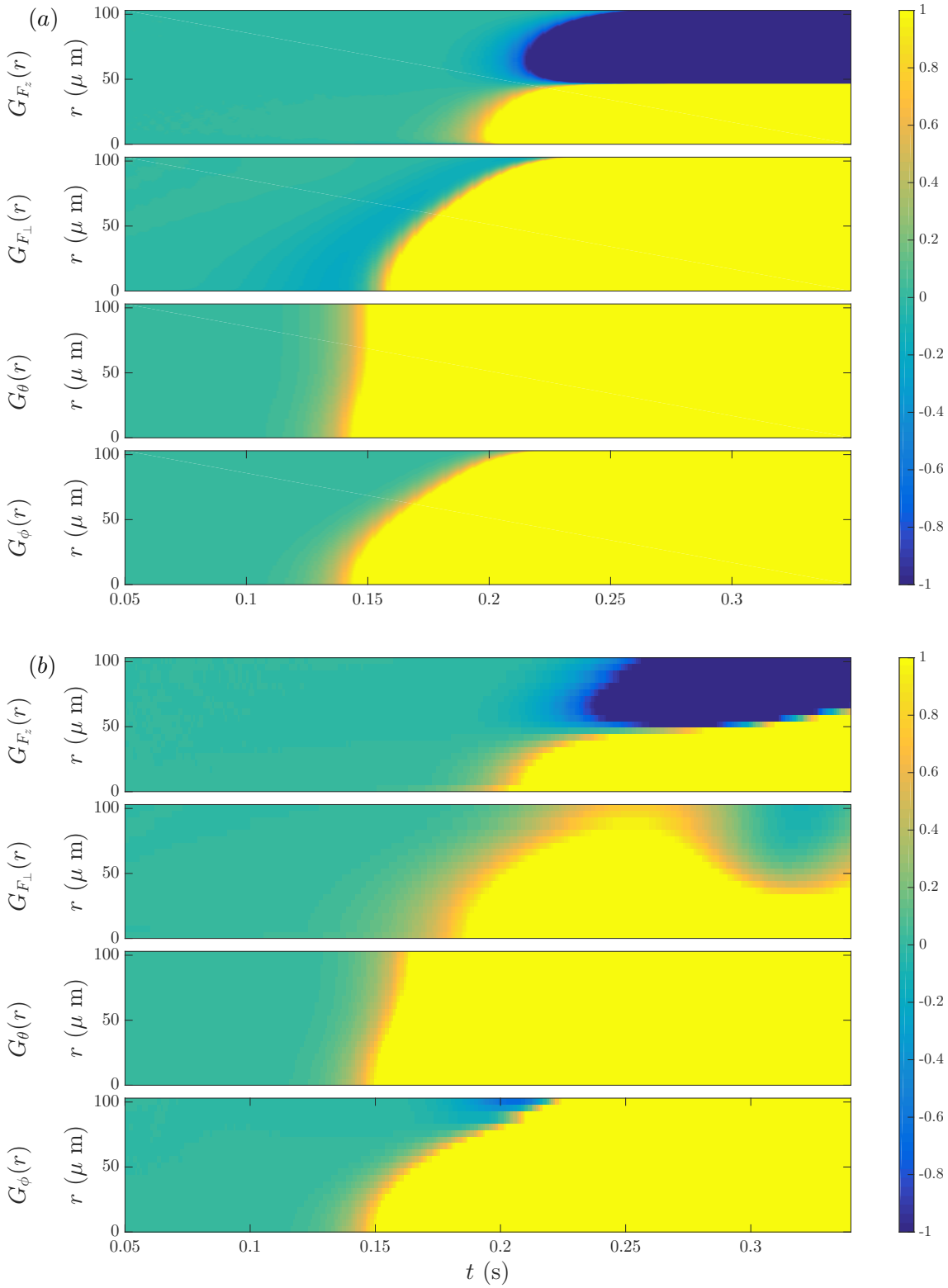

Figure 8.7: Correlation functions from (a) uniform Bogoliubov compared with (b) simulations for $q/h = -1.4$ Hz. Simulations are averaged over 64 trajectories with independent noise in the initial conditions.

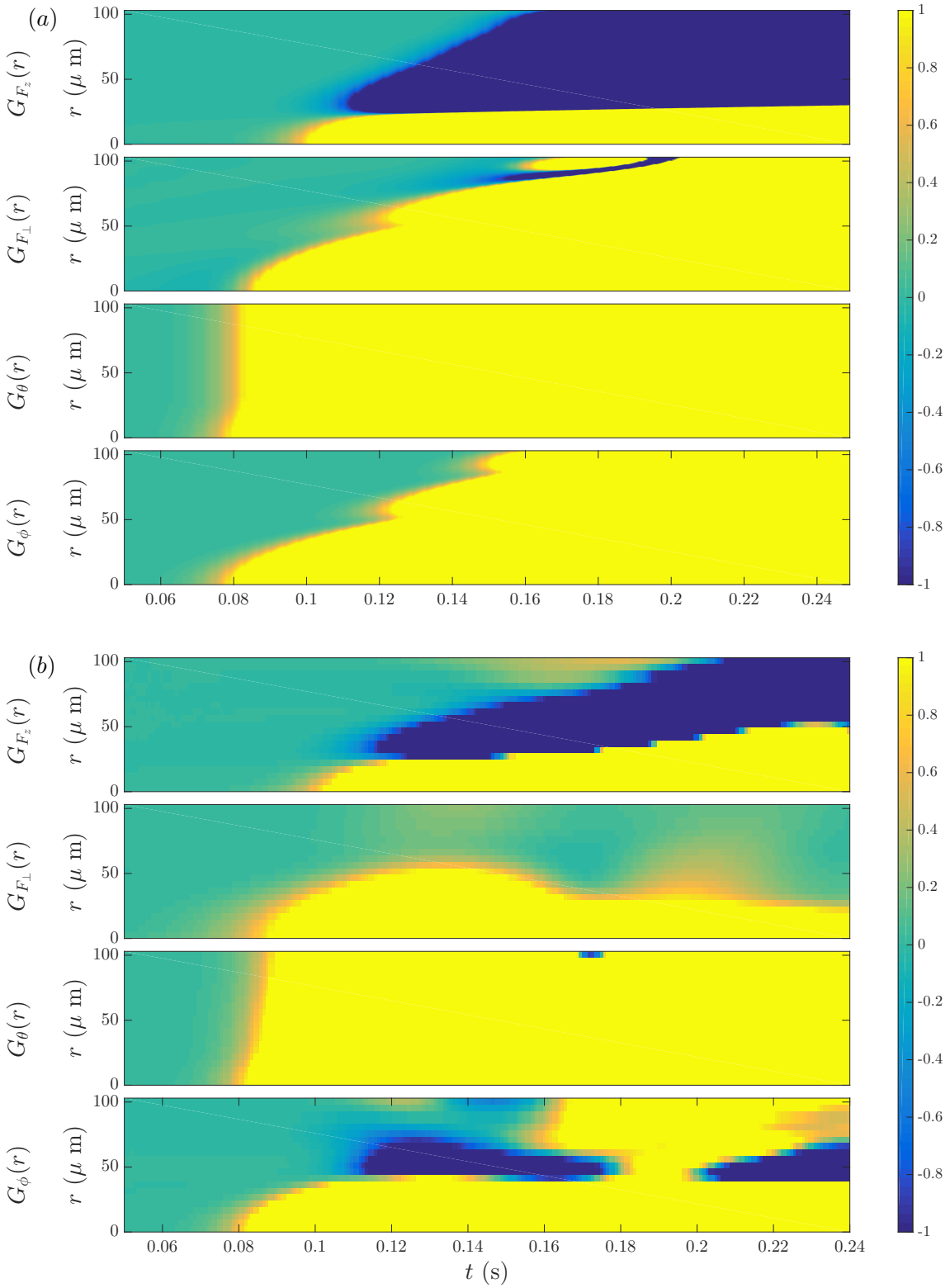

Figure 8.8: Correlation functions from (a) uniform Bogoliubov compared with (b) simulations for $q/h = -5.4$ Hz. Simulations are averaged over 64 trajectories with independent noise in the initial conditions.

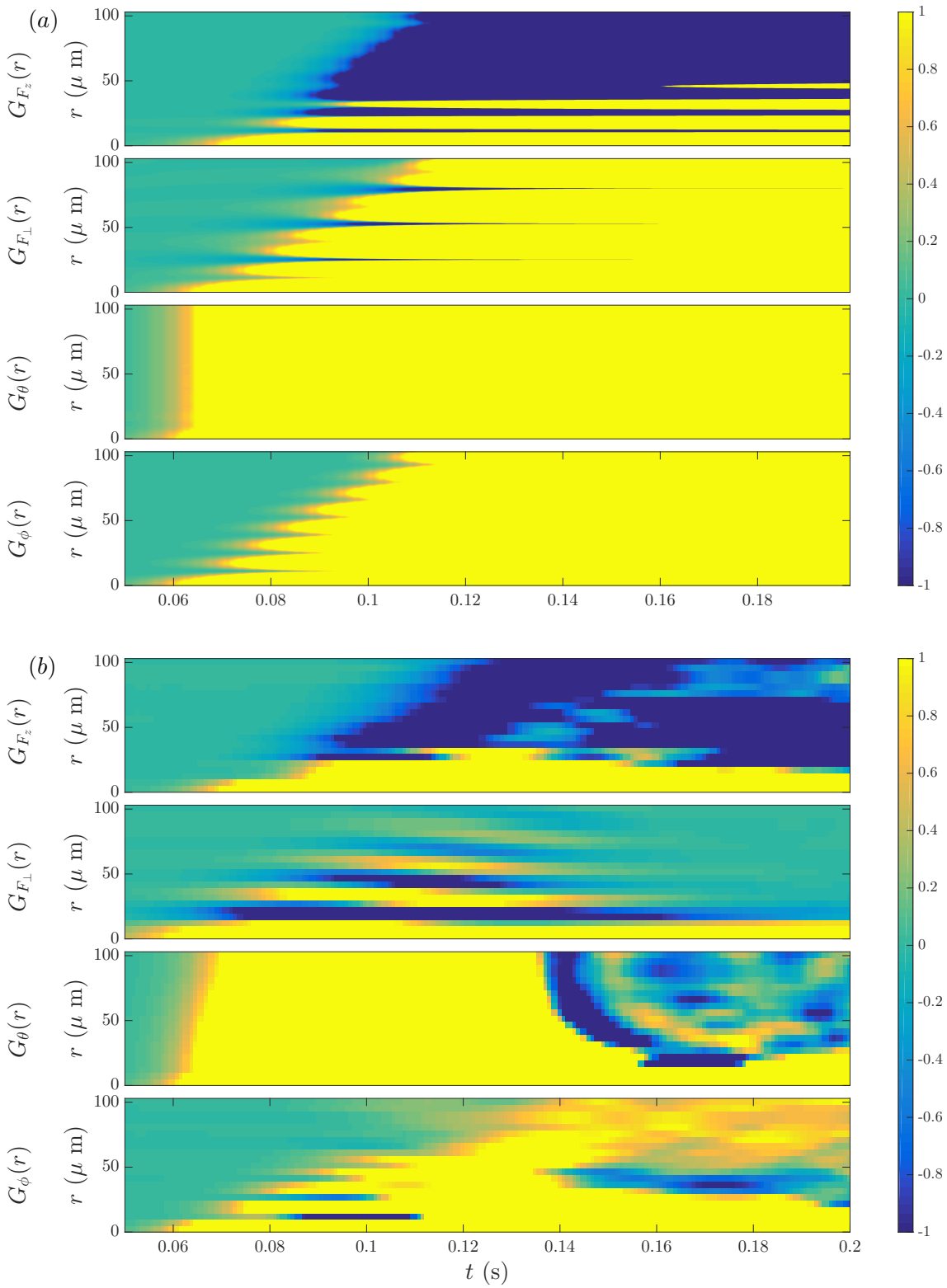

Figure 8.9: Correlation functions from (a) uniform Bogoliubov compared with (b) simulations for $q/h = -20$ Hz. Simulations are averaged over 64 trajectories with independent noise in the initial conditions.

8.5.4 Late-time coarsening of nematic domains

In the first part of this chapter we have focused on comparing our simulation results with the short-time dynamics observed in experiments. We have also introduced a simple approximate Bogoliubov theory that we have demonstrated as a capable description of this regime. We now turn to consider the late-time dynamics after the perpendicular alignment order of the EP state is locally established in the system. To do this we consider the evolution of the length scales associated with the correlation functions considered in the last subsection. As in the previous chapter, we define these as the length over which the spatially averaged correlation function decays to a quarter of its local value, i.e.

$$G_Q(L_Q) = \frac{1}{4}G_Q(0), \quad Q = \{F_z, F_\perp, \theta, \phi\}. \tag{8.63}$$

In Fig. 8.10, we present results for the evolution of these lengths for a shallow quench to $q = -1.4$Hz and a deeper quench to $q = -20$Hz.

For the shallow quench we see L_θ and L_ϕ grow first, with L_θ saturating to the system size and staying there throughout the post-instability dynamics, while L_ϕ rises to match it at late times in a manner that appears consistent with $t^{0.5}$ scaling (with a log correction). As expected in the EP phase the spin order is transient and both L_z and $L_\perp$ decay at long times as the nematic order embeds itself. For these shallow quenches the unstable modes have a long wavelength, comparable to the system size, so the domains that are initially established after the quench have little room to grow.

The deeper quench has curious transient behaviour where L_θ initially saturates close to the system size while all other length scales are suppressed by about an order of magnitude. This behaviour was also apparent in the correlation function evolution shown in Fig. 8.9. Then L_θ quickly decays down to a similar size as the other lengths[5]. The system now begins to exhibit very clear phase ordering: L_θ and L_ϕ grow like $t^{0.5}$ (with log correction) and approach the system size. Meanwhile, L_z and $L_\perp$ remain about an order of magnitude smaller. These results suggest that the experiments conducted by Kang *et al.* [150] for deeper quenches were in a regime where phase ordering could

[5] L_θ is initially very large due to the global phase coherence of the initial condition, which is initially carried over to $\psi_{\pm 1}$ in the short-time dynamics but subsequently disrupted by the collapse of the early-time order. This collapse is stronger with deeper quenches, and is responsible for breaking up the initial structures formed at early times.

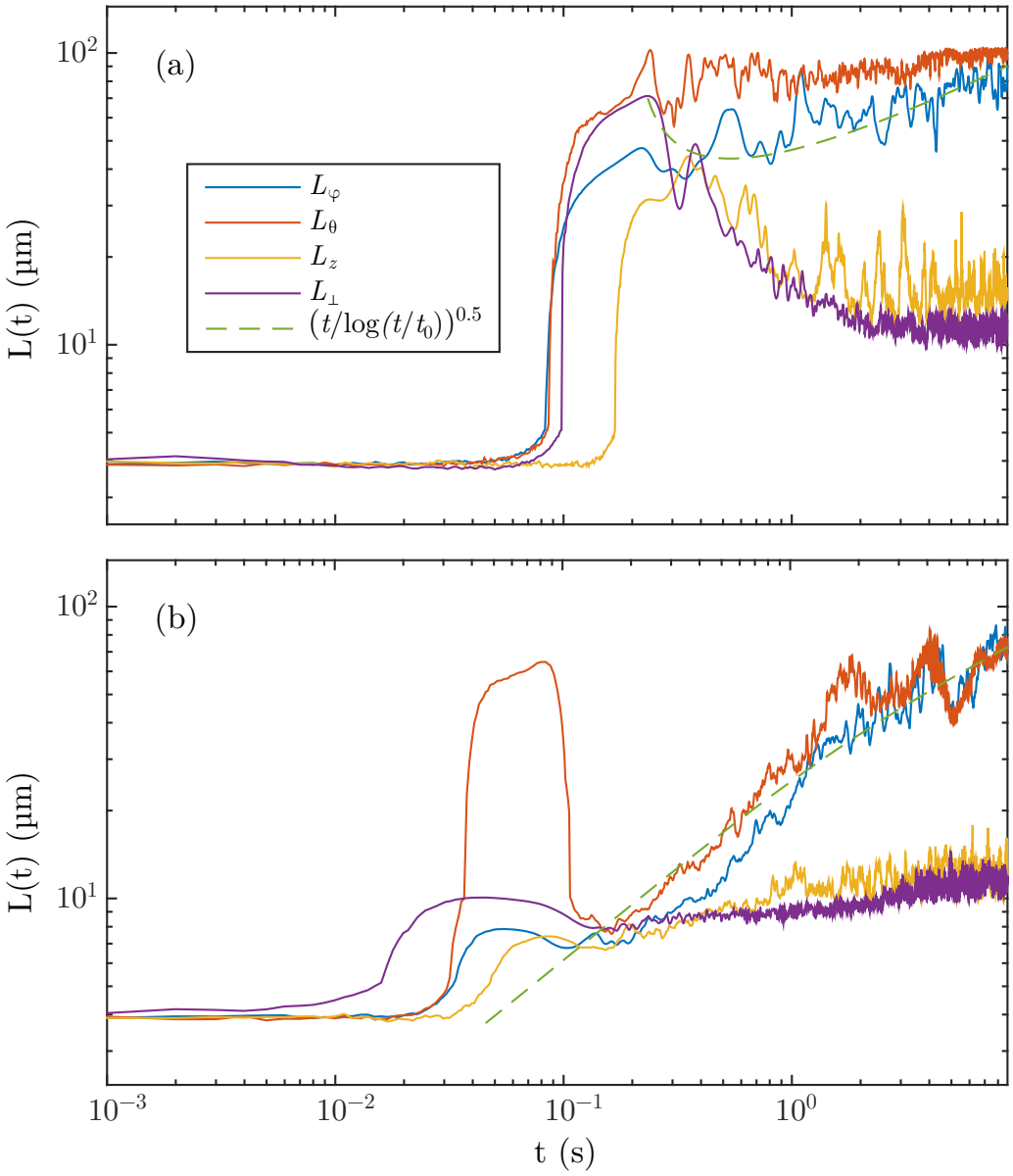

Figure 8.10: Growth of average domain size for several observables, for a shallow quench to $q = -1.4$ Hz in (a) and a deep quench to $q = -20$ Hz in (b). Dashed lines are fits of L_ϕ to a $t^{1/2}$ power law (with log correction). Correlation functions were averaged over four trajectories with independent noise in the initial conditions.

be observed. Indeed, nematic domains could potentially be observed to grow by about an order of magnitude in length over about 10 seconds of evolution.

8.5.5 Late-time decay of defects

While our results of the last subsection show that phase ordering occurs for deep quenches, currently it is not viable to measure the nematic order in experiments. However, the topological defects of the order, notably HQVs (see Section 3.3.1), are readily observable in experiments. In particular, their magnetized cores are readily imaged using magnetic sensitive *in-situ* imaging techniques. Here we consider the evolution of the HQV number as an alternative way to quantify the phase ordering in the system.

In Fig. 8.11 we show the decay of the average number of HQVs, where we count HQVs as the total number of vortices in the $m = \pm 1$ components restricted to the central windowed region of the trap. We also plot the expected number of HQVs, based on the length scale L_ϕ shown in Fig. 8.10. We find that for shallow quenches, the number of vortices decays to 1 very quickly, indicating that the system has reached an equilibrium state of one domain across the whole system. Thus for shallow quenches there is not enough time to observe the coarsening of multiple domains.

For deeper quenches, however, we find that the number of vortices scales with the expected number of HQVs for $0.1 < t < 2$, after which there are less than 10 vortices and we see finite-size effects of the system start to dominate as we approach zero vortices. This is evidence that deep quenches are accessing the universal coarsening regime, with the decay of vortices in $\psi_{\pm 1}$ revealing the growing length scale of domains.

8.6 Conclusion

We have carried out simulations of a recent spin-1 antiferromagnetic quench experiment, including a harmonic trapping potential and using experimental parameter values for the interactions. We find good qualitative agreement with many of the features observed in the decay of the initial condensate and the initial growth of F_z fluctuations. Both in our full calculations and in a simplified Bogoliubov theory we find that the decay saturates for large q-quenches, a prediction that differs from experiments and deserves

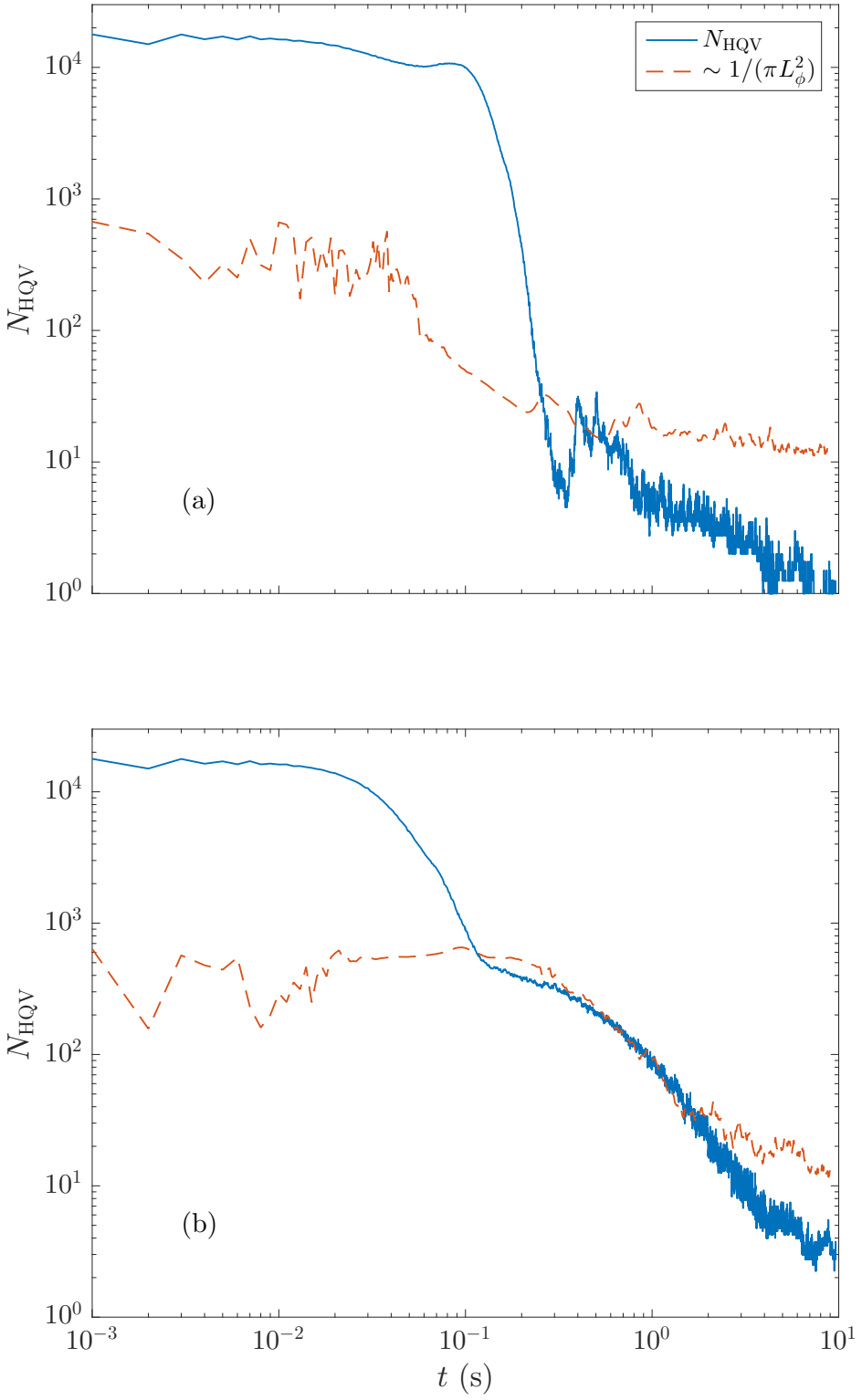

Figure 8.11: Decay of HQVs for a quench to $q = -1.4$ Hz in (a) and a quench to $q = -20Hz$ in (b). Dashed lines show scaling of the expected number of HQVs given the average size of nematic domains. Results are from the average of four trajectories with independent noise in the initial conditions.

further investigation.

Applying our formalism to the spin-1 antiferromagnetic quench, we measured our new perpendicular alignment order parameter, and found that it grows and saturates at long times. We show that the correlation function of this order parameter exhibits universal scaling at long times, with a $t^{0.5}$ growth law (with log correction), and find this is connected to the decay of vortices which separate the ordered domains.

Chapter 9

Spin-2 Cyclic quench

9.1 Introduction

In this Chapter we consider nematic quenches in the spin-2 system. The phase diagram for spin-2 is richer than that for spin-1 due to there being an extra independent nonlinear interaction, the spin singlet amplitude (see Chapter 2). As we explored in Section 3.2 of Chapter 3, the spin-2 system has two nematic phases roughly analogous to the spin-1 EA and EP polar phases, i.e. the UN (uniaxial nematic) and BN (biaxial nematic) phases. A new phase appears (at zero magnetic field) when all nonlinear interaction parameters are positive, the C_3 cyclic phase, which has third-order cyclic symmetry and supports 1/3 fractional spin-superfluid coupled vortices. The ground state phase diagram for $c_1 > 0$ and $4c_1 > c_2 > 0$, in the presence of a quadratic Zeeman shift q, has BN at large negative q, C_3 at $q = 0$, and UN at large positive q, with an interpolation phase D_2 for small $|q$.

We investigate quenching from both the UN and the BN phase into the cyclic phase at $q = 0$. We select appropriate order parameters sensitive to the cyclic symmetry of the C_3 ground state, which enable us to measure the fractional spin and global phase domains which appear following the quench.

Using our S4 symplectic algorithm (which is required to efficiently resolve the quench dynamics to sufficient accuracy), we carry out long-time simulations of the quench, out to 10^5 spin times. We consider correlation functions of the order parameters over time, and extract length scales to examine how they scale during long-time coarsening

dynamics. We compare the growth of domains with the decay of 1/3 global phase vortices supported by the cyclic phase and measured by our global phase order parameter.

9.2 UN and BN to Cyclic quenches

Recalling the phase diagram of Figure 3.6 in Chapter 3, we consider quenches into the cyclic phase at $q = 0$, starting from each of the UN and BN phases. As we saw in Section 3.2, the UN phase has $SO(2)$ symmetry, while the BN phase breaks $SO(2)$ symmetry but retains D_4 symmetry (the symmetry of a square in the x-y plane). This means that a UN to C_3 quench will form more defects since the ensuing dynamical instability will cause spontaneous symmetry breaking of a *continuous* symmetry. The BN to C_3 quench is more restricted in the defects that can form due to the BN phase already breaking $SO(2)$ symmetry.

9.2.1 Cyclic order parameters

The cyclic phase has higher order nematic symmetry, with the point group symmetry of a tetrahedron. Analysis of generalized nematics, with nematic order of an arbitrary point group symmetry, is a current area of theoretical development [172–177]. The experimental measurement of higher order nematics presents challenges due to their complex and subtle nature. The spin-2 system with the C_3 phase offers a potential pathway to experimental measurement of third order (octupolar) nematic symmetry.

To characterize the order of the cyclic phase, we use two order parameters: one to couple to the spin-nematic rotational order, and one that couples to the global phase superfluid order. The formalism of Chapter 3, in particular Section 3.2, shows that the octupolar order of the C_3 state is revealed by $\mathcal{T}^{(3)}$ [defined in Eq. (2.86)]. Indeed, revealing the presence of third order rotational symmetry requires a third order tensor order parameter [172]. $\mathcal{T}^{(3)}$ is the third order traceless symmetric observable in an irreducible multipole expansion of rotationally symmetric operators, and couples to the spin-nematic rotation angles. Considering the cyclic vortex states in Eq. (3.77), $\mathcal{T}^{(3)}$ is sensitive to the spin rotation ϕ that describes $SO(2)$ rotation of the spinor.

However, the $\mathcal{T}^{(3)}$ order parameter is not sensitive to superfluid order in the global phase, θ. To couple to θ requires an operator other than a spin-nematic $\psi^\dagger$-ψ operator

(e.g. Eq. (2.13) vs Eq. (2.36)).

Recall that the Cartesian representation of the cyclic state (see Section 3.2.3) is characterized by the spin-singlet trio amplitude [Eq. (3.62)],

$$\alpha_{30} = \psi_0^3 - 3\psi_0\left(\psi_{+1}\psi_{-1} + 2\psi_{+2}\psi_{-2}\right) + 3\sqrt{\frac{3}{2}}\left(\psi_{+1}^2\psi_{-2} + \psi_{+2}\psi_{-1}^2\right). \tag{9.1}$$

Substituting the cyclic vortex states of Eq. (3.77) into this, we find that $\alpha_{30} \sim e^{i3\theta}$, and is thus sensitive to the 1/3 and 2/3 superfluid windings that appear in cyclic vortices as explained in Section 3.3.3.

9.3 Initial conditions

The initial conditions for our spin-2 quenches are constructed in a similar manner to the spin-1 procedure we outlined in Chapter 7. We assume periodic boundary conditions and consider a 2D system of N^2 grid points with spatial area L_{sys}^2. We fix the spatial resolution to be $N/L_{\text{sys}} = 1.28$ in order to resolve the spin healing length, while keeping the system relatively coarse to resolve any length scales which grow large at long times.

We prepare the zero-temperature initial states

$$\psi(x, t=0)_{\text{UN quench}} = \psi_{UN} + \delta_{UN}, \tag{9.2}$$

$$\psi(x, t=0)_{\text{BN quench}} = \psi_{BN} + \delta_{BN}, \tag{9.3}$$

where the δ_{UN} and δ_{BN} are vectors with noise sampled according to the truncated Wigner prescription, i.e. we take the Bogoliubov modes about the ground state and populate them with quantum noise. By considering the large $|q|$ limit for $p = F_z = 0$, we have relatively simple excitations: for UN we have a phonon mode and four single-particle-like modes, while for BN we have a phonon mode, an axial magnon mode, and three single-particle-like modes.

9.3.1 UN Bogoliubov noise

The Bogoliubov excitation energies for the UN phase [32] are

$$E_{k,0} = \sqrt{\epsilon_k(\epsilon_k + 2(c_0 + c_2)n)}, \tag{9.4}$$

$$E_{k,\pm1} = \sqrt{(\epsilon_k + q)(\epsilon_k + q + 2(3c_1 - c_2)n)}, \tag{9.5}$$

$$E_{k,\pm2} = \sqrt{(\epsilon_k + 4q)(\epsilon_k + 4q - 2c_2 n)}. \tag{9.6}$$

In the large $|q|$ limit, the corresponding excitation modes $\hat{b}_{k,m}$ are

$$\hat{b}_{k,0} = u_0 \hat{a}_{k,0} + v_0 \hat{a}^\dagger_{-k,0}, \tag{9.7}$$

$$u_0 = \mathrm{sgn}(c_0 + c_2)\sqrt{\frac{\epsilon_k + (c_0 + c_2)n + E_{k,0}}{2E_{k,0}}}, \quad v_0 = \sqrt{u_0^2 - 1}, \tag{9.8}$$

$$\hat{b}_{k,\pm 1} = \mathrm{sgn}(3c_1 - c_2)\hat{a}_{k,\pm 1}, \tag{9.9}$$

$$\hat{b}_{k,\pm 2} = \mathrm{sgn}(-c_2)\hat{a}_{k,\pm 2}, \tag{9.10}$$

where $\hat{a}^\dagger_{k,m}$ creates a particle of momentum k in the spin component m and $\mathrm{sgn}(x)$ gives the sign of x. The $m = 0$ excitation is a phonon mode on top of the condensate in $m = 0$, while the other four modes (with $u_m = 1$ and $v_m = 0$) are single-particle-like. We construct the truncated Wigner noise as

$$\boldsymbol{\delta}^{UN}(\mathbf{x}) = \sum_{\boldsymbol{k}} \begin{pmatrix} \mathrm{sgn}(-c_2)\alpha_{\boldsymbol{k},2} e^{i\boldsymbol{k}\cdot\boldsymbol{x}} \\ \mathrm{sgn}(3c_1 - c_2)\alpha_{\boldsymbol{k},1} e^{i\boldsymbol{k}\cdot\boldsymbol{x}} \\ \alpha_{\boldsymbol{k},0} u_0 e^{i\boldsymbol{k}\cdot\boldsymbol{x}} - \alpha^*_{\boldsymbol{k},0} v_0 e^{-i\boldsymbol{k}\cdot\boldsymbol{x}} \\ \mathrm{sgn}(3c_1 - c_2)\alpha_{\boldsymbol{k},-1} e^{i\boldsymbol{k}\cdot\boldsymbol{x}} \\ \mathrm{sgn}(-c_2)\alpha_{\boldsymbol{k},-2} e^{i\boldsymbol{k}\cdot\boldsymbol{x}} \end{pmatrix}, \tag{9.11}$$

where the $\alpha_{\boldsymbol{k},m}$ are random complex gaussian fields with expectation $\langle \alpha^*_{\boldsymbol{k},m} \alpha_{\boldsymbol{k},m} \rangle = \frac{1}{2}$.

9.3.2 BN Bogoliubov noise

The Bogoliubov excitation energies for the BN phase [32] are

$$E_{k,2} = \sqrt{\epsilon_k(\epsilon_k + 2(c_0 + c_2)n)}, \tag{9.12}$$

$$E_{k,-2} = \sqrt{\epsilon_k(\epsilon_k + 2(4c_1 - c_2)n)}, \tag{9.13}$$

$$E_{k,\pm 1} = \sqrt{(\epsilon_k - 3q)(\epsilon_k - 3q + 2(c_1 - c_2)n)}, \tag{9.14}$$

$$E_{k,0} = \sqrt{(\epsilon_k - 4q)(\epsilon_k - 4q - 2c_2 n)}. \tag{9.15}$$

In the large $|q|$ limit, the corresponding excitation modes are

$$\hat{b}_{k,2} = u_2 \frac{\hat{a}_{k,2} + \hat{a}_{k,-2}}{\sqrt{2}} + v_2 \frac{\hat{a}^\dagger_{k,2} + \hat{a}^\dagger_{k,-2}}{\sqrt{2}}, \tag{9.16}$$

$$\hat{b}_{k,-2} = u_{-2} \frac{\hat{a}_{k,2} - \hat{a}_{k,-2}}{\sqrt{2}} + v_{-2} \frac{\hat{a}^\dagger_{k,2} - \hat{a}^\dagger_{k,-2}}{\sqrt{2}}, \tag{9.17}$$

$$\hat{b}_{k,\pm 1} = \mathrm{sgn}(c_1 - c_2)\hat{a}_{k,\pm 1}, \tag{9.18}$$

$$\hat{b}_{k,0} = \mathrm{sgn}(-c_2)\hat{a}_{k,0}, \tag{9.19}$$

$$u_2 = \mathrm{sgn}(c_0 + c_2)\sqrt{\frac{\epsilon_k + (c_0 + c_2)n + E_{k,2}}{2E_{k,2}}}, \tag{9.20}$$

$$u_{-2} = \mathrm{sgn}(4c_1 - c_2)\sqrt{\frac{\epsilon_k + (4c_1 - c_2)n + E_{k,-2}}{2E_{k,-2}}}, \tag{9.21}$$

where $\hat{a}^\dagger_{k,m}$ creates a particle of momentum k in the spin component m and $v_m = \sqrt{u_m^2 - 1}$. This includes a phonon mode, $\hat{b}_{k,2}$, a magnon mode $\hat{b}_{k,-2}$, and three single particle modes (with $u_m = 1$ and $v_m = 0$). We construct the truncated Wigner noise as

$$\boldsymbol{\delta}^{BN}(\mathbf{x}) = \sum_{\boldsymbol{k}} \begin{pmatrix} \frac{1}{\sqrt{2}}(u_2 + u_{-2})\alpha_{\boldsymbol{k},2} e^{i\boldsymbol{k}\cdot\boldsymbol{x}} - \frac{1}{\sqrt{2}}(v_2 + v_{-2})\alpha^*_{\boldsymbol{k},2} e^{-i\boldsymbol{k}\cdot\boldsymbol{x}} \\ \mathrm{sgn}(c_1 - c_2)\alpha_{\boldsymbol{k},1} e^{i\boldsymbol{k}\cdot\boldsymbol{x}} \\ \mathrm{sgn}(-c_2)\alpha_{\boldsymbol{k},0} e^{i\boldsymbol{k}\cdot\boldsymbol{x}} \\ \mathrm{sgn}(c_1 - c_2)\alpha_{\boldsymbol{k},-1} e^{i\boldsymbol{k}\cdot\boldsymbol{x}} \\ \frac{1}{\sqrt{2}}(u_2 - u_{-2})\alpha_{\boldsymbol{k},-2} e^{i\boldsymbol{k}\cdot\boldsymbol{x}} - \frac{1}{\sqrt{2}}(v_2 - v_{-2})\alpha^*_{\boldsymbol{k},-2} e^{-i\boldsymbol{k}\cdot\boldsymbol{x}} \end{pmatrix}, \tag{9.22}$$

where the $\alpha_{\boldsymbol{k},m}$ are random complex gaussian fields with expectation $\langle \alpha^*_{\boldsymbol{k},m} \alpha_{\boldsymbol{k},m} \rangle = \frac{1}{2}$.

9.4 Evolution & measurement procedure

We evolve the initial wavefunction in time using our S4 symplectic method developed in Chapter 5. We evolve to $t = 10^5 t_s$, using a time step of $\Delta t = 0.1$. This is close to the maximum allowed time step by the method, $\Delta t_{\max} = \pi/(\frac{1}{2}k^2_{\max} + 4|q|) = 0.19$, where $k_{\max} = \sqrt{2}N\pi/L_{\mathrm{sys}} = 5.7$.

Alternative integration methods, like S2 and RK4, require prohibitively small time steps to give the same low error growth as S4 symplectic method for the conserved quantities of the system of total number N, total F_z magnetization, and total energy E. With our choice of Δt we keep the relative energy error below 10^{-4}, the relative total number error below 10^{-8}, and the total F_z magnetization error (relative to total number) below 10^{-10}.

9.4.1 Early-time order and spatial correlations

After the quench, the singlet trio amplitude and octupole tensor are the relevant order parameters since they are sensitive to the cyclic order of the new ground state (see Section 3.2). We measure the total local order as

$$\langle |Q|^2 \rangle = \frac{1}{\lambda L_{\text{sys}}} \int d\mathbf{r}\ |Q|^2, \tag{9.23}$$

for

$$Q \in \{\mathcal{T}^{(3)}, \alpha_{30}, F_z, F_\perp, \alpha_{00}, N_0\}, \tag{9.24}$$

with $\lambda = n_c^2$ for all two-field operators, $\lambda = 2n_c^3$ for the trio amplitude α_{30}, and $\lambda = 18n_c^2$ for the octupole tensor $\mathcal{T}^{(3)}$. Note that the magnitude of the octupole tensor is given by the full trace, $\text{Tr}\{[T^{(3)}]^2\} = \sum_{abc} T_{abc}^2$.

We define the trio and octupole correlation functions as

$$G_\theta(r) = \frac{1}{2n_c^3} \langle \alpha_{30}^*(0)\alpha_{30}(r) \rangle, \tag{9.25}$$

$$G_\phi = \frac{1}{18n_c^2} \langle \text{Tr}\{\mathcal{T}^{(3)}(0)\mathcal{T}^{(3)}(r)\} \rangle, \tag{9.26}$$

which measure correlations of superfluid domains in the global phase and nematic domains in the spin degrees of freedom, respectively, as explained in Section 9.2.1.

We define the length scale of an average domain as the length where the correlation function decays to a quarter of its initial value, i.e.

$$G_{\theta,\phi}(L_{\theta,\phi}) = \frac{1}{4} G_{\theta,\phi}(0). \tag{9.27}$$

If the correlation function does not reach zero, we adjust to the following definition:

$$G_{\theta,\phi}(L_{\theta,\phi}) = \frac{1}{4}(G_{\theta,\phi}(0) - G_{\theta,\phi}^{\text{min}}), \tag{9.28}$$

where $G_{\theta,\phi}^{\text{min}}$ is the minimum value of G.

9.4.2 Spatial correlations and defects

We connect the length scale of average domains with vortices in the trio amplitude, which are 1/3 windings in the global phase. We detect vortices in α_{30} by first applying a gaussian blur two gridpoints wide (to remove nearest-neighbour, tightly-bound vortices) and then using a plaquette method to detect the grid points with phase windings of 2π.

9.5 Results

9.5.1 Early-time order

In Fig. 9.1 we plot the early-time dynamics of the local order operators defined in Eq. (9.24), for BN and UN initial conditions.

For the BN case (top), the initial unstable dynamics create trio amplitude α_{30}, octupolar order $\mathcal{T}^{(3)}$, and N_0 population. For the UN case (bottom), the initial dynamics create octupolar order, trio amplitude, and F_z population. While both initial conditions start with maximum spin-singlet order, i.e. $|\alpha_{00}|/n_c = 1$, the UN quench also has half the maximum trio amplitude and full population of N_0.

As the instability saturates at about $t = 3t_s$, both systems undergo rapid oscillations in their local order before settling into a new dynamical regime for $t > 5t_s$. In this regime the local order changes smoothly towards its long-time behaviour.

For both initial conditions, the long-time order looks similar, with octupolar order and spin-singlet trio amplitude order saturating, apart from the UN quench having more N_0 population. We note that the octupolar order is stronger than the spin-singlet trio order at these time scales.

9.5.2 Correlation functions

In Fig. 9.2 we plot the correlation functions G_θ and G_ϕ using coordinates rescaled by the length scales L_θ and L_ϕ, for BN and UN initial conditions. By definition, all correlation functions will cross through the point $r = 1$, $G = 0.25$. Collapse of the correlation functions above and below $r = 1$ gives evidence for being in the coarsening regime with universal scaling dynamics.

For both sets of initial conditions, G_θ and G_ϕ exhibit evidence of coarsening. For BN initial conditions it appears there may be two relevant length scales from $t = 10^2$ to $t = 10^4$ - a short range and a long range one - as there is a slight spread above and below $r/L = 1$. For UN initial conditions we have plotted the same time range, and the correlation function collapse for G_ϕ is similar to the BN case, while G_θ shows very good collapse at short length scales, indicating strongly scale invariant dynamics in this regime.

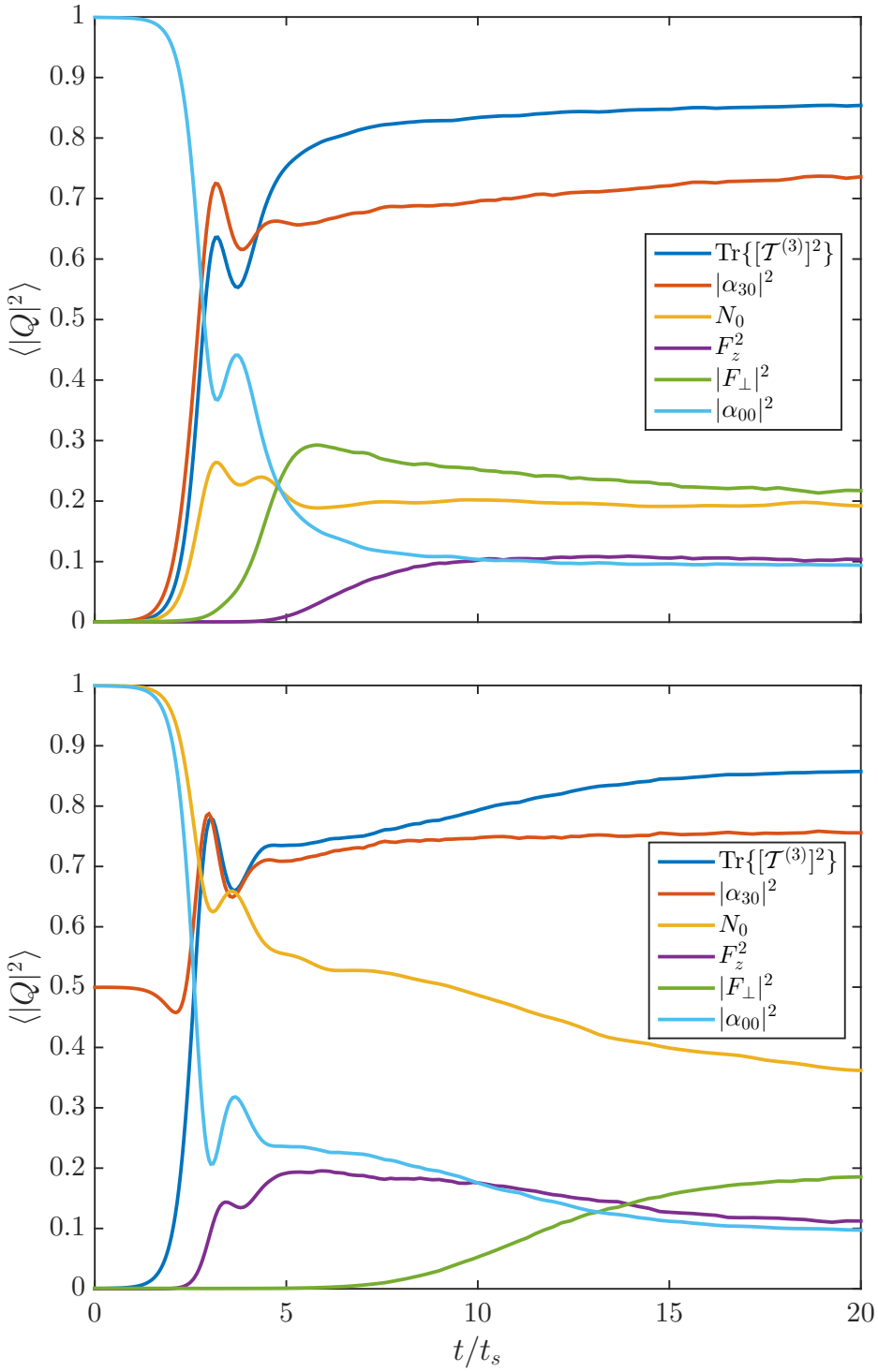

Figure 9.1: Early-time dynamics of several types of local order, for BN initial conditions (top) and UN initial conditions (bottom). Simulations were performed using S2 with $\Delta t = 0.01 \ll (\Delta t)_{\max} = 0.19$, on a 128^2 2D grid of spatial extent $(100\xi_s)^2$. We use length units of the spin healing length $\xi_s = \hbar/\sqrt{Mc_1 n}$, and time units of $t_s = h/c_1 n$. We set $q = 0$, $c_1 > 0$, and relative interaction strengths $c_0 = 10c_1$, $c_2 = 2c_1$.

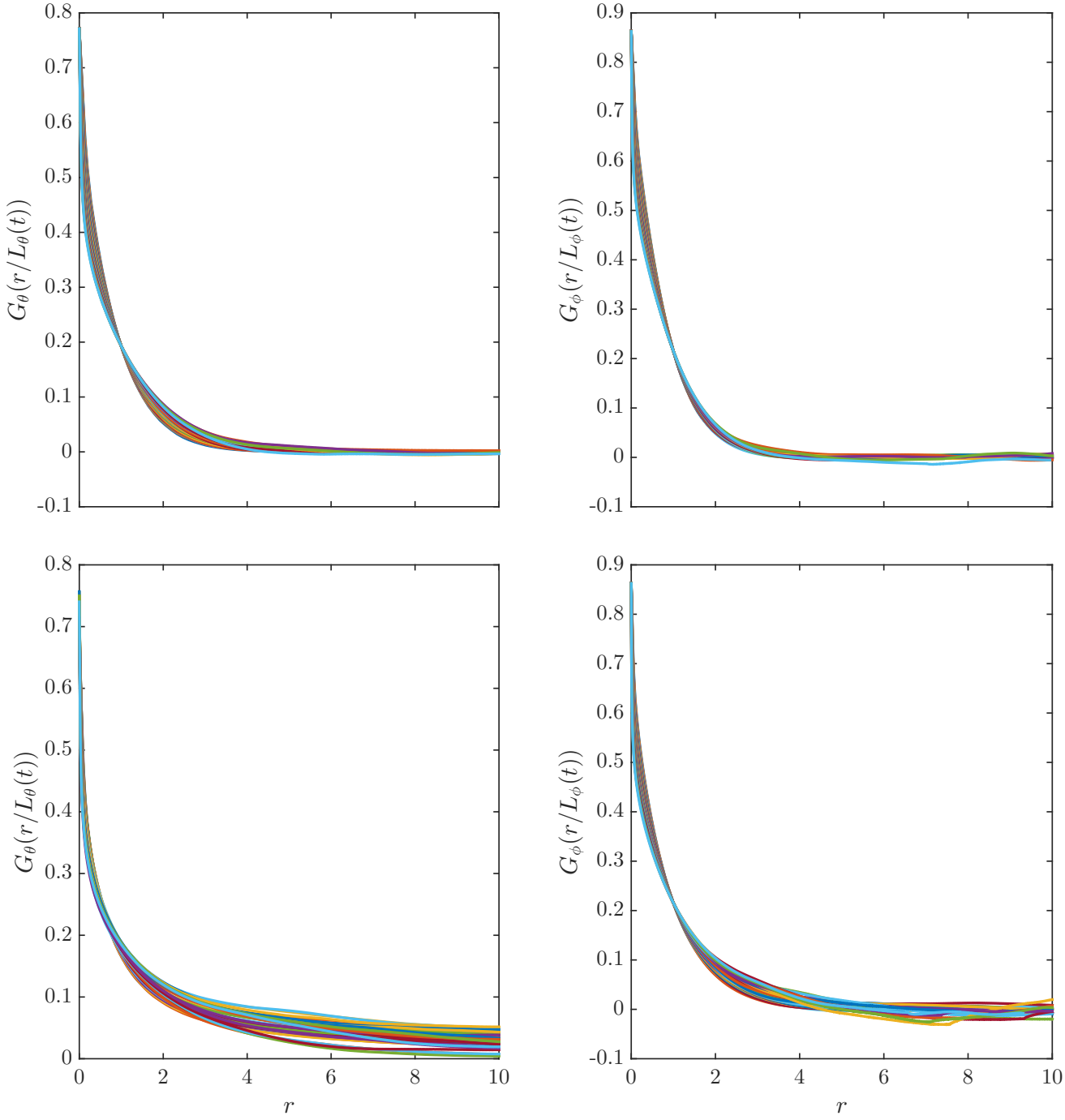

Figure 9.2: Collapsed correlation functions G_θ and G_ϕ for t in the range $[10^2, 10^4]$, for (top) BN initial conditions and (bottom) UN initial conditions. BN results are the average of four trajectories with spatial grids of 1024^2 points and spatial extent $(800\xi_s)^2$, and UN results are a single shot with a spatial grid of 2048^2 points and spatial extent $(1600\xi_s)^2$. Other parameters are the same as for Fig. 9.1.

9.5.3 Correlation lengths

In Fig. 9.3 we plot the length scales extracted from the correlation functions for BN and UN initial conditions. We find that F_z and $F_\perp$ have some early-time growth but decay to a background value at long times. We fit various power laws to the growing length scales of the trio amplitude and octupole order.

For BN initial conditions, the trio length initially grows the fastest, but after about $10t_s$ settles into growing at a rate of $t^{1/3}$. It is overtaken by the growth of the octupole length, whose growth we fit to a $t^{1/2}$ growth law (with log correction). Without a log correction, the octupole length grows as approximately $t^{0.4}$.

For UN initial conditions, the trio length starts with a fixed amount of order as the UN phase has a non-zero amplitude, i.e. $\alpha_{30}/n_c = 1$. As the octupole length reaches the trio length, they both continue growing at a similar rate in the early time dynamics. Past $t = 10t_s$ the trio length exhibits growth with power law $t^{1/3}$, while the octupole order grows faster. For the first two decades after $t = 10t_s$, the octupole length grows like $t^{1/2}$, but not for long enough to distinguish well between a bare power law versus a log-corrected one. At a few thousand spin times, the growth transitions to a $t^{1/3}$ power law. This is the same exponent as that fitted to the trio length, suggesting they become coupled together at late times.

9.5.4 Vortex number decay

In Fig. 9.4, we plot the decay of vortices in the trio amplitude for BN and UN initial conditions. We compare this with the expected number of vortices, calculated from the length scale of trio and octupole domains by estimating their domain size as $\sim L_{\theta,\phi}^D$, where D gives an effective dimension of the domains. The expected number of vortices is then the ratio of the system volume to the domain volume. We test $D = 2, 2.5, 3$ and use the exponents which show some agreement in early or late-time regimes.

We find that for BN initial conditions, the vortex number relates to L_θ as $L_{\rm sys}/\pi L_\theta^2$ initially but shifts to $L_{\rm sys}/\pi L_\theta^{2.5}$ at long times. L_ϕ becomes related to vortex number at long times as well, with the relationship $L_{\rm sys}/\pi L_\phi^2$. This suggests that the global phase starts with domains in 2D but changes character at later times, where it appears to couple to circular domains of the spin phase in two dimensions.

For UN initial conditions, the L_ϕ dependence at the onset of coarsening ($t = 100t_s$)

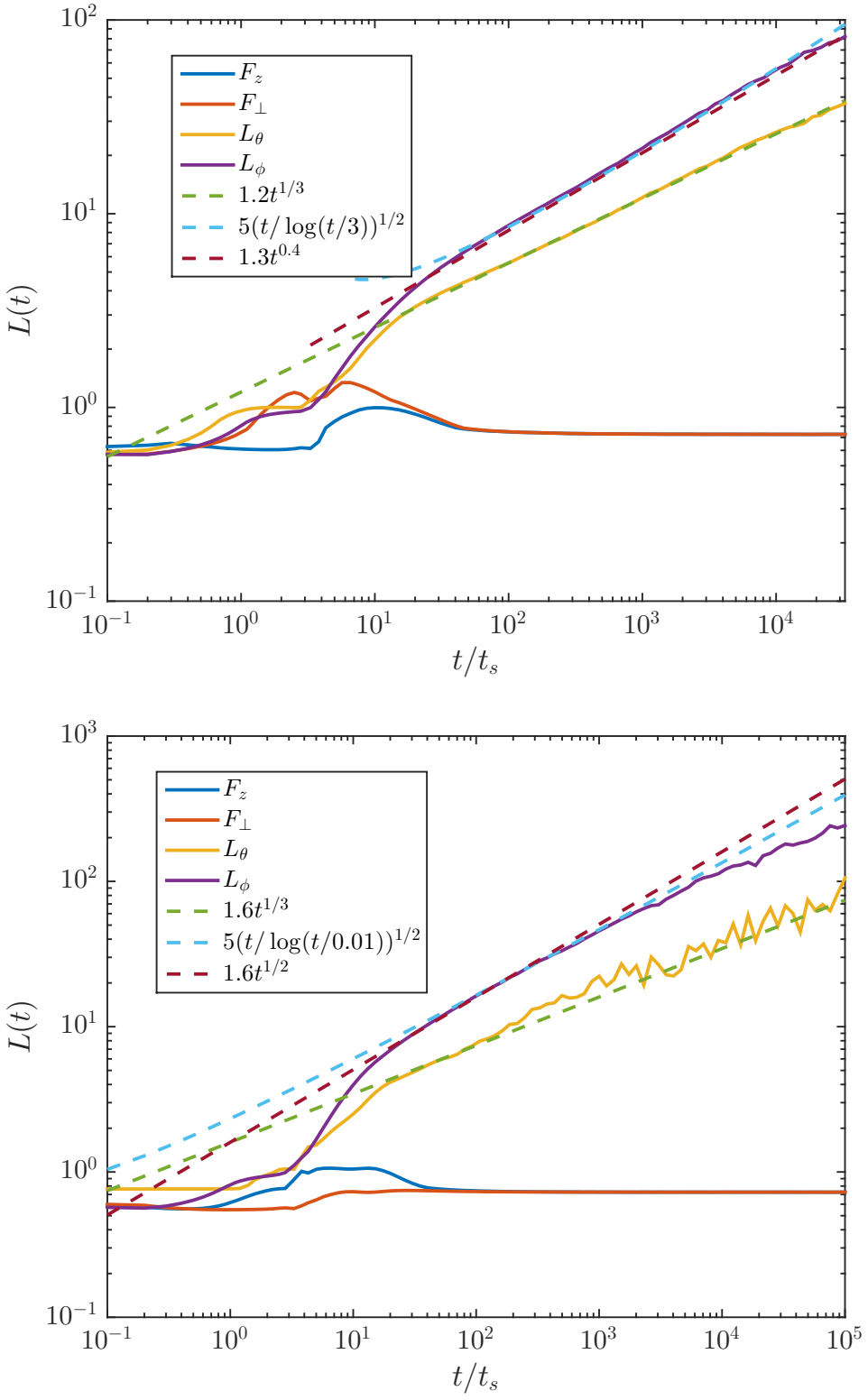

Figure 9.3: Correlation lengths for different types of order, for BN initial conditions (top) and UN initial conditions (bottom). Dashed lines are guides to the eye to indicate scaling with time. Simulation parameters are as for Fig. 9.2.

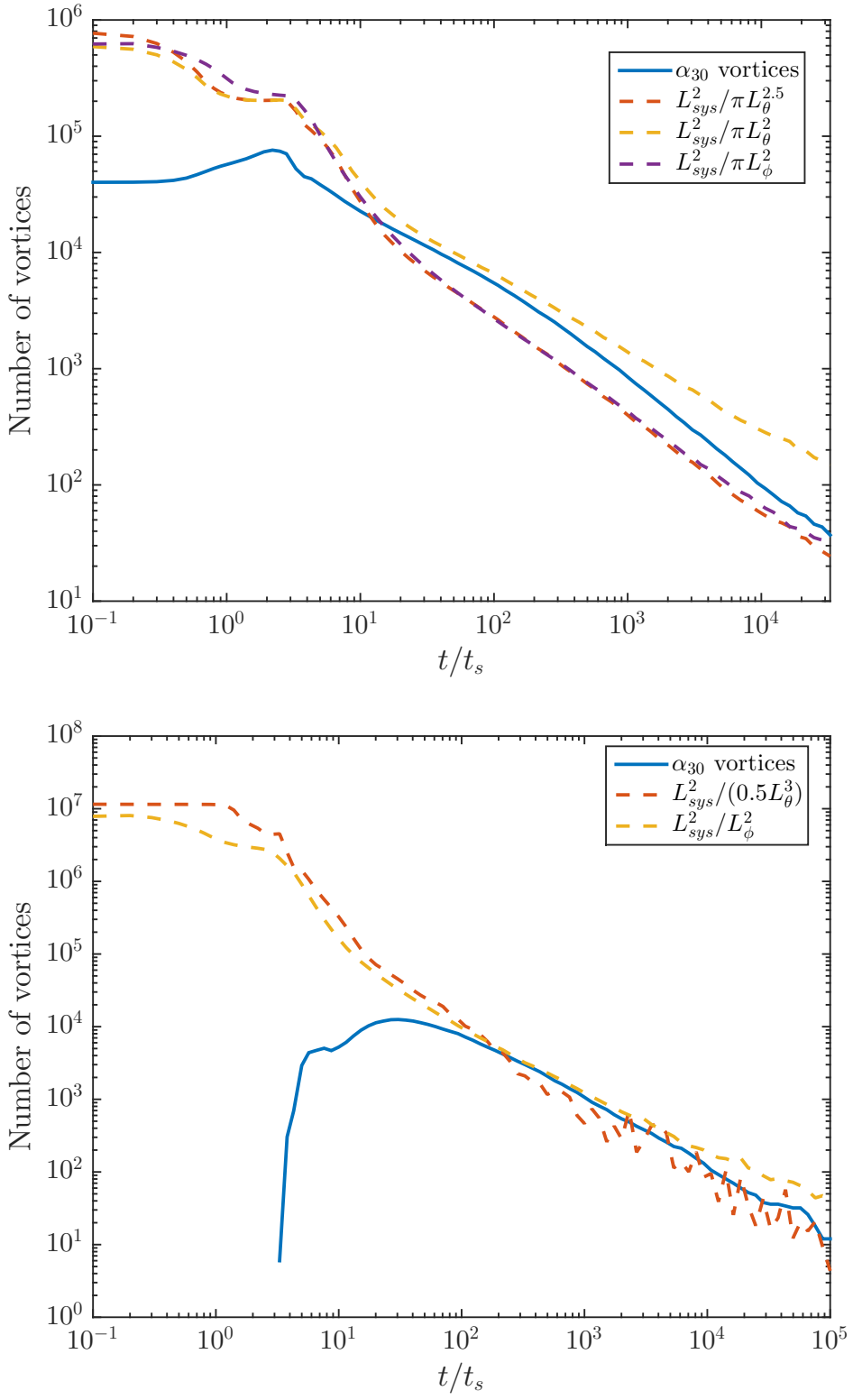

Figure 9.4: Decay of α_{30} vortices over time compared with inverse domain sizes, for BN initial conditions (top) and UN initial conditions (bottom). Dashed lines estimate the vortex number based on L_θ and L_ϕ (see Fig. 9.3). Simulation parameters are as for Fig. 9.3.

is $\sim L_{\rm sys}/L_\phi^2$, but at late times (about $t = 3000t_s$) this changes to $\sim L_{\rm sys}/L_\phi^3$. The L_θ dependence throughout the coarsening regime remains $\sim L_{\rm sys}/L^3$). This suggests that the spin phase revealed by the octupole order initially has two-dimensional domains, but at late times couples to the global phase which appears to be winding through a three-dimensional space throughout the coarsening regime.

9.6 Conclusion

We have considered a quench from two different quadrupolar nematic initial conditions at positive q and negative q to the cyclic phase at $q = 0$. Our results show a novel growth law of $t^{1/3}$ for the global phase domains revealed by the spin-triplet amplitude order parameter. For the spin domains, revealed by the octupole order parameter, we see $t^{1/2}$ scaling for UN and BN initial conditions, with a change in behaviour at late times to $t^{1/3}$ scaling observed for UN initial conditions. For BN initial conditions, the octupole length maintains $t^{1/2}$ scaling up to 10^5 spin times.

As the UN initial state has full $SO(2)$ symmetry, the quench dynamics are able to break this symmetry symmetrically, whereas the BN state already partially breaks $SO(2)$ symmetry and thus starts the quench biased in certain directions in spin space. At long times, for a large enough system, we would expect both sets of initial conditions to access the full $SO(3)$ symmetry of the cyclic phase. In this case the lowest energy vortices to persist would be $1/3 - 2/3$ fractional vortices. The UN initial conditions show that at long times both the octupole and trio amplitude length scales grow as $t^{1/3}$. The similar relationship between these length scales and the vortices in the trio amplitude indicates that they are coupled, with indications that the nematic order of the domains rotates through three spatial dimensions. This relationship is an interesting future theoretical problem to explore, which may provide an experimental pathway to measuring a new universal growth law by counting 1/3 fractional vortices.

Chapter 10

Conclusion

In this thesis we have given a new exact solution to the nonlinear dynamics of spin conserving nonlinear interactions for the spin-1 and spin-2 systems. Using these, we derived new numerical methods for simulating the mean-field dynamics of spinor condensates, and applied these methods to several interesting quenches. These methods are the first algorithms for simulating spinor systems that are fully symplectic; they maintain geometric features of the solution in phase space, including preserving conserved quantities of the motion to high accuracy. These properties have been crucial in enabling long-time ($\sim 10^5 t_s$) simulations of phase ordering dynamics in spinor systems. Our algorithms are already being used by others for ferromagnetic spinor phase ordering and turbulence studies [66, 178, 179].

Using our new symplectic numerical methods, we have conducted the first systematic theoretical and numerical studies of non-ferromagnetic phase ordering in spinor condensates using appropriate order parameters. Nematic phases in the spin-1 and spin-2 systems, with symmetries beyond vectorial spin order, required developing new order parameters sensitive to the spin-nematic rotational symmetry and global phase superfluid flow. For the nematic order parameters this involved deriving a general hierarchy of higher order multipole moments.

We developed explicit expressions for the first few multipoles, including quadrupole and octupole order parameters which can measure nematic order in the spin-1 EP and spin-2 cyclic phases. We measured global phase order in the spin-1 EP phase with the perpendicular component of the spin-singlet $\alpha_\perp$, and in the spin-2 cyclic phase with the spin-singlet trio α_{30}.

We showed that universal coarsening dynamics of ordered domains can be observed in experimentally accessible regimes for a trapped spin-1 system. We have also shown that the spin-2 cyclic phase exhibits a new type of growth law, with exponent 1/3. We connected this growth law to the decay of vortices in α_{30}, which in the cyclic phase are $1/3 - 2/3$ fractional vortices with coupled spin and global phase superfluid velocity fields.

10.1 Future directions

10.1.1 Numerical algorithm directions

There is potential to use the composition methods we have developed here to numerically solve more general c-field equations, which include noise terms to couple the condensate to a thermal bath, exchanging particles and/or energy. The simplest case is the projected spinor Gross-Pitaevskii equation, where we define a projector which restricts evolution of the wavefunction to a finite basis (e.g. of single-particle energy eigenstates). This is in contrast to our system, which has an implicit projector in momentum-space. The projection step can be applied at the end of a composition solution step and remain the same order algorithm as projecting at each step inside the composition. Thus, for low order methods, S2 could be used to solve the unprojected GPE part of the equation, with a projection afterwards, and remain second-order in time.

Our algorithms can be extended in several other relatively simple directions. We have currently implemented the kinetic energy subsystem using FFTs with periodic boundary conditions; this could be implemented using finite difference schemes that can handle systems with different boundary conditions.

For harmonically trapped systems, the trap could be joined with the kinetic energy subsystem and solved in a harmonic oscillator basis. This could give more stable and accurate results for the trapped case, especially when the trap frequencies are high. This would require a non-uniform grid however, with dense grids near the edges, which may create a tradeoff with memory considerations depending on the system size.

10.1.2 Spin-1 Experimental Quench extensions

The Seoul National University experimental spinor group have mentioned to us that they measured magnetic field gradients in their system, and believe these have an observable effect on the time evolution. Our algorithm can already handle a spatially varying linear Zeeman. Accounting for a spatially varying quadratic Zeeman would be an interesting extension of our work, and would require the nonlinear subsystem to include the quadratic Zeeman term. This has an exact solution with Jacobi elliptic functions and inverses [92, 93], so would be slower to compute than the solution of the spin-symmetric nonlinear subsystem.

Another extension would be to account for heating of the system and loss of atom number over time. This would require a more general approach to solving the dynamical equations, which could be to start from the master equations for the density matrix with noise terms to couple to a temperature bath, e.g. the treatment of 3-body loss processes using truncated Wigner in Ref. [180].

10.1.3 BN quench

For the spin-2 system, the EP phase becomes the BN phase, which breaks symmetry along two axes in spin space rather than just one. To measure the development of spin order in a quench to the BN phase, the fourth order multipole $T^{(4)}$ is the appropriate spin order parameter, with $\alpha_\perp$ (as for the spin-1 EP phase) the appropriate order parameter for measuring global phase order.

Both the spin order and the global phase order parameters should be coupled at long times so their domains grow with the same growth law. The late-time dynamics should reduce to a binary system, as the spin-1 EP system does, but the early-time dynamics will be much richer.

Additionally, the possible vortices in the BN phase form a non-Abelian group with interesting core structures and dynamics [181]. These vortices may be present following a quench, leading to complex dynamics as they annihilate.

10.1.4 Spin-2 Cyclic vortices

There are theoretical connections to be drawn between the $t^{1/3}$ growth law and $1/3-2/3$ fractional vortices seen in the cyclic phase. Realizing vortices in the cyclic phase has received some theoretical attention although experimental confirmation has been elusive [182–185].

The cyclic vortices form a non-Abelian group, which gives rise to interesting non-elastic vortex dynamics, with collisions between non-commuting vortex group elements forming rungs and thus encoding a history of their collisions. These vortices have recently been identified as anyons, and controlled braiding and fusion of their space-time worldlines has been numerically demonstrated [186]. Topological qubits are a promising avenue for pursuing fault-tolerant quantum computing [187, 188].

Cyclic vortices may also have links to QCD models of quark matter [189].

10.1.5 Higher spin

There many interesting theoretical questions about spin-1 and spin-2. For example, spinor BECs have a direct duality with electromagnetism (a physical spin-1 massless field) in the hydrodynamic picture, with nonlinear interactions contributing to a local chemical potential [32]. For spin-2 BECs, it would be interesting to see how they connect with physical spin-2 fields, of which there is only one: the graviton field, coupling to the stress-energy tensor, and thus describing general relativity. There is a charge-vortex duality for scalar BECs, which identifies the vortices of a bosonic field as fermionic charges of a fermionic theory. It would be interesting to see what a spin degree of freedom brings to this duality. Topological defects in spinor systems may also prove useful for investigating the AdS/CFT correspondence [190].

The effects of non-zero magnetism on vortices in the spin-1 system have been investigated in Refs. [191, 192]. Analogous studies in spin-2 and higher may be expected to show even richer structures appearing.

Many different domains and structures in cosmology [193] have potential for being simulated in cold matter systems that have similar symmetries. For $f \geq 3$ there are new nonlinear dynamics caused by higher-order multipole interactions. These would be quite interesting to investigate and connect with the higher symmetries appearing. For example, for $f = 3$, the interactions form a chain of symmetries

$U(7) \supset SO(7) \supset G_2 \supset SO(3)$, with G_2 the first exceptional group [96]. The appearance of G_2 breaks the separability of the general system, due to not having an independent quadratic Casimir invariant [it is the same as the one for $SO(7)$]. G_2 is an intriguing group, and work in this area could draw connections to string theories where G_2 plays an important role [194–196].

For higher spin systems, higher multipole observables $\mathcal{T}^k$ are required to observe the spin order of the new symmetry states that become possible, similar to how we characterized the spin order in the cyclic phase for spin-2 by the octupole moment with $k = 3$. Generalized high-spin singlet amplitude operators, possibly related to higher-spin (higher-order tensor) Cartesian representations, will be needed to couple to global phase order, e.g. beyond the singlet trio amplitude to the singlet quintet amplitude (α_{50}) and higher.

Appendices

Appendix A

Multipole operator decomposition procedure

Here we give pseudo-code for a general procedure to calculate decompositions of arbitrary order unsymmetrized multipole operators into symmetric operators. This was how we calculated the fourth order multipole irreducible decomposition (see Appendix B), and in theory would allow extension of the results given Section 2.4 to arbitrary order multipole operators.

Our main function can be written as

$$\begin{aligned}&\text{calc\_expansion\_func}(\mathrm{f}_{x_1,x_2,\cdots x_n})\\&= \mathrm{s}_{x_1,x_2,\cdots x_n} - \text{calc\_symmetric}(\mathrm{f}_{x_1,x_2,\cdots x_n}) + \frac{1}{n}\sum_{a=1}^{n}\text{swap\_index}(\mathrm{f}_{x_1,x_2,\cdots x_n},0,a),\end{aligned} \tag{A.1}$$

where

$$\text{calc\_symmetric}(\mathrm{f}_{x_1,x_2,\cdots x_n}) = \frac{1}{n}\sum_{a=1}^{n}(\mathrm{f}_a \mathrm{s}_{x_1,x_2,\cdots x_n \forall x_i \neq a}). \tag{A.2}$$

The function swap_index interchanges two indices using commutation relations. For swapping indices a and b where $a < b$, we swap a with its right neighbour using commutation relations until it has b as its right neighbour. We then swap b with its left neighbour until it has reached the original position of a. Each swap generates a commutator term which we collect and return with the final swapped-indices term. If the final swapped-indices term is higher than second order, a callback function recursively expands it into a symmetric decomposition, until all terms are second order in the antisymmetric terms.

The function calc_symmetric writes the symmetrized term as a sum of symmetric terms of one order less left-multiplied by a spin-matrix.

Once we have this decomposition, we go through the expression replacing antisymmetric second-order terms (which are multiplied on the left and/or right by spin-matrices) with the actual commutator and combining left and right spin-matrices. The resulting unsymmetrized terms are expanded, and we repeat the process until all terms are symmetric. The commutator brings in a sum over dummy indices. For order n we will have terms with products of $n-1$ sums. Each time we have an even number of sums in a product, we will expand the products of the Levi-Civita symbols and simplify. Thus we will end up with terms which have at most one Levi-Civita symbol.

The second order result is fundamental to this algorithm,

$$\mathrm{f}_{ab} = \mathrm{s}_{ab} + a_{ab}, \tag{A.3}$$

$$= \mathrm{s}_{ab} + \frac{i}{2}\varepsilon_{abc}\mathrm{f}_c. \tag{A.4}$$

The trace of the symmetric term is

$$\mathrm{s}_{aa} = \mathrm{f}_{aa} = \mathcal{F}(\mathcal{F}+1) \equiv \gamma, \tag{A.5}$$

with traceless term

$$\mathrm{t}_{ab} = \mathrm{s}_{ab} - \frac{1}{3}\gamma\delta_{ab}. \tag{A.6}$$

Thus we get the full result

$$\mathrm{f}_{ab} = \mathrm{t}_{ab} + \frac{i}{2}\varepsilon_{abc}\mathrm{f}_c + \frac{1}{3}\gamma\delta_{ab}. \tag{A.7}$$

The third order result is calculated using

$$\mathrm{calc\_symmetric}(\mathrm{f}_{abc}) = \frac{1}{3}\left(\mathrm{f}_a\mathrm{s}_{bc} + \mathrm{f}_b\mathrm{s}_{ac} + \mathrm{f}_c\mathrm{s}_{ab}\right), \tag{A.8}$$

giving initially

$$\mathrm{calc\_expansion\_func}(\mathrm{f}_{abc}) = \mathrm{s}_{abc} + \frac{1}{3}\left(\mathrm{f}_a a_{bc} - \mathrm{f}_c a_{ab} + 2a_{bc}\mathrm{f}_a + 3\mathrm{f}_b a_{ac} + 4a_{ab}\mathrm{f}_c\right). \tag{A.9}$$

Each antisymmetric term being multiplied by a spin matrix is then replaced with the commutator, and the unsymmetrized term inside the sum is expanded into symmetric

and non-symmetric parts. E.g.

$$\mathrm{f}_a a_{bc} = \mathrm{f}_a \left(\frac{i}{2}\varepsilon_{bcd}\mathrm{f}_d\right), \tag{A.10}$$

$$= \frac{i}{2}\varepsilon_{bcd}\mathrm{f}_{ad}, \tag{A.11}$$

$$= \frac{i}{2}\varepsilon_{bcd}(\mathrm{s}_{ad} + a_{ad}), \tag{A.12}$$

$$= \frac{i}{2}\varepsilon_{bcd}\mathrm{s}_{ad} + \frac{i}{2}\varepsilon_{bcd}a_{ad}, \tag{A.13}$$

$$= \frac{i}{2}\varepsilon_{bcd}\mathrm{s}_{ad} + \frac{i}{2}\varepsilon_{bcd}\varepsilon_{ade}f_e, \tag{A.14}$$

$$= \frac{i}{2}\varepsilon_{bcd}\mathrm{s}_{ad} + \frac{i}{2}\sum_{de}(\delta_{ab}\delta_{cd}\delta_{de} - \delta_{ab}\delta_{ce} - \delta_{ac}\delta_{bd}\delta_{de} + \delta_{ac}\delta_{be} + \delta_{ad}\delta_{bd}\delta_{ce} - \delta_{ad}\delta_{be}\delta_{cd})f_e, \tag{A.15}$$

$$= \frac{i}{2}\varepsilon_{bcd}\mathrm{s}_{ad} + \frac{i}{2}\left(\delta_{ac}\mathrm{f}_b - \delta_{ab}\mathrm{f}_c\right), \tag{A.16}$$

$$a_{bc}\mathrm{f}_a = \frac{i}{2}\varepsilon_{bcd}\mathrm{s}_{ad} - \frac{i}{2}\left(\delta_{ac}\mathrm{f}_b - \delta_{ab}\mathrm{f}_c\right). \tag{A.17}$$

The last terms in this expression are expanded by substituting the commutator and an expansion of the Levi-Civita product into Kronecker delta functions. Summing over dummy indices (using Sympy's deltasummation) we get the result

$$\mathrm{f}_{abc} = \mathrm{s}_{abc} + \frac{i}{2}\sum_{d=1}^{3}\left(\varepsilon_{abd}\mathrm{s}_{cd} + \varepsilon_{acd}\mathrm{s}_{bd} + \varepsilon_{bcd}\mathrm{s}_{ad}\right) + \frac{1}{6}\left(\delta_{ab}\mathrm{f}_c - 2\delta_{ac}\mathrm{f}_b + \delta_{bc}\mathrm{f}_a\right). \tag{A.18}$$

The trace of the symmetric term is

$$\mathrm{s}_{aac} = \mathrm{f}_{aac} - \frac{1}{3}\mathrm{f}_c, \tag{A.19}$$

$$= \left(\mathcal{F}(\mathcal{F}+1) - \frac{1}{3}\right)\mathrm{f}_c \tag{A.20}$$

$$\equiv \lambda_\nu \mathrm{f}_c. \tag{A.21}$$

with traceless term

$$\mathrm{t}_{abc} = \mathrm{s}_{abc} - \frac{1}{5}\lambda_\nu(\delta_{ab}\mathrm{f}_c + \delta_{ac}\mathrm{f}_b + \delta_{bc}\mathrm{f}_a). \tag{A.22}$$

This gives the full third order result

$$\mathrm{f}_{abc} = \mathrm{t}_{abc} + \frac{i}{2}\sum_{d=1}^{3}\left(\varepsilon_{abd}\mathrm{t}_{cd} + \varepsilon_{acd}\mathrm{t}_{bd} + \varepsilon_{bcd}\mathrm{t}_{ad}\right) + \frac{1}{10}(2\gamma+1)\left(\delta_{ab}\mathrm{f}_c + \delta_{ac}\mathrm{f}_b + \delta_{bc}\mathrm{f}_a\right) - \frac{1}{2}\delta_{ac}\mathrm{f}_b + \frac{i}{6}\gamma\varepsilon_{abc}. \tag{A.23}$$

Appendix B

Hexadecapole multipole order

Here we give the results of applying the method in Appendix A to decompose the fourth order multipole operator (hexadecapole) into symmetric operators. We then continue the decomposition to the irreducible multipole components of the operator and give results for the inner product. Finally, we review the symmetric inner product results for the first four multipole order moments.

B.1 Fourth order expansion

We find the expansion

$$\begin{aligned}\mathrm{f}_{abcd} = \mathrm{s}_{abcd} &+ \frac{i}{2}\sum_e \left(\varepsilon_{abe}\mathrm{s}_{cde} + \varepsilon_{ace}\mathrm{s}_{bde} + \varepsilon_{ade}\mathrm{s}_{bce} + \varepsilon_{bce}\mathrm{s}_{ade} + \varepsilon_{bde}\mathrm{s}_{ace} + \varepsilon_{cde}\mathrm{s}_{abe}\right) \\ &+ \frac{i}{6}\left(\sum_e \varepsilon_{abe}\delta_{cd}\mathrm{f}_e - \sum_e \varepsilon_{ace}\delta_{bd}\mathrm{f}_e - \mathrm{f}_c\varepsilon_{abd}\right) + \frac{1}{2}\left(\delta_{ad}\delta_{bc} - \delta_{ab}\delta_{cd}\right)\sum_e \mathrm{s}_{ee} \\ &+ \frac{1}{6}\left(5\mathrm{s}_{ab}\delta_{cd} + 5\mathrm{s}_{cd}\delta_{ab} - \delta_{ac}\mathrm{s}_{bd} - \delta_{bc}\mathrm{s}_{ad} - \delta_{bd}\mathrm{s}_{ac} - 7\mathrm{s}_{bc}\delta_{ad}\right). \end{aligned} \tag{B.1}$$

Taking the expectation and norm of both sides, we get

$$\sum_{abcd}\left(\mathcal{N}_{abcd}\right)^2 = \sum_{abcd}\left(\mathcal{S}_{abcd}\right)^2 - 5\sum_{abc}\left(\mathcal{S}_{abc}\right)^2 + \frac{23}{6}\sum_{ab}\left(\mathcal{S}_{ab}\right)^2 + \left(2\lambda^2 + \frac{1}{3}\lambda - \frac{5}{18}\right)F^2 - \frac{7}{6}\gamma^2 n^2, \tag{B.2}$$

where we have set

$$\gamma \equiv f(f+1), \tag{B.3}$$

$$\lambda \equiv \left(\gamma - \frac{1}{3}\right). \tag{B.4}$$

The symmetric fourth order tensor has subspaces

$$\rho_{ab} = \sum_c \mathrm{s}_{abcc} = \left(\lambda - \frac{1}{2}\right)\mathrm{s}_{ab} + \frac{1}{6}\gamma\delta_{ab}, \tag{B.5}$$

$$\mathrm{Tr}\{\rho\} = \sum_a \rho_{aa} = \sum_{ab} \mathrm{s}_{aabb} = \gamma\lambda\mathbb{1}. \tag{B.6}$$

The traceless symmetric fourth order tensor is then

$$\mathrm{t}_{abcd} = \mathrm{s}_{abcd} - \frac{1}{7}\sum_{\mathrm{sym}} \delta_{ab}\rho_{cd} + \frac{1}{35}\mathrm{Tr}\{\rho\}\sum_{\mathrm{sym}} \delta_{ab}\delta_{cd}, \tag{B.7}$$

$$= \mathrm{s}_{abcd} - \frac{1}{7}(\delta_{ab}\rho_{cd} + \delta_{ac}\rho_{bd} + \delta_{ad}\rho_{bc} + \delta_{bc}\rho_{ad} + \delta_{bd}\rho_{ac} + \delta_{cd}\rho_{ab}) + \frac{1}{35}\mathrm{Tr}\{\rho\}(\delta_{ab}\delta_{cd} + \delta_{ac}\delta_{bd} + \delta_{ad}\delta_{bc}). \tag{B.8}$$

The expectation is

$$\mathcal{T}_{abcd} = \mathcal{S}_{abcd} - \frac{1}{7}\left(P_{ab}\delta_{cd} + P_{ac}\delta_{bd} + P_{ad}\delta_{bc} + P_{bc}\delta_{ad} + P_{bd}\delta_{ac} + P_{cd}\delta_{ab}\right) + \frac{1}{35}\mathrm{Tr}\{P\}\left(\delta_{ab}\delta_{cd} + \delta_{ac}\delta_{bd} + \delta_{ad}\delta_{bc}\right), \tag{B.9}$$

where

$$P_{ab} = \psi^\dagger\rho_{ab}\psi = \left(\lambda - \frac{1}{2}\right)\mathcal{S}_{ab} + \frac{1}{6}\gamma\delta_{ab}n, \tag{B.10}$$

$$\mathrm{Tr}\{P\} = \sum_a P_{aa} = \gamma\lambda n. \tag{B.11}$$

Taking the norm of both sides of Eq. (B.9), we get

$$\sum_{abcd}(\mathcal{T}_{abcd})^2 = \sum_{abcd}(\mathcal{S}_{abcd})^2 - \frac{6}{7}\sum_{ab}(P_{ab})^2 + \frac{3}{35}\gamma^2\lambda^2n^2. \tag{B.12}$$

We expand the P_{ab} norm as

$$\sum_{ab}(P_{ab})^2 = \left(\lambda - \frac{1}{2}\right)^2\sum_{ab}(\mathcal{S}_{ab})^2 + \frac{1}{3}\left(\lambda - \frac{1}{4}\right)\gamma^2n^2. \tag{B.13}$$

Substituting this in, we have

$$\sum_{abcd}(\mathcal{T}_{abcd})^2 = \sum_{abcd}(\mathcal{S}_{abcd})^2 - \frac{6}{7}\left(\lambda - \frac{1}{2}\right)^2\sum_{ab}(\mathcal{S}_{ab})^2 + \frac{1}{7}\left(\frac{3}{5}\lambda^2 - 2\lambda + \frac{1}{2}\right)\gamma^2n^2. \tag{B.14}$$

Combining this with Eq. (B.2), we have

$$\sum_{abcd}(\mathcal{N}_{abcd})^2 = \sum_{abcd}(\mathcal{T}_{abcd})^2 - 5\sum_{abc}(\mathcal{S}_{abc})^2 + \left(\frac{6}{7}\left(\lambda - \frac{1}{2}\right)^2 + \frac{23}{6}\right)\sum_{ab}(\mathcal{S}_{ab})^2 + \left(2\lambda^2 + \frac{1}{3}\lambda - \frac{5}{18}\right)F^2 - \left(\frac{1}{7}\left(\frac{3}{5}\lambda^2 - 2\lambda + \frac{1}{2}\right)\gamma^2 + \frac{7}{6}\right)n^2. \tag{B.15}$$

B.2 Summary of symmetric relations

Here we summarize the relations between the symmetric and irreducible multipole inner products.

$$\sum_{ab} \mathcal{S}_{ab}^2 = \sum_{ab} \mathcal{T}_{ab}^2 + \frac{1}{3}\gamma^2 n^2, \tag{B.16}$$

$$\sum_{abc} \mathcal{S}_{abc}^2 = \sum_{abc} \mathcal{T}_{abc}^2 + \frac{3}{5}\left(\gamma + \frac{1}{3}\right)^2 F^2, \tag{B.17}$$

$$\sum_{abcd} \mathcal{S}_{abcd}^2 = \sum_{abcd} \mathcal{T}_{abcd}^2 + \frac{6}{7}\left(\lambda - \frac{1}{2}\right)^2 \sum_{ab} \mathcal{T}_{ab}^2 + \frac{1}{5}\lambda^2\gamma^2 n^2. \tag{B.18}$$

Appendix C

Parameters for the spin-1 continuous-wave solution

Here we briefly outline the relationships between the parameters of this continuous wave solution presented in Sec. 6.2.1, noting that additional details can be found in Ref. [128].

For Eqs. (6.2)- (6.4) to be a solution of the spin-1 GPE we must have

$$k_0 = \tfrac{1}{2}(k_+ + k_-), \tag{C.1}$$

$$\omega_0 = \tfrac{1}{2}(\omega_+ + \omega_-), \tag{C.2}$$

$$\theta_0 = \tfrac{1}{2}(\theta_+ + \theta_- + n_p\pi), \tag{C.3}$$

where $n_p = \{0, 1\}$, and the chemical potentials are given by

$$\omega_\pm = \tfrac{1}{2}k_\pm^2 + U_\pm + c_1\left[(-1)^{n_p}A_0^2 - 2A_+A_-\right]\frac{A_\mp}{A_\pm}, \tag{C.4}$$

$$\omega_0 = \tfrac{1}{2}k_0^2 + U_0 - c_1\left[A_0^2 - (-1)^{n_p}2A_+A_-\right], \tag{C.5}$$

where we have set $U_m \equiv (c_0 + c_1)(A_+^2 + A_0^2 + A_-^2) + qm^2$. From the constraint on ω_0 we find A_0 in terms of $A_\pm$

$$A_0^2 = 2(-1)^{n_p}A_+A_-\left(1 - \frac{\frac{1}{2}[(k_+ - k_-)/2]^2 + q}{c_1[A_+ + (-1)^n A_-]^2}\right). \tag{C.6}$$

Appendix D

Planar treatment of spin-1 nematic order

We can formulate our spin-1 EP polar order parameters from Chapter 7 by considering the Cartesian spinor field projected onto the plane:

$$\vec{\psi}_\perp \equiv (\psi_x, \psi_y)^T. \tag{D.1}$$

Recalling $\psi_x = \frac{1}{\sqrt{2}}(\psi_{-1} - \psi_1)$, $\psi_y = -\frac{i}{\sqrt{2}}(\psi_1 + \psi_{-1})$, we see that the planar treatment only depends on the $\{\psi_1, \psi_{-1}\}$ spherical components of the spinor.

We now proceed to develop a mathematical description of the spin properties of the planar-spin system analogously to the three-dimensional treatment developed in Section 3.1.3. We can decompose the planar spinor into two real planar vectors

$$\vec{\psi}_\perp = e^{i\theta_\perp}(\vec{u}_\perp + i\vec{v}_\perp), \tag{D.2}$$

which are orthogonal and satisfy the normalization condition

$$|\vec{u}_\perp|^2 + |\vec{v}_\perp|^2 = n_\perp, \tag{D.3}$$

where $n_\perp = \vec{\psi}_\perp^* \cdot \vec{\psi}_\perp = n_1 + n_{-1}$. We choose $\vec{u}_\perp$ to be the effective planar director and take it to be the longest vector, i.e. $|\vec{u}_\perp|^2 \geq \frac{1}{2}n_\perp \geq |\vec{v}_\perp|^2$. We emphasize that the vectors $\{\vec{u}_\perp, \vec{v}_\perp\}$ are not in general the projected versions of the three-dimensional vectors in Eq. (3.19) (e.g. projection of $\{\vec{u}, \vec{v}\}$ does not preserve their orthogonality).

Because our vectors are 2D we can only obtain a z-component of the cross product,

which yields the usual $F_z = |\psi_1|^2 - |\psi_{-1}|^2$ magnetization density, i.e.

$$F_z = -i\vec{\psi}_\perp^* \times \vec{\psi}_\perp = 2\vec{u}_\perp \times \vec{v}_\perp. \tag{D.4}$$

The $m = 0$ component projected out of the spinor prohibits us from quantifying the transverse magnetization. The singlet-amplitude to the planar system is defined as

$$\alpha_\perp \equiv \vec{\psi}_\perp \cdot \vec{\psi}_\perp = -2\psi_1\psi_{-1} \tag{D.5}$$

and we have the relation [c.f. Eq. (3.29)]

$$F_z^2 + |\alpha_\perp|^2 = n_\perp^2. \tag{D.6}$$

We can construct a symmetric traceless tensor [i.e. the one introduced in Eq. (7.1)] as

$$Q \equiv \frac{n_\perp}{2} I_2 - \frac{1}{2}\left(\vec{\psi}_\perp^* \otimes \vec{\psi}_\perp + \vec{\psi}_\perp \otimes \vec{\psi}_\perp^*\right), \tag{D.7}$$

$$= \frac{n_\perp}{2} I_2 - \left(\vec{u}_\perp \otimes \vec{u}_\perp + \vec{v}_\perp \otimes \vec{v}_\perp\right). \tag{D.8}$$

As noted in Sec. 7.3.1 the elements of Q in spherical spinor components are $Q_{xx} = \mathrm{Re}\{\psi_1^*\psi_{-1}\} = -Q_{yy}$ and $Q_{xy} = \mathrm{Im}\{\psi_1^*\psi_{-1}\}$, with $\det(Q) = -n_1 n_{-1}$.

By inspection of Eq. (D.8) we see $\{\vec{u}_\perp, \vec{v}_\perp\}$ are eigenvectors of Q with eigenvalues $\lambda_u = \frac{1}{2}n_\perp - |\vec{u}_\perp|^2$ and $\lambda_v = \frac{1}{2}n_\perp - |\vec{v}_\perp|^2$, respectively. Given our convention to choose $\vec{u}_\perp$ as the longer vector we have that λ_u is negative (i.e. the director corresponds to the lowest eigenvalue). Because the matrix is traceless the eigenvalues are given by $\pm\sqrt{-\det(Q)}$, i.e. $\lambda_u = -\sqrt{n_1 n_{-1}}$ and $\lambda_v = \sqrt{n_1 n_{-1}}$. The trace of Q^2 is then just the sum of the eigenvalues squared, and recalling the transverse alignment $\mathcal{A}_\perp = |\alpha_\perp| = \sqrt{2n_1 n_{-1}}$, we obtain

$$\mathrm{Tr}(Q^2) = \frac{1}{2}\mathcal{A}_\perp^2. \tag{D.9}$$

We also note that Q can be written in the form

$$Q = \frac{\mathcal{A}_\perp}{2}\begin{pmatrix} \cos 2\varphi & \sin 2\varphi \\ \sin 2\varphi & -\cos 2\varphi \end{pmatrix}, \tag{D.10}$$

where we have introduced $\varphi \equiv \frac{1}{2}\mathrm{Arg}(\psi_1^*\psi_{-1})$, i.e. $\psi_1^*\psi_{-1} = \frac{1}{2}\mathcal{A}_\perp e^{2i\varphi}$. Note that this has eigenvalues and eigenvectors:

$$\lambda_u = -\frac{\mathcal{A}_\perp}{2}, \quad \hat{\vec{u}}_\perp = \begin{pmatrix} \cos\varphi \\ \sin\varphi \end{pmatrix}, \tag{D.11}$$

$$\lambda_v = +\frac{\mathcal{A}_\perp}{2}, \quad \hat{\vec{v}}_\perp = \begin{pmatrix} -\sin\varphi \\ \cos\varphi \end{pmatrix}, \tag{D.12}$$

where the hats emphasize that these are unit vectors. We observe that the relative phase of the ψ_1 and ψ_{-1} components directly determines the orientation φ of the planar director $\vec{u}_\perp$. Note that this result is general for any spin-1 spinor, however for the particular case of the EP ground state (7.5) we have $\varphi \to \phi$, $\mathcal{A}_\perp \to n_c$.

D.1 Correlation functions

Using the results of the previous section we can provide an alternative motivation for the correlation functions used in the paper. Firstly, we will consider the orientation of the director at two different points in space. For a spin model this might be characterized by a correlation function of the form

$$G_u(\mathbf{r}) = \langle |\hat{\vec{u}}(\mathbf{0}) \cdot \hat{\vec{u}}(\mathbf{r})|^2 \rangle = \frac{1}{2}\langle \cos(2[\varphi(\mathbf{0}) - \varphi(\mathbf{r})]) + 1 \rangle, \tag{D.13}$$

where the inner product is squared to account for $\vec{u}$ and $-\vec{u}$ being the same. In terms of the fields our relevant quantity is the complex density $\Phi \equiv \psi_1^* \psi_{-1} = \frac{1}{2}\mathcal{A}_\perp e^{2i\varphi}$. Correlating this at two points in space we have

$$G_\Phi(\mathbf{r}) = \langle \Phi(\mathbf{0})\Phi^*(\mathbf{r}) \rangle, \tag{D.14}$$

$$= \langle \psi_1^*(\mathbf{0})\psi_{-1}(\mathbf{0})\psi_{-1}^*(\mathbf{r})\psi_1(\mathbf{r}) \rangle, \tag{D.15}$$

which is identical to G_ϕ as defined in (7.20) if we normalize by a factor of $4/n_c^2$.

From Eqs. (D.2) and (D.5) we see that the superfluid phase $\theta_\perp$ is related to the singlet-amplitude as

$$\alpha_\perp = -2\psi_1\psi_{-1} = -\mathcal{A}_\perp e^{2i\theta_\perp}, \tag{D.16}$$

where we can take $\theta_\perp = \frac{1}{2}\mathrm{Arg}(\psi_1\psi_{-1})$. Thus to correlate this superfluid order at two points we can consider the pairing-like field $\alpha_\perp$ at those two locations, i.e.

$$G_{\alpha_\perp}(\mathbf{r}) = \langle \alpha_\perp^*(\mathbf{0})\alpha_\perp(\mathbf{r}) \rangle, \tag{D.17}$$

$$= 4\langle \psi_1^*(\mathbf{0})\psi_{-1}^*(\mathbf{0})\psi_{-1}(\mathbf{r})\psi_1(\mathbf{r}) \rangle. \tag{D.18}$$

Normalizing by a factor of n_c^{-2} gives G_θ [Eq. (7.21)].

Bibliography

[1] D. J. Griffiths. *Introduction to Quantum Mechanics*. Pearson, 2005.

[2] K. Huang. On the zitterbewegung of the Dirac electron. *American Journal of Physics*, 20(8):479–484, 1952.

[3] A. O. Barut and A. J. Bracken. Zitterbewegung and the internal geometry of the electron. *Physical Review D*, 23(10):2454, 1981.

[4] A. O. Barut and N. Zanghi. Classical model of the Dirac electron. *Physical Review Letters*, 52(23):2009, 1984.

[5] H. C. Ohanian. What is spin? *American Journal of Physics*, 54(6):500–505, 1986.

[6] J. L. Jimenez and I. Campos. Models of the classical electron after a century. *Foundations of Physics Letters*, 12(2):127–146, 1999.

[7] V. Simulik. *What is the Electron?* Apeiron, 2005.

[8] J. Maruani. The Dirac electron as a massless charge spinning at light speed: implications on some basic physical concepts. In *Advances in Quantum Methods and Applications in Chemistry, Physics, and Biology*, pages 53–74. Springer, 2013.

[9] M. Morrison. Spin: All is not what it seems. *Studies in History and Philosophy of Science Part B: Studies in History and Philosophy of Modern Physics*, 38(3):529–557, 2007.

[10] C. T. Sebens. How electrons spin. *ArXiv preprint arXiv:1806.01121*, 2018.

[11] C. A. Lopez. Extended model of the electron in general relativity. *Physical Review D*, 30(2):313, 1984.

[12] A. Burinskii. The Dirac-Kerr-Newman electron. *Gravitation and Cosmology*, 14(2):109, 2008.

[13] A. Burinskii. Gravity vs. quantum theory: Is electron really pointlike? In *Journal of Physics: Conference Series*, volume 343.1, page 012019. IOP Publishing, 2012.

[14] S. Zhu, B. Wang, and L. Duan. Simulation and detection of dirac fermions with cold atoms in an optical lattice. *Physical Review Letters*, 98(26):260402, 2007.

[15] J. I. Cirac, P. Maraner, and J. K. Pachos. Cold atom simulation of interacting relativistic quantum field theories. *Physical Review Letters*, 105(19):190403, 2010.

[16] L. J. LeBlanc, M. C. Beeler, K. Jiménez-García, A. R. Perry, S. Sugawa, R. A. Williams, and I. B. Spielman. Direct observation of zitterbewegung in a Bose–Einstein condensate. *New Journal of Physics*, 15(7):073011, 2013.

[17] K. Maeda, G. Baym, and T. Hatsuda. Simulating dense QCD matter with ultracold atomic boson-fermion mixtures. *Physical Review Letters*, 103(8):085301, 2009.

[18] L. He. Nambu–Jona–Lasinio model description of weakly interacting Bose condensate and BEC-BCS crossover in dense QCD-like theories. *Physical Review D*, 82(9):096003, 2010.

[19] M. Eto and M. Nitta. Confinement of half-quantized vortices in coherently coupled Bose-Einstein condensates: Simulating quark confinement in a QCD-like theory. *Physical Review A*, 97(2):023613, 2018.

[20] R. P. Feynman. Feynman lectures on physics. Volume 2: Mainly electromagnetism and matter. *Reading, Ma.: Addison-Wesley, 1964, edited by Feynman, R. P.; Leighton, R. B.; Sands, M.*, 1964.

[21] G. Lochak. The symmetry between electricity and magnetism and the problem of the existence of a magnetic monopole. In *Advanced Electromagnetism: Foundations, Theory and Applications*, pages 105–147. World Scientific, 1995.

[22] K. Y. Bliokh, A. Y. Bekshaev, and F. Nori. Dual electromagnetism: helicity, spin, momentum and angular momentum. *New Journal of Physics*, 15(3):033026, 2013.

[23] K. Rosquist. Gravitationally induced electromagnetism at the Compton scale. *Classical and Quantum Gravity*, 23(9):3111, 2006.

[24] H. Pu and P. Meystre. Creating macroscopic atomic Einstein-Podolsky-Rosen states from Bose–Einstein condensates. *Physical Review Letters*, 85(19):3987, 2000.

[25] L. Duan, J. I. Cirac, and P. Zoller. Quantum entanglement in spinor Bose–Einstein condensates. *Physical Review A*, 65(3):033619, 2002.

[26] M. L. Néel. Propriétés magnétiques des ferrites; ferrimagnétisme et antiferromagnétisme. In *Annales de Physique*, volume 12, pages 137–198, 1948.

[27] S. Chakravarty, B. I. Halperin, and D. R. Nelson. Two-dimensional quantum Heisenberg antiferromagnet at low temperatures. *Physical Review B*, 39(4):2344, 1989.

[28] E. P. Gross. Structure of a quantized vortex in boson systems. *Il Nuovo Cimento (1955-1965)*, 20(3):454–477, 1961.

[29] L. P. Pitaevskii. Vortex lines in an imperfect Bose gas. *Sov. Phys. JETP*, 13(2):451–454, 1961.

[30] F. Dalfovo, S. Giorgini, L. P. Pitaevskii, and S. Stringari. Theory of Bose–Einstein condensation in trapped gases. *Reviews of Modern Physics*, 71(3):463, 1999.

[31] J. R. Anglin and W. Ketterle. Bose–Einstein condensation of atomic gases. *Nature*, 416(6877):211, 2002.

[32] Y. Kawaguchi and M. Ueda. Spinor Bose–Einstein condensates. *Phys. Rep.*, 520(5):253 – 381, 2012.

[33] F. Gerbier, A. Widera, S. Fölling, O. Mandel, and I. Bloch. Resonant control of spin dynamics in ultracold quantum gases by microwave dressing. *Phys. Rev. A*, 73:041602, April 2006.

[34] S. R. Leslie, J. Guzman, M. Vengalattore, J. D. Sau, M. L. Cohen, and D. M. Stamper-Kurn. Amplification of fluctuations in a spinor Bose–Einstein condensate. *Phys. Rev. A*, 79:043631, April 2009.

[35] R-B. Li, L. Zhou, J. Wang, and M-S. Zhan. Measurement of the quadratic zeeman shift of ^{85}Rb hyperfine sublevels using stimulated raman transitions. *Optics Communications*, 282(7):1340–1344, 2009.

[36] D. A. Steck. Rubidium 87 D line data, 2010. Revision 2.1.5, Date accessed: 28 June 2018.

[37] D. A. Steck. Sodium D line data, 2010. Revision 2.1.4, Date accessed: 28 June 2018.

[38] D. M. Stamper-Kurn, M. R. Andrews, A. P. Chikkatur, S. Inouye, H.-J. Miesner, J. Stenger, and W. Ketterle. Optical confinement of a Bose–Einstein condensate. *Phys. Rev. Lett.*, 80:2027–2030, March 1998.

[39] M. H. Anderson, J. R. Ensher, M. R. Matthews, C. E. Wieman, and E. A. Cornell. Observation of Bose–Einstein condensation in a dilute atomic vapor. *Science*, 269(5221):198–201, 1995.

[40] K. B. Davis, M. O. Mewes, M. R. Andrews, N. J. van Druten, D. S. Durfee, D. M. Kurn, and W. Ketterle. Bose–Einstein condensation in a gas of sodium atoms. *Phys. Rev. Lett.*, 75:3969–3973, November 1995.

[41] C. C. Bradley, C. A. Sackett, J. J. Tollett, and R. G. Hulet. Evidence of Bose–Einstein condensation in an atomic gas with attractive interactions. *Phys. Rev. Lett.*, 75:1687–1690, August 1995.

[42] T.-L. Ho. Spinor Bose condensates in optical traps. *Phys. Rev. Lett.*, 81(4):742–745, July 1998.

[43] T. Ohmi and K. Machida. Bose–Einstein Condensation with Internal Degrees of Freedom in Alkali Atom Gases. *J. Phys. Soc. Jpn*, 67(6):1822–1825, 1998.

[44] M. D. Barrett, J. A. Sauer, and M. S. Chapman. All-optical formation of an atomic Bose–Einstein condensate. *Phys. Rev. Lett.*, 87(1):010404, June 2001.

[45] A. Görlitz, T. L. Gustavson, A. E. Leanhardt, R. Löw, A. P. Chikkatur, S. Gupta, S. Inouye, D. E. Pritchard, and W. Ketterle. Sodium Bose–Einstein condensates in the $F = 2$ state in a large-volume optical trap. *Phys. Rev. Lett.*, 90:090401, March 2003.

[46] H. Schmaljohann, M. Erhard, J. Kronjäger, M. Kottke, S. van Staa, L. Cacciapuoti, J. J. Arlt, K. Bongs, and K. Sengstock. Dynamics of $F = 2$ spinor Bose–Einstein condensates. *Phys. Rev. Lett.*, 92:040402, January 2004.

[47] Q. Beaufils, R. Chicireanu, T. Zanon, B. Laburthe-Tolra, E. Maréchal, L. Vernac, J.-C. Keller, and O. Gorceix. All-optical production of chromium Bose-Einstein condensates. *Phys. Rev. A*, 77:061601, June 2008.

[48] H. Pu, C. K. Law, S. Raghavan, J. H. Eberly, and N. P. Bigelow. Spin-mixing dynamics of a spinor Bose–Einstein condensate. *Physical Review A*, 60(2):1463, 1999.

[49] A. T. Black, E. Gomez, L. D. Turner, S. Jung, and P. D. Lett. Spinor dynamics in an antiferromagnetic spin-1 condensate. *Physical Review Letters*, 99(7):070403, 2007.

[50] Ö. E. Müstecaplıoğlu, M. Zhang, and L. You. Spin squeezing and entanglement in spinor condensates. *Physical Review A*, 66(3):033611, 2002.

[51] C. D. Hamley, C. S. Gerving, T. M. Hoang, E. M. Bookjans, and M. S. Chapman. Spin-nematic squeezed vacuum in a quantum gas. *Nature Physics*, 8:305, 2012.

[52] L. E. Sadler, J. M. Higbie, S. R. Leslie, M. Vengalattore, and D. M. Stamper-Kurn. Spontaneous symmetry breaking in a quenched ferromagnetic spinor Bose–Einstein condensate. *Nature*, 443(7109):312–315, 09 2006.

[53] Subroto Mukerjee, Cenke Xu, and J. E. Moore. Dynamical models and the phase ordering kinetics of the $s = 1$ spinor condensate. *Phys. Rev. B*, 76:104519, September 2007.

[54] K. Kudo and Y. Kawaguchi. Magnetic domain growth in a ferromagnetic Bose–Einstein condensate: Effects of current. *Phys. Rev. A*, 88:013630, July 2013.

[55] K. Kudo and Y. Kawaguchi. Coarsening dynamics driven by vortex-antivortex annihilation in ferromagnetic Bose–Einstein condensates. *Phys. Rev. A*, 91:053609, May 2015.

[56] L. A. Williamson and P. B. Blakie. Universal coarsening dynamics of a quenched ferromagnetic spin-1 condensate. *Phys. Rev. Lett.*, 116:025301, January 2016.

[57] T. Zibold, V. Corre, C. Frapolli, A. Invernizzi, J. Dalibard, and F. Gerbier. Spin-nematic order in antiferromagnetic spinor condensates. *Phys. Rev. A*, 93:023614, February 2016.

[58] Y. Liu, S. Jung, S. E. Maxwell, L. D. Turner, E. Tiesinga, and P. D. Lett. Quantum phase transitions and continuous observation of spinor dynamics in an antiferromagnetic condensate. *Phys. Rev. Lett.*, 102:125301, March 2009.

[59] E. M. Bookjans, A. Vinit, and C. Raman. Quantum Phase Transition in an Antiferromagnetic Spinor Bose–Einstein Condensate. *Phys. Rev. Lett.*, 107:195306, November 2011.

[60] A. Vinit and C. Raman. Precise measurements on a quantum phase transition in antiferromagnetic spinor Bose–Einstein condensates. *Phys. Rev. A*, 95:011603, January 2017.

[61] A. Vinit, E. M. Bookjans, C. A. R. Sá de Melo, and C. Raman. Antiferromagnetic spatial ordering in a quenched one-dimensional spinor gas. *Phys. Rev. Lett.*, 110:165301, April 2013.

[62] S. W. Seo, S. Kang, W. J. Kwon, and Y. Shin. Half-quantum vortices in an antiferromagnetic spinor Bose–Einstein condensate. *Phys. Rev. Lett.*, 115:015301, July 2015.

[63] Sang Won Seo, Woo Jin Kwon, Seji Kang, and Y. Shin. Collisional dynamics of half-quantum vortices in a spinor Bose–Einstein condensate. *Phys. Rev. Lett.*, 116:185301, May 2016.

[64] L. A. Williamson and P. B. Blakie. Coarsening and thermalization properties of a quenched ferromagnetic spin-1 condensate. *Phys. Rev. A*, 94:023608, August 2016.

[65] L. A. Williamson and P. B. Blakie. Coarsening dynamics of an isotropic ferromagnetic superfluid. *ArXiv e-prints arXiv:1703.09360*, March 2017.

[66] A. Bourges and P. B. Blakie. Different growth rates for spin and superfluid order in a quenched spinor condensate. *Phys. Rev. A*, 95:023616, February 2017.

[67] D. M. Stamper-Kurn and M. Ueda. Spinor Bose gases: Symmetries, magnetism, and quantum dynamics. *Rev. Mod. Phys.*, 85:1191–1244, July 2013.

[68] J. Schwichtenberg. *Physics from Symmetry.* Springer, 2015.

[69] C. V. Ciobanu, S.-K. Yip, and T.-L. Ho. Phase diagrams of $F = 2$ spinor Bose–Einstein condensates. *Physical Review A*, 61(3):033607, 2000.

[70] Erich J. Mueller. Spin textures in slowly rotating Bose–Einstein condensates. *Phys. Rev. A*, 69:033606, March 2004.

[71] E. Yukawa and M. Ueda. Hydrodynamic description of spin-1 Bose–Einstein condensates. *Phys. Rev. A*, 86:063614, December 2012.

[72] R. R. Silva. The trace formulas yield the inverse metric formula. *Journal of Mathematical Physics*, 39(11):6206–6213, 1998.

[73] T.-L. Ho and L. Yin. General structure of Bose–Einstein condensates with arbitrary spin. *Phys. Rev. Lett.*, 84:2302–2305, March 2000.

[74] J. L. Song, G. W. Semenoff, and F. Zhou. Uniaxial and biaxial spin nematic phases induced by quantum fluctuations. *Physical Review Letters*, 98(16):160408, 2007.

[75] A. M. Turner, R. Barnett, E. Demler, and A. Vishwanath. Nematic order by disorder in spin-2 Bose–Einstein condensates. *Physical Review Letters*, 98(19):190404, 2007.

[76] H. Mäkelä, Y. Zhang, and K.-A. Suominen. Topological defects in spinor condensates. *Journal of Physics A: Mathematical and General*, 36(32):8555, 2003.

[77] H. Mäkelä. Explicit expressions for the topological defects of spinor Bose–Einstein condensates. *Journal of Physics A: Mathematical and General*, 39(23):7423, 2006.

[78] U. Leonhardt and G. E. Volovik. How to create an Alice string (half-quantum vortex) in a vector Bose-Einstein condensate. *JETP Letters*, 72(2):46–48, 2000.

[79] P. Öhberg and L. Santos. Vortex-vortex interaction in two-component Bose–Einstein condensates. *Phys. Rev. A*, 66:013616, July 2002.

[80] M. Eto, K. Kasamatsu, M. Nitta, H. Takeuchi, and M. Tsubota. Interaction of half-quantized vortices in two-component Bose–Einstein condensates. *Phys. Rev. A*, 83:063603, June 2011.

[81] K. Kasamatsu, M. Eto, and M. Nitta. Short-range intervortex interaction and interacting dynamics of half-quantized vortices in two-component Bose–Einstein condensates. *Phys. Rev. A*, 93:013615, January 2016.

[82] A.-C. Ji, W. M. Liu, J. L. Song, and F. Zhou. Dynamical creation of fractionalized vortices and vortex lattices. *Phys. Rev. Lett.*, 101:010402, July 2008.

[83] W. E. Shirley, B. M. Anderson, C. W. Clark, and R. M. Wilson. Half-quantum vortex molecules in a binary dipolar Bose gas. *Phys. Rev. Lett.*, 113:165301, October 2014.

[84] S. Sternberg. *Lectures on differential geometry*, volume 316. American Mathematical Soc., 1999.

[85] P. J. Channell and C. Scovel. Symplectic integration of Hamiltonian systems. *Nonlinearity*, 3(2):231, 1990.

[86] K. Feng and M. Qin. *Symplectic geometric algorithms for Hamiltonian systems*. Springer, 2010.

[87] F. Strocchi. Complex coordinates and quantum mechanics. *Reviews of Modern Physics*, 38(1):36, 1966.

[88] G. Marmo and G. Vilasi. Symplectic structures and quantum mechanics. *Modern Physics Letters B*, 10(12):545–553, 1996.

[89] L. Gergely. On Hamiltonian formulations of the Schrödinger system. *Annals of Physics*, 298(2):394–402, 2002.

[90] G. Liang, Q. Guo, and Z. Ren. Canonical equations of Hamilton for the nonlinear Schrödinger equation. In *Journal of Physics: Conference Series*, volume 633, page 012041. IOP Publishing, 2015.

[91] Hanquan Wang. A time-splitting spectral method for computing dynamics of spinor F=1 Bose–Einstein condensates. *Int. J. Comput. Math.*, 84(6):925–944, 2007.

[92] M.-S. Chang, Q. Qin, W. Zhang, L. You, and M. S. Chapman. Coherent spinor dynamics in a spin-1 Bose condensate. *Nat. Phys.*, 1:111, 2005.

[93] W. Zhang, D. L. Zhou, M.-S. Chang, M. S. Chapman, and L. You. Coherent spin mixing dynamics in a spin-1 atomic condensate. *Physical Review A*, 72(1):013602, 2005.

[94] D. A. Takahashi. An inequality for spinor Bose–Einstein condensates. *Journal of the Physical Society of Japan*, 84(2):025001, 2015.

[95] T. L. Curtright, D. B. Fairlie, and C. K. Zachos. A compact formula for rotations as spin matrix polynomials. *SIGMA*, 10(084):084, 2014.

[96] S. Uchino, T. Otsuka, and M. Ueda. Dynamical symmetry in spinor Bose–Einstein condensates. *Phys. Rev. A*, 78:023609, August 2008.

[97] R. I. McLachlan and G. R. W. Quispel. Splitting methods. *Acta Numerica*, 11:341–434, 2002.

[98] S. P. Auerbach and A. Friedman. Long-time behaviour of numerically computed orbits: Small and intermediate timestep analysis of one-dimensional systems. *Journal of computational physics*, 93(1):189–223, 1991.

[99] R. D. Skeel and C. W. Gear. Does variable step size ruin a symplectic integrator? *Physica D: Nonlinear Phenomena*, 60(1-4):311–313, 1992.

[100] E. Hairer. Variable time step integration with symplectic methods. *Applied Numerical Mathematics*, 25(2-3):219–227, 1997.

[101] A. S. Richardson and J. M. Finn. Symplectic integrators with adaptive time steps. *Plasma Physics and Controlled Fusion*, 54(1):014004, 2011.

[102] R. Courant, K. Friedrichs, and H. Lewy. On the partial difference equations of mathematical physics. *IBM journal of Research and Development*, 11(2):215–234, 1967.

[103] R. W. Hockney and J. W. Eastwood. *Computer simulation using particles*. crc Press, 1988.

[104] A. K. Mazur. Common molecular dynamics algorithms revisited: accuracy and optimal time steps of Störmer–Leapfrog integrators. *Journal of Computational Physics*, 136(2):354–365, 1997.

[105] H. Yoshida. Construction of higher order symplectic integrators. *Physics letters A*, 150(5-7):262–268, 1990.

[106] J. M. Sanz-Serna and M.-P. Calvo. Symplectic numerical methods for Hamiltonian problems. *International Journal of Modern Physics C*, 4(02):385–392, 1993.

[107] E. Hairer, C. Lubich, and G. Wanner. *Geometric numerical integration: structure-preserving algorithms for ordinary differential equations*, volume 31. Springer Science & Business Media, 2006.

[108] S. Blanes and P.C. Moan. Practical symplectic partitioned Runge-Kutta and Runge-Kutta-Nyström methods. *J. Comput. Appl. Math.*, 142(2):313 – 330, 2002.

[109] R. I. McLachlan and G. R. W. Quispel. Geometric integrators for ODEs. *J. Phys. A Math. Gen.*, 39(19):5251, 2006.

[110] W. Bao and Y. Cai. Mathematical models and numerical methods for spinor Bose–Einstein conensates. *ArXiv preprint arXiv:1709.03840*, 2017.

[111] K. Gawryluk, T. Karpiuk, M. Gajda, K. Rzążewski, and M. Brewczyk. Unified way for computing dynamics of Bose–Einstein condensates and degenerate fermi gases. *International Journal of Computer Mathematics*, pages 1–19, 2017.

[112] W. Bao, H. Li, and J. Shen. A generalized-Laguerre–Fourier–Hermite pseudospectral method for computing the dynamics of rotating Bose–Einstein condensates. *SIAM J. Sci. Comput.*, 31(5):3685–3711, 2009.

[113] W. Bao and Y. Zhang. Dynamical laws of the coupled Gross-Pitaevskii equations for spin-1 Bose–Einstein condensates. *Methods Appl. Anal.*, 17(1):49–80, 03 2010.

[114] H. Wang. An efficient numerical method for computing dynamics of spin $F = 2$ Bose–Einstein condensates. *J. Comput. Phys.*, 230(15):6155 – 6168, 2011.

[115] G. R. Dennis, J. J. Hope, and M. T. Johnsson. XMDS2: fast, scalable simulation of coupled stochastic partial differential equations. *Comput. Phys. Commun.*, 184(1):201 – 208, 2013.

[116] W. Bao, I. Chern, and F. Y. Lim. Efficient and spectrally accurate numerical methods for computing ground and first excited states in Bose–Einstein condensates. *Journal of Computational Physics*, 219(2):836–854, 2006.

[117] W. Bao and H. Wang. A mass and magnetization conservative and energy-diminishing numerical method for computing ground state of spin-1 Bose–Einstein condensates. *SIAM Journal on Numerical Analysis*, 45(5):2177–2200, 2007.

[118] F. Y. Lim and W. Bao. Numerical methods for computing the ground state of spin-1 Bose–Einstein condensates in a uniform magnetic field. *Phys. Rev. E*, 78:066704, December 2008.

[119] W. Bao and F. Y. Lim. Computing ground states of spin-1 Bose–Einstein condensates by the normalized gradient flow. *SIAM Journal on Scientific Computing*, 30(4):1925–1948, 2008.

[120] W. Bao, I. Chern, and Y. Zhang. Efficient numerical methods for computing ground states of spin-1 Bose–Einstein condensates based on their characterizations. *Journal of Computational Physics*, 253:189–208, 2013.

[121] Q. Sheng. Solving linear partial differential equations by exponential splitting. *IMA Journal of numerical analysis*, 9(2):199–212, 1989.

[122] M. Suzuki. General theory of fractal path integrals with applications to many-body theories and statistical physics. *Journal of Mathematical Physics*, 32(2):400–407, 1991.

[123] F. W. Strauch. Any-order propagation of the nonlinear Schrödinger equation. *Physical Review E*, 76(4):046701, 2007.

[124] P. Bader, S. Blanes, and F. Casas. Solving the Schrödinger eigenvalue problem by the imaginary time propagation technique using splitting methods with complex coefficients. *The Journal of Chemical Physics*, 139(12):124117, 2013.

[125] S. A. Chin and J. Geiser. Multi-product operator splitting as a general method of solving autonomous and nonautonomous equations. *IMA Journal of Numerical Analysis*, 31(4):1552–1577, 2011.

[126] S. Gautam and S. K. Adhikari. Spontaneous symmetry breaking in a spin-orbit-coupled $f = 2$ spinor condensate. *Phys. Rev. A*, 91:013624, January 2015.

[127] S. A. Chin. Higher-order splitting algorithms for solving the nonlinear Schrödinger equation and their instabilities. *Phys. Rev. E*, 76(5):056708, 2007.

[128] R. S. Tasgal and Y. B. Band. Continuous-wave solutions in spinor Bose–Einstein condensates. *Phys. Rev. A*, 87:023626, February 2013.

[129] E. Hairer, R. I. McLachlan, and A. Razakarivony. Achieving Brouwer's law with implicit Runge-Kutta methods. *BIT*, 48(2):231–243, 2008.

[130] H. E. Nistazakis, D. J. Frantzeskakis, P. G. Kevrekidis, B. A. Malomed, and R. Carretero-González. Bright-dark soliton complexes in spinor Bose–Einstein condensates. *Phys. Rev. A*, 77:033612, March 2008.

[131] M. Ueda and M. Koashi. Theory of spin-2 Bose–Einstein condensates: Spin correlations, magnetic response, and excitation spectra. *Phys. Rev. A*, 65:063602, May 2002.

[132] L. M. Symes, R. I. McLachlan, and P. B. Blakie. Efficient and accurate methods for solving the time-dependent spin-1 Gross-Pitaevskii equation. *Phys. Rev. E*, 93:053309, May 2016.

[133] H. Orihara and Y. Ishibashi. Dynamics of disclinations in twisted nematics quenched below the clearing point. *J. Phys. Soc. Jpn.*, 55(7):2151–2156, 1986.

[134] I. Chuang, N. Turok, and B. Yurke. Late-time coarsening dynamics in a nematic liquid crystal. *Phys. Rev. Lett.*, 66:2472–2475, May 1991.

[135] I. Chuang, R. Durrer, N. Turok, and B. Yurke. Cosmology in the laboratory: Defect dynamics in liquid crystals. *Science*, 251(4999):1336–1342, 1991.

[136] B. Yurke, A. N. Pargellis, and N. Turok. Coarsening dynamics in nematic liquid crystals. *Mol. Cryst. Liq. Cryst. Sci. Technol., Sect. A*, 222(1):195–203, 1992.

[137] T. Nagaya, H. Hotta, H. Orihara, and Y. Ishibashi. Experimental study of the coarsening dynamics of +1 and −1 disclinations. *J. Phys. Soc. Jpn.*, 61(10):3511–3517, 1992.

[138] R. E. Blundell and A. J. Bray. Phase-ordering dynamics of nematic liquid crystals. *Phys. Rev. A*, 46:R6154–R6157, November 1992.

[139] I. Chuang, B. Yurke, A. N. Pargellis, and N. Turok. Coarsening dynamics in uniaxial nematic liquid crystals. *Phys. Rev. E*, 47:3343–3356, May 1993.

[140] N. T. Phuc, Y. Kawaguchi, and M. Ueda. Fluctuation-induced and symmetry-prohibited metastabilities in spinor Bose–Einstein condensates. *Phys. Rev. A*, 88:043629, October 2013.

[141] J. Jiang, L. Zhao, M. Webb, and Y. Liu. Mapping the phase diagram of spinor condensates via adiabatic quantum phase transitions. *Phys. Rev. A*, 90:023610, August 2014.

[142] J. Lovegrove, M. O. Borgh, and J. Ruostekoski. Energetically stable singular vortex cores in an atomic spin-1 Bose–Einstein condensate. *Phys. Rev. A*, 86:013613, July 2012.

[143] I. Carusotto and E. J. Mueller. Imaging of spinor gases. *Journal of Physics B: Atomic, Molecular and Optical Physics*, 37(7):S115, 2004.

[144] J. M. Higbie, L. E. Sadler, S. Inouye, A. P. Chikkatur, S. R. Leslie, K. L. Moore, V. Savalli, and D. M. Stamper-Kurn. Direct nondestructive imaging of magnetization in a spin-1 Bose–Einstein gas. *Phys. Rev. Lett.*, 95:050401, July 2005.

[145] D. Baillie and P. B. Blakie. Spin-dependent Bragg spectroscopy of a spinor Bose gas. *Phys. Rev. A*, 93:033607, March 2016.

[146] M. Karl, B. Nowak, and T. Gasenzer. Universal scaling at nonthermal fixed points of a two-component Bose gas. *Phys. Rev. A*, 88:063615, December 2013.

[147] J. Sethna. What is Coarsening?, Jun 2006. Date accessed: 4 July 2018.

[148] A. J. Bray and A. D. Rutenberg. Growth laws for phase ordering. *Phys. Rev. E*, 49:R27–R30, January 1994.

[149] A. J. Bray. Coarsening dynamics of phase-separating systems. *Phil. Trans. R. Soc. A*, 361(1805):781–792, 2003.

[150] S. Kang, S. W. Seo, J. H. Kim, and Y.-i. Shin. Emergence and scaling of spin turbulence in quenched antiferromagnetic spinor Bose–Einstein condensates. *ArXiv e-prints arXiv:1701.01559*, January 2017.

[151] E. Witkowska, T. Ś, and M. Matuszewski. Thermal fluctuations and quantum phase transition in antiferromagnetic Bose–Einstein condensates. *Phys. Rev. A*, 90:033604, September 2014.

[152] P. G. de Gennes and J. Prost. *The Physics of Liquid Crystals*. International Series of Monographs on Physics. Clarendon Press, 1995.

[153] P. B. Blakie, A. S. Bradley, M. J. Davis, R. J. Ballagh, and C. W. Gardiner. Dynamics and statistical mechanics of ultra-cold Bose gases using c-field techniques. *Adv. Phys.*, 57:363, 2008.

[154] A. Lamacraft. Quantum quenches in a spinor condensate. *Phys. Rev. Lett.*, 98:160404, April 2007.

[155] H. Saito, Y. Kawaguchi, and M. Ueda. Kibble-Zurek mechanism in a quenched ferromagnetic Bose–Einstein condensate. *Phys. Rev. A*, 76:043613, October 2007.

[156] R. Barnett, A. Polkovnikov, and M. Vengalattore. Prethermalization in quenched spinor condensates. *Phys. Rev. A*, 84:023606, August 2011.

[157] J. Guzman, G.-B. Jo, A. N. Wenz, K. W. Murch, C. K. Thomas, and D. M. Stamper-Kurn. Long-time-scale dynamics of spin textures in a degenerate $F = 1$ ^{87}Rb spinor Bose gas. *Phys. Rev. A*, 84:063625, December 2011.

[158] A.J. Bray. Theory of phase-ordering kinetics. *Advances in Physics*, 43(3):357–459, 1994.

[159] B. Yurke, A. N. Pargellis, T. Kovacs, and D. A. Huse. Coarsening dynamics of the XY model. *Phys. Rev. E*, 47:1525–1530, March 1993.

[160] A. J. Bray, A. J. Briant, and D. K. Jervis. Breakdown of scaling in the nonequilibrium critical dynamics of the two-dimensional XY model. *Phys. Rev. Lett.*, 84:1503–1506, February 2000.

[161] M. Kulczykowski and M. Matuszewski. Phase ordering kinetics of a nonequilibrium exciton-polariton condensate. *Phys. Rev. B*, 95:075306, February 2017.

[162] A. N. Pargellis, P. Finn, J. W. Goodby, P. Panizza, B. Yurke, and P. E. Cladis. Defect dynamics and coarsening dynamics in smectic-C films. *Phys. Rev. A*, 46:7765–7776, December 1992.

[163] K. Nam, B. Kim, and S. J. Lee. Coarsening kinetics of a two-dimensional O(2) Ginzburg–Landau model: the effect of reversible mode coupling. *J. Stat. Mech*, 2011(03):P03013, 2011.

[164] A. Singh, S. Ahmad, S. Puri, and S. Singh. Ordering dynamics of nematic liquid crystals: Monte Carlo simulations. *EPL*, 100(3):36004, 2012.

[165] A. Singh and S. Singh. Phase ordering kinetics in uniaxial nematic liquid crystals with second- and fourth-rank interactions. *Eur. Phys. J. E*, 36(10):122, 2013.

[166] A. J. Bray and S. Puri. Asymptotic structure factor and power-law tails for phase ordering in systems with continuous symmetry. *Phys. Rev. Lett.*, 67:2670–2673, November 1991.

[167] A. M. Turner. Mass of a spin vortex in a Bose–Einstein condensate. *Phys. Rev. Lett.*, 103:080603, August 2009.

[168] L. A. Williamson and P. B. Blakie. Dynamics of polar-core spin vortices in a ferromagnetic spin-1 Bose–Einstein condensate. *Phys. Rev. A*, 94:063615, December 2016.

[169] C. D. Hamley, C. S. Gerving, T. M. Hoang, E. M. Bookjans, and M. S. Chapman. Spin-nematic squeezed vacuum in a quantum gas. *Nature Physics*, 8(4):305, 2012.

[170] L. M. Symes and P. B. Blakie. Nematic ordering dynamics of an antiferromagnetic spin-1 condensate. *Physical Review A*, 96(1):013602, 2017.

[171] C. Samuelis, E. Tiesinga, T. Laue, M. Elbs, H. Knöckel, and E. Tiemann. Cold atomic collisions studied by molecular spectroscopy. *Physical Review A*, 63(1):012710, 2000.

[172] K. Liu et al. *Gauge theory and nematic order: the rich landscape of orientational phase transition*. PhD thesis, Leiden University, 2016.

[173] K. Liu, J. Nissinen, R.-J. Slager, K. Wu, J. Zaanen, et al. Generalized liquid crystals: Giant fluctuations and the vestigial chiral order of I, O, and T matter. *Physical Review X*, 6(4):041025, 2016.

[174] J. Nissinen, K. Liu, R.-J. Slager, K. Wu, J. Zaanen, et al. Classification of point-group-symmetric orientational ordering tensors. *Physical Review E*, 94(2):022701, 2016.

[175] A. J. Beekman, J. Nissinen, K. Wu, and J. Zaanen. Dual gauge field theory of quantum liquid crystals in three dimensions. *Physical Review B*, 96(16):165115, 2017.

[176] K. Liu, J. Nissinen, J. de Boer, R.-J. Slager, J. Zaanen, et al. Hierarchy of orientational phases and axial anisotropies in the gauge theoretical description of generalized nematic liquid crystals. *Physical Review E*, 95(2):022704, 2017.

[177] K. Liu, J. Greitemann, L. Pollet, et al. Generic first-order phase transitions between isotropic and orientational phases with polyhedral symmetries. *Physical Review E*, 97(1):012706, 2018.

[178] N. Shitara, S. Bir, and P. B. Blakie. Domain percolation in a quenched ferromagnetic spinor condensate. *New Journal of Physics*, 19(9):095003, 2017.

[179] L. A. Williamson. *Phase ordering dynamics in a ferromagnetic spin-1 Bose-Einstein condensate*. PhD thesis, University of Otago, 2017.

[180] A. A. Norrie, R. J. Ballagh, C. W. Gardiner, and A. S. Bradley. Three-body recombination of ultracold Bose gases using the truncated Wigner method. *Physical Review A*, 73(4):043618, 2006.

[181] M. O. Borgh and J. Ruostekoski. Core structure and non-Abelian reconnection of defects in a biaxial nematic spin-2 Bose-Einstein condensate. *Physical Review Letters*, 117(27):275302, 2016.

[182] G. W. Semenoff and F. Zhou. Discrete symmetries and 1/3 quantum vortices in condensates of $F = 2$ cold atoms. *Phys. Rev. Lett.*, 98:100401, March 2007.

[183] M. Kobayashi, Y. Kawaguchi, M. Nitta, and M. Ueda. Collision dynamics and rung formation of non-abelian vortices. *Phys. Rev. Lett.*, 103(11):115301, 2009.

[184] J. A. M. Huhtamäki, T. P. Simula, M. Kobayashi, and K. Machida. Stable fractional vortices in the cyclic states of Bose-Einstein condensates. *Physical Review A*, 80(5):051601, 2009.

[185] T. Mawson, T. C. Petersen, and T. Simula. Collision dynamics of two-dimensional non-Abelian vortices. *Physical Review A*, 96(3):033623, 2017.

[186] T. Mawson, T. Petersen, and T. Simula. Braiding and fusion of non-Abelian vortex anyons. *ArXiv preprint arXiv:1805.10009*, 2018.

[187] M. H Freedman. P/NP, and the quantum field computer. *Proceedings of the National Academy of Sciences*, 95(1):98–101, 1998.

[188] A. Y. Kitaev. Fault-tolerant quantum computation by anyons. *Annals of Physics*, 303(1):2–30, 2003.

[189] M. Eto, Y. Hirono, M. Nitta, and S. Yasui. Vortices and other topological solitons in dense quark matter. *Progress of Theoretical and Experimental Physics*, 2014(1), 2014.

[190] S. H. Hendi, B. E. Panah, M. Momennia, and S. Panahiyan. Three dimensional nonlinear magnetic AdS solutions through topological defects. *The European Physical Journal C*, 75(9):457, 2015.

[191] J. Lovegrove, M. O. Borgh, and J. Ruostekoski. Energetic stability of coreless vortices in spin-1 Bose-Einstein condensates with conserved magnetization. *Physical Review Letters*, 112(7):075301, 2014.

[192] J. Lovegrove, M. O. Borgh, and J. Ruostekoski. Stability and internal structure of vortices in spin-1 Bose-Einstein condensates with conserved magnetization. *Physical Review A*, 93(3):033633, 2016.

[193] T. W. B. Kibble. Topology of cosmic domains and strings. *Journal of Physics A: Mathematical and General*, 9(8):1387, 1976.

[194] M. J. Duff. M-theory on manifolds of G2 holonomy: the first twenty years. *ArXiv preprint hep-th/0201062*, 2002.

[195] K. Behrndt. Singular 7-manifolds with G2 holonomy and intersecting 6-branes. *Nuclear Physics B*, 635(1-2):158–174, 2002.

[196] E. Witten. Deconstruction, G2 Holonomy, and Doublet-Triplet Splitting. *ArXiv preprint hep-ph/0201018*, 2002.